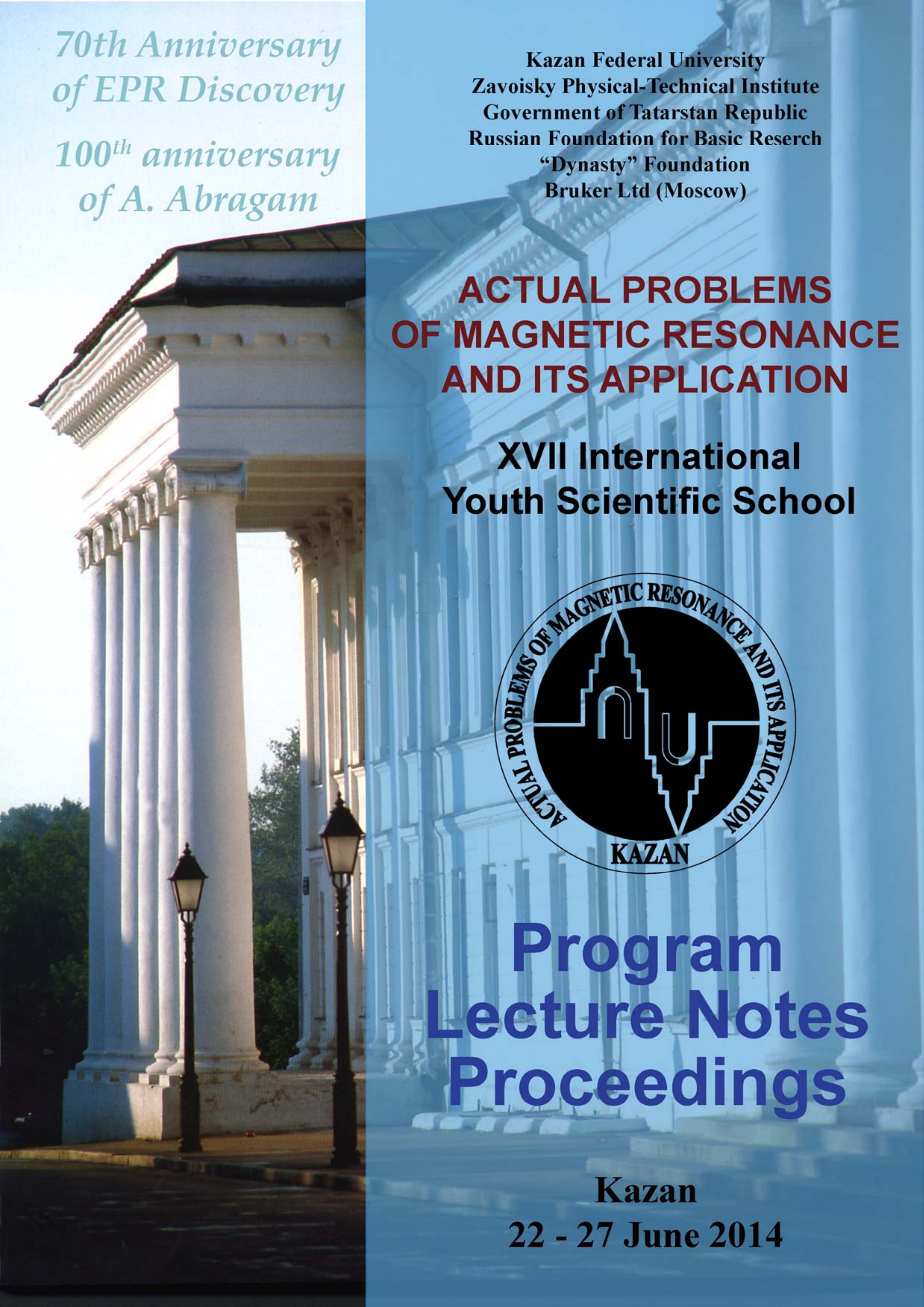

70th Anniversary of EPR Discovery

100th anniversary of A. Abragam

Kazan Federal University
Zavoisky Physical-Technical Institute
Government of Tatarstan Republic
Russian Foundation for Basic Reserch
“Dynasty” Foundation
Bruker Ltd (Moscow)

ACTUAL PROBLEMS OF MAGNETIC RESONANCE AND ITS APPLICATION

XVII International Youth Scientific School

ACTUAL PROBLEMS OF MAGNETIC RESONANCE AND ITS APPLICATION
KAZAN

Program
Lecture Notes
Proceedings

Kazan
22 - 27 June 2014

Kazan Federal University
Zavoisky Physical-Technical Institute
Government of Tatarstan Republic
Russian Foundation for Basic Reserch
“Dynasty” Foundation
Bruker Ltd (Moscow)

ACTUAL PROBLEMS OF MAGNETIC RESONANCE AND ITS APPLICATION

XVII International Youth Scientific School

Program
Lecture Notes
Proceedings

Kazan
22 – 27 June 2014

KAZAN UNIVERSITY
2014

УДК 537
ББК 22.334
А 19

The administration of School

Professor M.S. Tagirov (KFU, Kazan) — rector
Professor V.A. Zhikharev (KSTU, Kazan) — vice-rector
V.K. Voronkova (KFTI RAS, Kazan) — scientific secretary
I.P. Volodina (KFU, Kazan) — secretary

The program committee

The chairman
Professor V.A. Atsarkin (IREE, Moscow)

Committee members

Professor A.V. Aganov (KFU, Kazan)
Professor B.I. Kochelaev (KFU, Kazan)
Professor I.V. Ovchinnikov (KFTI RAS, Kazan)
Professor K.M. Salikhov (KFTI RAS, Kazan)

The organizing committee

M.S. Tagirov, V.A. Zhikharev, I.P. Volodina, I.G. Motygullin, A.V. Klochkov,
V.V. Semashko, A.S. Nizamutdinov, A.K. Naumov, E.M. Alakshin, I.V. Romanova,
O.N. Chibisova, M.P. Rodionova, R.R. Gazizulin, E.I. Kondratyeva, T.R. Safin,

Actual problems of magnetic resonance and its application: program lecture notes proceedings of the XVII International Youth Scientific School (Kazan, 22 – 27 June 2014) / edited by M.S. Tagirov (Kazan Federal University), V.A. Zhikharev (Kazan State Technological University). – Kazan: Kazan University, 2014. – 165 p.

ISBN 978-5-00019-222-1

The reports of young scientists submitted on XVII International Youth Scientific School “Actual problems of magnetic resonance and its application” carry out by Kazan Federal (Volga Region) University and Zavoisky Physical-Technical Institute are included in the present collection.

УДК 537
ББК 22.334

ISBN 978-5-00019-222-1

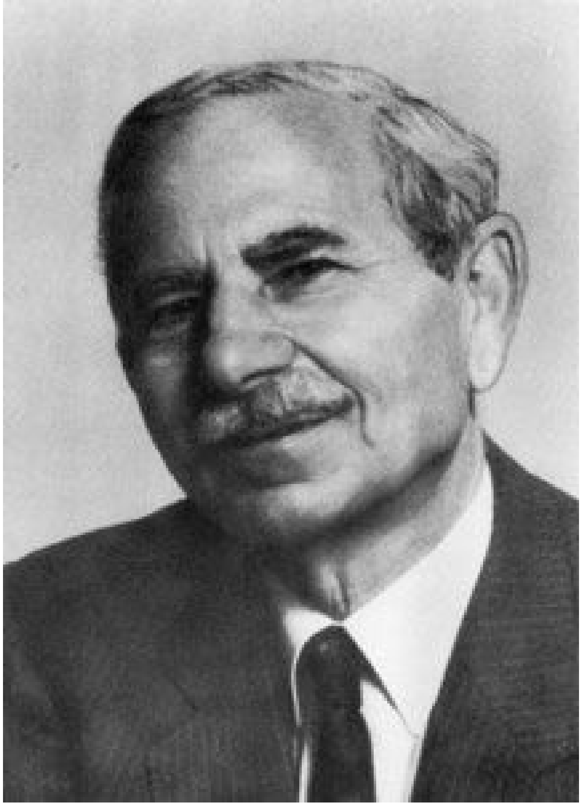

In 2014 the world physics community celebrates the 100th anniversary of the birth of Anatole Abragam, one of the most prominent scientists in the field of magnetic radiospectroscopy. He was the Professor of the College de France, the member of the French Academy, the President of the French Physics Society, the Commander of the Ordre de la Legion d'Honneur... All these regalia belong to a man with an inquisitive mind, a great organizer of science, friendly colleague and witty conversationalist. In the history of science the name of A. Abragam is associated with the discovery of dynamic polarization of nuclei, nuclear anti-ferromagnetism, and his thorough research of hyperfine structure of magnetic resonance spectra. For many scientists, the world of magnetic resonance phenomena opened with a brilliant A. Abragam's book — "Nuclear Magnetism". Written in 1961, this book to this day has not lost its honorable place among the books in which the balance between the depth of subject penetration and the simplicity of explanations is brought to perfection. One can be sure that young scientists working in any modern branch of magnetic resonance studies will find in the Anatole Abragam's books and papers the answers to their questions and an inspiration for their own discoveries for many years to come.

M.S. Tagirov and V.A. Zhiharev

Program

Sunday, June 22

Institute of Physics

8:30 **Registration**

Auditorium 210. Institute of Physics.

9:30 – 9:45 **Opening Ceremony of School-2014**

Lectures

Auditorium 110. Institute of Physics.

Chairman – **M.S. Tagirov**

9:45 – 10:30 **U. Eichhoff** (Bruker BioSpin GmbH, Silberstreifen, Germany), “Medical Applications of EPR”

10:30 – 11:15 **N.M. Sergeyev** (Moscow State University, Moscow, Russia), “70 Years of nuclear magnetic resonance study of water. What is still not clear?”

11:15 – 11:30 **Coffee break**

Oral Session

Auditorium 110. Institute of Physics.

Magnetic Resonance in Solids.

Chairman – **M.S. Tagirov**

11:30 – 11:45 **A.A. Bayazitov,** “Development of quadrature coils “Neck” for low field MRI”

11:45 – 12:00 **T.B. Biktagirov,** “Multi-frequency EPR/ENDOR and DFT study of impurities in (nano)hydroxyapatite”

12:00 – 12:15 **B.F. Gabbasov,** “Electron paramagnetic resonance of the $SrTiO_3$:Mn crystals”

12:15 – 12:30 **M.D. Galimov,** “Prototyping of gradient controller for MRI scanner”

12:30 – 12:45 **L.V. Konopleva,** “Assessment of correctness of MRI based Fiber Tracks”

12:45 – 13:00 **T.A. Zaripov,** “Studies of correlation between viscosity oil and nuclear magnetic relaxation characteristics”

Auditorium 112. Institute of Physics.

Coherent Optics and Optical Spectroscopy

Chairman – **V.V. Semashko**

11:30 – 11:45 **O.R. Akhtyamov,** “Ultrashort pulsed UV lasers based on the $Ce^{3+}:LiCaAlF_6$ and $LiLuYF_4:Ce^{3+}$ crystals”

11:45 – 12:00 **A.I. Galiev,** “Photodynamic processes in $LiCaAlF_6:Ce^{3+}$ UV active medium”

12:00 – 12:15 **V.G. Gorieva,** “$LiY_{0.3}Lu_{0.7}F_4$: Ce^{3+}, Pr^{3+} mixed crystal as a perspective up-conversionally pumped UV active medium”

12:15 – 12:30 **R.A. Idrisov,** “The development of polymer laser-active media with improved performances”

12:30 – 12:45 **A.V. Lovchev,** “Up-conversion luminescence of $LaF_3:Pr^{3+}$ crystal”

12:45 – 13:00 **M.S. Pudovkin,** “Toxicity of photoactive fluoride nanoparticles PrF_3 and LaF_3 for biological organisms (bacteria, cancer cells) under the laser irradiation”

13:00 – 14:00 **Lunch**

Auditorium 110. Institute of Physics.

Magnetic Resonance in Solids.

Chairman – **F.S. Dzeparov**

14:00 – 14:15 **G.R. Nureeva,** “Pulse and CW EPR techniques to study of biradical systems”

14:15 – 14:30 **I.R. Sitdikov,** “Development of hardware-software complex to switch between sensors for measuring magnetic field homogeneity of resonance magnetic tomograph”

14:30 – 14:45 **I.V. Yatsyk,** “Existence of the two-dimensional electron gas at the interface multiferroic/ferroelectric $GdMnO_3/SrTiO_3$ detected by ESR”

14:45 – 15:00 **K.M. Yunusova,** “Pulsed EPR study of photoinduced paramagnetic centres in meteoritic nanodiamonds”

15:00 – 15:30 **V.O. Sakhin,** “Local magnetization above T_c in the $La_{2-x}Sr_xCuO_4$ single crystals studied by EPR”

15:30 – 15:45 **P.A. Agzamova,** “Magnetic hyperfine interactions on ^{51}V nucleus in pyrochlore $Lu_2V_2O_7$”

Auditorium 112. Institute of Physics.

Coherent Optics and Optical Spectroscopy

Chairman – **A.S. Nizamutdinov**

14:00 – 14:15 **N.F. Rakhimov,** “Optical and physical properties of fluorite crystala CaF_2: Ce^{3+}, Yb^{3+}, Lu^{3+}”

14:15 – 14:30 **I.I. Farukhshin,** “Study of laser characteristics of active medium $LiLu_{0.7}Y_{0.3}F_4:Ce^{3+}$ in ultra-short pulse mode”

14:30 – 14:45 **A.A. Shavelev,** “Grows of solid solutions with colquiriite structure $LiCa_{1-X}Sr_XAlF_6:Ce^{3+}$”

14:45 – 15:00 **S.A. Shnaidman,** “Dynamical processes investigation in $CaF_2:Ce^{3+}+Yb^{3+}$ and mixed $CaF_2 – LuF_3:Ce^{3+} + Yb^{3+}$ crystals”

15:00 – 15:30 **V.V. Pavlov,** “Photoinduced processes in Ce^{3+} doped $SrAlF_5$ crystal”

15:30 – 15:45 **M.A. Smirnov,** “The effect of chromophores concentration on the quadratic nonlinear optical activity of methacrylic compymers with azochromophores in the side chain”

11:15 – 11:30 **Coffee break**

Auditorium 110. Institute of Physics.

Magnetic Resonance in Solids.

Chairman – **E.B. Fel’dman**

16:00 – 16:15 **O.A. Babanova,** “NMR study of reorientational and translational motion of BH_4 groups in novel bimetallic perovskite-type borohydrides”

16:15 – 16:30 **Z.N. Volkova,** “Melting of the orbital order in $LaMnO_3$: the ^{17}O, ^{139}La NMR study”

16:30 – 16:45 **A.I. Dmitriev,** “Magnetic phase transition in ε-$In_{0.24}Fe_{1.76}O_3$ nanowires”

16:45 – 17:00 **V.O. Ievleva,** “^1H NMR study of hydrogen site occupancy in hydrides of disordered Ti-Nb”

17:00 – 17:15 **R.D. Nevmyvako,** “NMR in $Li_2M_3Al(MoO_4)_4$ triple molybdates (M = Rb,Cs)”

17:15 – 17:30 **I.N. Razmislov,** “Ferromagnetic resonance properties of nanocomposite ferromagnetic thin films”

17:30 – 17:45 **A.G. Smolnikov,** “$^{63,65}Cu$ NMR/NQR study on the geometric frustrated multiferroic $CuCrO_2$”

17:45 – 18:00 **A.F. Sadykov,** “The features of the magnetic properties of low-dimensional isostructural cuprates $NaCu_2O_2$ and $LiCu_2O_2$ investigated by NMR”

Auditorium 112. Institute of Physics.

Magnetic Resonance in Chemistry, Biology and Medicine

Chairman – **A.V. Klochkov**

16:00 – 16:15 **Yu.Yu. Titova,** “Magnetic resonance (NMR, ESR) in the study of the formation mechanism of catalysts based on nickel phosphine complexes and boron trifluoride etherate in the lower alkenes dimerization”

16:15 – 16:30 **O.V. Aganova,** “The study of the conformation and dynamics derivative of the new quaternary phosphonium salts by NMR spectroscopy”

16:30 – 16:45 **V.E. Vorobeva,** “Coexistence of spin crossover and magnetic ordering in the dendrimeric iron(III) complex”

16:45 – 17:00 **I.Z. Rakhmatullin,** “Complex formation between pravastatin and sodium dodecyl sulfate micelle studied by NMR spectroscopy”

17:00 – 17:15 **K.S. Usachev,** “Solution NMR structures of the Arctic and the wild types of Alzheimer’s Aβ peptides in membrane mimicking environment”

17:15 – 17:30 **K.B. Konov,** “The study of sugars influence on mobility of lipid bilayer”

17:30 – 17:45 **I.E. Apanasenko,** “NMR and optical study of supramolecular complexes of carotenoids lutein and zeaxanthin”

17:45 – 18:00 **Yu.V. Berestneva,** “Interaction of the 1,1,3-trimethyl-3-(4-methylphenyl)butyl hydroperoxide with tetraethylammonium bromide”

18:00 – 18:15 **Coffee break**

Auditorium 110. Institute of Physics.

Magnetic Resonance in Solids.

Chairman – **S.B. Orlinskii**

18:15 – 18:30 **E.A. Sviridov,** “Determination of d(CAGCGGCGTG)·d(CACGCCGCTG) DNA-duplex spatial structure by NMR-spectroscopy”

18:30 – 18:45 **T.A. Soldatov,** “Collapse of the spinon doublet in the spin-liquid phase of Cs_2CuCl_4”

18:45 – 19:00 **V.A. Soltamov,** “Optical and electrical manipulation of a silicon vacancy related defects spin states in Silicon Carbide”

19:00 – 19:15 **M.Yu. Zakharov,** “^{1}H NMR of water colloidal solutions of nanosized crystalline particles $LaF_3:Gd^{3+}$”

19:15 – 19:30 **A.A. Kamashev,** “Effect of superconducting spin valve and triplet superconductivity in Fe1/Cu/Fe2/Cu/Pb heterostructures”

19:30 – 19:45 **Yu.S. Kutin,** “W-band ENDOR study of V^{2+} and Mn^{2+} in ZnO”

19:45 – 20:00 **B.V. Yavkin,** “Fluoride-modified nanodiamonds studied by HF EPR”

Auditorium 112. Institute of Physics.

Magnetic Resonance in Chemistry, Biology and Medicine

Chairman – **V.A. Zhikharev**

18:15 – 18:30 **Yu.Yu. Titova,** “EPR, and hydrogenation, and polymerization catalysis by systems based on nickel complexes with 1,4-diaza-1,3-butadiene (α-diimine) ligands”

18:30 – 18:45 **E.D. Gerts,** “Analysis of experimental and simulated spectra of thermotropic liquid crystals”

18:45 – 19:00 **D.A. Mainichev,** “Supramolecular chemistry of cucurbit[7]uril in solution - inclusion compounds with serine and isoleucine”

19:00 – 19:15 **I.D. Markova,** “The influence of metal chelation on photoinduced generation of free radicals by anticancer quinone. NMR and CIDNP study”

19:15 – 19:30 **V.A. Timoshnikov,** “UV light induced photodegradation of deferiprone chelate complexes. NMR and CIDNP study”

19:30 – 19:45 **M.F. Iakovleva,** “Investigation of kagome-compound $YBaCo_3AlO_7$ by magnetic methods”

19:45 – 20:00 **D.P. Pavlov,** “Crystal field analysis and magnetic properties of the EuF_3 Van-Vleck paramagnet”

20:00 – 20:15 **E.M. Gataullin,** “ESR investigation of $YbNi_2$ nanometric alloys”

Monday, June 23

Lectures

Auditorium 112. Institute of Physics.

Chairman – **V.A. Zhikharev**

9:00 – 9:45 **A.P. Burlaka** (R.E. Kavetsky Institute of Experimental Pathology, Oncology and Radiobiology, Kiev, Ukraine), “Electron Paramagnetic Resonance in the experimental and clinical oncology”

Auditorium 110. Institute of Physics.

10:00 – 10:30 **Opening Ceremony of Conference MR-70**

Lectures

Auditorium 110. Institute of Physics.

10:30 – 11:00 **M. Scheffler** (Stuttgart, Germany), “ESR on $YbRh_2Si_2$ at mK temperatures”

11:00 – 11:30 **A.A. Mukhin** (Moscow, Russia), “Magnetic resonance in multiferroic rare-earth borates”

11:30 – 12:00 **H. Keller** (Zürich, Switzerland), “Probing fundamental properties of unconventional superconductors under hydrostatic pressure”

12:00 – 12:20 **Coffee break**

Auditorium 112. Institute of Physics.

12:30 – 13:50 **Bruker BioSpin Users Meeting**

14:00 – 15:30 **Lunch**

15:30 – 17:00 **Bruker BioSpin Users Meeting**

17:00 – 17:20 **Coffee break**

Auditorium 110. Institute of Physics.

17:20 – 17:40 **M.V. Eremin** (Kazan, Russia), “Magnetic properties of rare-earth ions with orbital degenerate states”

17:40 – 18:10 **F.S. Dzheparov** (Moscow, Russia), “Magnetic resonance and relaxation of polarized beta-active nuclei. Modern state and visible trends”

18:10 – 18:30 **A.V. Duglav** (Kazan, Russia), “Zavoiskii and NMR: the analysis of the logbooks and rerunning of the experiments”

19:30 – 22:00 **Welcome Party**

Tuesday, June 24

Lectures

Auditorium 110. Institute of Physics.

9:00 – 9:30 **L. Berliner** (Denver, USA), “Early history, developments and the future in magnetic resonance applications to biology and medicine”

9:30 – 10:00 **R. Kaptein** (Utrecht, Netherlands), “Protein-DNA recognition: how does the protein find its target?”

10:00 – 11:30 **V. Polshakov** (Moscow, Russia), “NMR studies of protein-ligand interactions”

10:30 – 11:00 **J. Hennig** (Freiburg, Germany), “New horizons in spatial encoding in MRI”

11:00 – 11:20 **Coffee break**

11:30 – 11:50 **P. Andjus** (Belgrad, Serbia), “MRI studies on ALS animal models”

11:50 – 12:20 **H. Hirata** (Hokkaido, Japan), “In vivo tumor extracellular pH monitoring using EPR spectroscopy”

13:00 – 14:30 **Lunch**

Auditorium 112. Institute of Physics.

14:30 – 15:00 **G. Gecheidt** (Graz, Austria), “Following the reactivity of radicals by time-resolved EPR and CIDNP”

15:00 – 15:30 **D. Goldfarb** (Rehovot, Israel), “New developments and applications of distance measurements using Gd^{3+} spin labels”

15:30 – 16:00 **L.B. Krivdin** (Irkutsk, Russia), “Recent advances in the structural applications of the high-level non-empirical calculations of the NMR parameters”

16:00 – 16:30 **M. Bowman** (Tuscaloosa, USA), “Electron spin relaxation at high radical concentrations”

16:30 – 17:00 **Coffee break**

17:00 – 19:00 **Master Class**

Wednesday, June 25

Lectures

Auditorium 110. Institute of Physics.

9:00 – 9:30 **H.W. Spiess** (Mainz, Germany), “Advanced magnetic resonance studies of functional materials and signal enhancement”

9:30 – 10:00 **S. Zvyagiin** (Drezden, Germany), “High-field ESR studies of the triangle-lattice antiferromagnet Cs_2CuBr_4”

10:00 – 10:30 **H. Ohta** (Kobe, Japan), “Developments and applications of multi-extreme THz ESR”

10:30 – 11:00 **A. Schengelaya** (Tbilisi, Georgia) “Novel magnetic resonance technique to detect magnetoelectric coupling in multiferroic materials”

11:00 – 11:20 **Coffee break**

11:20 – 11:50 W. Lubits (Mülheim, Germany), “EPR — a key technique to understand metal biocatalysis”

11:50 – 12:20 **K. Moebius** (Berlin, Germany), “Advanced EPR on biomolecules - crossing the gap to NMR”

13:00 – 14:30 **Lunch**

14:30 – 19:30 **Excursion tour**

Thursday, June 26

Lectures

Auditorium 110. Institute of Physics.

9:00 – 9:30 **J. Schiclschmidt** (Dresden, Germany), “ESR on correlated ferromagnetic metals”

9:30 – 10:00 **B. Actas** (Gebze. Turkey), “Spin-dynamics in magnetic multilayers by FMR investigations”

10:00 – 10:30 **V.N. Glazkov** (Moscow, Russia), “Magnetic resonance in spin-gap magnets”

10:30 – 11:00 **M. Fu** (Hamilton, Canada), “^{17}O single crystal NMR study on S = 1/2 Kagome lattice $ZnCu_3(OH)_6Cl_2$”

11:00 – 11:20 **Coffee break**

11:20 – 11:50 **S. Vasiliev** (Turku, Finland), “Dynamic Nuclear Polarization of Phosphorus in Silicon in Strong Magnetic Fields and Low Temperatures”

11:50 – 12:20 **T. Takui** (Osaka, Japan), “NMR-paradigm pulse ESR spectroscopy: Coherent multi-frequency spin manipulation technology for spin-based quantum computers and quantum information processing”

12:20 – 12:50 **I. Geru** (Chisinau, Moldova), “Non-traditional approach to quantum computing”

13:00 – 14:30 **Lunch**

Auditorium 110. Institute of Physics.

14:30 – 15:00 **E.B. Fel’dman** (Chernogolovka, Russia), “Multiple quantum NMR in one-dimensional and nanoscale systems: theory and computer simulations”

15:00 – 15:30 **S.B. Orlinskii** (Kazan, Russia), “High-Frequency EPR and ENDOR Spectroscopy on Nanostructures”

16:00 – 16:30 **Coffee break**

16:30 – 20:00 **Poster Session of MR-70**

Friday, June 27

Lectures

Auditorium 110. Institute of Physics.

9:00 – 9:30 **Yu.M. Bun'kov** (Grenoble, France), "The coherent precession of magnetization"

9:30 – 10:00 **R. Khasanov** (Brugg, Switzerland), "Pressure induced magnetic order in Yb_2Pd_2Sn:occurrence of two quantum critical points"

10:00 – 10:30 **B.Z. Rameev** (Gebze, Turkey), "FMR studies of the magnetic anisotropies in half metallic and diluted magnetic oxides"

10:30 – 11:00 **V.A. Ivan'shin** (Kazan, Russia), "Dualism of 3d electrons in YbT_2Zn_{20} (T=Co; Fe): ESR evidence"

11:00 – 11:20 **Coffee break**

11:20 – 11:50 **A.I. Smirnov** (Moscow, Russia), "ESR experiments on spin liquid phases in crystals"

11:50 – 12:20 **A.V. Klochkov** (Kazan, Russia), "Application of ^{3}He NMR in porous media"

12:20 – 12:50 **L.E. Svistov** (Moscow, Russia), "Experiments on exotic magnetic phases in quasi-one-dimensional frustrated magnets"

12:50 – 13:20 **V.V. Dmitriev** (Moscow, Russia), "NMR studies of superfluid ^{3}He in "nematically ordered" aerogel"

13:30 – 14:30 **Lunch**

Auditorium 110. Institute of Physics.

14:30 **Closing Ceremony of Conference MR-70 and School-2014**

Medical Applications of EPR

U. Eichhoff, P. Höfer

Bruker BioSpin GmbH, Silberstreifen, D-76287 Rheinstetten/Germany

e-mail: Uwe.Eichhoff@bruker-biospin.de

EPR in medical and pharmaceutical investigations is based on the quantitative determination of free radicals in the organism, mainly of Reactive Oxygen Species (ROS) and Reactive Nitrogen Species (NOS). Reactive oxygen species like superoxide and hydroxide are formed by radiation or by malfunctions of some enzymes. They are always indication of a pathological state. ROS normally have low concentration and short lifetime. Spin labels allow to add a paramagnetic center to the EPR-silent molecules and allow detection by EPR. Shortlived radicals can be catched by spin traps and form long living radicals, which then become also accessible to EPR. Antioxydant activity can be monitored through the reaction with diphenylpicrylhydrazine (DPPH). ROS are involved in aging, cancer, diabetes, cardiovascular and inflammatory diseases. Their concentration in blood plasma is increased by stress but can be diminished by physical exercise. Sports medicine and monitoring organ transplantation are additional applications. Measurements must be performed at clearly defined temperature and oxygen partial pressure.

The NO-radical, which is involved in many processes in the organism, can be detected directly. Peroxynitrite gives no EPR-signal, but forms with the reactive oxygen species EPR-active long living nitroxyl-radicals. Nitric oxide binds to hemoglobin forming a long living spin-labeled adduct with is detectable at low temperature and allows to determine the NO-concentration in blood plasma.

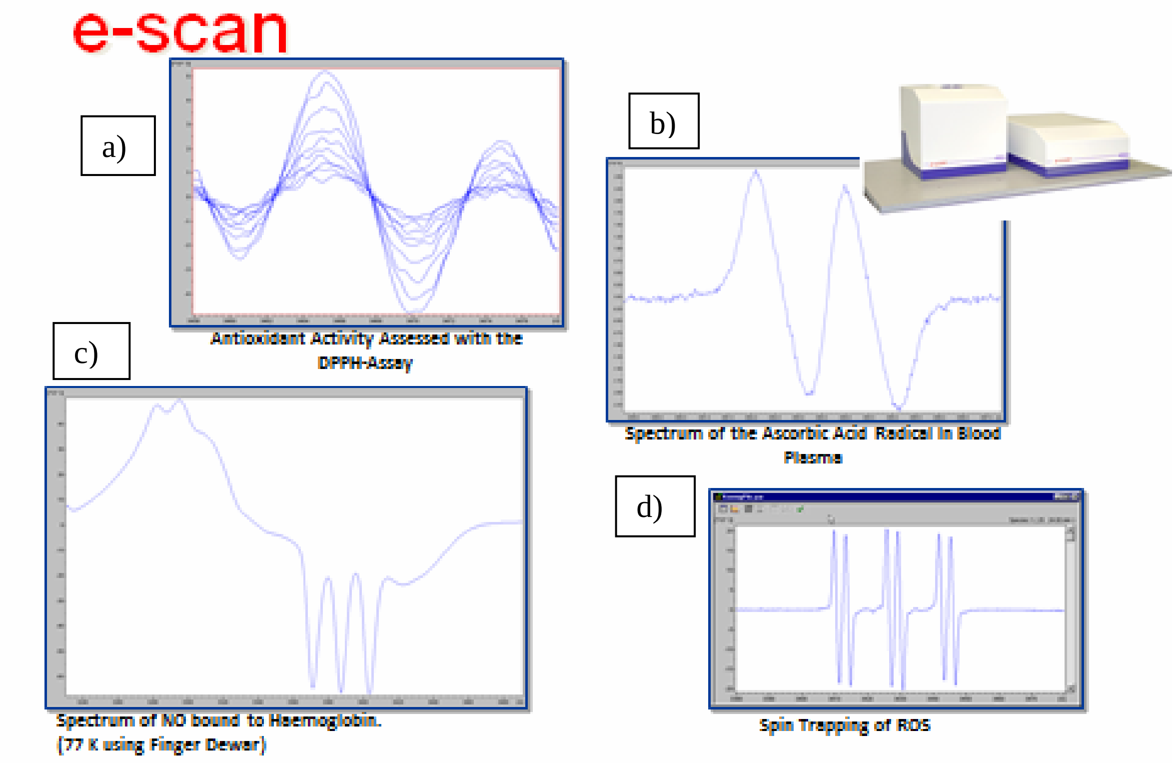

Antioxidant Activity Assessed with the DPPH-Assay

Spectrum of the Ascorbic Acid Radical in Blood Plasma

Spectrum of NO bound to Haemoglobin.
(77 K using Finger Dewar)

Spin Trapping of ROS

Fig.1. EPR measurements of Reactive Oxygen and Reactive Nitrogen Species:
a) antioxidant activity with DPPH assay; b) ascorbic acid in radical in blood plasma;
c) NO bound to hemoglobin; d) spin trapping of reactive oxygen species

Ionizing radiation leads to disruption of chemical bonds and formation of free radicals. The amplitude of the corresponding EPR signal is over a wide range proportional to the radiation dose. In the regions, which suffered from the Chernobyl accident in Russia, Belorussia and Ukraine, EPR spectrometry is used for tooth enamel dosimetry. The EPR signal of tooth enamel reflects the total radiation dose, which a person has accumulated during its life. EPR spectrometers for these investigations need a very high sensitivity and stability.

Any EPR spectrometer can be extended to EPR imaging by adding gradient coils with a special power supply and appropriate software. For medical applications the strong absorption by water in the X-band is an additional obstacle. Biological objects due to their greater size and high water content are therefore better investigated in the L-band and S-band with a special large bore magnet and gradient assembly. For material science X- and Q-band are preferable due to higher sensitivity. A standard universal EPRI system includes two magnet systems for X- and L-band.

In contrary to MRI, EPR imaging relies mainly on continous wave-methods (cw). The short relaxation times in EPR (nsec-μsec), further shortened by the strong imaging gradients, do not allow to apply pulse sequences and Fourier-Imaging, which are standard in MRI. But for the time being the EPR-cw-spectrum measured in the presence of a gradient, which is stepped in two or three coordinate directions and the image is obtained by back-projection like in X-ray tomography.

In EPR tomography the relationships between FOV, resolution, pixel bandwidth and gradient strength are the same as for MRI. In practice, however, there is a large difference regarding the pixel bandwidth. In low and medium filed MRI the gradient strength is often large enough to ensure that no chemical shift distortion appears in the image. In EPRI suppression of hyperfine interaction in any image would require enormous gradients. Instead, the spectral distortion from gradients is removed by deconvolution with the original EPR spectrum. For an EPR line width of 100mG a resolution of 25μ can be achieved.

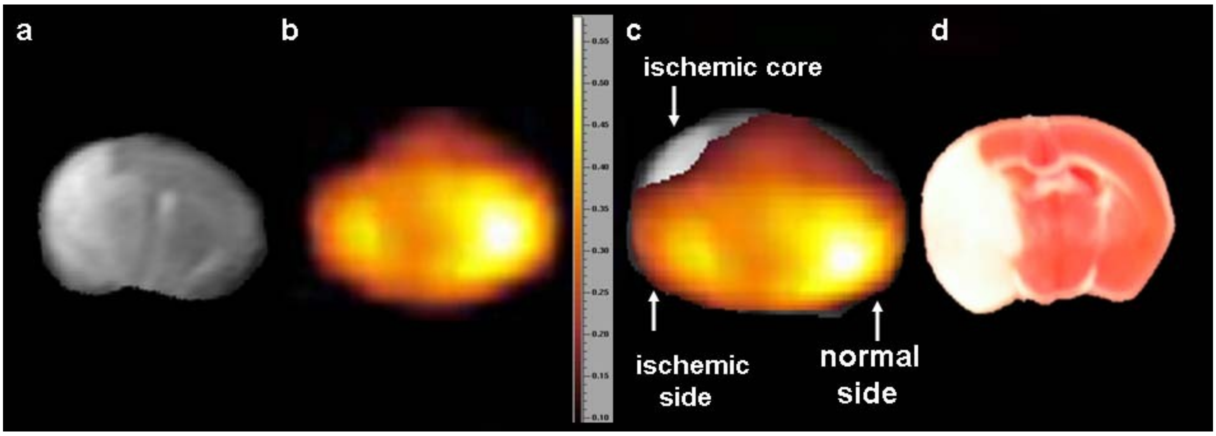

Fig.2. Ischemic stroke in rat brain: a) MR-diffusion-image; b) EPR line width-image; c) MRI/EPRI overlay; d) histology

One of the most promising applications of EPR imaging is oximetry. The width of the EPR line depends on the partial oxygen pressure. The line width can be calibrated against the partial oxygen pressure and then the partial oxygen pressure can be calculated from the EPR line width and displayed in a colour code. The image therefore reflects the oxygen concentration in the sample and ischemic conditions can be easily detected with EPR oximetry. An overlay on a MRI image relates the ischemic area to the anatomy. In malignant tumors like melanoma [1] radicals are created, which allow the imaging of core tumor and metastases.

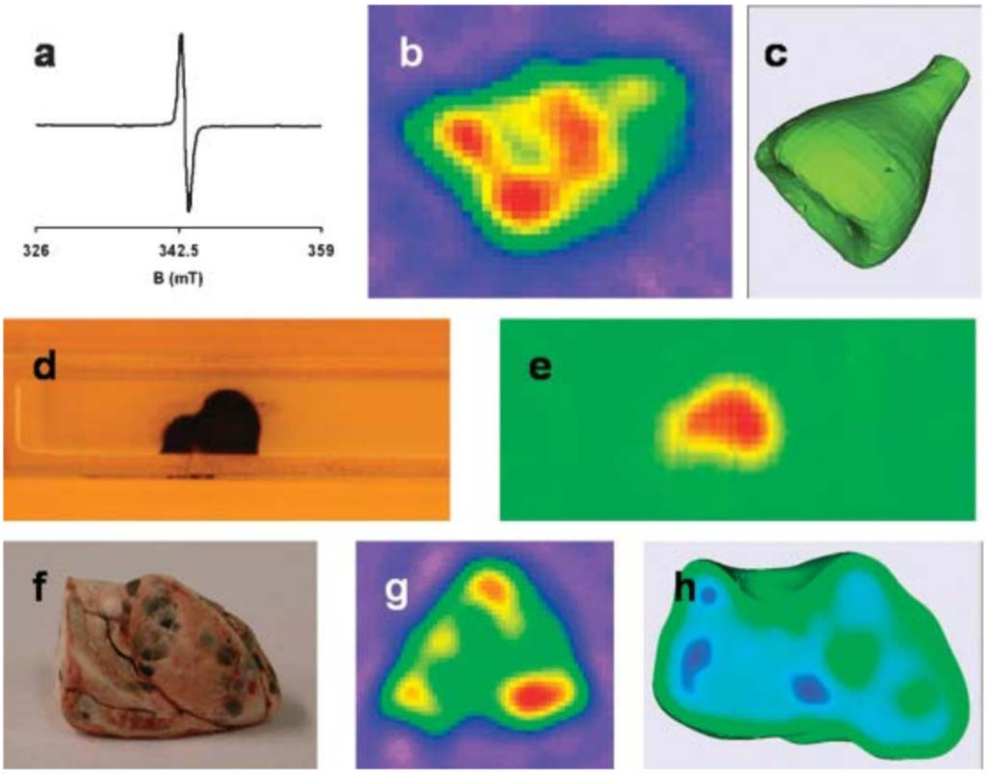

Fig.3. In vitro EPR spectra and images from melanoma B16 metastases in mice lung [1]
a: spectrum from a freeze-dried melanoma; **b**: 2D image; **c**: 3D image;
d: picture from a fresh melanoma slice; **e**: corrresponding EPR image;
f: picture of freeze dried lungs with metastases; **g**: 2D transversal EPR image;
h: longitudinal section through a 3D EPR image

EPR imaging in cw mode is very time consuming. Recent promising developments in Pulse EPR technology may decrease imaging time for certain applications by an order of magnitude.

References

[1] E.Vanea,N. Charlier, J. DeWever, M. Dinguizli, NMR Biomed. 2008; 21: 296 O. Feron,J.F. Baurain and B. Gallez

70 Years of nuclear magnetic resonance study of water. What is still not clear?

N.M. Sergeyev

Department of Chemistry, Moscow State University, Moscow, RF

e-mail: sergeyev@nmr.chem.msu.ru

Practically in this 2014 year it is possible to celebrate the 70 anniversary of use of of nuclear magnetic resonance spectroscopy for water studying. Hundreds (or may be even thousands) researches were devoted to water that included use of various techniques (with use of spectroscopy of a nuclear magnetic resonance on various nuclei ^{1}H. ^{17}O, ^{2}H, and also with application of various relaxation techniques, temperature dependences, etc.). However, as it often happens in science, with increase in volumes of researches becomes clear that the true understanding of a problem is removed to the future. For water the central problems connected with structure of liquid water (distribution of various clusters by dimensions), with exchange processes between various clusters, (in particular, with a contribution of processes of tunneling to exchange processes) still aren't solved, and only one remains clear — the solution of these problems is removed in the uncertain future.

Electron Paramagnetic Resonance in the experimental and clinical oncology

A.P. Burlaka

R.E. Kavetsky Institute of Experimental Pathology, Oncology and Radiobiology NAS of Ukraine, Kyiv, Ukraine

e-mail: apburlaka@gmail.com

This lecture presents a main output of our long-term EPR experience in the experimental and clinical oncology studies acquired in the R.E. Kavetsky institute of Experimental Pathology, Oncology and Radiobiology of the National Academy of Science of Ukraine. Some applications of the conventional X-band EPR measurements combined with the spin trapping techniques to study the mechanisms of the chemical, radiation induced and hormonal carcinogenesis; to investigate the influence of the regulators of the cell proliferation; to diagnose and differentiate the tumors; to monitor the effectiveness of the therapeutic treatment of the malignant tumors, etc., are shown.

An understanding of the nature of cancer is an urgent medical and social problem of our Society. According to the reports of International Agency for Research of Cancer (IARC), cancer is the biggest cause of mortality worldwide — there were an estimated 8.2 million deaths from cancer in 2012 and cancer cases are forecast to rise by 75% and reach to 25 million over the next two decades [1]. The complexity of the cancer related studies demands an application of different analytical tools and approaches for the investigations at the fundamental levels, in the pre-clinical research, clinical diagnostics, to estimate the effectiveness of the theraupetic treatments, etc. Soon after the discovery of the electron paramagnetic resonance (EPR) phenomenon in 1944 by E.K. Zavoisky at Kazan University, it became clear that EPR can give a unique information in the biological and medical related studies [2 – 6].

Since 1960 different EPR approaches including spin trapping were and are used in the Institute of Experimental Pathology, Oncology and Radiobiology to study the mechanisms of the chemical, radiation induced and hormonal carcinogenesis; to investigate the influence of the regulators of the cell proliferation; to diagnose and differentiate the tumors; to monitor the effectiveness of the therapeutic treatment of the malignant tumors. Some of the results are gathered in the monographs [2 – 4]. This paper presents an attempt to summarize the most significant original output of our research complemented by the recent ones [1, 5 – 7].

A growing interest to the clinical applications of the EPR methods is to observe last decade (see [9] for the list of the references on this issue). Along with the use of the high filed/ high frequency EPR techniques, EPR imaging and their Fourier-transformed variations, appearance on the market of a number of the “easy-in-use” table-top EPR spectrometers with the enhanced sensitivity and stability turn EPR into the powerful tool for the (bio)medical research that can cover a wide range of expertise from the fundamental studies to the routine screening. We hope that all these in combination with other experimental and theoretical approaches, finally, could significantly help in the cancer related investigations to unravel the tricks of the Nature.

References

[1] B.W. Stewart, C.P. Wild, World Cancer Report (IARC, Lyon, 2014):pp. 1-630

[2] N.M. Emanuel, R.E. Kavetskii, B.N. Tarusov, E.P Sidorik, Cancer Biophysics, (Naukova dumka, Kiev, 1976), pp. 1-296 (in Russian)

[3] R.E. Kavetskii, Z.A. Butenko, E.P. Sidorik, Problems of the Carcinogenesis and Anticarcinogenesis, (Naukova dumka, Kyiv, 1979), pp. 52-109 (in Russian)

[4] A.P. Burlaka, E.P. Sidorik, Radical Forms of Oxygen and Nitrogen Oxide in the Tumors Process, (Naukova dumka, Kiev, 2006), pp. 1-228 (in Ukrainian)

[5] A.P. Burlaka, I.I. Ganusevich, M.R. Gafurov, S.N. Lukin, E.P. Sidorik, Cancer Microenviron. 6, 273 (2013)

[6] A.P. Burlaka, I.I. Ganusevich, S.N. Lukin, E.P. Sidorik, Oncology 15, 197 (2013) (in Ukrainian).

[7] A. Burlaka, M. Selyuk, M. Gafurov, S. Lukin, V. Potaskalova, E. Sidorik, Int. Journ. Rad. Biol. 90, 357 (2014)

Development of quadrature coils “Neck” for low field MRI

A.A. Bayazitov[1], P.I. Chumarov[1,2]

[1]Zavoisky Physical-Technical Institute of the Kazan Scientific Center of the Russian Academy of Sciences, 420029, Sibirsky tract, Kazan, Russia

[2]Kazan Federal University, 420008, Kremlyovskaya St., Kazan, Russia

e-mail: bajazitv.alf@rambler.ru

In modern medical equipment based on the nuclear magnetic resonance, different types and configurations of receiving coils with high resolution are used. Among them — multiple loop systems of sensors (connected), capable to work both jointly, and independent from each other. The images of objects received at present with use of these receiving sensors can be considered as very successful.

The purposes of this work are to conduct research and upgrade of the sensor of surface type. To justify a choice of construction of the receiving sensor about the best sensitivity and a signal-to-noise ratio.

Researches were conducted for sensors taking into account magnetic field strength of 0.06 T. The sensor is a part of the “TMR — 0,06 — KFTI“ MRI system. Operating frequency is *f* = 2.5 MHz.

In this operation research of the sensors “Kidney”, "Spine" of surface type was conducted. The different experiments were delivered: the calculation of the shape of the sensor, measurement of signal level, the use of different types of shielding. During the experiment with the use of external screen in the form of a closed loop, there was an increase in signal level in the studied region fig.1.

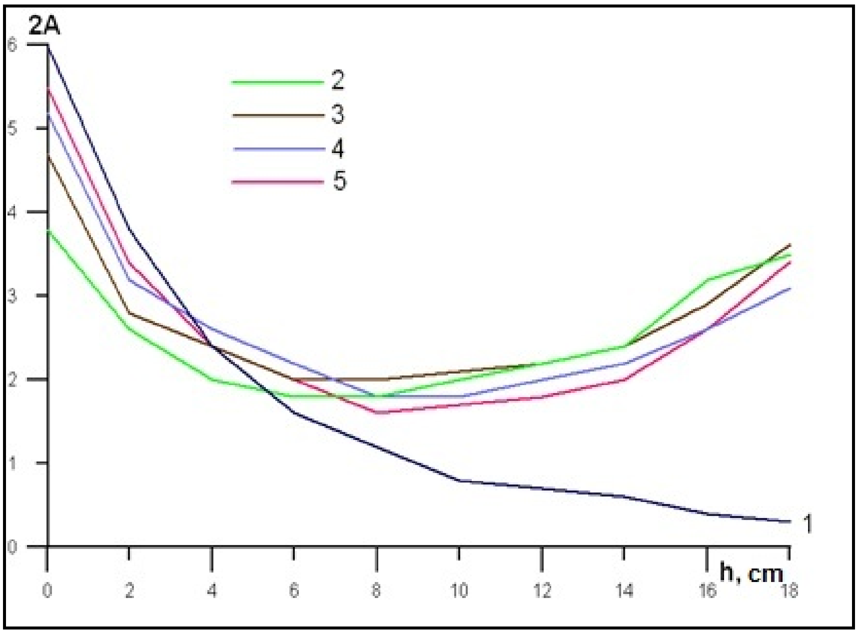

Fig.1. The signal level with the screen (2 – 5) and without screen (1)

Good quality of system shall be an order 200 – 300. In the course of experiments obtained image with different types of sensors. An output are made will help by development of the new "Neck" sensor. Results received during research can be applied to other types of tomographs with corrections of operating frequency.

Multi-frequency EPR/ENDOR and DFT study of impurities in (nano)hydroxyapatite

T.B. Biktagirov[1], M.R. Gafurov[1], G.V. Mamin[1], K.B. Iskhakova[1], E.S. Klimashina[2],
V.I. Putlayev[2], S.B. Orlinskii[1]

[1]Institute of Physics, Kazan Federal University, 420008, Kremlevskaya 18, Kazan, Russia
[2]Department of Chemistry, Moscow State University, 119992, Leninskie Gory, Moscow, Russia

e-mail: tibbiktagirov@kpfu.ru

We demonstrate the application of combined experimental-computational approach for studying ionic substitutions in the structure of hydroxyapatite $Ca_{10}(PO_4)_6(OH)_2$ nanocrystals (nano-HAp).

Our initial interest to the nano-HAp was motivated by the search for reliable prognostic markers to trace the atherosclerotic plaque development at the early stages of atherosclerosis. We have exploited the increased sensitivity and resolution of the high-frequency electron paramagnetic resonance (EPR) for studying the tissues of aorta walls of male patients and synthesized nano-HAp as model systems for the calcified tissues [1].

We have spread our studies onto the investigations of different nano-HAp samples by means of X- (9.5 GHz) and W-band (94 GHz) EPR and double resonance (ENDOR) pulsed techniques. It is demonstrated that during the wet synthesis process nitrate anions from the by-products can incorporate into the nano-HAp. The comparison of the experimental data with spectroscopic and structural information as followed from *ab initio* density functional theory (DFT) calculations (cf. Fig.1) allowed us determining the nature of the NO_3^-/NO_3^{2-} impurity and the particular crystallographic site of the nitrate location in nano-HAp.

We have proposed the implication of the NO_3^-/NO_3^{2-} species to probe the effects of co-doping of nano-HAp by different types of ionic substitutions. In particular, the competitive behavior of interplay between the simultaneously incorporated nitrate and carbonate anionic dopants was observed. Furthermore, complexation between the oppositely charged impurities was suggested when the nitrate is introduced in nano-HAp together with Mn^{2+} ions. All the experimental observations were supported by DFT calculations.

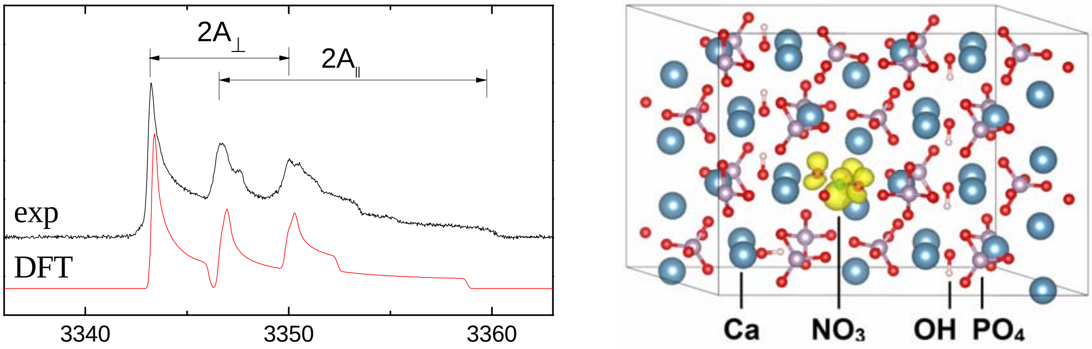

Fig.1. Electron spin echo detected EPR spectrum of the NO_3^{2-} radical in nano-HAp at 94 GHz at T = 297 K (exp) along with the curve simulated using the spectroscopic parameters followed from DFT analysis (DFT) and the corresponding structure of HAp containing NO_3^{2-} impurity as used in simulation.

References

[1] M.R. Gafurov et al. Atherosclerotic plaque and hydroxyapatite nanostructures studied by high-frequency EPR *Magn. Reson. Solids*, 2013, **15**, 13102.

Electron paramagnetic resonance of the $SrTiO_3$:Mn crystals

B.F. Gabbasov[1], D.G. Zverev[1], R.V. Yusupov[1], A.A. Rodionov[1], V.A. Trepakov[2,3]

[1]Kazan Federal University, Kazan, Tatarstan, 420008 Russia
[2]Ioffe Physical Technical Institute, Russian Academy of Sciences, St. Petersburg, 194021 Russia
[3]Institute of Physics AV CR, 18221 Prague 8, Czech Republic

e-mail: bulgabbasov@gmail.com

Abstract

In this paper the results of the Mn^{4+} impurity centers EPR study in the high-quality $SrTiO_3$ single crystals are reported. For the thin platelet-shaped crystals with the plane perpendicular to the [001] axis in the *m3m* cubic phase ($T > 105$ K) the small but clearly detected tetragonal distortion of the Mn^{4+} centers is found. For a square prism-shaped sample a height change leads to the systematic modification of the anisotropy degree, with a zero-field splitting inversely proportional to the height value. Observed phenomenon is related to an effect of the shape-induced anisotropy of the $SrTiO_3$ host crystal which origin is to be understood.

Introduction

Strontium titanate $SrTiO_3$ (STO) serves as an object of scientific interest for already several decades and still the new intriguing phenomena are reported. STO has a simple cubic perovskite structure above $T_c = 105$ K, symmetry group *m3m*. At T_c the compound experiences a second order antiferrodistorsive structural phase transition to the tetragonal phase with the space group *I*4/*mcm*. Below T_c the structural domains are formed in the crystalline samples with the tetragonal axes oriented along the three quasicubic [001] axes. In principle, a single-domain sample may be obtained by an empirically found procedure that consists in cutting of the (110) oriented [001] elongated plates [1] and temperature “training”. In fact, low-temperature structure of STO as studied using X-ray diffraction is still a matter of a debate.

Manganese-doped STO is also studied for quite a long time [2]. The electron paramagnetic resonance spectroscopy has proven to be a powerful tool for investigations of the impurity center structure and properties. It has been reported that Mn ions incorporate in the STO host lattice in various oxidation states [3].

Recently, the interest to STO:Mn was revived due to the reports on the so-called “magnetoelectric multiglass” behavior with an observation of both the ferromagnetic and ferroelectric responses in heavily-doped ceramics at low temperatures [4, 5]. One of the open questions is how the manganese impurity induces this multiglass phase.

Already in one of the earliest papers on STO:Mn by K.-A. Müller it was mentioned that the EPR spectra of Mn^{4+} centers in the cubic phase reveal the small but clearly detected departure of the symmetry from cubic to tetragonal [2]. However, no any consistent explanation was proposed for this observation.

In this paper we report on a systematic study of the small tetragonal distortion detected by the EPR spectroscopy for the impurity Mn^{4+} centers in the high-quality STO:Mn single crystals. It is found that this distortion in the case of [001] oriented platelet is inversely proportional to its thickness and thus is clearly specimen shape-induced.

Materials and Methods

High quality $SrTiO_3$:Mn single crystals (Furuuchi Chemical Corp., Tokyo) grown by the Verneuil method from high purity (99.999%) initial components were taken for investigation. The series of STO:Mn crystals that was at our disposal consisted of 12 samples grown in different atmosphere (oxidizing/reducing/neutral), with different stoichiometry compositions and doped with either MnO or MnO_2.

Initially, the reported phenomenon was observed in the thin, 0.3 – 0.4 mm thick, plates with the plane oriented perpendicular to the [001] crystal axis. For a systematic study of the EPR spectrum anisotropy dependence on the specimen shape the right angle square prism with the dimensions of $1.35 \times 1.35 \times 2.20$ mm^3 was cut from a boule with the faces perpendicular to the cubic [001] axes of the crystal. Then the initial sample height was step-by-step reduced by polishing. At each step the EPR spectra were recorded at T = 150 K.

EPR spectra were measured with a commercial Bruker ESP300 spectrometer operating in the microwave X range (9.4 GHz) in a standard ER4102ST rectangular cavity with the TE_{102} microwave mode. The sample temperature was controlled by an ER4112HV continuous flow helium system produced by Oxford Instruments.

Results and Discussion

All the samples of the STO:Mn series revealed in the room-temperature EPR spectra the signals of the manganese ions in the oxidation states of Mn^{4+}, Mn^{3+} and Mn^{2+}. Impurity centers of Mn^{4+} and Mn^{2+} ions at 300 K were represented in the spectra by the sextets due to the hyperfine interaction with its own ^{55}Mn nucleus. The spectra could be nicely described in the cubic symmetry approximation. However, with the temperature decrease the spectra of Mn^{4+} and Mn^{2+} experienced significant transformation. Thus, the lines of the Mn^{2+} center broadened significantly which was related recently to slowing down of the intrinsic dynamics within the presumably equivalent off-center positions [6]. On the contrary, the EPR spectrum of the Mn^{4+} centers revealed line narrowing on cooling down and below 200 K the triplet structure for each hyperfine component was readily resolved.

Some of our samples had the shape of the thin platelets. The EPR spectrum of thin platelet sample of the $SrTiO_3$:Mn^{4+} measured at T = 150 K is presented in fig.1 by the black line. One could notice also the low-intensity broad lines of the Mn^{2+} center.

It is known that the hyperfine interaction of Mn^{4+} ion ($S = 3/2$) with its own ^{55}Mn nucleus ($I = 5/2$) affects EPR lines position of different fine structure component in the EPR spectrum. The splitting caused by this influence is symmetric with respect to the $|M_I|$ and for $M_I = \pm 5/2$ equals to 0.8 mT (lower trace in fig.1). However, in the experimental spectrum the splitting of the high- and low-field components is strikingly different. This behavior is specific for the paramagnetic centers with the presence of zero-field splitting caused by the symmetry lowering. As a result, using the spin-Hamiltonian

$$H = g\beta(\mathbf{H}\cdot\mathbf{S}) + D\left(S_Z^2 - \frac{S(S+1)}{3}\right) + A(\mathbf{S}\cdot\mathbf{I}),$$

with $g = 2.004$, $D = 6$ MHz and Gaussian distribution of D with a width of $\delta D = 17$ MHz and $A = -215$ MHz it is possible to calculate the EPR spectrum essentially identical to the experimental one (fig.1, middle trace). The distribution of the fine structure parameter D leads to the broadening of the side components of the EPR spectra (transitions $|M_S = \pm 3/2\rangle \to |M_S = \pm 1/2\rangle$). Observation of nonzero D looks quite unusual because at $T = 150$ K the crystal is in the cubic phase. Moreover, the splitting between the side components depends on the sample shape. To study the influence of the sample shape on the

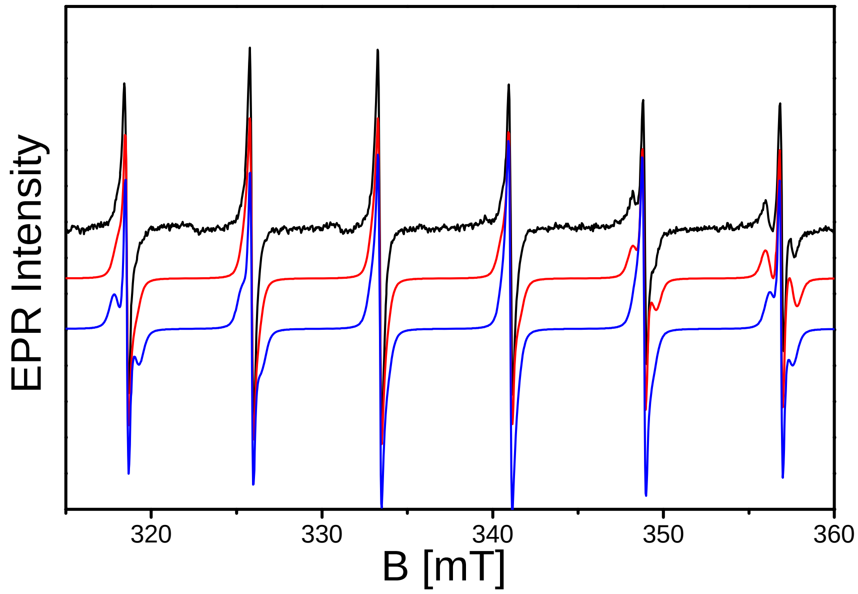

Fig.1. EPR spectrum of the SrTiO$_3$:Mn (001) platelet sample, T = 150 K, B||[001] (upper trace), simulated spectrum for zero (lower trace) and optimized nonzero fine structure parameter *D* (middle trace).

splitting the measurements of the sample with a square (001)-oriented 1.35 × 1.35 mm^2 base and various heights (starting with 2.2 mm) were performed. The investigation was done using the same sample and successive height decrease followed by the EPR measurements at $T = 150$ K.

Fig.2 represents the high-field component of the EPR spectrum ($M_I = +5/2$) at several sample heights. It is clearly seen that the splitting between the fine structure components increases with a decrease in the sample height. The dependence of this splitting as the

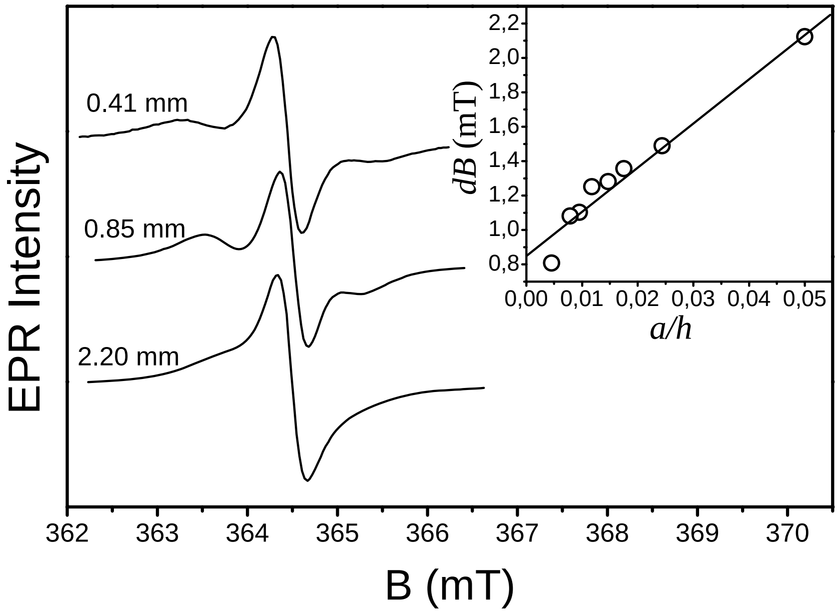

Fig.2. EPR spectra of the high-field hyperfine component of the Mn^{4+} center in SrTiO$_3$ single crystal for different height values at $T = 150$ K and B || [001]. Inset depicts the dependence of the splitting between the fine structure components on the sample shape anisotropy parameter (*a*/*h*).

function of the sample shape anisotropy parameter (*a*/*h*), where *a* is the length of the base edge and *h* is the height is presented in the inset of fig.2. Clearly, the splitting is proportional to the sample shape anisotropy.

One can look at the observed spectrum dependence on the shape of the STO:Mn sample as reflecting the host crystal structure via the Mn^{4+} EPR probe. Indeed, measured integral concentration of manganese ions in our samples didn't exceed 0.05 at.%, the Mn^{4+} ion ground state is an orbital singlet and thus shouldn't impact the crystal structure. In this case we face the macroscopic effect induced by the perturbation that for diamagnetic and paraelectric materials is generally treated as rather weak. In our opinion, the generality of the phenomenon should be studied with the EPR probes different than Mn^{4+}.

Conclusion

Thus, the EPR study of the Mn^{4+} impurity centers in $SrTiO_3$ single crystals has revealed the unusual for the cubic symmetry splitting of the fine structure levels. At the temperature corresponding to the cubic phase of $SrTiO_3$ the axial anisotropy observed in the spectra of Mn^{4+} ions is found to be proportional to the sample shape anisotropy. The origin of this anisotropy is not yet understood and perhaps is related to the incipient electric polarization formed in the crystal with temperature decrease.

Acknowledgement

The EPR spectra presented in the paper were measure with the equipment of the Federal Center of Shared Facilities of Kazan Federal University. This work was partially supported by Russian Foundation for Basic Research (project no. 14-02-31166 mol_a).

References

[1] Müller K. A., Berlinger W., Capizzi M., Grenicher H. // Sol. State. Comm. 1970. V. 8. P. 549.

[2] Müller K. A. // Phys. Rev. Lett. 1959. V. 2. P. 341.

[3] Serway R. A., Berlinger W., Müller K. A., Collins R. W. // Phys. Rev. B. 1977. V. 16. P. 4761.

[4] Lemanov V.V., Smirnova E.P., Sotnikov A.V., Weihnacht M. // Phys. Solid State. 2004. V. 46. P. 1442.

[5] Tkach A., Vilarinho P. M., Kholkin A. L., Pashkin A., Veljko S., Petzelt J. // Phys. Rev. B. 2006. V. 73. P. 104113.

[6] Zverev D.G. et al, Opt. and Spectr. 2014. V. 116. P. 818.

Prototyping of gradient controller for MRI scanner

M.D. Galimov

Zavoisky Physical-Technical Institute of the Kazan Scientific Center of the Russian Academy of Sciences, 420029, Sibirsky tract, Kazan, Russia

e-mail: galimov.mmf@kfti.knc.ru

Main idea of this work is developing hardware device for controlling gradient system of MRI scanner. Before final device realizing we should develop a prototype of final device for testing and debugging. Most important element of our future device (which will be develop in early time) is gradient impulse former. Circuit diagram of this base element illustrated on fig.1.

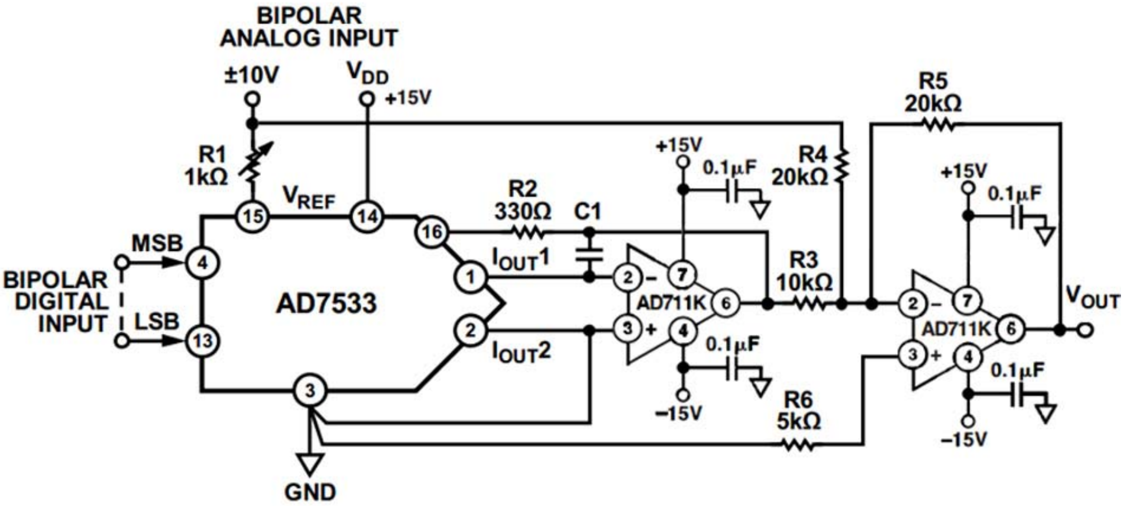

Fig.1. Gradient impulse former circuit diagram for single channel of MRI scanner gradient system

AD7533 is CMOS Low Cost 10-Bit Multiplying DAC with DIP package. AD711 is Precision Low Cost High Speed BiFET Op Amp with DIP package. Both chips from Analog Devices.

Prototype block diagram illustrated on fig.2. Altera DE1 development kit using for 10 control bits forming which using for DAC control on device prototype. We have internal FIFO interface on Altera DE1 and external UART interface on FTDI UM232R module. Both interface using for communicating between PC and device prototype. Mean Well RT-50C is power supply for DAC's and operational amplifiers on prototype. We can see triplicated gradient impulse former circuit diagram for single channel of MRI scanner gradient system (from fig.1) for all gradient channels (X, Y, Z on fig.2). We will create printed board for prototype of gradient controller for MRI scanner based on diagrams from fig.1 and fig.2 in early.

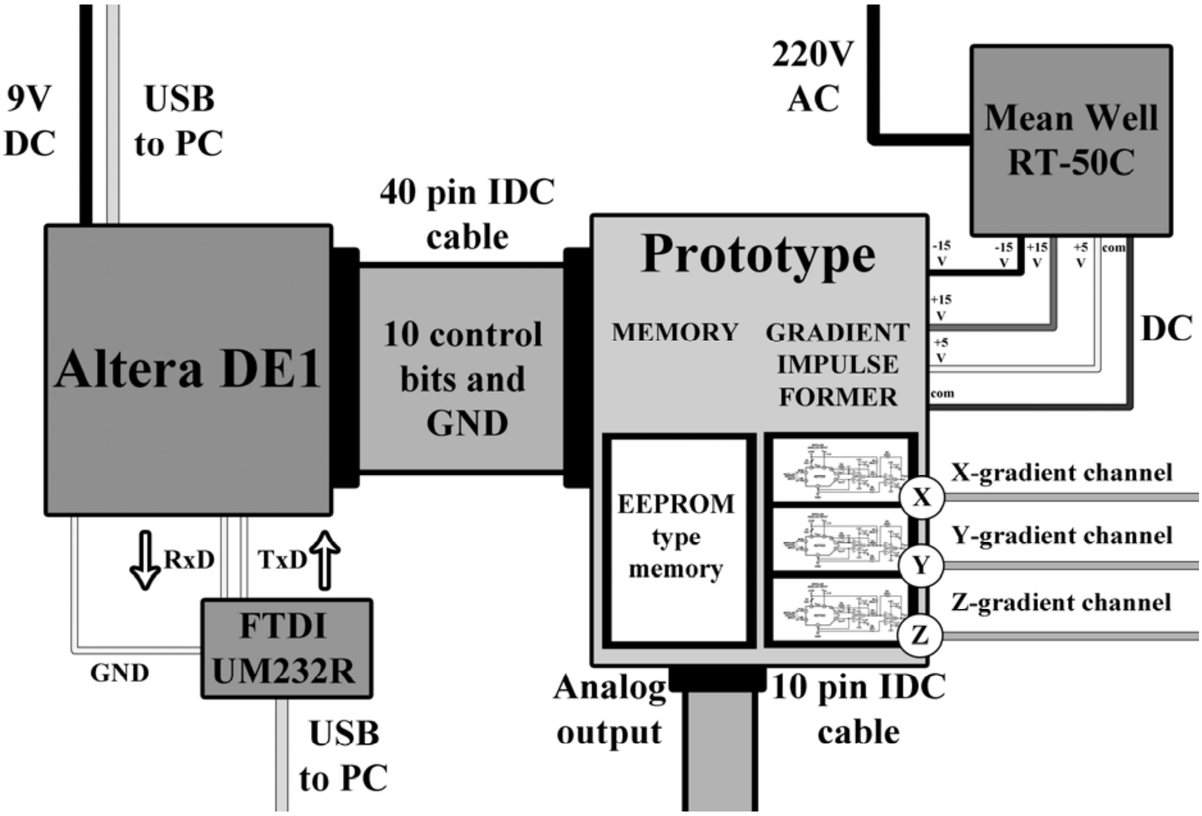

Fig.2. Prototype block diagram

Assessment of correctness of MRI based Fiber Tracks

L.V. Konopleva, O.V. Nedopekin, K.A. Il’yasov

Institute of Physics, Kazan University, Kremlevskaya 8, 420008 Kazan, Russian Federation

e-mail: lidia.konopleva@gmail.com

Abstract

In this work, methods have been proposed to validate results of MRI Fiber Tracking (FT). Several parameters have been considered, which can give information about correctness of localization of axonal tracts. The method is based on the constancy of probability and entropy along the tract. Calculations were made on numerical phantoms and on real MRI data too. As a result , it was found that the entropy is more resistant to noise parameter, than probability.

Introduction

Diffusion measurements with MRI gives possibility to investigate the structure of biological tissues *in vivo*. Mean diffusion distance of water molecules during the measurement time is of the same scale as size of cells, therefor the method is very sensitive to any tissue microstructure changes [1]. In particular, diffusion measurement provides information about the architecture of the human brain. Various methods based on the diffusion-weighted images are used for this purpose, one of which is axonal tractography.

Fiber tracking algorithms (FT) use this local information to find out fiber pathways, and so connectivity between different regions of brain can be noninvasively determined, what opens new possibilities for neuroscience and clinical diagnostics. In clinical practice, this method is used for pre-planning of neurosurgical operations, as for planning the rehabilitation treatment of patients after cerebral stroke. Furthermore, FB method can be used to monitor the development of the brain in infants [1]. However, spatial resolution of MRI is limited to a few millimeters, what is by several orders of magnitude larger than fiber diameter. Such averaging over voxel gives correct directional information for fiber bundles with diameter of several millimeters and for fibers with different directions within a voxel only averaged direction can be found. Lack of correct directional information in crossing regions, partial volume effects and noise in measured data lead to different errors in FT.

In this work a numerical fiber tracking phantom has been used to validate the results of various methods of FT [1-4], because it is very difficult to work with real object, in addition, we can not verify the correctness of the calculation results in vivo. Developed methods were also applied to a real MRI data. The main parameters for assessing the correctness of results are the change in entropy and probability along the tract. It was found, that the entropy is a parameter more resistant to noise.

Mathematical description of diffusion effects

In biomedical objects the apparent diffusion coefficient can depend on measurement parameters since the self-diffusion of water molecules in biological tissues is limited by intracellular and interstitial barriers. In the literature on MRI biomedical objects word "self" is usually omitted, therefore, further in this work the diffusion of water will mean the self-diffusion of water molecules [1].

If diffusion is anisotropic, then the diffusion tensor is usually described like this:

$$DT = \begin{bmatrix} D_{xx} & D_{xy} & D_{xz} \\ D_{xy} & D_{yy} & D_{yz} \\ D_{xz} & D_{yz} & D_{zz} \end{bmatrix} \tag{1}$$

Since the tensor is symmetric, the off-diagonal elements are equal. Selecting the appropriate coordinate system, the DT can be diagonalized:

$$DT = \left[\nu_1\, \nu_2\, \nu_3\right]^T \begin{bmatrix} \lambda_1 & 0 & 0 \\ 0 & \lambda_2 & 0 \\ 0 & 0 & \lambda_3 \end{bmatrix} \left[\nu_1\, \nu_2\, \nu_3\right], \tag{2}$$

where λ_i — eigenvalues of the diffusion tensor, they characterize the rms displacement along the corresponding direction. Eigenvectors describe the transformation of the coordinate system, in which the measurements are carried out (it is associated with the location of the gradient coils), to the coordinate system, where the diffusion tensor is diagonal. To determine the direction of pathways in the brain as part of the method most important for us is the eigenvector $\nu_{\max}$, corresponding to the eigenvalue $\lambda_{\max}$ [1].

Probability and entropy

To validate results of FB three parameters have been used - the probability, entropy, and Renyi entropy. According to our assumption, these parameters should remain constant along the entire tract.

Probability is calculated using the formula from the Koch's article [5] (the probability of reaching the voxel m from voxel n):

$$p(m \to n) = \frac{\left[d\left(r_{mn}, m\right) + d\left(r_{mn}, n\right)\right]^a}{\sum_{n=1}^{S}\left[d\left(r_{mn}, m\right) + d\left(r_{mn}, n\right)\right]^a}, \tag{3}$$

where $d\left(r_{mn}, m\right)$ — «diffusion coefficient», r_{mn} — vector from voxel m to voxel n. Coefficient $a = 7$, as it is a given value of a coefficient obtained the best results [5].

«Diffusion coefficient» may be calculated by the following formula:

$$d(r, m) = \frac{r}{|r|} DT(m) \frac{r}{|r|}. \tag{4}$$

To calculate the information entropy in the voxel m, the following formula has been used:

$$H(m) = -\sum_{i=1}^{n} p(i) \log_2 p(i), \tag{5}$$

where $p(i)$ — previously considered probability coefficients.

Calculations using the Renyi entropy give good results for complex systems [6]. Since the human brain is a complex fractal system, it has been assumed that the Renyi entropy can be used in our case.

$$H_\alpha(m) = \frac{1}{1-\alpha} \log\left(\sum_{i=1}^{n} p_\alpha^i\right), \tag{6}$$

where α — is the fractal coefficient, which characterizes dimensionality of the system.

Description of the phantoms and results

Several phantoms have been numerically simulated For the phantom consisting of straight lines (fig.1), results are shown in table 1.

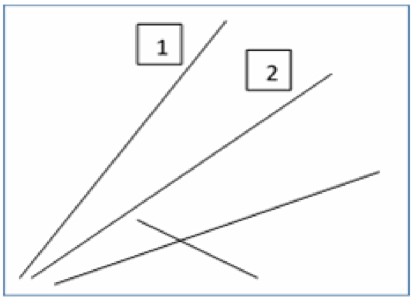

Fig.1. Schematic representation of the phantom consisting of intersecting lines

As shown in Table 1 with an increase of noise in the image increases the entropy and standard deviation of the probability. However, this effect is stronger for the probability than for the entropy. Mean value of the probability changes, whereas the mean entropy remains approximately at the same level.

Table 1. Mean values of probability and entropy along the directions 1 and 2 shown in fig.1 for the different levels of signal/noise ratio, the probability is given on a logarithmic scale

SNR	Direction 1			Direction 2		
	Probability (ln)	Entropy	Renyi Entropy	Probability (ln)	Entropy	Renyi Entropy
No noise	-2,280	2,883	2,835	-2,178	2,908	2,854
100	-2,512 (±0,017)	2,926 (±0,003)	2,881 (±0,003)	-2,3545 (±0,017)	2,996 (±0,004)	2,994 (±0,004)
40	-2,497 (±0,041)	2,922 (±0,006)	2,877 (±0,006)	-2,556 (±0,047)	2,996 (±0,011)	2,944 (±0,011)

In crossing regions only averaged directions can be found. Lack of correct directional information leads to different errors. In these areas (fig.1) there is a sharp increase in entropy and a decrease in the probability that the observed and experimentally measured data (fig.2).

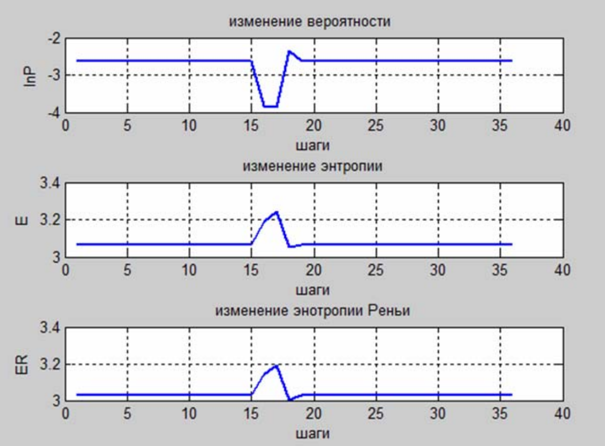

Fig.2. change in the probability and entropy for intersecting axonal tracts

Based on the hypothesis of the constancy of probability and entropy within the axonal tract, it has been suggested the mean probability decreases and the entropy increases accordingly along the pathway, which doesn't correspond anatomical structures. It will provide an opportunity to establish, how well was determined localization of axonal tract. This assumption was confirmed by numerical simulations on a phantom. In addition, the hypothesis has been verified by actual data (fig.3). The curve 1 corresponds to the tightly packed bundles of nerve fibers, the curve 2 does not correspond to any anatomical structures.

Calculations were also done for the corticospinal tract of human brain. The calculations has been also performed along the another curves, which do not correspond any anatomical structure. The results are shown in table 2.

In this case entropy was not the best parameter to validate the results. This can be explained by the fact that, that the probability describes direction itself and entropy describes surrounding voxels. And both sets of curves have a similar environment.

Table 2. Mean values of probability and entropy for corticospinal tract and along the curve which does not correspond the directions of observed fiber tracks. The probability is given in logarithmic scale, in parenthetic id the standard deviation of the parameter along the tract

	Corticospinal tract	Various direction
Probability	-2,86 (±1,90)	-6,42 (±1,80)
Total probability	-25, 72	-57,76
Entropy	3,17 (±0,10)	3,37 (±0,30)
Total Entropy	28,54	30,32
Renyi Entropy	2,98 (±0,10)	3,17 (±0,40)
Total Renyi entropy	26,82	28,51

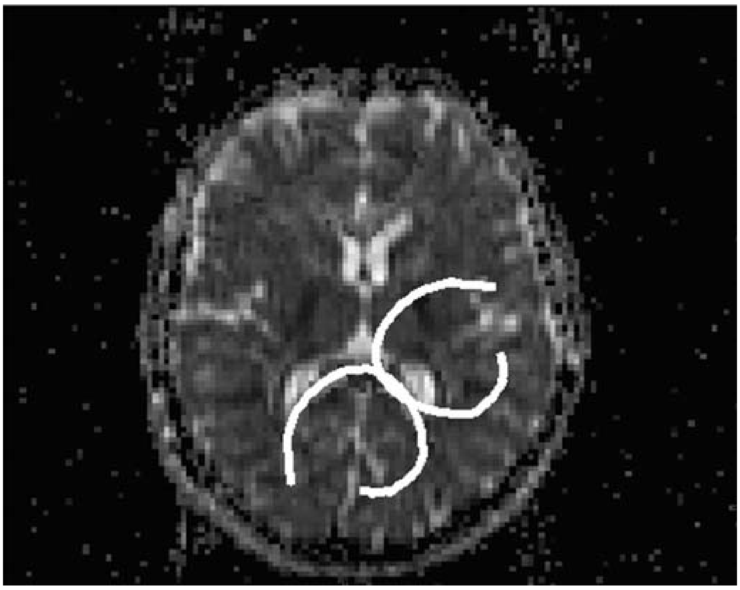

Fig.3. Diffusion-weighted image of the brain

Conclusions

In this work, we proposed a method of validating results of MRI-based axonal fiber tracking results. The method is based on the assumption that the probability is maximal and entropy is minimal along the tract. Verification of the method on the numerical phantom showed that the above parameters allow us to estimate the correctness of the passage of nerve fibers. In addition, the change of probability and entropy can be used to identify areas of intersection of axonal tracts. Probability characterizes the direction itself and entropy characterizes surrounding pixels. Simulation data with different signal / noise ratio showed that the entropy is more resistant to noise parameter. Application of the method on real data also confirmed our assumptions.

Acknowledgments

This work was supported by RFFI grant 13-02-00925.

References

[1] Il’yasov K.A., Aganov A.V., Krecher B.V. Diffusion tensor MRI in brain microstructure and connectivity investigations // Tech. of living systems (Russ). 2012. T. 9. №6.

[2] Conturo T.E., Lori N.F., Cull T.S., Akbudak E. et al. Tracking neuronal fiber pathways in the living human brain // Proc. Natl. Acad. Sci. USA. 1999. V. 96. № 18. P. 10422−10427.

[3] Kreher B.W., Schnell S., Mader I., Il'yasov K.A. et al. Connecting and merging fibres: pathway extraction by combining probability maps // Neuroimage. 2008. V. 43. № 1. P. 81−89.

[4] S. Mori, B. J. Crain, V. P. Chacko, P. C. van Zijl. Three-dimensional tracking of axonal projections in the brain by magnetic resonance imaging //Ann Neurol. 1999. V. 45. № 2. P. 265-269.

[5] Koch M.A., Norris D.G., Hund-Georgiadis M. An investigation of functional and anatomical connectivity using magnetic resonance imaging //Neuroimage. 2002. V. 16. № 1. P. 241−250.

[6] Rényi A. On measures of information and entropy//Proc. Fourth Berkeley Symp. on Math., Statist. and Prob.,1960. V. 1. P. 547-561

Studies of correlation between viscosity oil and nuclear magnetic relaxation characteristics

T.A. Zaripov[1], B.I. Gizatullin[1], T.R. Abdullin[2]

[1]Kazan Federal University, 420000, Kremlin str. 18, Kazan, Russia.
[2]OOO "NTC TATNEFT", 423236, Musa Djalil str. 32, Bugulma city, Russia

e-mail: zaripovta@gmail.com

It is necessary to determine the reservoir properties (RP) a collector to evaluate the performance and profitability of the well. The reservoir properties can be divided into geometric and dynamic. Geometric properties include capacity φ and permeability μ. Dynamic property is viscosity η. The average rate of filtration $\langle v\rangle$ by Darcy's is:

$$\langle v\rangle = \frac{Q}{S} = -\frac{\mu}{\eta}\nabla P, \qquad (1)$$

where Q — volumetric flow, S — cross-section, ∇P — pressure gradient.

Therefore, the definition of fluid viscosity is an important task in assessing the reservoir. Modern viscometry methods are mostly laboratory, their application in field conditions is difficult, and impossible in the borehole.

NMR is using increasingly in the well logging. Therefore it is necessary to find a way to determine viscosity by nuclear magnetic resonance characteristic.

We use a several models for definition this evaluation. McConnell model is dipole-dipole relaxation by rotational diffusion spheres with associated magnetic moment in a viscous medium. In this model the relaxation speed T_2^{-1} is proportional to the rotational correlation time $\tau_c - T_2^{-1} \sim \tau_c$. It is known, that substances viscosity is associated with correlation time through viscous relaxation time

$$\vartheta_c \sim \eta \frac{R^2}{T}\vartheta_c \sim \tau_c, \qquad (2)$$

$$\vartheta_c \sim \tau_c. \qquad (3)$$

Complex of these models describes well simple, mono-component systems. Apply them to describe the complex, multi-component systems, such as oil. We have dispersion of rotational correlation times in mixtures. Therefore there is a dispersion of speed of spin-spin relaxation.

To describe the viscosity of the system through the NMR characteristics, we considered three models to be analyzed and the degree of applicability.

1. Rheological model for parallel connected viscosity elements. Slow modes of motion are most significant (fig.1)

$$\eta \sim \vartheta_c \sim \sum\nolimits_p n_p \tau_p \sim \sum\nolimits_p n_p \frac{1}{\tau_{2p}} \qquad (4)$$

2. Rheological model for serially connected viscosity elements. Fast modes of motion are most significant (fig.2)

$$\eta^{-1} \sim \vartheta_c^{-1} \sim \sum\nolimits_p n_p \tau_p^{-1} \sim \sum\nolimits_p n_p T_{2p} \qquad (5)$$

3. Energy model. The activation times are averaged in the mixture. Rotational correlation time is nonlinear included in the viscosity (fig.3)

$$\ln\eta \sim \ln\vartheta_c \sim \sum\nolimits_p n_p \ln\tau_p \sim -\sum\nolimits_p n_p \ln T_{2p} \qquad (6)$$

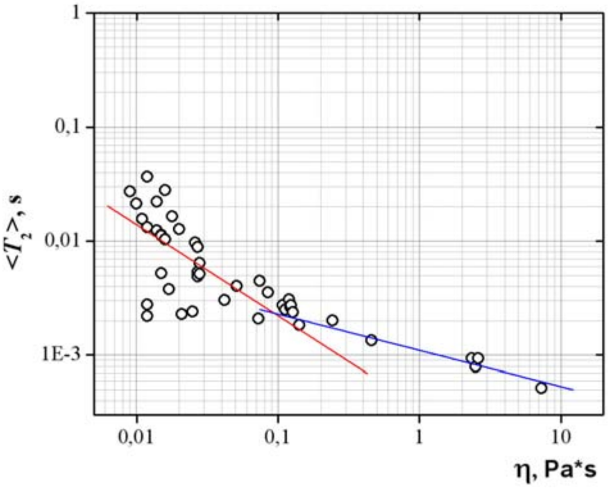

Fig.1. Dependence of the time <T2> on the viscosity of oil samples calculated from the model №1 (4)

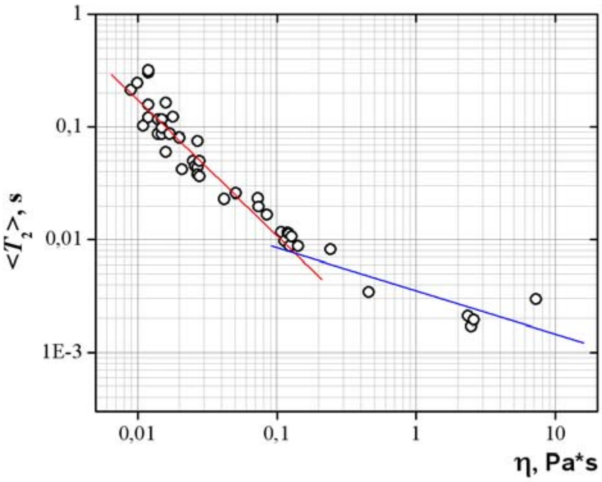

Fig. 2. Dependence of the time <T2> on the viscosity of oil samples calculated from the model №2 (5)

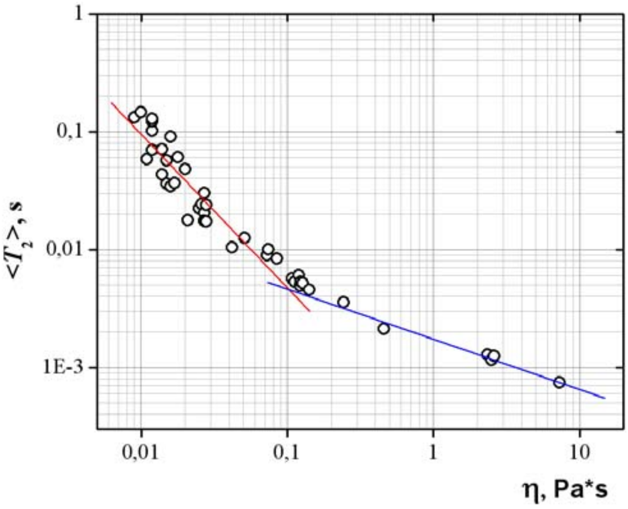

Fig.3. Dependence of the time <T_2> on the viscosity of oil samples calculated from the model №3 (6)

The measurements were performed on the spectrometer Chromatec Proton 20M, 20 MHz. CPMG sequence used for the curve of the transverse magnetization decay. Recession transverse magnetization has a multi-exponential character. Obtain spectra of relaxation times using regularization algorithms (Tikhonov method).

It can be concluded from the literature that there are two areas: low-and high-viscosity oil, for which the correlation of the relaxation time with viscosity has a different character [2]. Therefore analyzed range was broken into two parts: before and after 0.1 Pa*s to assess the correlation.

The first model is characterized by a large spread in the area of high viscosity (inactive) oils. Correlation increases with increasing viscosity. Dependence has a high correlation coefficient in the field of high-viscosity oils (table 1). This is because the viscosity of heavy oils is largely determined by high molecular weight components of oil with low value of the relaxation time.

Table 1.

	1\T	T	lnT
Light oil	0,58	0,88	0,91
Heavy oil	0,95	0,84	0,98

The second model, in contrast, the best correlation between relaxation time and viscosity is observed at low viscosity oils.

The third, the "energy" model, characterized by the absence of obvious artifacts in the experimentally obtained data.

The data obtained suggest that the most correct model of the presented model is taking into account average activation energy for all molecules of the mixture.

Thus, it is shown that the best model is the description takes into account the average of the energy of activation.

However, none of these models is not possible to describe correctly the experimental data. This means that it is necessary to introduce more complex models that take into account more complex molecular mechanisms.

Acknowledgements

This work is supported by contract №8-2014 from 3.04.2014 between Kazan Federal University and «NTC TATNEFT» and results were measured with the equipment of the Federal Center of Shared Facilities of Kazan Federal University.

References

[1] D.K. Nurgaliyev, V.E. Kosarev, V.M. Murzakaev, M.S. Tagirov, V.D. Skirda, V.F. Tyurin, B.I. Gizatullin /The nuclear magnetic resonance equipment for the research in laboratory and field conditions of full-sized core samples// Georesursy – Georesources,2012, no. 4(46), pp 16-18

[2] Brown, R.J.S. / The Earth's-field NML development at Chevron // Concepts in Magnetic Resonance no. 6(13): pp.344-366.

Ultrashort pulsed UV lasers based on the Ce^{3+}:$LiCaAlF_6$ and $LiLuYF_4$:Ce^{3+} crystals

O.R. Akhtyamov, A.S. Nizamutdinov, M.A. Marisov, V.V. Semashko

Institute of Physics, Kazan federal university, Kremlevskaja 18, 420008 Kazan, Russia

e-mail: akhtyamovo@mail.ru

An important problem of quantum electronics is the generation of laser radiation in the form of ultrashort pulses in UV spectral range. The family of cerium-doped laser crystals [1] offer an attractive all-solid-state route providing valuable tunable laser oscillation in the UV directly with simpleness and attractive properties of solid-state laser (beam divergence, energy distribution) which is problematic for nonlinear converters.

Here we report on UV laser oscillation on colquiriite structure fluoride mixture crystals of Ce^{3+}:$LiCaAlF_6$ (Ce:LiCAF) and $LiLuYF_4$:Ce^{3+} (Ce:LiLuYF) active media which can be pumped at around 266 nm, and so can utilize frequency-quadrupled Nd-based pump lasers [2]. We carried out experiments to generate subnanosecond pulses on Ce:LiCAF crystal at energies well above the lasing threshold. Experimental results are presented in fig.1a.

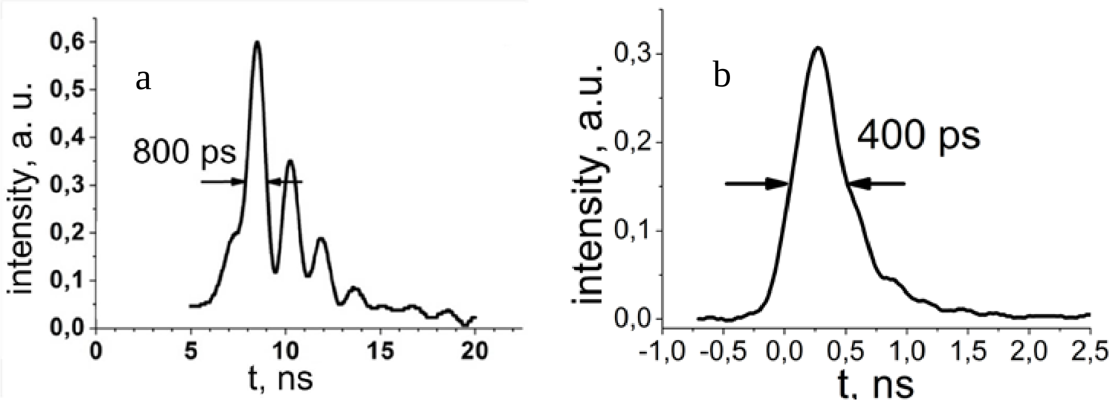

Fig.1. Temporal distribution Ce:LiCAF laser (with external mirror) (a); temporal distribution Ce:LiLuYF laser

The composite laser cavity consist of a short length low Q-factor pulse-seeding laser cavity and a feedback laser cavity. The pulse-seeding laser cavity provide only spiking mode. Regenerative amplification was organized using long feedback cavity [1,2], and as a result we see a stable ultrashort “pulse-train” with pulse duration at about 800 ps and a period defined by the design of the cavity. It is important that length of the external cavity should be tuned so that the second pulse of pulse-train occur before generation of the second stochastic pike. In this case the lasing pulse is circulating into external laser cavity will use the inversion and regenerative amplification will occure preventing stochastic laser oscillation.

The second step was in single picosecond pulse generation experiments. Here we discuss the possibility of using photodynamic processes for intracavity losses modulation. Internal UV pump induced losses in active medium could be utilized to shorten the laser pulse. Ce:LiLuYF crystal is advantageous here as color centers formation is well pronounced in it [3]. We report on single pulse generation of about 400 ps duration from Ce:LiSAF (fig.1b) in convenient Fabri-Perrot cavity and discuss conditions of pulse shortening in UV active medium by photodynamic processes.

References

[1] N. Sarukura, Z. Liu, Y. Segawa, V.V. Semashko, A.K. Naumov et al. J. Appl. Phys. Lett., 1995, 67, 602.

[2] N. Sarukura, Z. Liu, S. Izumida, M.A. Dubinskii, R.Y. Abdulsabirov, S.L. Korableva. J. Appl. Opt., 1998, 37, 6446.

[3] O.R. Akhtyamov, A.S. Nizamutdinov, V.V. Semashko, A.K. Naumov, S.L. Korableva. Proc. SPIE, 2011, 7994, 79940I.

Photodynamic processes in LiCaAlF$_6$:Ce^{3+} UV active medium

A.I. Galiev, V.V. Semashko, O.R. Akhtyamov, S.A. Shnaidman, M.A. Marisov,
A.S. Nizamutdinov

Kazan Federal University, Institute of Physics, Kremlevskaya str. 18, 420008 Kazan, Russia
e-mail: Almaz.Galiev.Isl@gmail.com

One of the key problems of quantum electronics is prospects estimation of using new materials as laser media. Existing methods of traditional optical spectroscopy are often can’t give a definite answer to this question, because when trying to get lasing active substance exposed much more intense impacts than those that take place in the case of the use of these methods. It is that why intense optical pumping is accompanied by additional effects associated with the appearance on the excited states of the investigated medium large electronic populations that may impede, impair or even completely exclude the possibility of exciting laser action [1]. One of the effective ways to assess the real "laser potential" new media are "pump-probe" spectroscopy methods, which suggest the creation of conditions for the excitation of the material close to the conditions of the laser tests. The most informative studies are absorption/transmission coefficient of samples versus intensity and wavelength exposure radiation. The specific role is playing interpretation methodology of the experimental data. Thus it is possible to fully characterize the active madium, quantify its prospects of realization, energetic and tunability properties of laser based on it.

This work is part of photodynamic processes in cerium-activated fluoride crystals researches. The objectives of this paper are experimental studies of pump-induced effects in LiCaAlF$_6$: Ce^{3+} single crystals, computer model elaboration and a appropriated software package engineering. The last one have to allow either calculate the nonlinear absorption/gain characteristics of the excited sample from the known parameters of the active medium, or find its previously unknown parameters from pump-probe experimental dependences.

Methods of pump-probe spectroscopy have been registered absorption and/or gain coefficient of LiCaAlF$_6$: Ce^{3+} crystals in the 4f ↔ 5d transitions of Ce^{3+} ions spectral ranges versus the intensity of the pump and probe radiation. Interpretation of these dependencies is realized using a hypothetic model of photodynamic processes described in [1] and shown in fig.1. The model included four level scheme laser oscillator supplemented with transitions from excited states localized in the conduction band of the crystal host, recombination

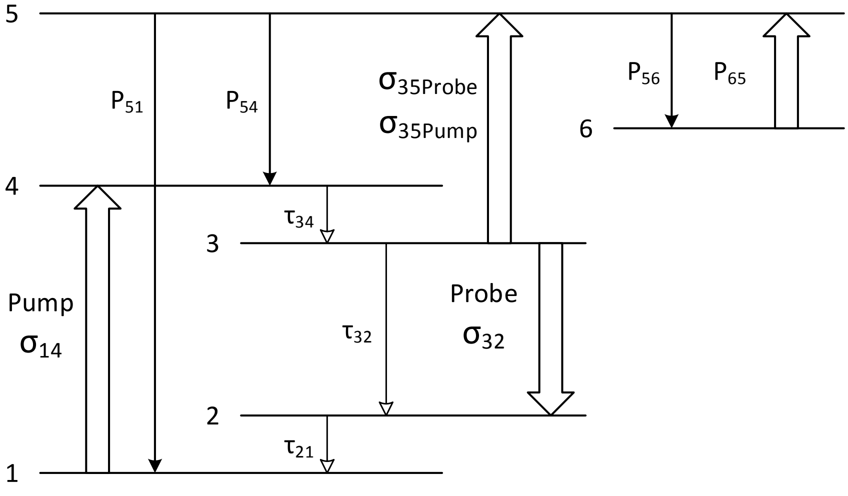

Fig.1. Stochastic model of photodynamic processes in LiCaAlF$_6$:Ce^{3+} active media

processes and the processes of formation and destruction of the color centers. Part of the model parameters are known with adequate accuracy from the literature [2, 3] and spectral-kinetic studies of the samples. The remaining parameters were the subject of an optimization procedure ("fitting"), carried out in such a way as to ensure a minimum residual between the experimentally determined and calculated data. The results are shown in fig.2.

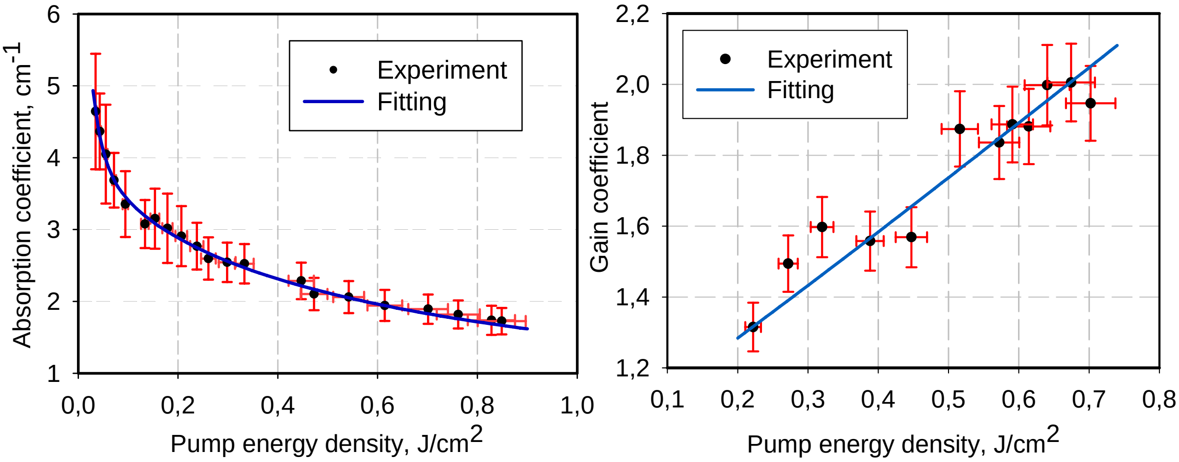

Fig.2. Pumping radiation absorption (λ=266 nm) and gain (λ=290 nm) coefficients depending on the pumping radiation energy density and fitting results

Estimated 5d-excited-state photoionization cross-sections of Ce^{3+} ions and pump-induced color centers at pumping and probe beams wavelength together with rates of recombination processes of free charge carriers in crystals $LiCaAlF_6:Ce^{3+}$ are shown in the Table 1.

Table 1. Parameters of photodynamic processes from $LiCaAlF_6:Ce^{3+}$ resulting from computer simulation.

Absorption cross-sections, cm^2		Probabilities, s^{-1}		Concentration, cm^{-3}	
σ_{35pump}	$(4 \pm 0.3)\cdot10^{-18}$	P_{51}	$(5 \pm 0.4)\cdot10^{8}$	Ions Ce^{3+}	$(5 \pm 1.2)\cdot10^{17}$
σ_{65pump}	$(9 \pm 0.3)\cdot10^{-16}$	P_{54}	$(3 \pm 0.3)\cdot10^{8}$	Color centers	$(1 \pm 0.3)\cdot10^{16}$
$\sigma_{35probe}$	$(4 \pm 0.2)\cdot10^{-18}$	P_{56}	$(3 \pm 0.2)\cdot10^{9}$		
$\sigma_{65probe}$	$(3 \pm 0.4)\cdot10^{-20}$				

Research results and developed software can be used for further design of ultrashort pulse laser based of the $LiCaAlF_6:Ce^{3+}$active medium, as well as for studies of photodynamic processes in other activated materials [4].

References

[1] V.V. Semashko Phys. Solid State 47, 1507 (2005)

[2] Marshall, C. D., et al. " Ultraviolet laser emission properties of Ce^{3+}-doped $LiSrAlF_6$ and $LiCaAlF_6$." *JOSA B*11.10 (1994): 2054-2065. (1994)

[3] Coutts, David W., and Andrew JS McGonigle. "Cerium-doped fluoride lasers."*Quantum Electronics, IEEE Journal of* 40.10 (2004): 1430-1440.

[4] Akhtyamov, O.R., et.al. “UV sub-nanosecond laser based on Ce:LiCaAlF6 active medium.” Izv. VUZov. Fizika. 56.22 (2013):39-42 (in Russian)

$LiY_{0.3}Lu_{0.7}F_4$: Ce^{3+}, Pr^{3+} mixed crystal as a perspective up-conversionally pumped UV active medium

V.G. Gorieva, V.V. Semashko, S.L. Korableva, M.A. Marisov

Kazan Federal University, 420008, 18 Kremlevskaya st, Kazan, Russia

e-mail: ekorre_v@mail.ru

Currently tunable solid-state optical quantum generators of UV range are most easily implemented on interconfigurational $4f^{n-1}5d – 4f^n$ transitions of rare-earth ions in wide-bandgap insulators. In this case the pumping of the laser is usually carried out by UV harmonics of visible and infrared radiation generated by of commercially available lasers, or powerful radiation of excimer lasers. However, UV pumping radiation induces in solid-state active elements various photodynamic processes (PDP), which cause degradation of the optical properties of active media. One of the ways to avoid or significantly reduce harmful manifestations of PDP is to use up-conversion pumping [1]. The two schemes of up-conversion excitation of 4f5d level of Pr^{3+} ion in $LiLuF_4$ [1] is present in fig.1. Finding ways to realize such up-conversion pumping is a topic problem in the view of future implementation of effective solid-state UV-active media with the use of semiconductor lasers as a pumping source and compact solid-state quantum electronics devices of UV range in general.

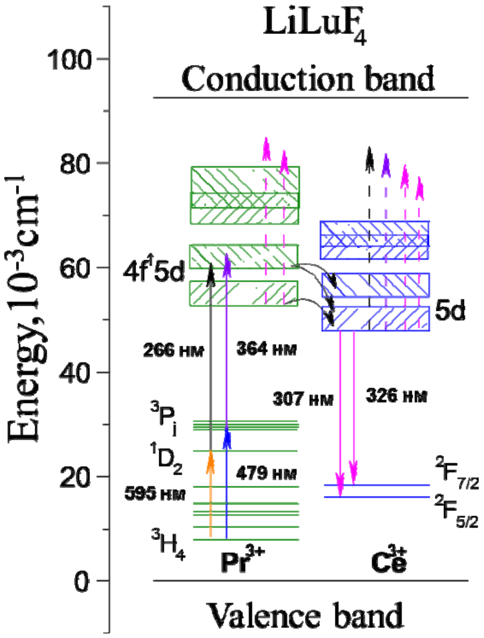

Fig.1. The two schemes of up-conversion excitation of 4f5d level of Pr^{3+} ion in $LiLuF_4$

Here we investigate an opportunity of effective population of states of 5d-configuration of Ce^{3+} ions in $LiY_{0.3}Lu_{0.7}F_4$ (LYLF) crystals by stepwise $^3H_4 – ^3Pj – 4f5d$ up-conversion excitation of states of 4f5d-configuration of Pr^{3+} ions, followed by the transfer of excitation energy from Pr^{3+} to Ce^{3+} ions. We discuss the possibility of increasing energy transfer efficiency in Pr, Ce: LYLF mixed crystals by doping rising, because before it was the one of obstacles which prevent optical gain on 5d – 4f transitions of Ce^{3+} ions in Pr,Ce:$LiLuF_4$ crystals [2]. In particularly, it is shown that the real concentrations of Pr^{3+} and Ce^{3+} ions of about 0.23 at.% and 0.47 at.% are achieved in mixed LYLF crystal respectively. The spectral and kinetic characteristics of Pr,Ce:LYLF crystal are presented. The coefficients of excitation energy transfer from the Pr^{3+} ions to Ce^{3+} ions are estimated by means of Pr^{3+} luminescence decays analysis at a wavelength of 255 nm. It reaches 31% in case of real concentrations of Ce^{3+} ions C(Ce) = 0.28% and Pr^{3+} ions C(Pr) = 0.38% in Pr, Ce: LYLF crystal.

Preliminary results on the energy transfer between of Pr^{3+} and Ce^{3+} ions experiments are presented and discussed. Three crystals with real concentrations of Pr^{3+} and Ce^{3+} ions 0,38 at.% and 0,16 at.%; 0,38 at.% and 0,28 at.%; 0,24 at.% and 0,47 at.% respectively were studied. Samples were up-conversionally pumped by two laser beams at 595 nm and 266 nm. The temporary delay between 595 nm and 266 pulses were about 7 ns. The results of the experiment are the dependences of integral luminescence of Ce^{3+} ions on energy densities of pumping beams. Such parameters as excited 4f5d state photoionization cross-section of Pr^{3+} ions, ground state cross-section of Ce^{3+} ions at 266 nm wavelengths and energy transfer coefficients of energy transfer from Pr^{3+} to Ce^{3+} ions were estimated. These parameters were determined by mathematical modeling of the integral luminescence dependencies of Ce^{3+} ions on energy densities of pumping beams and comparing with experimental ones.

Obtained results demonstrate good prospects of using crystal $LiY_{0.3}Lu_{0.7}F_4:Ce^{3+}$, Pr^{3+} as an active medium of solid-state laser with up-conversion pumping provided that color center formation processes suppression and rising Pr^{3+} – Ce^{3+} energy transfer efficiency.

References

[1] V.V. Semashko, M.F. Joubert, E. Descroix, S. Nicolas, R.Yu. Abdulsabirov, A.K. Naumov, S.L. Korableva, A.C. Cefalas, Proc. Of SPIE. -2000. –V. 4061 –P. 306-316.

[2] S. Nicolas, E. Descroix, M.F. Joubert, Y. Guyot, M. Laroche, R. Moncorge, R.Y. Abdulsabirov, A.K. Naumov, V.V. Semashko, A.M. Tkachuk, M. Malinowski, Opt. Mat. -2003. -V.22 -P.139-146.

The development of polymer laser-active media with improved performances

R.A. Idrisov[1], V.N. Serova[1], I.I. Farukhshin[2], A.S Nizamutdinov[2], V.V. Semashko[2],
A.V. Lovchev[2], A.K. Naumov[2]

[1] Kazan National Research Technological University, 420015, K. Marks str., Kazan, Russia.

[2] Kazan (Volga region) Federal University, 420008, Kremlevskaya str., Kazan, Russia

e-mail: rav1409@mail.ru

The optically transparent polymers doped with laser dyes are a new class of solid-state laser-active mediums (LAM). Research results of their properties are described in [1] and other numerous papers. The polymeric LAM are successfully replace liquid LAM-solutions of laser dyes. However, in order to broaden their area of practical application is necessary to improve their performance properties and mostly, the photochemical stability under optical pumping conditions. This requires a search for new highly stabilizers.

The novel derivatives of thiazole and thiourea (DTT) synthesized in Institute of Organic and Physical capable inhibit the free radical chain processes, were chosen us for the study as stabilizing compounds. This work is the development of research carried us on approbation of new nitrogen-and sulfur-containing organic compounds to stabilize of colorless and dyed with Rhodamine 6G methacrylic copolymers.

The purpose of this work is the study of spectral-fluorescent properties of samples of organic glasses doped with Rhodamine 6G and DTT, and to elucidate the possibility of using them as LAM with improved performance characteristics.

Registration of absorption spectra was carried out on a dual-beam scanning spectrophotometer «Lambda 35» (Perkin-Elmer, USA). To excite samples fluorescence UV solid-state Ce: LLF picosecond laser (Ultraviolet Solution LLC) was used. It was tuned to $\lambda = 310$ nm and provide single 400 ps laser pulses with pulse repetition rate 10 Hz. The fluorescence spectra were studied by Stellarnet spectrometer and fluorescence kinetics were taken by Alphalas UPD photodiodes with 50 ps rise time and 3.5 GHz bandwidth Tektronix DPO 7354 digital oscilloscope. The fluorescence spectra were also measured using a spectrofluorimeter Cary Eclipse (Varian, USA). Studies of lasing properties has been carried out under pumping by second harmonic radiation of Nd: YAG laser ($\lambda = 532$ nm) from TII LOTIS. The lasing photostability was determined by the number of pump pulses at a constant energy density (63 and 146 mJ/cm^2) to reduce energy generation by 50%.

It was established that DTT in polymer matrix possess the properties of UV absorbers and furthermore intrinsic fluorescence at $\lambda = 425$ nm. Study the kinetics decay of fluorescence show that DTT doping is not impact on fluorescence kinetics of Rhodamine 6G. View of the fluorescence spectra depends on the amount DTT in the polymer matrix. For instance, in case of the concentration of DTT more than 0.1 mol.%, there are occured reabsorption of fluorescence dye. Laser tests have showed that using of small amount of DTT (about 0.01 – 0.02 mol.%) leads to increase the lasing power and to improve photostability of Rhodamine 6G in polymer matrix.

References

[1] Serova V. N. Polymer optical materials. – S.-Petersburg: Naychnye Osnovy i Tehnologii Publ., 2011. 384 p.

Up-conversion luminescence of LaF_3:Pr^{3+} crystal

O.A. Morozov, A.K. Naumov, A.V. Lovchev, E.Yu. Tselishcheva

Kazan (Volga region) Federal University, 420008, Kremlevskaya 18, Kazan, Russia

e-mail: alovchev@ksu.ru

The problem of creating a solid-state infrared quantum counter (IRQC) is actual in view of circumstances. IRQC is a system, which allows to convert infrared radiation in the visible region by the direct conversion of light to light. Moreover, such system is not afraid overexposure, in contrast to other similar operating principles. The greatest efficiency in these systems can be achieved by using up-conversion transitions between levels of rare earth ions in a crystal [1, 2]. The operation of such systems is based on the absorption of visible quantum and infrared one by the activated crystal through an intermediate level of the activator. Energy from the excited higher state decay radiatively with the summary quantum.

As a basis of IRQC for research we chose the crystal LaF_3:Pr^{3+}. There are a number of works that implement IRQC on this crystal, but all of them work in the range from 0.8 to 1.5 um [3, 4]. The operation of this IRQC in the range from 2 to 6 um has not been studied yet, despite all the signs. This work is devoted to study of this problem.

In this work we studied the properties and interpreted up-conversion luminescence excited by visible and infrared radiation (fig.1).

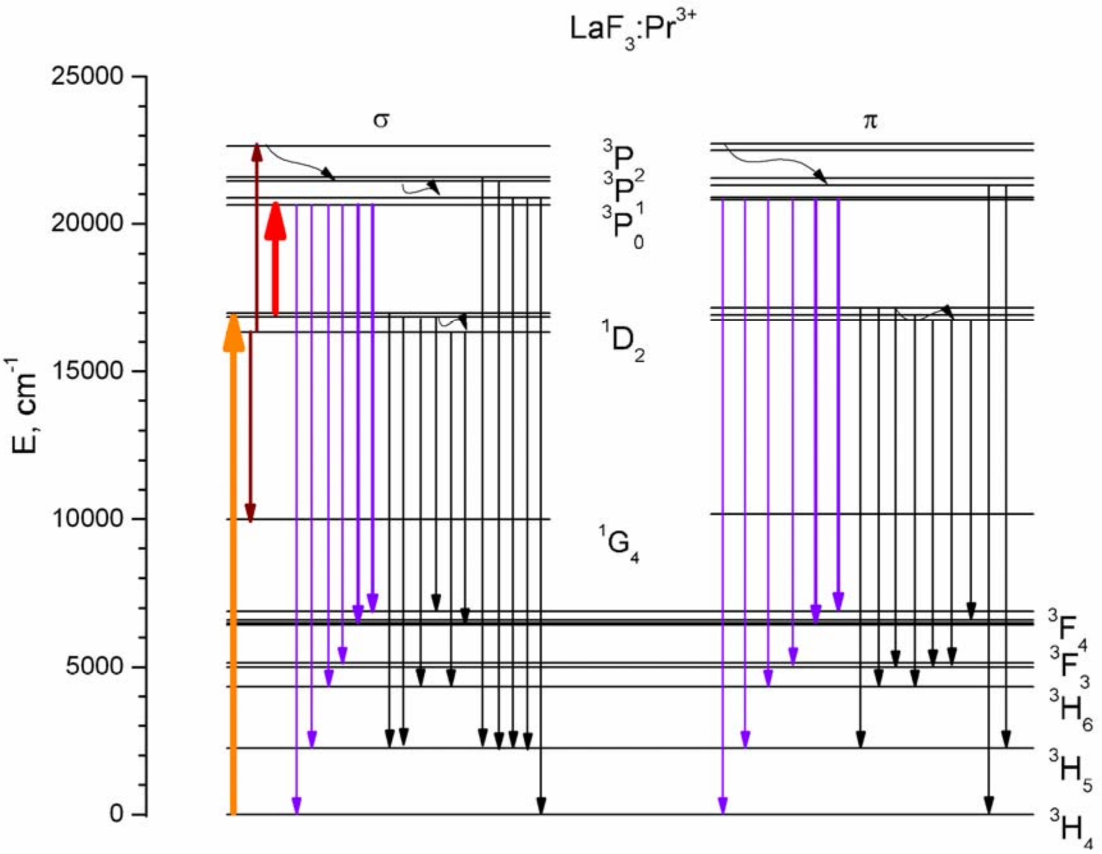

Fig.1. The energy level diagram of Pr^{3+} ions in the LaF_3 crystal and transitions between them, which explain reaction of the pumped sample (by radiation with a wavelength of 0.5945 um) of this crystal to additional illumination by IR radiation with a wavelength of 3 um.

Increment of up-conversion luminescence under IR illumination of pumped $LaF_3:Pr^{3+}$ crystal is found and interpreted. The results were obtained under the following conditions: crystal was pumped by a pulsed laser with a wavelength of 0.5945 um and IR illumination had wavelength of 3 um and a power of 10.7 W. 5% increase in the intensity of individual up-conversion luminescence lines was observed at low temperature. This effect occurred in two temperature points 170 K and 210 K. The results demonstrate operability of $LaF_3:Pr^{3+}$ crystal as a IRQC.

References

[1] N. Bloembergen. Phys. Rev. Lett. V.2, N3, 84, 1959.

[2] H. Lengfellner, K.F. Renk. IEEE J. Quant. Electron. V.13, N6, 421, 1977.

[3] L. Esterowitz, A. Schnitzler, J. Noonan, J. Bahler. Appl. Opt. V.7, N10, 2053, 1968.

[4] N.E. Byer, T.C. Ensign, W.M. Mularie, S.E. Stokowski. J. Appl. Phys. V.44, N4, 1733, 1973.

Toxicity of photoactive fluoride nanoparticles PrF_3 and LaF_3 for biological organisms (bacteria, cancer cells) under the laser irradiation

S.L. Korableva, A.O. Krashennicova, A.S. Nizamutdinow, M.S. Pudovkin, V.V. Semashko,
P.V. Zelenihin

Kazan Federal University, 420008, 18 Kremlin str., Kazan, Russia

e-mail:jaz7778@list.ru

Because of the unique physical and chemical properties of nanoparticlers they can be used in a broad range of biological applications. Several last researches [1 – 4] have reported that photoactive nanoparticles could cause oxidative stress and they can be activated by UV and visible irradiation generating reactive oxygen species (ROS). The ROS can damage cellular components and oxide different organic contaminants [5]. In consequence, the photoactive nanoparticles can be applied in waste water treatments, environmental remediation, organic contaminants mineralization, and cancer treatment [5, 6]. Cancer is the third leading cause of death (after heart disease and stroke) in developed countries and the second leading cause of death (after heart disease) in the United States [1]. Moreover, there are 2,8 millions cancer carriers in Russia by the beginning of 2014 according to the Russian Ministry of health. Recently, new therapeutic strategies that take advantage of increased reactive oxygen species producing a state of oxidative stress selectively in cancer cells have gained importance [6]. Semiconductor nanostructures like TiO_2, ZnO with photocatalytic activity are used in the reports [1 – 3]. But these semiconductor nanostructures have low photocatalytic activity. Besides, they are activated only by UV irradiation. This fact makes the problem of using this nanostructures more complex. The depositing nanoparticles of noble metals, that have less diameter on the surface of semiconductor nanostructures can enhance photocatalytic activity of the nanostructures and shift absorption frequencies to the visible region. But it makes the process of producing such nanostructures expensive and time consuming. So the search for new photoactive nanostructured materials is a topical problem. Here we are presenting toxicity results of photoactive fluoride nanoparticles PrF_3 and LaF_3 for biological organisms (bacteria, cancer cells) under the laser irradiation.

Materials and methods

There are very few reports about toxicity of photoactive fluoride nanoparticles PrF_3 and LaF_3. In spite of this they are discussed at different international scientific conferences. These nanoparticles have a large possibility in using in different biological applications. Because of their high absorption capacity in range of 450 – 550 nm and high photoenergy conversion efficiency they can be used in cancer treatment [7]. The team of the S.A. Altshullers' laboratory of quantum electronics and radiospectroscopy of Kazan (Volga region) federal university has developed a technology of synthesizing fluoride photoactive nanoparticles PrF_3 and LaF_3 by chemical methods. The HRTEM imagines of them are shown at the fig.1. To stimulate a toxicity of nanoparticles we have used CW semiconductor lasers operated at 532 nm (green light) and 473 nm (blue light) wavelengths with maximal power of about 30 mW. We irradiated the cells in the saline in the beaker by the laser irradiation with average radiation density of about 400 mW/cm^2. We studied two kinds of cells: *Salmonella typhimuriumTA 98,* lung carcinoma A549 cells.

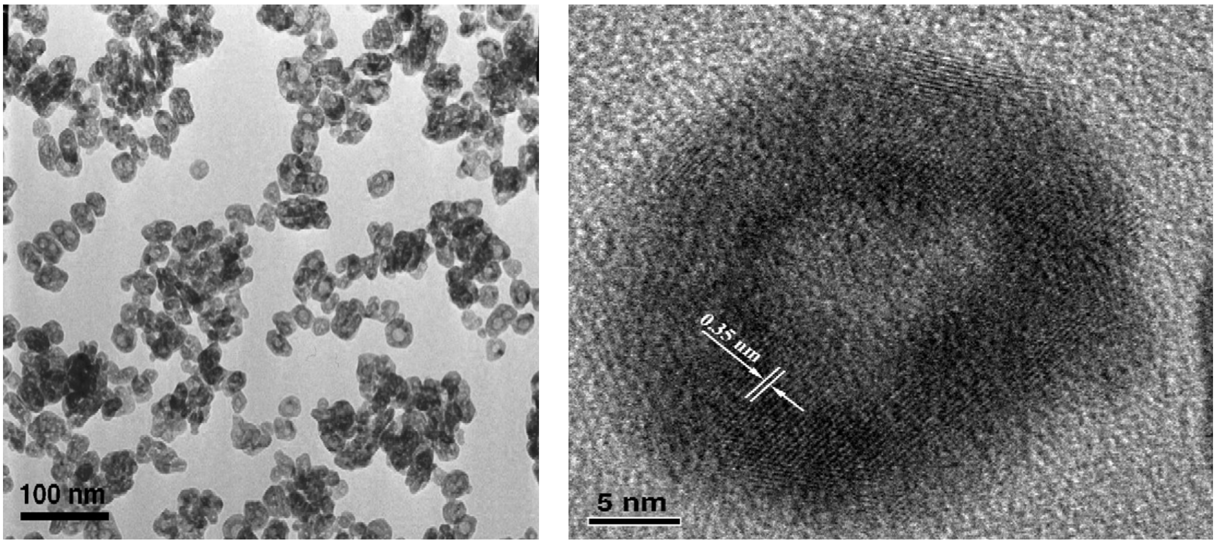

Fig.1. The HRTEM imagines fluoride photoactive nanoparticles PrF_3 synthesized in Kazan university

The investigation toxicity of photoactive fluoride nanoparticles PrF_3 and LaF_3 cells Salmonella typhimuriumTA 98

One of the main aims of our research was to taste hypothesis of toxicity of photoactive fluoride nanoparticles PrF_3 and LaF_3 for biological organisms under laser irradiation with definite wavelength. The cells *Salmonella typhimuriumTA 98* were chosen as a first object of investigation. The scheme of the experimental setup is shown in fig.2.

The focus of the lens (2) was 7.5 cm. The beaker with the cells and the nanoparticles (1) was exposure under the laser irradiation for 5 minutes. We made the experiments for laser wavelengths 473 nm and 532 nm. We have investigated the influence of laser irradiation on the cells in tree configuration of experimental setup: the beaker was exposure under the laser irradiation without the lens, the beaker was in the visual focus of the lens, and the beaker was behind the visual focus of the lens. We have also investigated the influence of nanoparticles on the biological species without the laser irradiation and the influence of laser irradiations without the nanoparticles. The first experiments showed the rise of photoenergy conversion efficiency for the beaker being behind the visual focus of the lens under laser irradiation with wavelength 532 nm. In this case, survival of the cells was 28% and 35% for PrF_3 and LaF_3, respectively. So, we have continued to investigate toxicity of the photoactive fluoride nanoparticles PrF_3 and LaF_3 with this configuration of experimental setup.

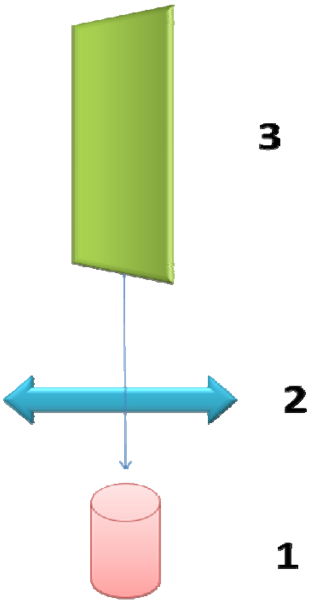

Fig.2. Experimental setup scheme.
1 – sample, 2 – lens,
3 – laser

The influence of exposure time of Salmonella typhimuriumTA 98 cells with the nanoparticles under the laser irradiation on the cells survival

In the second series of experiments we have investigated the influence of exposure time of the laser irradiation on the *Salmonella typhimuriumTA 98 cells* with the nanoparticles PrF_3 and LaF_3. Three duration of exposure time: 5 minutes, 15 minutes, 30 minutes were chosen.

In case of PrF_3 nanoparticles survival was 39%, 34%, 20% for exposure time 5 minutes, 15 minutes and 30 minutes correspondingly under laser irradiation with wavelength 532 nm. The same experiment with wavelength 473 nm for PrF_3 have not shown significant bactericidal activity. The experiment with LaF_3 nanoparticles under the laser irradiation with wavelengths 532 nm and 473 nm have not shown significant bactericidal activity.

The investigation of mutagenic effect on living cells

The same experiments with *S. Typhimurium* TA98 cells have shown that PrF_3 nanoparticles provides mutagenic effect on living cells under the laser irradiation with wavelength 532 nm. LaF_3 nanoparticles have not demonstrated mutagenic effect on living cells under the laser irradiation with both 532 nm and 473 nm.

The investigation toxicity of photoactive fluoride nanoparticles PrF_3 and LaF_3 lung carcinoma A549 cells

In this series of experiments we have investigated the influence of exposure time of the laser irradiation on the lung carcinoma A549 cells with the nanoparticles. Three duration of exposure time: 5 minutes, 15 minutes, 30 minutes were chosen. The PrF_3 nanoparticles have apoptosis inducing activity for lung carcinoma A549 *cell.* The proportion of cells in the state of apoptosis after 5 min, 15 min and 30 min irradiation with a laser with a wavelength of 532 nm was 23%, 33% and 45%, respectively. The same experimental with wavelength 473 nm for PrF_3 and wavelengths 532 nm and 473 nm for LaF_3 have not shown significant apoptosis inducing activity.

Conclusions

The fluoride photoactive nanoparticles PrF_3 and LaF_3 were synthesized by chemical methods. We have confirmed the hypothesis toxicity of photoactive fluoride nanoparticles PrF_3 and LaF_3 for biological organisms (*Salmonella typhimuriumTA 98,* lung carcinoma A549 cells). We have defined time exposure parameters for Salmonella *typhimuriumTA 98* cells under which the highest bactericidal activity was observed. And we also have confirmed the hypothesis of apoptosis inducing activity of photoactive fluoride nanoparticles PrF_3 for lung carcinoma A549 cell under the laser irradiation.

References

[1] F. Melissa, M. José, M. Amadeu. S. Barata. Science of the Total Environment. V.470–471, P. 379–389, 2014.

[2] V. Apalangya, V. Rangari, B. Tiimob, S. Jeelani, T. Samuel. Applied Surface Science. V.295, P.108– 114, 2014.

[3] O. Socorro, Z. Rodolfo, P. Blanca. Journal of Hazardous Materials. V.263, P.28–35, 2013.

[4] M.A. Behnajady, E. Hamed. Chemical Engineering Journal. V. 228, P. 1207–1213, 2013.

[5] A. Raghavendra, W. Gunveen, D. Niranjan, P. Bonamali// Environ Sci Pollut Res. V.20, P.6521–6530, 2013.

[6] H. Weiwei, K. Hyun-Kyung, W. Wayne, M. David, C. John, Y. Jun-Jie//J. Am. Chem. Soc. V.136, P.750−757, 2013.

[7] E.M. Alakshin, B.M. Gabidullin, A.T. Gubaidullin, A.V. Klochkov, S.L. Korableva, M.A. Neklyudovac, A.M. Sabitova, M.S. Tagirov. arXiv., V.1104, P.0208, 2011.

Pulse and CW EPR techniques to study of biradical systems

G.R. Nureeva[1], R.B. Zaripov[2]

[1]Kazan (Volga Region) Federal University, 420008 Kazan, Russia
[2]Zavoisky Physical-Technical Institute of the Kazan Scientific Center of the Russian Academy of Sciences, 420029 Kazan, Russia

e-mail: nureeva.gulina@rambler.ru

This work is devoted to study of parameters of radical systems by Electron Paramagnetic Resonance (EPR). In this work model biradical B1 (synthesized by professor Galyametdinov Yu.G. KNITU, Kazan) and biradical derivative of fullerene C60 B2 (synthesized by professor Nuretdinov I.A. IOPC KSC RAS, Kazan) are investigated. The aim of the work is consisted in determination of spin-spin interaction for the subsequent finding of distance between radical fragments. It is known that spin – spin interaction can be determine by the analysis of EPR line shape. In particular, weak dipolar interactions can be directly obtained by using the protocol of the Pulse ELectron DOuble Resonance (PELDOR). For both biradicals of B1 and B2 the spin - spin interaction values were obtained.

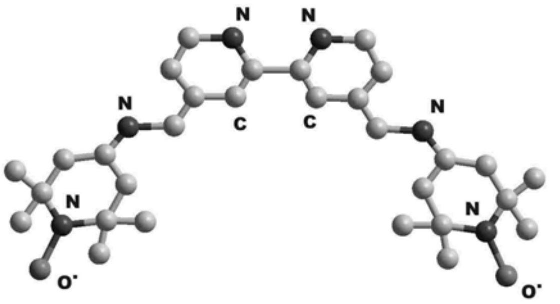

B1

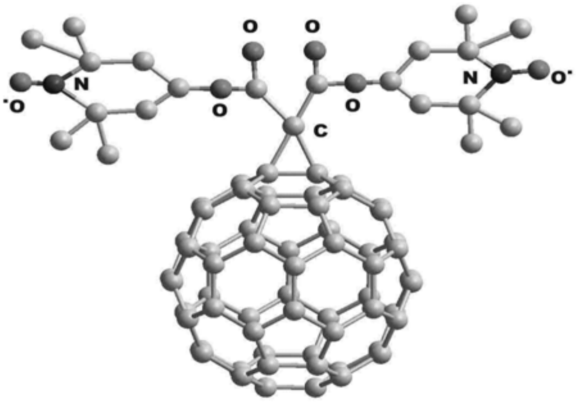

B2

Authors are grateful in part to the President Grant for Government Support of Young Russian Scientists (grant №14.120.14.4957-MK) for financial support

Development of hardware-software complex to switch between sensors for measuring magnetic field homogeneity of resonance magnetic tomograph

I.R. Sitdikov[1], A.R. Fakhrutdinov[2]

[1]Kazan Federal University , Institute of Physics, 420008, Kazan, Kremlyovskaya st. 18,
Russian Federation
[2] Kazan E. K. Zavoisky Physical-Technical Institute, 420029, Kazan, Siberian Trakt st. 10/7,
Russian Federation

e-mail: iskandersit@gmail.com

Tomographic imaging quality depends on many factors: a hardware and a software, the physical processes that affect the collection of data, the properties of the investigated object and the environment. The most important factors, which influence on the quality of images obtained by tomographic equipment - are a stability and a homogeneity of the static magnetic field. Have to work with large gradients at large magnetic field inhomogeneities.

There is not magnet which could make an ideal magnetic field. When we use the magnetic-resonanse tomography we have to make the static magnetic field with the homogeneity not more than 10^{-5} in the the investigated area.

Setting of the magnetic field of magnetic resonance scanners was producing carried out manually in KPTI.

For solution of this problem it was suggested to develop a sensor for measuring the magnetic field homogeneity and the printed circuit board with a microcontroller board for controlling the multiplexer, which is able to select sensor circuit with preset coordinates.

It should been solved the following tasks for implementation:

- develop and manufacture a cost of the control board;
- Write a program that controls the operation of the sensor.

A Multiplexing board is used to connect to the desired contour of the sensor at time. For solution of this problem was designed a switching mechanism. It consists of using multiplexers to switch sequentially between the coils.

A Multiplexing board is necessary to connect / switch at a certain moment of the desired contour of the sensor. “The multiplexer” term means a device which allows to switch between multiple inputs and output response to a control signal.

Search was made for devices that meet the requirements. As a result, plan to use Multiplexers ADG728 AnalogDevices company [1]. Because they contain 8 input channels and one output. And also have a two-wire serial interface.

We plan to develop and debug code for the microcontroller board AT90s8535 series AVR Atmel company [2], which allows to manage sensors magnetic field homogeneity in the future.

Also, tie AT90S8535 microcontroller board with the computer, providing functionality microcontroller board. For this it is necessary to implement the software. Block diagram of automated system for measuring the uniformity of the magnetic field is shown on fig.1. An algorithm for the microcontroller is shown on fig.2.

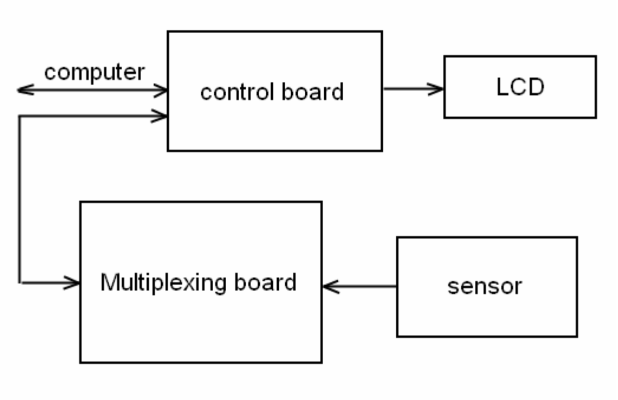

Fig 1. Schematic diagram of automatic complex for switching between the sensors

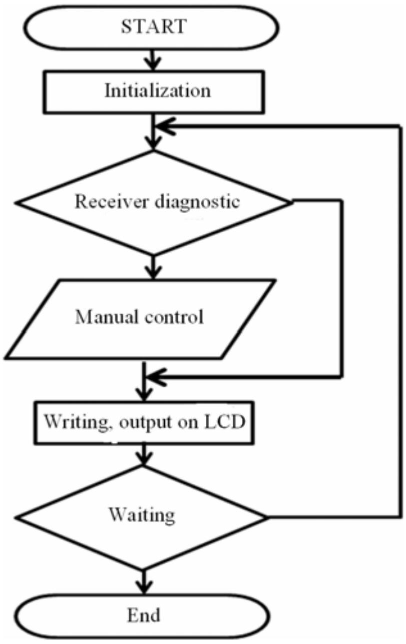

Fig.2. An algorithm of microcontroller’s work

Plan to use the demonstration version of C compiler for microprocessor cards - AVR Studio 4.0. Compiler AVR Studio 4.0 is an integrated environment for programming in C, with the following important characteristics:

- Integrated compiler C / C + +;
- Integrated simulator.

References

[1] *AD731 Datasheet,* Analog Devices Inc. (2003): http://www.analog.com/UploadedFiles/Data_Sheets/38931112587709ADG725_31_a.pdf

[2] *AT90S8535 Datasheet,* Atmel Corp. (2001): http://www.atmel.com/dyn/products/product_card.asp?family_id=607&family_name=AVR+8%2DBit+RISC+&part_id=2000

Existence of the two-dimensional electron gas at the interface multiferroic/ferroelectric $GdMnO_3/SrTiO_3$ detected by ESR

R.M. Eremina[1,2], T.P. Gavrilova[1], I.I. Fazlizhanov[1], I.V. Yatsyk[1,2], D.V. Mamedov[2],
V.I. Chichkov[3], N.V. Andreev[3]

[1]Zavoisky Physical -Technical Institute RAS, 420029, Kazan, Russia
[2]Kazan (Volga Region) Federal University, 420018, Kazan, Russia
[3]National University of Science and Technology MISiS,119049, Moscow, Russia

e-mail: i.yatzyk@gmail.com

The present work was stimulated by the discovery of the popular phenomena, including superconductivity and magnetism, in the two-dimensional electron liquid (2-DEL) at the interface between the insulators lanthanum aluminate ($LaAlO_3$) and strontium titanate ($SrTiO_3$) [1]. The origin of this 2-DEL, however, is highly debated, with focus on the role of defects in the $SrTiO_3$, while the $LaAlO_3$ has been assumed perfect. Authors [1] demonstrated through experiments and first principle calculations, that the cation stoichiometry of the nominal $LaAlO_3$ layer is key to 2-DEL formation; although extrinsic defects, including oxygen deficiency, are known to render $LaAlO_3/SrTiO_3$ samples conducting, their results show that in the absence of such extrinsic defects an interface 2-DEL can form.

Within this research the thin film of the multiferroic $GdMnO_3$ of thickness about 100 nm was deposited onto ferroelectric material $SrTiO_3$ ($GdMnO_3/SrTiO_3$). $GdMnO_3/SrTiO_3$ was investigated using electron spin resonance (ESR) in the wide temperature range.

The most interesting result was observed in the temperature range from 40 K to 100 K where except the exchange-narrowed line from $GdMnO_3$ we observed the oscillations of the absorption power (fig.1a). The intensity of the oscillations increases with increasing the external magnetic field or with decreasing the temperature.

We detected the anomalous jump in the temperature dependence of the ESR linewidth (fig.1b). We suggested that this anomalous behavior of the magnetic and electrical properties of $GdMnO_3/SrTiO_3$ at T = 80 K is connected with the structural phase transition in $GdMnO_3$. Since the minimal value of the ESR linewidth in orthorhombic monocrystal $GdMnO_3$ is 2700 Oe and in hexagonal ceramic $YbMnO_3$ is about 800 Oe, it is most likely that we

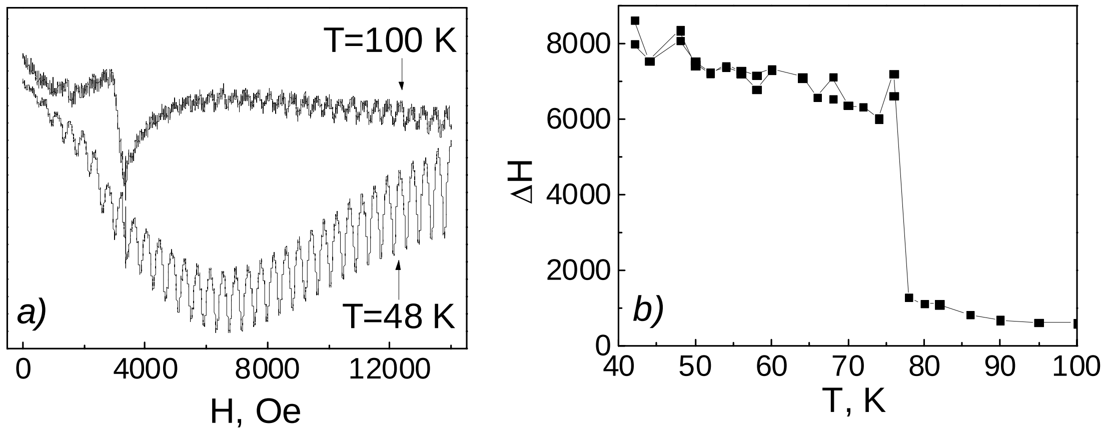

Fig.1. $GdMnO_3/SrTiO_3$: a) ESR spectra at T = 100 K.
b) Temperature dependence of the ESR linewidth in X-band.

observed the structural transition for $GdMnO_3$ in $GdMnO_3/SrTiO_3$.

Chen et al. observed similar oscillations of resistance in the two-dimensional electron gas in the magnetic field at the spinel/perovskite interface of γ-$Al_2O_3/SrTiO_3$ [2]. To understand the origin of the oscillations of the absorption power in the ESR spectra in $GdMnO_3/SrTiO_3$ it is necessary to imagine that two-dimensional electron gas exists on this interface as in the case above mentioned heterostructures [1, 3]. 2-DEG actually means the presence of the thin metal surface, which we put in an external static and radiofrequency magnetic fields and at the same time this metal layer is feeling the impact of the electric field from the $SrTiO_3$ substrate, because this material becomes ferroelectric under external influence (pressure, doping) below T = 100 K. The same oscillation were investigated by Gantmakher V.F. and Kaner E.A. in 1960-s [4, 5] in metal. According to Abrikosov A. in the case of high field electron drift along the magnetic field there is a large effect associated with the formation of bursts of high-frequency field inside the metal and the amplitude of the oscillation is proportional to $\exp(-\Delta/H)$ what we see in our experiments (see. fig.2). Probably, the oscillation of microwave absorption associated with two-dimensional conducting gas, which is formed at the interface of thin film $GdMnO_3$ and the substrate $SrTiO_3$.

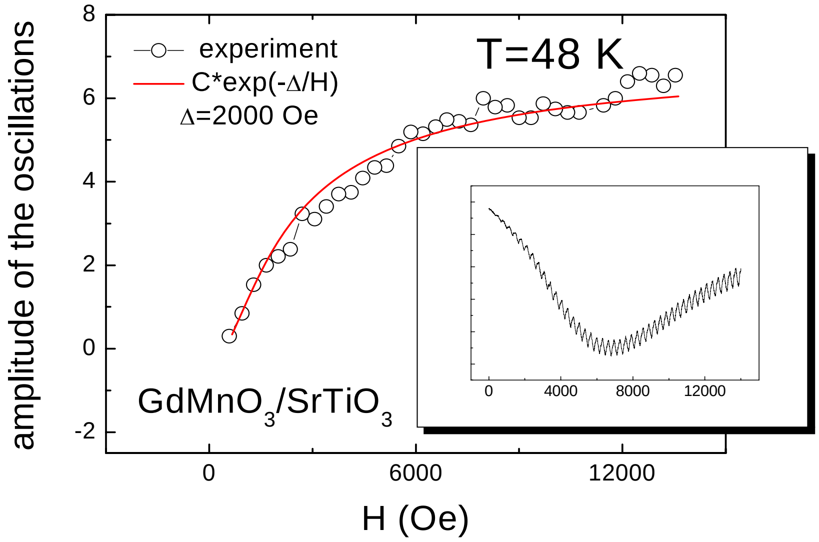

Fig.2. Field dependence of the amplitude of the oscillations of the absorption power in ESR spectra in $GdMnO_3/SrTiO_3$ at T = 48K.

The reported study was partially supported by RFBR, research project No. 13-02-97120.

References

[1] M.P. Warusawithana, C. Richter, J.A. Mundy, et al. Nature Communications **4**, Article number: 2351 (2013).

[2] Y.Z. Chen, N. Bovet, F. Trier, et al. Nature Communications **4**, Article number: 1371 (2013).

[3] A. Ohtomo and H. Y. Hwang. Nature **427**, 423426 (2004).

[4] V. F. Gantmakher. Progr. Low Temp. Phys. **5**, 181 (1967).

[5] V. F. Gantmakher and E. A. Kaner. Soviet Physics JETP **21**, 1053 (1965).

Pulsed EPR study of photoinduced paramagnetic centres in meteoritic nanodiamonds

K.M. Yunusova, G.V. Mamin, S.B. Orlinskii, B.V. Yavkin

Institute of Physics, Kazan Federal University, 420008, Kremlevskaya Street 18, Kazan,
Russian Federation

e-mail: kam.chaos@gmail.com

Nanodiamonds are intensely studied due a currently considered possibility of their use in medicine [1] and in development of quantum computers [2]. Meteoritic “presolar” nanodiamonds are of particular interest: presence in them of anomalous isotope composition [3] suggests that these crystals have a greater age than the Solar System and, therefore, were created in specific growth conditions, details of which can be obtained through the study of lattice defects in these nanoparticles. So far photoinduced paramagnetic centres in meteoritic nanodiamonds were not studied, and their structure has not been established.

The measurements were performed with Bruker Elexsys 680 spectrometer operating in the W-microwave band (94 GHz). EPR spectra were measured as an intensity of two-pulse Hann echo sequence $\pi/2 - \tau - \pi - \tau - echo$. The durations of the first $\pi/2$ and the second π pulses were 32 and 64 ns, respectively. Experiments were performed at two τ time intervals between pulses: 200 and 1000 ns. The sample temperature was controlled using continuous gas flow system and varied over a wide range (10 – 300 K). The optical illumination was implemented using a set of solid state lasers (the wavelength and power magnitudes are given in table 1).

Table 1. – Solid state lasers’ wavelength and power magnitudes

Wavelenght, nm	226	355	405	532	640
Power, mW	20	10	100	200	100

Currently, the most common and studied defects in nanodiamonds are nitrogen-containing ones. For centre EPR spectra of the NV (nitrogen-vacancy) centres in the presence and absence of illumination have been measured previously: the intensity and shape of some peaks changed significantly [4]. In this paper the results of the search for photoinduced paramagnetic centers in meteoritic nanodiamonds under laser irradiation with wavelengths shown in Table 1 are reported. Observed EPR spectra are shown in fig.1. No NV-defects’ signals were detected. Spectrum 1 was obtained at τ = 200 ns under the 266 nm illumination, spectrum 2 — without illumination. With τ increased to 1000 ns under the same illumination a particular spectroscopic features appeared (Spectrum 3 in fig.1).

In order to understand the nature of the observed paramagnetic centers the simulation of the EPR spectrum was carried out using the EasySpin software module [5]. The model employed considered two centres — the inner one, associated with hydrogen, and the exciton. The EPR spectrum parameters obtained from the simulation allow to assign the observed spectra to Wannier-Mott exciton [6].

Irradiation of the sample during the experiment affects the intensity and the shape of the spectrum. The greatest modifications were observed in the case of large time interval between the pulses (τ = 1000 ns) and short-wavelength illumination (266 nm correspond to 4.7 eV), as shown in fig.2.

Diamonds as semiconductors have a bandgap of 5.4 eV [7]. Reducing the crystal size from macroscopic to nanoscale causes an increase of the gap due to the fact that the number of atoms becomes less and the overlap of energy levels weakens. Levels are not so dense anymore; only higher energy levels degenerate into the conduction band and only lower energy levels – into the valence band. Bands' borders are not blurred, and then separate levels appear.

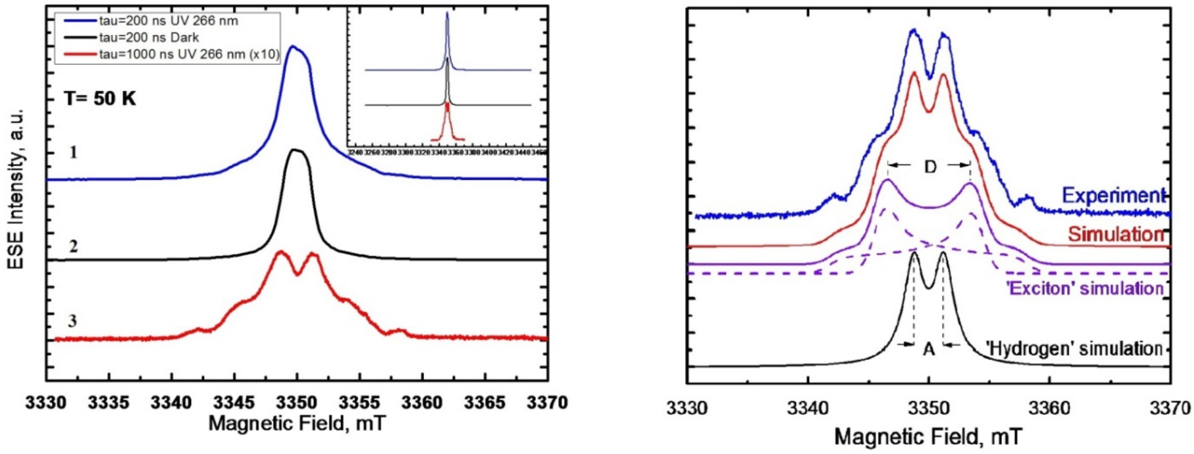

Fig.1. (Left) The EPR spectra of meteoritic nanodiamonds recorded with $\tau = 200$ ns under illumination with $\lambda = 266$ nm (1), without illumination (2), with $\tau = 1000$ ns illuminated with $\lambda = 266$ nm (3). (Right) the simulation of the spectrum 3 in the left panel by the superposition of the exciton and the hydrogen centres' signals.

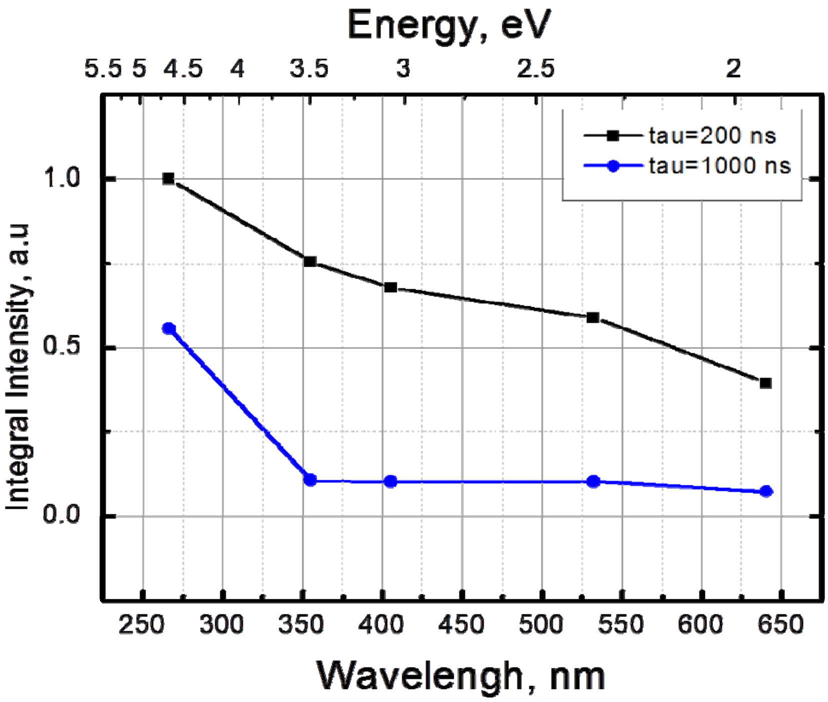

Fig.2. Dependence of the integral intensity of the EPR spectra on the laser wavelength for the two durations of the interval between the microwave pulses.

Therefore, we claim that even a photon with the energy of 4.7 eV in no case can create paramagnetic centres by measures the interband transitions. Consequently, observed EPR spectra belong to the defects whose energy levels are localized in the bandgap.

Thus, it was found that in meteoritic nanodiamonds there is the effect of photogeneration of paramagnetic centres on separate levels in the band gap; apparently, photogeneration occurs by the formation of Wannier-Mott exciton.

References

[1] Baughman R.H., Zakhidov A.A., Heer W.A. Carbon Nanotubes-the Route Toward Applications // Science. - 2002. - V. 297. - P. 787–792.

[2] Geiselmann M., Juan M. L., Regner J., Say J.M. et al. Three-dimensional optical manipulation of a single electron spin // Nature Nanotechnology. – 2013. – I. 3. – V. 8. – P. 175-179.

[3] Lewis R.S., Srinivasan B., Anders E. Host phase of a strange xenon component in Allende // Science, - 1975. – V.190. – P. 1251-1262.

[4] Yavkin B. V., Mamin G.V., Orlinskii S.B., Kidalov S.V. et al. Room-temperature high-field spin dynamics of NV defects in sintered diamond // Applied magnetic resonance. - 2013. –V.44. –P.1235-1244.

[5] Stoll S., Schweiger A. EasySpin, a comprehensive software package for spectral simulation and analysis in EPR // Journal of Magnetic Resonance, - 2006. – V. 178(1). – P. 42-55.

[6] Wannier G.H. The Structure of Electronic Excitation Levels in Insulating Crystals // Physical Review, - 1937. – V.52 – I. 3 – P.191-197.

[7] Clark C. D., Dean P. J., Harris P. V. Intrinsic Edge Absorption in Diamond / Proceeding of the Royal Society A, - 1964. – V. 277 – No. 1370. – P. 312-329.

Local magnetization above T_c in the $La_{2-x}Sr_xCuO_4$ single crystals studied by EPR

V.O. Sakhin[1], Yu.I. Talanov[2], G.B. Teitel'baum[2]

[1]Institute of Physics, Kazan (Volga region) Federal University, 420015, Kremlevskaya, 18,
Kazan, Russia.

[2]Zavoisky Physical-Technical Institute, Russian Academy of Sciences, 420029, Sibirsky tract,
10/7, Kazan, Russia.

e-mail: urfinjus67@gmail.com

$La_{2-x}Sr_xCuO_4$ (LSCO) is a cuprate high-temperature superconductor. The recent studies [1,2,3] have shown that magnetic state of superconductors of this class can exhibit some superconducting features above critical temperature T_c. These features may manifest themselves through the magnetic field inhomogeneities inside a sample and over its surface. We use the electron paramagnetic resonance (EPR) measurements as effective method to detect those weak inhomogeneities.

The samples we studied were single crystals of $La_{2-x}Sr_xCuO_4$ with different strontium doping concentrations. The crystal with the Sr concentration of $x = 0.16$ is optimally doped and undergoes a superconducting transition at 39 K. T_c of the underdoped crystal ($x = 0.077$) is 18 K, and the third sample has Sr concentration near to "1/8 anomaly" doping level ($x = 0.116$, $T_c = 27$ K).

To obtain the information about distribution of magnetic field on the sample surface the EPR method of the surface paramagnetic probe was used. This so-called "EPR-decoration method" was proposed in the work [4] for the study of the magnetic field distribution in the Abrikosov vortex lattice. In present study a thin layer of 2,2-diphenyl-1-picrylhydrazyl (DPPH) was used as a probe. To obtain the spatial characteristics of the magnetic field inhomogeneities near the sample surface we investigated the EPR spectrum variation with the probe-sample distance through the placement of the paraffin buffer layer between the paramagnetic probe and the sample surface.

The temperature dependences of EPR signal parameters were obtained. According to the behavior of EPR signal shift, we assumed that there are two contributions to the shift: paramagnetic and diamagnetic ones. The relation between these contributions determines total shift. The distance dependence of the shift indicates that parts of the sample, that exhibit paramagnetic behavior, and parts, that exhibit diamagnetic behavior, have different size. The scale of these areas at temperature range close to the superconducting transition was estimated. For paramagnetic areas it is 50 μm, for diamagnetic ones it equals 200 nm. It is probable that the electron phase separation results in the formation of stripes which are pinned on the LSCO structural domains.

This work has been supported by the Russian Foundation for Basic Research (RFFI) under Grant no. 13-02-97036.

References

[1] Lee P.A., Nagaosa N., Wen X.-G. *Reviews of modern physics* **78**, 17 (2006)

[2] Gomes K.K., Pasupathy A.N., Pushp A, Ono S., Ando Y., Yazdani A. *Nature B* **47**, 569 (2007)

[3] Wang Y, Li L., Ong B. *Physical Review B* **73**, 024510 (2006).

[4] Rakvin B., Pozek M., Dulcic A. *Solid State Commun* **72**, 199 (1989)

Magnetic hyperfine interactions on ^{51}V nucleus in pyrochlore $Lu_2V_2O_7$

P.A. Agzamova[1,2], V.P. Petrov[2], V.A. Chernyshev[2], A.E. Nikiforov[2]

[1]Institute of metal physics UB RAS, S. Kovalevskaya str., Yekaterinburg, Russia
[2]Ural federal university named after B.N. Yeltsin, Mira av., Yekaterinburg, Russia

email: polly@imp.uran.ru

The vanadium pyrochlores $R_2V_2O_7$ (R = rare earth or Y) being the geometrically frustrated magnetic systems are attractive for both theoretical and experimental investigations due intriguing electronic and magnetic properties. Among these systems $Lu_2V_2O_7$ is most simple object for studying since Lu^{3+} ion is nonmagnetic at R-site and its electronic and magnetic properties formed by the sublattice of V^{3+} magnetic ions. In addition, $Lu_2V_2O_7$ is ferromagnet with $T_C = 70$ K and at the same time Mott insulator contrary to the common belief that ferromagnetism leads usually to metallic conductivity [1]. Many investigators suppose that the orbital moment of 3*d* ions (V^{4+}) affects on such magnetic properties of vanadium pyrochlores as magnetic susceptibility, the Curie temperature etc. The orbital ordering pattern of $R_2V_2O_7$ pyrochlores was determined by the neutron diffraction measurements [2], which showed that each orbital extended along the four local <111> directions towards the center-of-mass of the elementary V_4-thetrahedron. On the other hand, recently the presence of the orbital fluctuations and the orbital liquid state in the Mott insulators became the subject under hot discussions. There are many experimental techniques for orbital physics investigations. Among them the NMR technique has an advantage in observing each orbital state directly with a quantitative evaluation of 3*d* quadrupole moment which is the order parameter for the orbital degree of freedom. Thereby, the NMR method can give additional information about the presence or absence of orbital fluctuations in 3*d*-ions sublattice. In paper [3] ^{51}V NMR measurements in $Lu_2V_2O_7$ have been performed to investigate the orbital ordering of this compound. With rotation of $Lu_2V_2O_7$ single crystal in an external magnetic field, NMR spectra showed a characteristic angle dependence, which reproduced V 3*d* orbital states and clearly identified the orbital ordering of $Lu_2V_2O_7$.

In this work we try to explain theoretically the available experimental NMR data in $Lu_2V_2O_7$ pyrochlore. We have proposed the theoretical model of magnetic hyperfine interactions formation on $3d^1$-ion (V^{4+}) nuclei in vanadium pyrochlores. Our model includes the isotropic (Fermi-contact) and anisotropic (electron-dipole-nuclear-dipole) hyperfine interaction, where the last of them contains 3*d* quadrupole moment of V, for quantitative explaining of the orbital ordering pattern in these compounds. Moreover, we have performed the ab initio calculations of NMR spectra parameters in the molecular orbital method approximation in CRYSTAL09 package [4], dedicated to the periodical system, by the unrestricted Hartree-Fock method with using of all-electron basis sets to evaluate the isotropic and anisotropic magnetic hyperfine interactions parameters on ^{51}V nuclei. Our results are in a good agreement with the experimental data [3] for $Lu_2V_2O_7$.

Support by RFBR (# 14-02-00260) is acknowledged.

References

[1] J.S. Gardner, M.J.P. Gingras, J.E. Greedan, *Rev. Mod. Phys.*, **82** (2010) 53.

[2] H. Ichikawa, L. Kano, M. Saitoh et al, *JPSJ*, **74** (2005) 1020.

[3] T. Kiyama, T. Shiraoka, M. Itoh et al, *Phys. Rev. B*, **73** (2006) 184422.

[4] R. Dovesi, V.R. Saunders, C. Roetti et al, *CRYSTAL09 User's Manual* (2009).

Optical and physical properties of fluorite crystala CaF_2: Ce^{3+}, Yb^{3+}, Lu^{3+}

N.F. Rakhimov, A. Nizamutdinov, V.V. Semashko, M.A. Marisov, S.A.Shnaidman

Kazan Federal University, 420008, Kremljovskaja str., 18, Kazan, Russian Federation
e-mail: niyaz_06@mail.ru

Introduction

Fluorite crystals CaF_2:Ce^{3+} have promising optical properties for generating tunable laser oscillation in the UV spectral range, but exhibit poor photochemical stability [1, 2].

The aim of this study is to investigate the influence of Yb^{3+} and Lu^{3+} activator ions on optical characteristics and photo dynamical processes in crystals of CaF_2:Ce^{3+}. Spectral characteristics of a series samples of fluorites, activated by Ce^{3+}, Yb^{3+} and Lu^{3+}, were investigated including absorption spectra of color centers, induced by radiation resonant to transitions of ions Ce^{3+}.

Physical premises to control the optical properties

Impurity centers of Ce^{3+} ions in CaF_2 were first investigated by Feofilov, in the series of alkaline earth fluorides with a fluorite structure MeF_2 (Me = Ca, Sr, Ba), which form a homologous series [3-6]. In these crystals the formation of several types of impurity centers is observed with different mechanisms of compensation of the excess positive charge and, therefore, with different local symmetries of the crystal field.

In CaF_2: Ce^{3+} crystals pumped by radiation resonant to 4f-5d transitions of Ce^{3+} ions formation of different types of color centers absorbing at the wavelengths of luminescence of Ce^{3+} ions was observed (Figure 1a). The origin of the emergence of dynamical processes is the appearance of free charge carriers in the conduction band and valence band of the crystal released by the two-step photoionization of the impurity center. After thermalization these free charge carriers can be captured by a variety of traps, such as uncompensated charges in the crystal lattice, lattice defects, or recombine at the impurity centers (fig.1b).

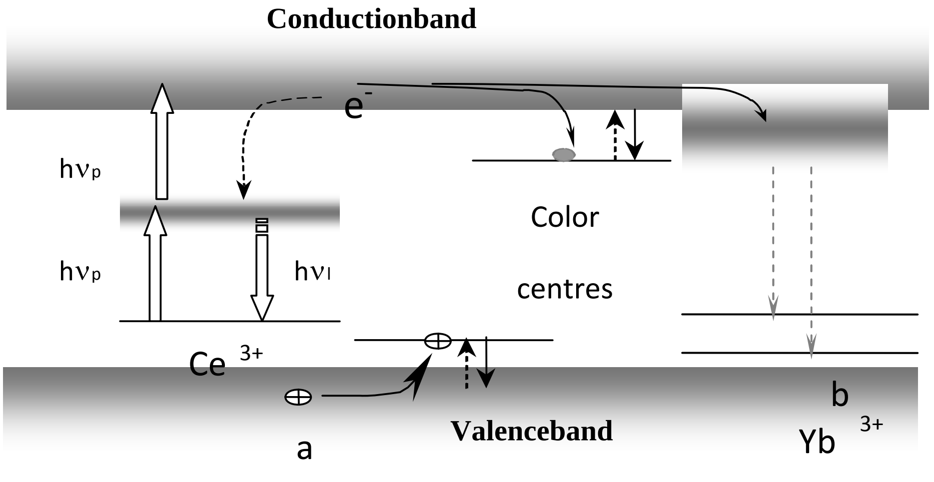

Fig.1. a) the model of solarization of the active medium, activated by Ce^{3+} ions, under UV radiation, and b) accelerating the recombination of free charge carriers through the states of the ion-activator

The objects of study of the presented work are fluoride crystals with the fluorite structure, namely CaF_2: Ce^{3+} (Ce ~ 1%), CaF_2: Ce^{3+} + Yb^{3+} (Ce ~ 0.5%, Yb ~ 1%), CaF_2 (80%) + LuF_3 (20%): Ce^{3+} + Yb^{3+} (Ce ~ 0.5%, Yb ~ 1%), CaF_2 (95%) + LuF_3 (5%): Ce^{3+} + Yb^{3+} (Ce ~ 0.5%,Yb ~ 1%)

Results. The absorption and luminescence

Fig.2a shows the absorption spectra and luminescence of CaF_2: Ce^{3+} crystal. Visible characteristic two-humped spectrum of luminescence of Ce^{3+}, due to the transitions from the excited 5d state to $^2F_{7/2}$ and $^2F_{5/2}$states of 4f configuration.

In the case of the sample activated by Yb^{3+} (fig.2b) there is an absorption band in the region of 360 nm which is characteristic for Yb^{2+} [6]. Such an impurity center may have formed as a result of dynamic processes, namely the capture of electron from the conduction band by Yb^{3+} ion [1, 2]. It is connected with the fact that the crystal was irradiated before the absorption spectra were recorded.

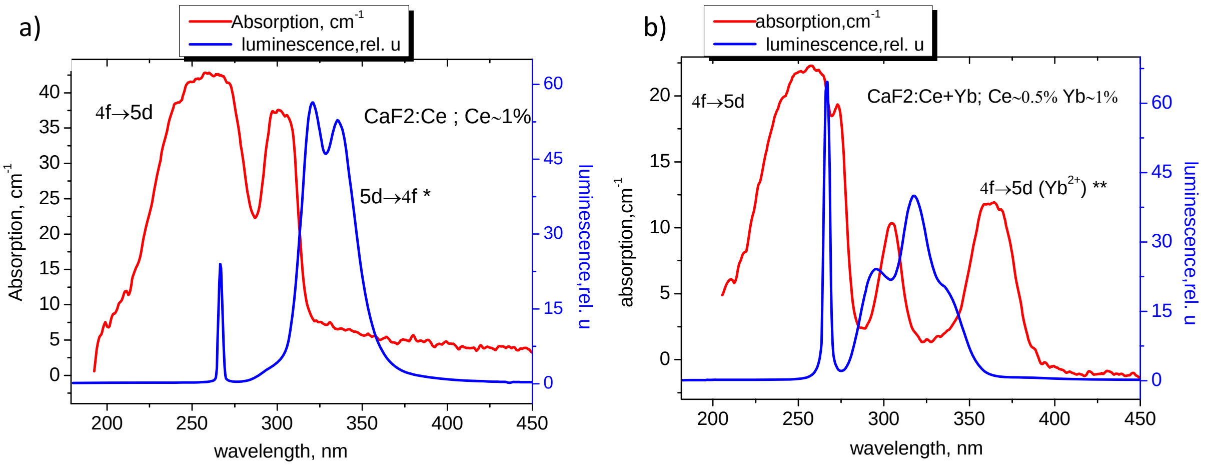

Fig.2. The absorption and luminescence of CaF_2: Ce^{3+} (a) and CaF_2: Ce^{3+} (b), SCe (0.5 at.%), Yb (1 at.%).

Fig.3 shows the absorption and luminescence spectra of crystals, which are doped by Lu^{3+} in addition to Ce^{3+} and Yb^{3+}. The absorption spectra are not qualitatively different from

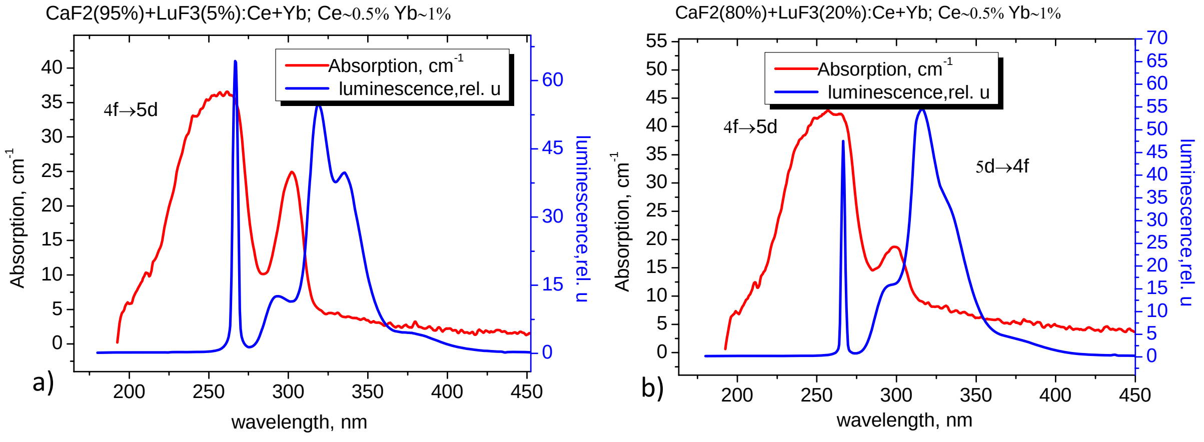

Fig.3. The absorption spectra and luminescence crystal CaF_2: Ce^{3+} (0,5 atm.%), Yb^{3+} (1 atm.%), Lu^{3+} (5 at.%) (a) And CaF_2: Ce^{3+} (0,5 atm.%), Yb^{3+} (1 atm.%), Lu^{3+} (20 at.%) (b)

ones observed for previous samples. Luminescence spectrum reveals not only bands of Ce^{3+} center of tetragonal symmetry but also the band peaked at 380 nm, which can be attributed to the transition of Ce^{3+} impurity center with non-local charge compensation (according to the published data).

Conclusion

We have investigated the effect of doping by Yb^{3+} and Lu^{3+} on the optical characteristics and photo dynamical processes in CaF^2: Ce^{3+} crystals.

As a result of doping by Lu^{3+} ions of CaF_2: Ce^{3+} + Yb^{3+} crystal luminescence spectrum of Ce^{3+} ions reveals new band peakedat 380 nm, which may be interpreted as a transition within Ce^{3+} impurity center with non-local charge compensation.

In this work we have studied mechanisms for controlling the optical characteristics of fluorite crystals activated by rare-earth ions by shifting the balance of dynamical processes. Effective recombination channels providedbyYb^{3+} ions suppress the formation of color centers, but there is an absorption band of Yb^{2+}, which degrades the optical properties of the crystal as the active medium. Additional doping byLu^{3+} ions can suppress the formation of Yb^{2+}.

References

[1] G.J. Pogatshnik, D.S. Hamilton, Phys. Rev. B. 1987. V. 36. № 16. P. 8251–8257.

[2] R.Yu. Abdulsabirov, S.L. Korableva, A.S. Nizamutdinov, M.A. Marisov, A.K. Naumov, V.V. Semashko, Proc. SPIE, 6054, (2006) 172.

[3] I.V. Stepanov, P.P. Feofilov. Dok. AN SSSR. – 1956. – T. 108. – № 4. – S. 615–618.

[4] Feofilov P.P. Linejchataja ljuminescencija aktivirovannyh kristallov (redkozemel'nye iony v monokristallah MeF2)

[5] I.V. Stepanov, P.P. Feofilov, Dok. AN SSSR. – 1956. – T. 108. – № 4. – S. 615–618.

[6] A.A. Kapljanskij, P.P. Feofilov, Opt.i spek. – 1962. – T.13. – S. 235–241.

Study of laser characteristics of active medium $LiLu_{0.7}Y_{0.3}F_4:Ce^{3+}$ in ultra-short pulse mode

I.I. Farukhshin, A.S. Nizamutdinov, V.V. Semashko, S.L. Korableva

Kazan (Volga region) Federal University, 420008, Kremlevskaya str., Kazan, Russia.

e-mail: burusha16@gmail.com

Introduction.

Today new technologies express demandon lasersoscillating in ultraviolet (UV)spectral range and having short pulse duration [1]. Main methods of obtaining UV laser radiation are nonlinear and parametric conversion of non UV laser radiation. This method can be technically difficult and it takes a lot of space. But on the other hand we can obtain UV lasing by use offluoride crystals doped by ions Ce^{3+}as active media [2,3]. Fluoride crystals doped by ions Ce^{3+} allow us to obtain short pulses with duration from several to tens of nanoseconds. To obtain shorter pulses we should use Q-switching or mode-locking.

There are photodynamic processes in active medium of UV band, the result of which arecolor centers.Color centers absorb energy of laser radiation and determine losses in active medium. Previously, it was observed that level of losses of color centers depends on various factors (some of them are external additional irradiation and temperature) and doesn't remain constant during experiment [4]. Using of these processes for mode-locking seems to be perspective.

The aim of this work was obtaining laser pulses with ultra-short duration of UV spectral range and studyof laser characteristicsof active medium $LiLu_{0.7}Y_{0.3}F_4:Ce^{3+}$ in ultra-short pulse mode.

Experimental methods.

The sample used in our measurements was crystal of $LiLu_{0.7}Y_{0.3}F_4$containing 1 at. % of Ce^{3+} ions. This sample was grown by Stella L. Korableva in Kazan (Volga region) Federal University.

The experimental setup of the $LiLu_{0.7}Y_{0.3}F_4:Ce^{3+}$ laser is shown in fig.1.

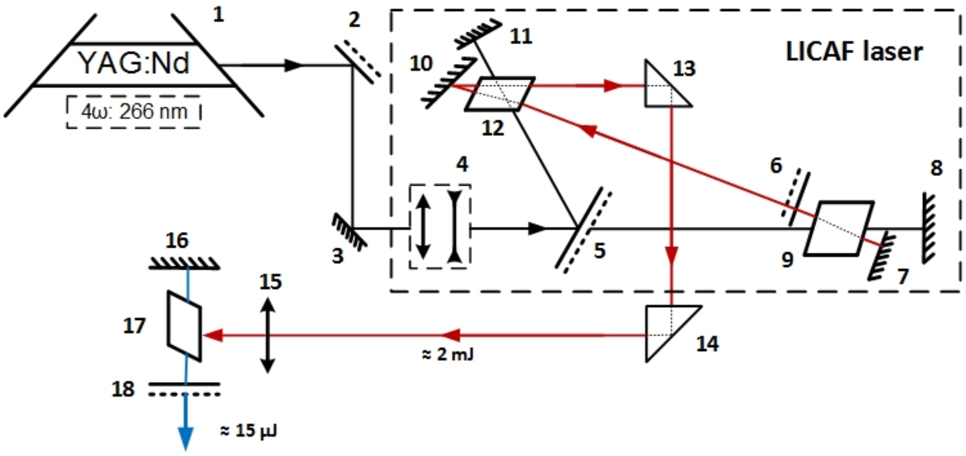

Fig.1. Experimental setup of the LLYF laser. Consist of: 1 — laser YAG:Nd; 2 — spectrum splitter; 3, 7, 8, 10, 11, 16 — reflector R = 99,9%; 4 — telescope; 5 — reflector R = 30%; 6, 18 — reflector R = 65%; 9, 12 — crystal LICAF; 13, 14 — rectangular prisms; 15 — converging lens; 17 — crystal LLYF.

Discussion.

In this study laser oscillationwas obtainedin pulse mode at the wavelength λ = 311 nm and with pulse duration t = (400 ± 10) ps. Laser radiation of pumping was pulsed with pulse duration t = (6,375 ± 0,025) ns.

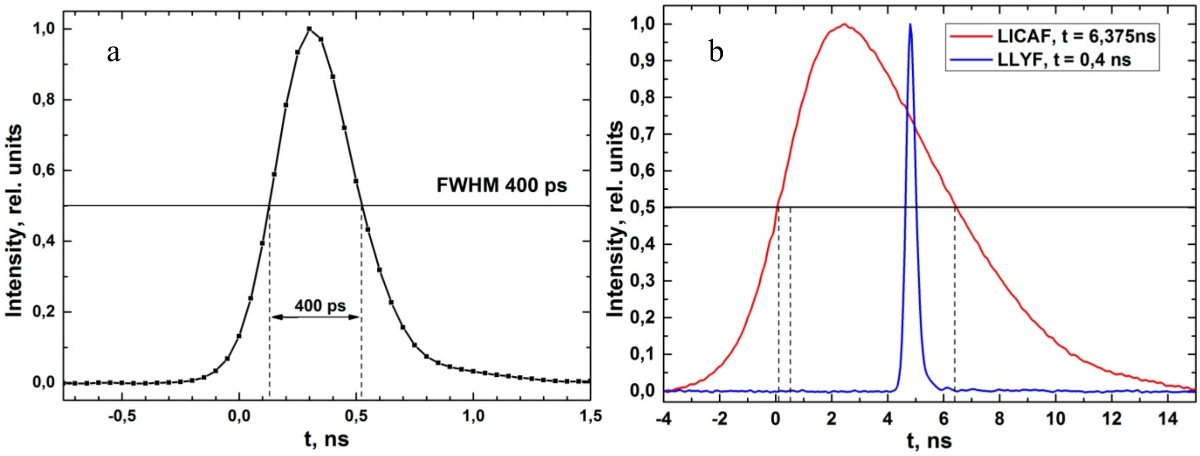

Fig.2.Temporal distribution of laser pulses obtained fromCe:LLYF (a) and Ce:LICAF (b).

The photon lifetime in the resonator is $\tau_c = 281$ ps. Pulse duration of Ce:LLYF laser radiation is greater than the photon lifetime in the resonator, so it means that we have multimode nature of the laser radiation. However, we see single pulse, which tells about possible Q-switching.

Results of research dependence of the laser radiationenergy on pump radiation energy for different reflection coefficients of output mirrors showed that reflection coefficientincrease leads to reduction of hysteresis loop square, which proportional to the number of color centers. This color centers were observed in the active medium Ce:LLYF.

Studies of the intracavity losses get us some methods of Q-switching control. Increased pumping energy and pulse frequency lead to increased losses in the resonator.

Conclusion

Laser oscillationwas obtained in active medium Ce:$LiLu_{0.7}Y_{0.3}F_4$in a pulse mode at the wavelength λ = 311 nm and with pulse duration t = (400 ± 10) ps. Pumping pulse was at wavelength λ = 289 nm with pulse duration t = (6,375 ± 0,025) ns. Shortening the pulse duration achieved by passive Q-switch, which is caused by bleaching of color centers in the volume of the active medium absorbing the laser generation. Controls methods of Q-switching change are pumping energy or pulse frequency changing.

References.

[1] B. Wellmann, D. J. Spence and D.W. Coults, Opt. Lett, Vol. 39, No. 5 (2014).

[2] M.A. Dubinskii, V.V. Semashko, A.K. Naumov, R.Yu. Abdulsabirov,S.L. Korableva, Jr. of Modern Optics, Vol. 40, No. 1. (1993).

[3] S. Nobuhiko, L. Zhenlin, S. Yusaburo, V.V. Semashko, A.K. Naumov, S.L. Korableva, R.Yu. Abdulsabirov, M.A. Dubinskii, Opt. Lett. Vol. 20, No. 6 (1995).

[4] Ki-Soo Lim and D.S. Hamilton, J. Opt. Soc. Am., Vol. 6, No. 7 (1989)

Grows of solid solutions with colquiriite structure $LiCa_{1-X}Sr_XAlF_6$:Ce^{3+}

A.A. Shavelev, A.S. Nizamutdinov

Institute of Physics, Kazan Federal University, 420008, Kremlevskaya 18, Kazan, Russia
e-mail: alexey.shavelev@gmail.com

Fluoride crystals with the colquiriite structure, activated by rare earth ions are effective active media of solid-state lasers [1]. The advantages of these compounds over oxide crystals — the melting point is significantly lower and the band gap is much wider. Significant inhomogeneous broadening of the vibrational laser transitions of these ions causes a broad amplification band which gives ability to wavelength tuning and ultrashort pulses generation [2].

The main disadvantage of these compounds is the low isomorphous capacity of crystal lattice with respect to the rare earth ions, which leads to a low concentration of impurities or high quantity of defects if we want to obtain highly concentrated samples. It is known, that varying the chemical structure of the compound, namely a set of crystal lattice cations, one can improve the optical quality by increasing the isomorphous capacity of solid solution [3].

The aim of this work are experiments on growing new materials based on fluoride crystals with the colquiriite structure, as well as the study of their phase composition.

Conditions, characteristics and growing complexity of the materials

Since the composition is multicomponent:

1) It is necessary to perform a thorough mixing of the powder before placing it into a crucible.
2) At the growth process the crystal should grow on seeding crystal and the temperature gradient can be considered 50^0C on 1 cm.

Complexity of growing is in the fact that aluminum is volatile, therefore: it is not allowed to overheat the melt, since the components include the aluminum fluoride, which is a compound with a high saturated wapor pressure and does not exist in a liquid state, so overheating of the melt will lead to depletion of this component. Also when the temperature is set, taking the value with an excess (about 20^0C) to ensure melting of the substance.

Given all the above, crystal growth method was chosen for the Bridgman -Stockbarger, which allows to perform the growth in the closed crucible. This method consists in pulling crucible with overheated melt through the chamber. Mode has been realized by means of the vertical movement of the crucible with the melt from the high to the low temperature region. As a result, crystallization starts at the bottom of the crucible and after grows a boule of single crystal.

Crucible also participates in the formation of a temperature gradient. The wall thickness of the crucible should be minimal to distort the temperature field as little as possible. Meanwhile, wall must have enough thickness to hold strength of the structure of the crucible. As practice shows, thickness of the walls of the crucible should be in the order of 2 – 3 mm.

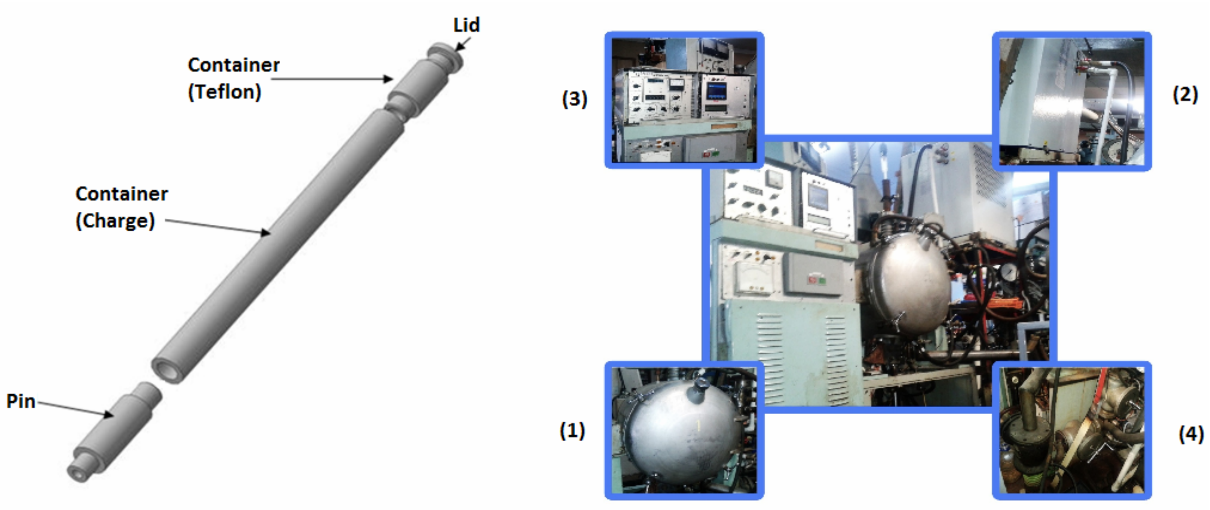

Fig.1. Crucible and the crystal growth equipment, which consists: (1) The growth chamber; (2) The water cooling system; (3) Automated system for process control in the chamber; (4) Pumping system, which consisted of a backing and a diffusion pump.

Diffractometry results

Due to the low isomorphic capacity of crystals with respect to rare-earth ions Ce^{3+} when grown by the Bridgman - Stockbarger there is a gradient of concentration of impurities. As this may affect the phase composition of the material crystallization, the samples were tested in several areas (fig.2).

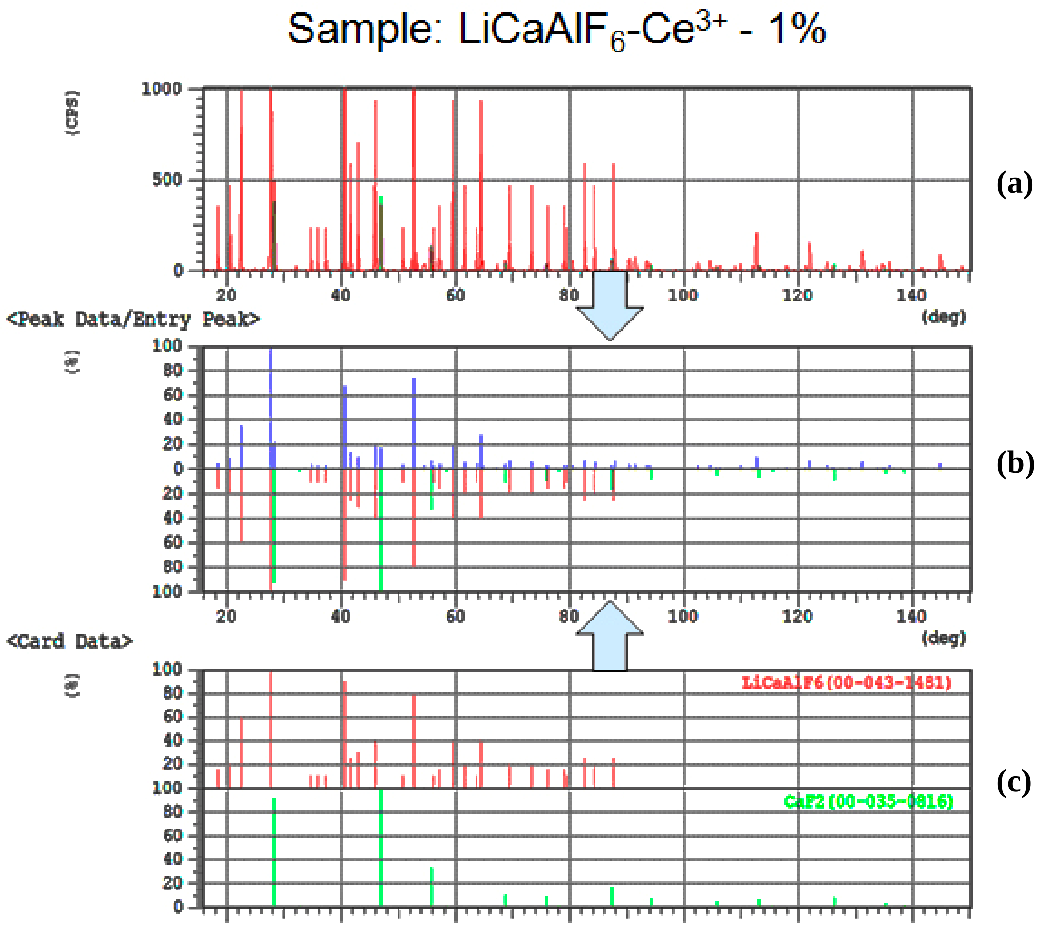
Sample: $LiCaAlF_6$-Ce^{3+} - 1%

Fig.2. Experimental (a), table (c) and comparison (b) data.

As a result, all samples showed a diffraction pattern corresponding to colquiriite structure, but yet in a sample taken from the hat, the presence of CaF_2 is notable.

We have also obtained the diffraction lattice constant dependence on the concentration ratio of mixed and unmixed samples (fig.3).

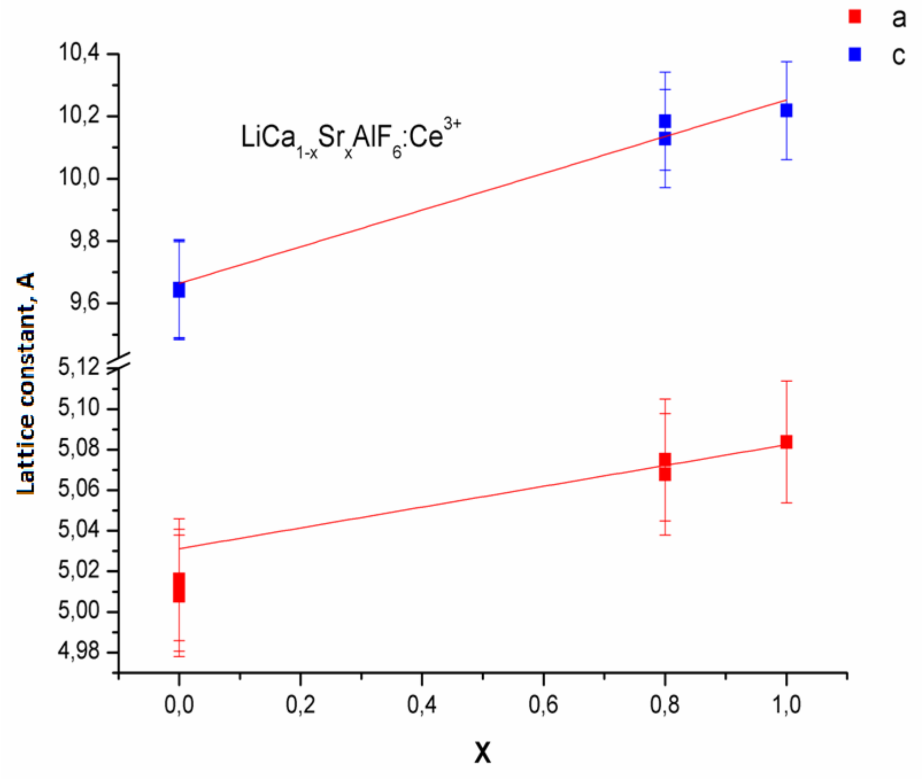

Fig.3. Dependence of the lattice constant of the content of SrF_2.

Dependence of the lattice constant of the content of SrF_2 in the transition from $LiCaAlF_6$ crystal to $LiSrAlF_6$ crystal is linear.

Conclusion

Crystals of $LiCa_{1-X}Sr_XF_6$ doped with Ce^{3+} ions were grown. It is shown that for a series of crystals $LiCa_{1-X}Sr_XF_6$ distribution of reflections observed corresponds to the colquiriite structure, and the dependence of the lattice constant in the transition from $LiCaAlF_6$ crystal to $LiSrAlF_6$ crystal is linear. These facts indicate that the synthesized crystals are single-phase crystals.

References

[1] M. A. Dubinskii, V. V. Semashko, A. K. Naumov, R. Y. Abdulsabirov, S. L. Korableva Ce^{3+}-doped colquiriite a new concept of all solid-state tunable ultraviolet laser // J. Modern Opt. 1993. V. 40. P.1-5.

[2] N.Sarukura, Z.Liu, H.Ohtake, Y.Segawa, M.A.Dubinskii, V.V.Semashko, A.K.Naumov, S.L.Korableva, R.Yu.Abdulsabirov Ultraviolet short pulses from an all-solid-state Ce:LiCaF master-oscillator-power amplifier system // Opt.Lett. 1997. V.22. N.13. P.994-996.

[3] Nizamutdinov A.S., Semashko V.V., Naumov, A.K., Efimov V.N., Korableva S.L., Marisov M.A. On the distribution coefficient of Ce^{3+} ions in $LiF-LuF_3-YF_3$ solid-solution crystals // JETP LETTERS. 2010. V. 91. P.23-25.

Dynamical processes investigation in CaF_2:Ce^{3+}+Yb^{3+} and mixed CaF_2 – LuF_3:Ce^{3+} + Yb^{3+} crystals

S.A. Shnaidman, A.S. Nizamutdinov, V.V. Semashko, S.L. Korableva, M.A. Marisov

Kazan Federal University, 420008, Kremlevskaja 18, Kazan, Russia

e-mail: sofia.shnaidman@gmail.com

Here we report on pump-probe studies of CaF_2 doped with Ce^{3+} and Yb^{3+} ions. The crystals CaF_2:Ce^{3+} show advantageous spectral characteristics for tunable UV lasers application but have poor photochemical stability [1,2]. Their properties under intense UV pumping are affected by excited state absorption and color centers formation.

This work was aimed at dynamic processes investigation induced by laser radiation of UV spectral range in CaF_2 doped with Ce^{3+} and Yb^{3+} ions.

The project has carried out comprehensive research into new materials for quantum electronics – fluoride crystals with fluorite-type crystal structure MeF_2, MeY_3F_{10} and their solid solutions doped with Ce^{3+} and Yb^{3+} ions. Series of crystals with varied content of solid solution component LuF3, activator ion Yb^{3+}, were grown by Bridgman-Stockbarger technique. Results of X-ray diffraction investigations have shown that synthesized crystals are single-phase monocrystals.

Experiments on optical spectroscopy reveal the formation of new types of impurity centers in CaF_2:Ce^{3+}+Lu^{3+} and CaF_2:Ce^{3+}+Yb^{3+}+Lu^{3+} with high concentration of dopants (0,2-2 at. %). Luminescence spectra under 266 nm pump contains 285 nm line with 20 ns lifetime unlike the observed 40 ns for tetragonal centers of Ce^{3+} in CaF_2.

Excitation trapping was observed for interconfigurational Ce^{3+} transitions as result of luminescence investigation. Luminescence decay times of powdered samples are about two times less than for the crystal ones.

5d-4f luminescence of dominating Ce^{3+} centers in fluorite crystals was clarified what is important for evaluation of photo-dynamic processes parameters and optical gain characteristics.

Mechanism for crystal chemical managing of optical properties has been justified for crystals with fluorite-type crystal structure MeF_2, MeY_3F_{10} and their solid solutions doped with rare-earth ions, under conditions of UV irradiation at 4f-5d bands of Ce^{3+} ions. The idea for this mechanism is activation with appropriate ions capable for efficient recombination of free charges, thus excluding formation of color centers and additional losses in laser oscillation channel.

The pump-probe technique allowed us to observe nonlinear dynamic in absorption coefficient vs pumping radiation intensity in CaF_2:Ce^{3+}+Yb^{3+} and spectral dependence of small signal gain coefficient in CaF_2:Ce^{3+}+Yb^{3+}. Optical gain was observed on CaF_2:Ce^{3+}+Yb^{3+} in the range 325-335 nm for the first time which justifies the proposed . Nonlinear dynamic was observed in gain coefficient vs probe intensity showing ability to control gain coefficient. Thus the mechanism for optical properties dynamic managing was proposed and justified for crystals under intense of UV irradiation at 4f-5d bands of Ce^{3+} ions.

Interpretation of experimental results was based on model of photodynamic processes which included recombination transitions at impurity centers of Ce^{3+} and Yb^{3+} also.

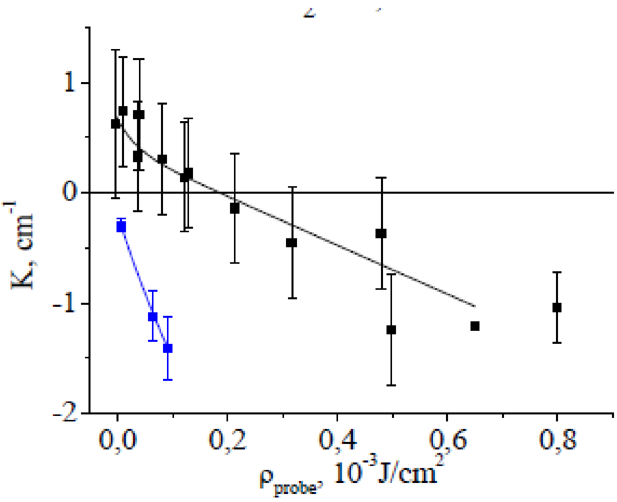

Fig.1. Probe radiation density dependence of gain coefficient for $CaF_2:Ce^{3+}$ (0,5 at.%) + Yb^{3+} (2 at.%)

References

[1] D.J. Pogashnik, D.S. Hamilton, Phys. Rev.B., 36, N16, (1987) 8251.

[2] R.Yu. Abdulsabirov, S.L. Korableva, A.S. Nizamutdinov, M.A. Marisov, A.K. Naumov, V.V. Semashko, Proc. SPIE, 6054, (2006) 172.

[3] V.V. Semashko, B.M. Galyautdinov, M.A. Dubinskii, R.Yu. Abdulsabirov, A.K. Naumov, S.L. Korableva, Proc. Internat. Conf. on LASERS 2000 (Albuquerque, NM, Dec. 4 - 8,2000), STS Press, McLean, VA (2001) 668.

Photoinduced processes in Ce^{3+} doped $SrAlF_5$ crystal

V.V. Pavlov, V.V. Semashko, A.N. Yunusova, M.A. Marisov

Kazan Federal University, 18 Kremlevskaya, 420008 Kazan, Russian Federation
e-mail: Vitaly.V.Pavlov@gmail.com

Introduction

Until recently Ce-doped $SrAlF_5$ crystal was considered as a promising active medium for UV lasers [1]. However stable laser action in this crystal has not been obtained till now. This is due to the fact that high energy UV radiation initiates the nonlinear photodynamic processes, which deteriorate optical and laser properties of active media. These nonlinear processes are characteristic feature for the vast majority of UV solid-state active media, but for Ce-doped $SrAlF_5$ crystal these processes almost completely suppress laser action and only single laser pulse around 291 nm is observed at the beginning pumping acts by pulsed 248 nm KrF-laser radiation [2].

The reason of photodynamic processes is one- or multi-photon ionization of activator ions (depending on the impurity ion and crystalline matrix). Impurity photoionization leads to the generation of free charge carriers (electrons and holes) in the appropriate energy bands of the crystal, that could be captured by lattice defects (color center formation). Besides the absorption bands of color centers are localized in UV spectral range (in spectral range of laser action) [3].

One of ways to improve laser efficiency in Ce^{3+} doped fluoride crystals is the co-activation of Yb^{3+} ions. It is known that additional activation by Yb^{3+} ions creates a supplementary recombination channel for free carriers, which successfully competes with the capture of carriers by cerium ions [4]. Therefore the arm of this study is to investigate the influence of Yb^{3+} ions on optical characteristics of Ce^{3+}:$SrAlF_5$ crystal and parameters of photoinduced nonlinear processes. This work presents investigation of two crystals: $SrAlF_5$ crystal doped with Ce^{3+} (0.5 at.%) and $SrAlF_5$ crystal doped with Ce^{3+} (0.5 at.%), Yb^{3+} (0.5 at.%).

Experimental

Two experimental techniques were applied to achieve assigned task. At the beginning we studied nonlinear absorption of UV radiation in the investigated crystals. Studies were carried out using the fifth harmonic of Nd:YAG laser (213 nm) and the third harmonic of tunable Ti: Al_2O_3 laser (240 – 280 nm). Energy of UV radiation was measured by means of pyroelectric detector Ophir.

Second one is a microwave resonant technique. Among all techniques of dielectric spectroscopy a microwave resonant technique, described in [5, 6], is the most informative for studying the characteristics of photoinduced processes in the rare earth doped crystals. This technique permits to study of change of the complex permittivity of the matter undergoing different external influences (optical irradiation in particular). The feature of the microwave resonance technique is the ability to separate the variations of real and imaginary parts of the complex permittivity. The variation of imaginary part of the permittivity is caused by the appearance of free charge carriers generated in the host bands, in other words, by photoconductivity effect. The variation of its real part is associated with localized electrons or holes at impurity ions or traps (color centers), in other words, with photodielectric effect. The variations of these both parts lead to a shift of the resonance frequency and change of the cavity quality (Q) factor measured by the sensitive microwave receiver system.

Operating frequency of the Gunn diode generator was 35.4 GHz and its microwave power was about 70 mW. The unloaded quality factor Q_u of the cavity is about 800. The time constant of the measuring system enabled us to investigate transient responses of the dielectric permittivity of the crystals with about 5 ns time resolution. The samples were excited by radiation of the third harmonic of the tunable Ti:Al_2O_3 laser. The pulse duration and pulse-repetition rate of the exciting radiation were 10 ns and 10 Hz, respectively. All experiments were carried out at room temperature.

Experimental results

Dependences of the absorption coefficient on the energy density of UV excitation radiation for investigated crystals have been obtained. At small energy density of radiation (less 0.2 J/cm^2) the absorption coefficient for all samples linearly increases with increasing energy density. Then the absorption coefficient reaches a plateau and does not depend on energy density of excitation radiation. As an example the absorption coefficient of Ce^{3+}:$SrAlF_5$ crystal at 213 nm as a function of energy density of excitation radiation is shown in fig.1a.

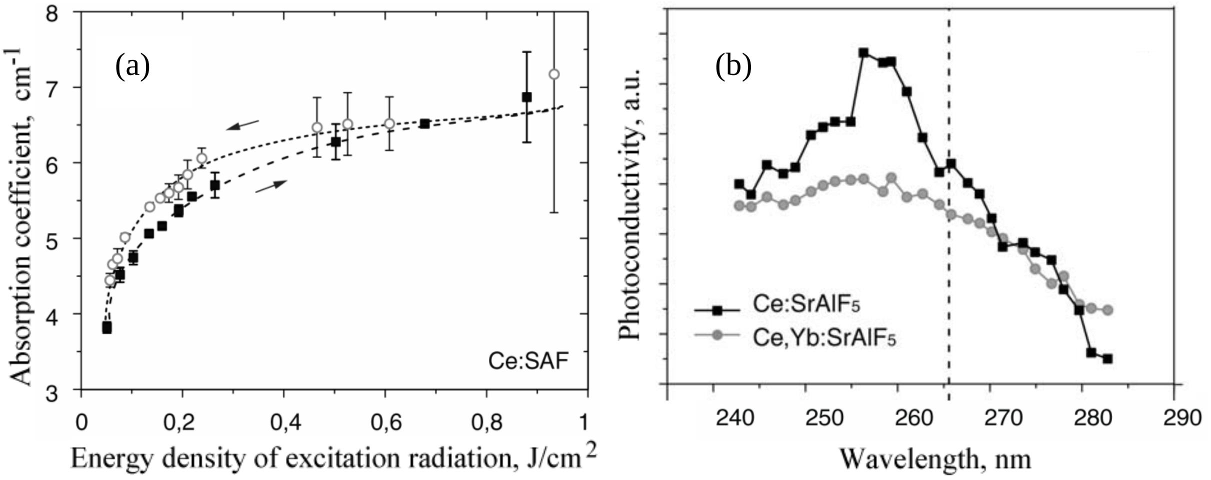

Fig.1. (a) — absorption coefficient of Ce^{3+}:$SrAlF_5$ crystal at 213 nm as a function of energy density of excitation radiation; (b) — photoconductivity spectrum of Ce^{3+}:$SrAlF_5$ and Ce^{3+},Yb^{3+}:$SrAlF_5$ crystals. T = 300 K

It has been found that saturation of the absorption coefficient is caused by excited state absorption from the 5d-states of Ce^{3+} ions. We also observed that the energy dependence of absorption coefficient for Ce^{3+}:$SrAlF_5$ crystal has a hysteresis effect (fig.1a). This effect can be explained by existence of long-lived color centers in Ce^{3+}:$SrAlF_5$ crystal which also absorb pumping radiation. As a result of pulsed laser irradiation (10 Hz) the long-lived color centers stock up in crystal and step-by-step rise the absorption coefficient. Hysteresis effect in the energy dependence of absorption coefficient was not detected for Ce^{3+}, Yb^{3+}: $SrAlF_5$ crystal. This confirms the fact that the additional activation by Yb^{3+} ions engages a supplementary recombination channel for free carries and decreases the long-living color centers content.

Then obtained experimental data have been used to calculate the basic parameters of photodynamic processes. For this purpose we elaborated the model of photodynamic processes, which describes two-step absorption and ionization of an impurity center, formation and destruction of the color centers, capture and recombination of the free charge carriers. Numerical solution of the 6-level system of rate equations allowed us to estimate basic parameters of photodynamic processes: excited state photoionization, color center ionization, free electrons recombination and trapping by lattice defects cross-sections.

We also registered the photoconductivity spectra of investigated crystals by means of the microwave resonant technique. As it can be seen from fig.1b the photoconductivity spectrum of Ce^{3+}:$SrAlF_5$ crystal reveals the band with a maximum at about 260 nm. Linear dependence of the photoconductivity signal on the energy density of excitation radiation at 260 nm suggests that the photoionization spectrum at 260 nm is essentially caused by one-photon ionization process. Since the energy gap of $SrAlF_5$ crystal is close to 10 – 12 eV, one-photon ionization of Ce^{3+} ions is not possible in this case. Therefore we can suggest that 260 nm - band in photoconductivity spectrum of Ce^{3+}:$SrAlF_5$ crystal corresponds to ionization of color center. It is confirmed by absence of 260 nm - band for Ce^{3+},Yb^{3+}:$SrAlF_5$ crystal in which additional activation by Yb^{3+} ions decrease the concentration of photoinduced color centers.

Summary

We investigated nonlinear absorption of UV radiation and photoconductivity spectrum in $SrAlF_5$ crystal doped by Ce^{3+} and Yb^{3+} ions. The basic parameters of photodynamic processes have been estimated.

References

[1] M.A. Dubinskii, K.L. Schepler, V.V. Semashko et al., *J. Mod. Optic.* **45**, 221 (1998).
[2] A.N.Yunusova, V.V. Semashko, G.M. Safiullin, et.al., *J. of Lum.* **145**, 443 (2014).
[3] A.S. Nizamutdinov, Ph.D.Thesis, Kazan State University, 2007.
[4] A.S. Nizamutdinov, V.V. Semashko, A.K. Naumov et al., *J. Lum.* **127**, 71 (2007).
[5] M.-F. Joubert, S.A. Kazanskii, Y. Guyot, et al., *Opt. Mat.* **24**, 137 (2003).
[6] V.V. Pavlov, V.V. Semashko, R.M. Rakhmatullin et al., *JETP Letters* **97**, 1 (2013).

The effect of chromophores concentration on the quadratic nonlinear optical activity of methacrylic compymers with azochromophores in the side chain

M.A. Smirnov[1], A.S. Mukhtarov[1], N.V. Ivanova[1], T.A. Vakhonina[1], V.V. Semashko[2], M.Yu. Balakina[1]

[1]A.E. Arbuzov Institute of Organic and Physical Chemistry, Kazan Scientific center, RASc, 420088, Arbuzov str. 8, Kazan, Russia

[2]Kazan Federal University, 420008, Kremlevskaya str.18, Kazan, Russia

e-mail: macs-ne@mail.ru

Methacrylic copolymers with incorporated organic nonlinear optical (NLO) chromophore groups represent one of the classes of polymer materials with quadratic NLO response to the applied electric field. In order to exhibit quadratic NLO activity the material should be noncentrosymmetric, what is achieved by poling the chromophore groups in the static electric field applied to the material heated up to the temperature close to the glass transition one [1]. Here we present the study of methacrylic copolymers with azochromophores in the side chain, the concentration of chromophore-containing comonomer (MAZ) being 5 mol%, 8 mol%, 17 mol% and 37 mol%. The method of copolymers obtaining was described in [2]. Polymer films were spin cast and NLO coefficients of the corresponding polymers were measured by the Second Harmonic Generation (SHG) technique (Nd:YAG laser, $\lambda = 1064$ nm, $\tau = 15$ ns). Film thickness and some parameters of time-temperature protocol for poling using the corona-triode device are given in table 1.

Table 1. Characteristics of the studied polymer films.

MAZ concentration, mol%	Film thickness, nm	T_g, °C	T_p,°C	t_p, min	Order parameter, η
5	310	126	125	20	0.04
8	340	128	125	20	0.30
8	350	128	112	20	0.33
17	500	131	126	20	0,3
17	480	131	125	20	0,32
37	490	138	127	20	0.36
37	510	138	126	20	0.37

The results of measurements are presented in fig.1 in the form of dependence of NLO coefficients on the MAZ concentration in the studied methacrylic copolymers. It can be easily seen that maximum value of NLO coefficient was obtained for the polymer with MAZ concentration of about 10 mol%, α-quartz plate (X-cut) being used as a standard.

We have also studied the dependence of the SHG intensity on the angle of the incident laser beam. Thus, it was found that for most of the studied polymer films maximum SHG intensity was about 57 degrees.

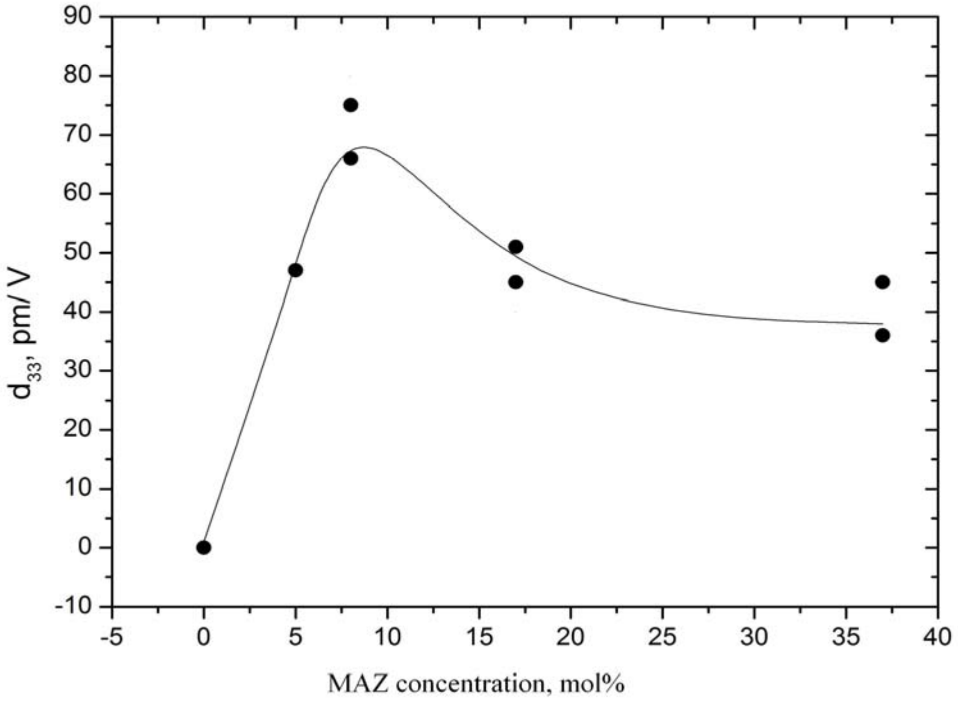

Fig.1. The dependence of NLO coefficients on the MAZ concentration in the studied methacrylic copolymers.

References

[1] D.M. Burland, R.D. Miller, C.A. Walsh, *Chem. Rev*. 1994, **94**, 31.

[2] T.A. Vakhonina, N.I. Ivanova, N.N. Smirnov, A.V. Yakimansky, M.Yu. Balakina, O.G. Sinyashin, *Mendeleev Commun.* 2014, **24**, 138.

NMR study of reorientational and translational motion of BH_4 groups in novel bimetallic perovskite-type borohydrides

O.A. Babanova[1], R.V. Skoryunov[1], A.V. Soloninin[1], A.V. Skripov[1], P. Schouwink[2],
R. Černý[2]

[1]Institute of Metal Physics, Ural Branch of the Russian Academy of Sciences, 620990,
S. Kovalevskoi 18, Ekaterinburg, Russia

[2]Laboratory of Crystallography, DPMC, University of Geneva, 1211, 24 quai Ernest-Ansermet, Geneva, Switzerland

e-mail: babanova@imp.uran.ru

Introduction

Borohydrides are ionic compounds, consisting of metal cations and tetrahedral $[BH_4]^-$ anions. These compounds are considered as promising materials for hydrogen storage due to their exceptional volumetric and gravimetric hydrogen densities [1], but their stability with respect to thermal decomposition and the slow sorption kinetics remain the major drawbacks for a practical use. Apart from the practical relevance, these compounds are of considerable interest as model systems for studying the reorientational motion of complex ions. The reorientational motion of BH_4 groups can be represented by rotations around three 2-fold axes and four 3-fold axes. Elucidation of hydrogen dynamics in complex hydrides may contribute to improving their hydrogen-storage properties.

In this work, we report the results of the first nuclear magnetic resonance study of atomic jump motion in new bimetallic perovskite-type borohydrides $CsCa(BH_4)_3$ and $RbCa(BH_4)_3$. Measurements of the ^1H and ^{11}B NMR spectra and spin-lattice relaxation rates were performed over wide ranges of temperatures (84 – 580 K) and resonance frequencies (14 – 90 MHz). NMR appears to be especially effective for studies of atomic motion in borohydrides [2], because nuclear spin-lattice relaxation rates in these compounds do not contain any significant contributions not related to atomic motion (such as the conduction-electron contribution in metallic systems). This allows us to trace the atomic jump rates in borohydrides systems over the range of 6 orders of magnitude (10^6 – 10^{12} s^{-1}).

Experimental methods

^1H and ^{11}B NMR measurements were performed on a modernized Bruker SXP pulse spectrometer with quadrature phase detection at the frequencies $\omega/2\pi$ = 14, 28 and 90 MHz for ^1H, 14 and 28 MHz for ^{11}B. The magnetic field was provided by a 2.1 T iron-core Bruker magnet. A home-built multinuclear continuous-wave NMR magnetometer working in the range 0.32 – 2.15 T was used for field stabilization. For NMR measurements at $T \leq 460$ K, a probehead with the sample was placed into an Oxford Instruments CF1200 continuous-flow cryostat using N_2 as a cooling agent. The sample temperature, monitored by a chromel-(Au-Fe) thermocouple, was stable to ± 0.1 K. Measurements in the temperature range 460 – 580 K were performed using a furnace probe head; for this setup, the sample temperature, monitored by a copper-constantan thermocouple, was stable to ± 0.5 K. The nuclear spin-lattice relaxation rates were measured using the saturation – recovery method. NMR spectra were recorded by Fourier transforming the solid echo signals (pulse sequence $\pi/2_x - t - \pi/2_y$). For NMR experiments, the sample was flame-sealed in a glass tube under vacuum.

Results and discussion

The temperature dependences of the proton spin-lattice relaxation rates R_1^{H} measured for $CsCa(BH_4)_3$ and $RbCa(BH_4)_3$ at three resonance frequencies $\omega/2\pi$ are shown in fig.1 and fig.2, respectively. The general features of the observed behavior of R_1^{H} are typical of the relaxation mechanism due to nuclear dipole-dipole interaction modulated by thermally

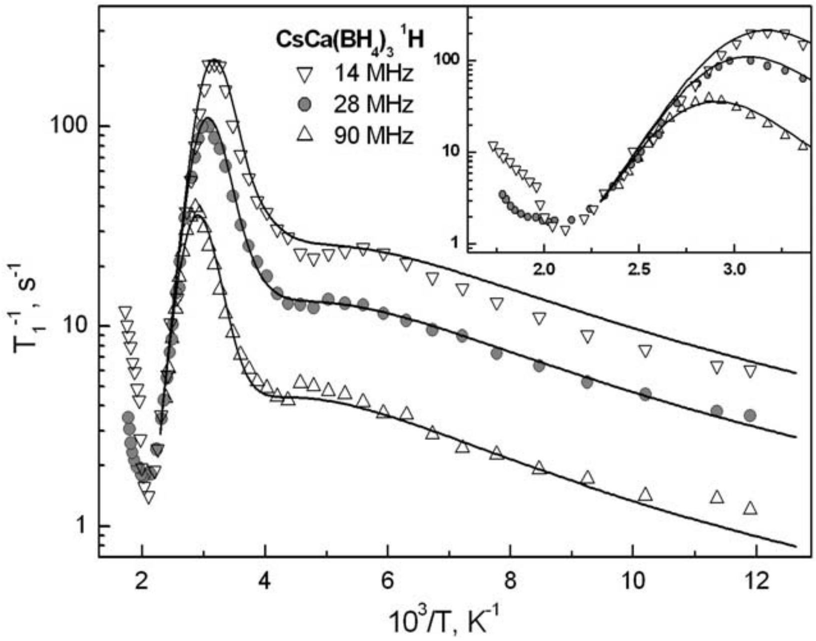

Fig.1. Proton spin-lattice relaxation rates measured at three resonance frequencies as functions of the inverse temperature for $CsCa(BH_4)_3$. The solid lines show the simultaneous fits of the 'three-peak' model to the data at $T < 426$ K.

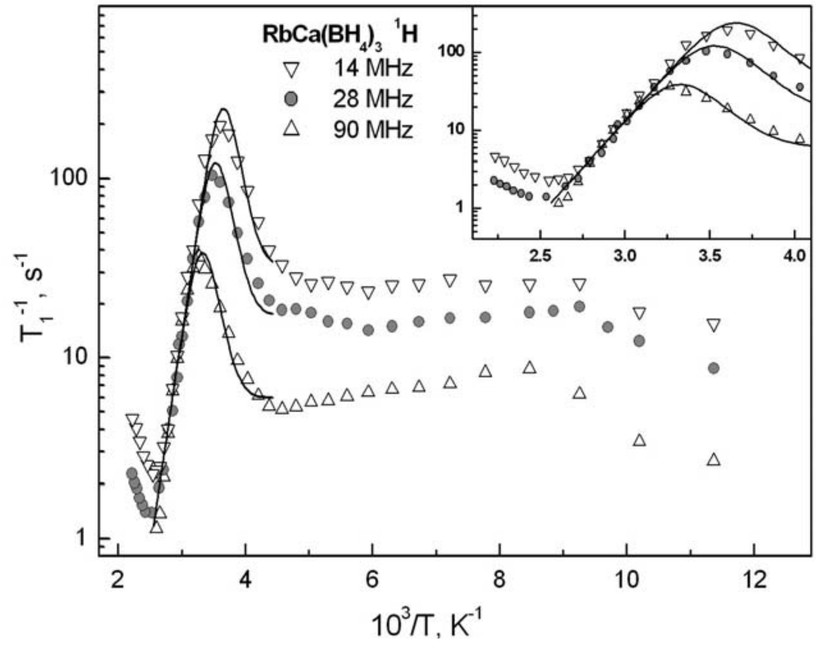

Fig.2. Proton spin-lattice relaxation rates measured at three resonance frequencies as functions of the inverse temperature for $RbCa(BH_4)_3$. The solid lines show the simultaneous fits of the standard model to the data in the region of the main high-trmpereture peak.

activated atomic motion. This motion is localized and can be identified as reorientations of the BH_4 tetrahedra. In the studied temperature range, the proton spin-lattice relaxation rates R_1^H exhibit a frequency-dependent peak near 320 K for $CsCa(BH_4)_3$ and near 290 K for $RbCa(BH_4)_3$. Such a peak is expected to occur at the temperature at which the reorientational jump rate of BH_4 groups (governed by the Arrhenius law) becomes nearly equal to the resonance frequency ω. The main frequency-dependent relaxation rate peak for $RbCa(BH_4)_3$ is observed at somewhat lower temperature than for $CsCa(BH_4)_3$. This means that for $RbCa(BH_4)_3$ the reorientational jump process responsible for the main peak is somewhat faster than for $CsCa(BH_4)_3$. The experimental results for $CsCa(BH_4)_3$ have been described in terms of the 'three-peak' model including three types of jump motion and a Gaussian distribution of activation energies for the low-temperature process at $T < 426$ K. For $RbCa(BH_4)_3$, experimental data in the region of the main high-trmpereture peak have been described by the standard model with the Arrhenius-type temperature dependence of reorientational jump rate [3]. The results of the fit for $CsCa(BH_4)_3$ and $RbCa(BH_4)_3$ are shown by the solid lines in fig.1 and fig.2. The reorientational motion responsible for the main peak is characterized by the activation energy of 0.50 eV for $CsCa(BH_4)_3$ and 0.52 eV for $RbCa(BH_4)_3$.

It is found, that for both systems some additional motional processes contribute to the low-temperature data; this leads to the presence of an additional smeared peak at low temperatures. Generally, the behavior of $R_1^H(T)$ for $CsCa(BH_4)_3$ at $T < 380$ K and for $RbCa(BH_4)_3$ at $T < 340$ K resembles that for α-$Y(BH_4)_3$ [4], where the linear coordination of a BH_4 tetrahedron by two metal atoms is believed to lead to coexistence of several inequivalent types of reorientations [5].

The expanded views of the $R_1^H(T)$ data for $CsCa(BH_4)_3$ and $RbCa(BH_4)_3$ in the region of high temperatures are shown in the insets of fig.1 and fig.2, respectively. It can be seen that for $CsCa(BH_4)_3$ slightly above 500 K the proton relaxation rate exhibits a jump (most pronounced at the frequency of 14 MHz). This feature can be attributed to the phase transition. For $RbCa(BH_4)_3$, such proton relaxation rate jump is not observed. The reappearance of the frequency dependence of R_1^H accompanied by the increase in R_1^H with the increasing temperature has been found for $CsCa(BH_4)_3$ at $T > 500$ K and for $RbCa(BH_4)_3$ at $T > 400$ K. Such a behavior indicates the onset of an additional motional process corresponding to translational diffusion of intact BH_4 groups. This is supported by the

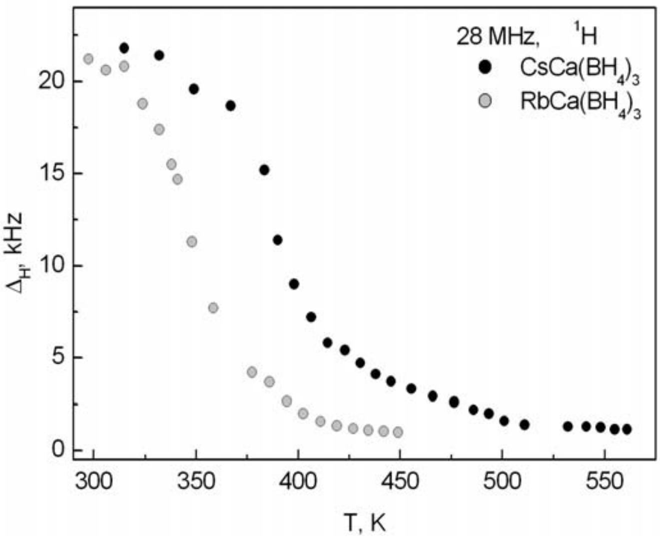

Fig.3. Temperature dependences of the width (full width at half-maximum) of the proton NMR spectra measured at 28 MHz for $CsCa(BH_4)_3$ and $RbCa(BH_4)_3$.

temperature dependence of the ^1H and ^{11}B NMR line widths which drop to very small values (~ 1 kHz) at high temperatures. The temperature dependences of the 1H NMR line widths Δ_H (full width at half-maximum) for $CsCa(BH_4)_3$ and $RbCa(BH_4)_3$ are shown in fig.3. The 1H NMR line narrowing is observed near 380 K for $CsCa(BH_4)_3$ and near 350 K for $RbCa(BH_4)_3$. The pronounced drop of Δ_H indicates the onset of the jump motion of H-containing species with the rate exceeding 10^5 s^{-1}. The fact that at high temperatures the values of Δ_H are very small (~1 kHz) shows that this motion leads to complete averaging out of dipole-dipole interactions; this can occur only in the case of translational diffusion.

References

[1] L. Schlapbach, A. Zuttel, *Nature*, 2001, 414, 353.

[2] O.A. Babanova, A.V. Soloninin, A.P. Stepanov, A.V. Skripov, Y.Filinchuk, *J. Phys. Chem. C* 2010, 114, 3712.

[3] Abragam, A. *The Principles of Nuclear Magnetism*, Clarendon Press: Oxford, 1961.

[4] A.V. Soloninin, A.V. Skripov, Y. Yan, A. Remhof, *J. Alloys Compd.* 2013, 555, 209.

[5] A.V. Skripov, A.V. Soloninin, O.A. Babanova, H. Hagemann, Y. Filinchuk, *J. Phys. Chem.C* 2010, 114, 12370.

Melting of the orbital order in $LaMnO_3$: the ^{17}O, ^{139}La NMR study

Z.N. Volkova[1], S.V. Verkhovskii[1], A.P. Gerashenko[1], K.N. Mikhalev[1], A. Trokiner[2]

[1]Institute of Metal Physics, Ural Branch of Russian Academy of Sciences, 620041,
Ekaterinburg, Russia

[2]LPEM, ESPCI ParisTech, UMR 8213, CNRS, 75005, Paris, France

e-mail: volkovazn@mail.ru

The oxide $LaMnO_3$ is a key system for experimental and theoretical studies that aim to resolve the relative importance of the electron-electron and electron-lattice interactions for the orbital physics of manganites [1]. In this work we resolve issues about the Mn–Mn spin correlation anisotropy and its variation across the orbital order (O'-phase) – orbital disorder (O-phase) transition at $T_{JT} = 750$ K in $LaMnO_3$ by means of ^{17}O, ^{139}La NMR.

There are two structural oxygen sites: O1 (along the *c* axis) and O2 (in the *ab* plane) in orthorhombic (*Pbnm* space group) $LaMnO_3$. The pathway of the superexchange interaction between two Mn neighbors involves O1 and O2 sites. The nuclear spin, ^{17}I, probes the unpaired electronic spins of its two Mn^{3+} neighbors at each site through the transferred hyperfine interactions. The nuclear spin, ^{139}I, of the La cation probes the electron spin density transferred to the La (6*s*) orbital through the $Mn(t_{2g})$-$O2(2p_\pi)$-$La(6s)$ path from its eight Mn^{3+} neighbors.

The ^{17}O and ^{139}La NMR spectra (fig.1a) were acquired up to 950 K in magnetic field $H = 11.7$ T. At this field the ^{17}O and ^{139}La spectra overlap but they can be separated and O1, O2 lines can be identified as was described in [2]. The simulation of the ^{139}La quadrupolar split spectra including both the central ($m_I = -1/2 \leftrightarrow +1/2$) and the satellite transitions was performed to determine the components of the magnetic shift $\{K_{ii}\}$ tensor as well as the quadrupole frequency $\nu_Q = 3eQV_{zz}/2I(2I-1)h$ and asymmetry parameter $\eta = |(V_{xx} - V_{yy})/V_{zz}|$ of the electric field gradient (EFG) tensor $\{V_{ii}\}$. The ^{17}O spin-echo decay rate, $^{17}T_2^{-1}$, was measured on the peak of each ^{17}O NMR line.

Spin and charge environment of La

The thermal variation of isotropic magnetic shift and EFG parameters of the ^{139}La nucleus are represented in fig.1b and fig.1c respectively. The isotropic magnetic shift, $^{139}K_{iso} \equiv 1/3\mathrm{Tr}\{K_{ii}\}$, scales well the thermal behavior of χ [3]. $^{139}K_{iso}(T)$ follows the Curie-Weiss law: $K_0 + C_{La}/(T - \Theta_{La})$ with $K_0 = 0.07(4)\% << {}^{139}K_{iso}(T)$, $\Theta_{La}(O') = 55(12)$ K and $\Theta_{La}(O) = 160(40)$ K. Thus the ^{139}La NMR data confirm that the Mn−Mn exchange coupling becomes more ferromagnetic in high temperature O-phase.

Parameters of EFG tensor, ν_Q and η, in the O'-phase remain practically unchanged up to about 500 K, smoothly decrease at higher temperature, and drop upon crossing T_{JT}. The nonzero value of the asymmetry parameter, $\eta \approx 0.3$, is in agreement with the symmetry of the O-phase which was found still orthorhombic [4]. The drop of ν_Q and η upon crossing T_{JT} is due to the fact that although there is no change in symmetry, the MnO_6 octahedra become more regular in the O-phase and the observed lattice appears cubic ($a \approx b \approx c/\sqrt{2}$) [5].

Anisotropy of the Mn−Mn exchange interaction: ^{17}O NMR

Below 750 K the ^{17}O NMR powder spectrum consists of two lines, O1 and O2 (fig.1a). The line displaying the largest ^{17}K was attributed to oxygen atoms in the O2 site [2]. From 200 K up to T_{JT} $^{17}K_{O2}(T)$ data follow the Curie-Weiss law: $K_0 + C_{O2}/(T - \Theta_{O2})$ with a chemical

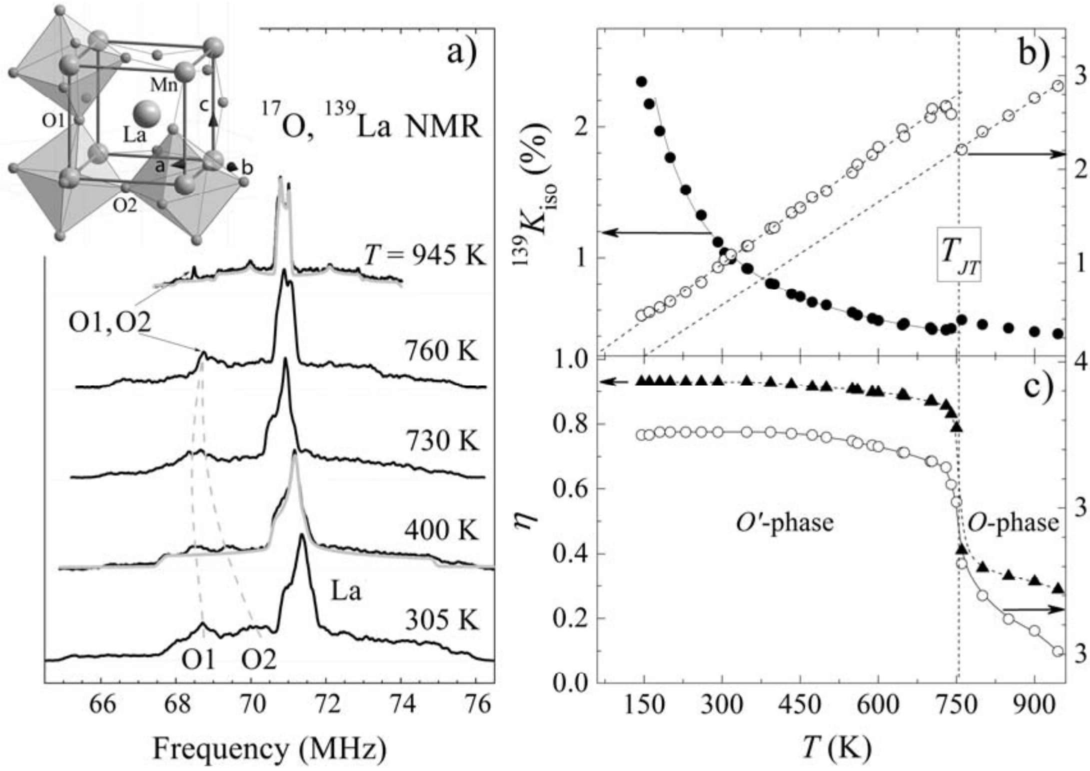

Fig.1. (a) The ^{17}O and ^{139}La NMR powder spectra of stoichiometric LaMnO$_3$. The gray curve beneath the spectrum at $T = 400$ K and 945 K is the corresponding ^{139}La NMR spectrum simulation. Inset: schematic structure (pseudocubic cell) of orthorhombic LaMnO$_3$ showing O1 and O2 sites. **(b)** ^{139}La isotropic shift, $^{139}K_{\text{iso}}$, vs T (●) and inverse of ($^{139}K_{\text{iso}} - K_0$) vs T (○). The solid curve is the Curie-Weiss fit for $T < 750$ K, the dotted lines are the fits to $(^{139}K_{\text{iso}} - K_0)^{-1}$. **(c)** Thermal behavior of the quadrupolar frequency, ν_Q (○), and EFG asymmetry parameter, η (▲), at the La site.

shift $K_0(\text{O2}) = 0.025(10)\%$ and $\Theta_{\text{O2}} = 35(10)$ K (fig.2a). The positive value of Θ_{O2} evidences the FM nature of superexchange interaction between Mn neighbors in the *ab* plane. In contrast to ^{139}La and ^{17}O$_2$ the mean-field law fits $^{17}K_{\text{O1}}(T)$ data only up to $T^* \approx 550$ K with $\Theta_{\text{O1}} = -15(20)$ K and $K_0(\text{O1}) = K_0(\text{O2})$ (fig.2a). The slightly negative value of Θ_{O1} demonstrates the AF nature of the interaction between adjacent Mn along *c*. Above T^* $^{17}K_{\text{O1}}(T)$ deviates from the Curie-Weiss law and tends toward $^{17}K_{\text{O2}}(T)$. The merging of O1 and O2 NMR lines at the *O'−O* transition indicates that the two structurally distinct O sites have the same magnetic environment. Above 750 K the linear fit of $(^{17}K(T) - {}^{17}K_0)^{-1}$ yields $\Theta_{\text{O1,O2}} = 260(50)$ K. Thus ^{17}O NMR demonstrates that the Mn−Mn exchange interaction changes from anisotropic ($\Theta_{\text{O2}} = 35$ K, $\Theta_{\text{O1}} = -15$ K) to isotropic ($\Theta_{\text{O2}} = \Theta_{\text{O1}} = 260$ K) at T_{JT} and that in the *O*-phase the isotropic exchange coupling is strongly FM-enhanced.

The low-frequency dynamics of the Mn spins was studied by measuring the ^{17}O spin-echo decay rate, T_2^{-1}, on O1 and O2 lines. The data in fig.2b show that as long as the mean-field behavior holds for $^{17}K_{\text{Oi}}(T)$ T_2^{-1} is almost T-independent. Indeed, T_2^{-1}(O2) is constant up to $T \approx T_{JT}$ whereas T_2^{-1}(O1) is constant only up to T^*. Above T^* T_2^{-1}(O1) starts to increase and approaches T_2^{-1}(O2) values close to T_{JT}. In the *O*-phase T_2^{-1} displays a maximum near 900 K. This behavior reflects the thermal activation of an additional fluctuating mechanism which becomes visible for the O1 site above T^*. Such behavior of Mn spin fluctuations means that collective modes of adjacent MnO$_6$ octahedra should be considered for this slow mechanism which yields changes of spin correlations between Mn neighbors along *c* axis. The activation component $(T_2^{-1})_a = [T_2^{-1}(T) - T_2^{-1}(293\text{ K})]$ has an exponential behavior versus $1/T$ below

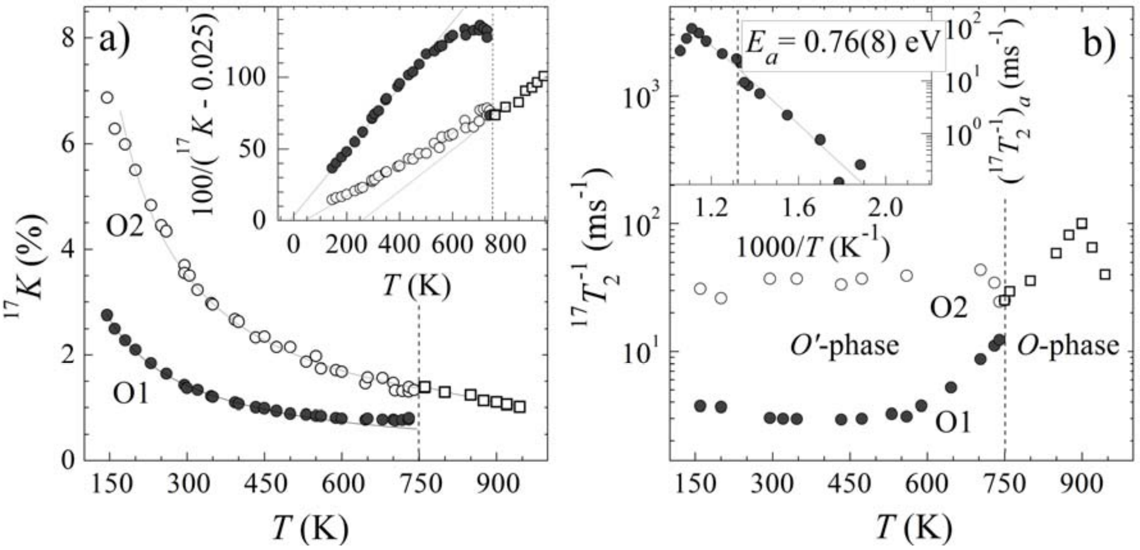

Fig.2. (a) Oxygen isotropic magnetic shift, ^{17}K, vs T for O1 (●) and O2 (○) sites in the O'-phase and for the single magnetic oxygen site (□) in the O-phase. Inset: inverse shift $(^{17}K - {}^{17}K_0)^{-1}$ vs T. The solid curves are the Curie-Weiss fit to O1, O2 and to the single magnetic oxygen site above 750 K. **(b)** Thermal behavior of ^{17}O echo decay rate, $^{17}T_2^{-1}$, for O1 (●) and O2 (○) sites in the O'-phase and for the single magnetic oxygen site (□) in the O-phase. Inset: thermally activated component $(^{17}T_2^{-1})_a = [^{17}T_2^{-1}(T) - {}^{17}T_2^{-1}(293\text{K})]$ vs 1000/T.

900 K (inset in fig.2b) with activation energy $E_a = 0.76(8)$ eV which is in consistent with estimates the Jahn-Teller splitting of the e_g state [6].

Acknowledgments

This work is supported by the Russian Foundation for Basic Research (grant № 12-02-00358-a) and Basic Research Program Project of Ural Branch of Russian Academy of Sciences № 12-U-2-1025.

References

[1] M.B. Salamon and M. Jaime, Rev. Mod. Phys. **73**, 583 (2001).
[2] L. Pinsard-Gaudart et al., Solid State Commun. **151**, 1968 (2011).
[3] A. Trokiner et al., Phys. Rev. B **87**, 125142 (2013).
[4] M.C. Sanchez et al., Phys. Rev. Lett. **90**, 045503 (2003).
[5] J. Rodriguez-Carvajal et al., Phys. Rev. B **57**, R3189 (1998).
[6] E. Pavarini and E. Koch, Phys. Rev. Lett. **104**, 086402 (2010).

Magnetic phase transition in ε-$In_{0.24}Fe_{1.76}O_3$ nanowires

A.I. Dmitriev

The Institute of Problems of Chemical Physics of the Russian Academy of Sciences,
Academician Semenov avenue 1, Chernogolovka, Moscow region, 142432, Russia

e-mail: aid@icp.ac.ru

The polymorphic modification ε-Fe_2O_3 is known from as far back as 1934 [1]. Structural studies of ε-phase were carried out, however, many years later [2, 3]. The ε-Fe_2O_3 phase remains the least studied thus far, because until quite recently no reliable and easily reproducible method of isolation of this phase was known. While there are methods permitting one to obtain ε-Fe_2O_3 in the form of inclusions in other phases of iron oxide, but no straightforward way of isolating the ε-phase in pure form has not existed until quite recently. One more difficulty consists in the ε-phase being very unstable and transforming spontaneously to α-Fe_2O_3. Moreover, ε-Fe_2O_3 exists exclusively in the form of nanoparticles because of its low surface energy [4]. Isolation of ε-Fe_2O_3 nanoparticles was first reported in [5].

The magnetic properties of the ε-Fe_2O_3 phase turned out to be still more remarkable than those of α-Fe_2O_3. It was established, in particular, that ε-Fe_2O_3 possesses a giant coercive force (up to 2.34 T) at room temperature. Coercive force is one of the main criteria of applicability of a material in magnetic memory engineering and spintronics). In addition, the ε-Fe_2O_3 phase exhibits magnetoelectric properties [6] and is known to be a good absorber of millimetre electromagnetic waves [7]. ε-Fe_2O_3 nanoparticles absorb efficiently microwaves with frequencies up to 182 GHz [7, 8], because this frequency matches in ε-Fe_2O_3 nanoparticles the “natural” ferromagnetic resonance in zero external magnetic field. The microwave field frequency corresponding to resonance absorption can be varied within a broad range by introducing into the sample various impurities (Al, Ga, In) [9, 10]. And it is this aspect, as well as attempts to obtain basic information on the mechanisms governing magnetization of the ε-phase of the iron oxide Fe_2O_3, that are stimulating interest to dilute magnetic compounds of the type of ε-$In_{0.24}Fe_{1.76}O_3$. The present study was conducted on adequately certified arrays of oriented ε-$In_{0.24}Fe_{1.76}O_3$ nanowires (fig.1) doped with indium and containing no inclusions of other polymorphic modifications of iron oxide.

Besides a SQUID magnetometer, we used an electron paramagnetic resonance (EPR) spectrometer permitting one to record and study separately the contributions of the various magnetic subsystems of a sample. The objectives pursued by the study can be formulated as follows:

1. Separation of the contributions of the high-temperature hard-magnetic and the low-temperature phases to the static magnetization and dynamic magnetic susceptibility of ε-$In_{0.24}Fe_{1.76}O_3$ nanowires.
2. Search for a magnetic resonance response to the magnetic phase transition in ε-$In_{0.24}Fe_{1.76}O_3$ nanowires.
3. Determination of the types of magnetic ordering in the high- and low-temperature magnetic phases of ε-$In_{0.24}Fe_{1.76}O_3$ nanowires.
4. Recognizing the part played by the substitutional indium impurity in evolvement of the magnetic properties of nanowires in the ε-phase of the iron oxide Fe_2O_3.

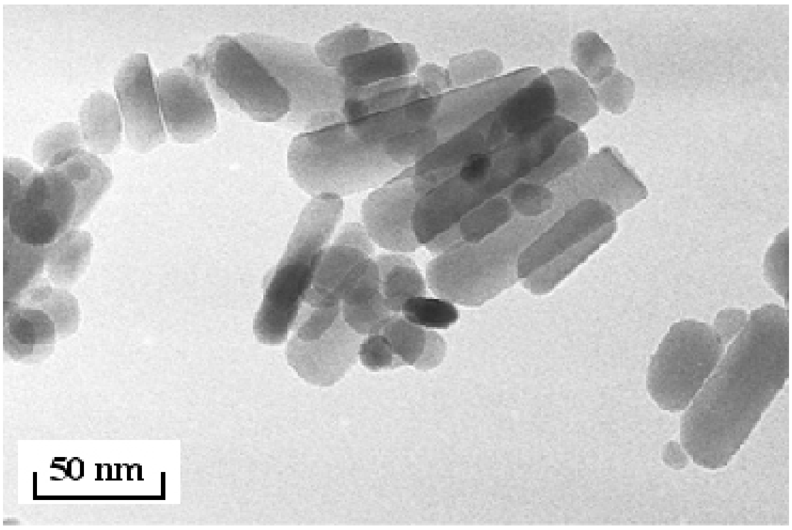

Fig.1. Image of a ε-$In_{0.24}Fe_{1.76}O_3$ nanowires obtained with a transmission electron microscope.

The electron spin resonance spectra (fig.2) were obtained with a JEOL spectrometer operating in the X-ray frequency range (microwave field frequency $\nu = 9.4$ GHz), with a type H_{102} rectangular resonator, modulation frequency 100 kHz and the dc magnetic field sweeping range 0 – 14 kOe. The electron spin resonance spectra were recorded in the form of the first derivative of the imaginary part of magnetic susceptibility $d\chi''/dH$. The temperature was varied within the 4 – 300 K range in an ESR 900 Oxford Instruments cryostat.

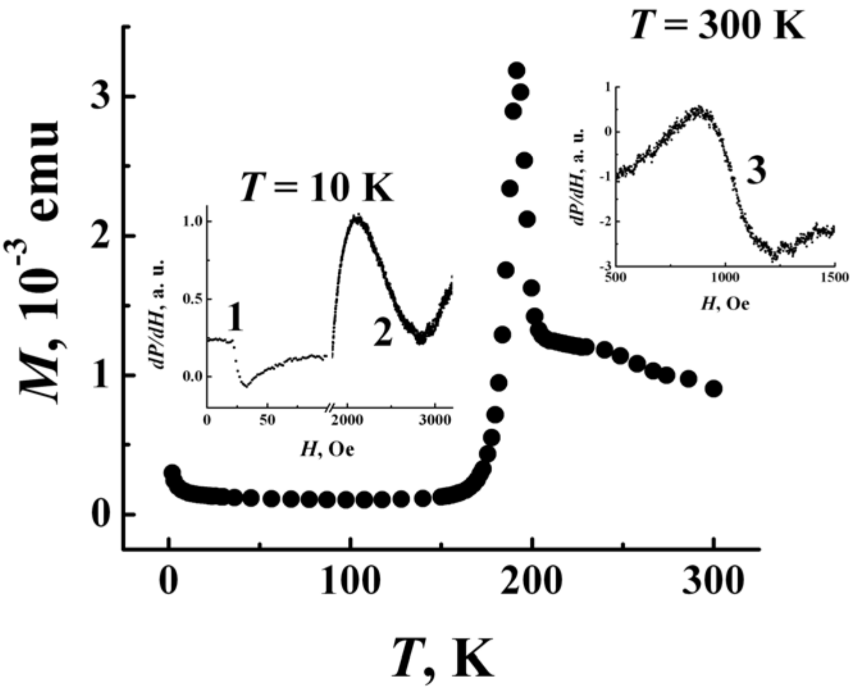

Fig.2. Temperature dependence of the magnetization M of ε-$In_{0.24}Fe_{1.76}O_3$ nanowires measured in a magnetic field of 1 kOe under cooling. Inset shows fragments of electron spin resonance spectra corresponding to the high- and low-temperature phases. The numbers identify the resonance lines in the spectrum.

The magnetization of the nanowires (fig.2) was measured with a Quantum Design MPMS 5XL SQUID magnetometer. We measured the temperature dependence of nanowire magnetization M under cooling in a dc magnetic field 1 kOe. The hysteresis loops were obtained at temperatures of 300 and 100 K in a dc magnetic field 0 – 50 kOe.

The spectrum of ε-$In_{0.24}Fe_{1.76}O_3$ nanowires obtained below the temperature of the magnetic phase transition consists of two lines, 1 and 2 (see inset to fig.2). Following the magnetic transition, only line 3 remains in the spectrum (inset to fig.2). The nonresonant signal close to zero magnetic field, which can be induced by the “natural” ferromagnetic resonance. The resonance fields of lines 2 and 3 corresponding to the low- and high-temperature phases, respectively, differ strongly from one another (inset to fig.2). The positions of the resonance lines are sensitive to canting of the easy magnetization axis relative to the constant magnetic field of the spectrometer. The magnetic phase transition brings about a noticeable rearrangement of the electron spin resonance spectrum.

This work reports on a study of magnetic properties of ordered arrays of ε-$In_{0.24}Fe_{1.76}O_3$ nanowires possessing a room-temperature coercive force of 6 kOe. Lowering the temperature below 190 K brings about a sharp decrease of the coercive force and magnetization of nanowires driven by the spin-reorientation transition [11]. Lines related to the high-temperature and low-temperature phases have been identified in ferromagnetic resonance spectra of the nanowires. A line lying near zero magnetic field and evolving from “natural” ferromagnetic resonance has also been detected.

Acknowledgments

Support by the Grant of the President of Russia MK-1598.2014.3.

Author is grateful to scientific adviser Professor R. B. Morgunov and Professor S. Ohkoshi for samples providing.

References

[1] H. Forestier, G. Guoit-Guillain. C. R. Academie des Sciences 199 (1934)720.

[2] E. Tronc, C. Chaneac, J. P. Jolivet. J. Solid State Chem. 139 (1998) 93.

[3] K. Kelm, W. Mader. Z. Anorg. Allg. Chem. 631 (2005) 2383.

[4] J. Tucek, R. Zboril, A. Namai, S. Ohkoshi. Chem. Mater. 22 (2010) 6483.

[5] J. Jin, S. Ohkoshi, K. Hashimoto. Adv. Mater. 16 (2004) 48.

[6] M. Gich, C. Frontera, A. Roig, J. Fontcuberta, E. Molins, N. Bellido, Ch. Simon, C. Fleta. Nanotechnology 17 (2006) 687.

[7] S. Ohkoshi, S. Kuroki, S. Sakurai, K. Matsumoto, K. Sato, S. Sasaki. Angew. Chem. 46 (2007) 8392.

[8] M. Yoshikiyo, A. Namai, M. Nakajima, T. Suemoto, S. Ohkoshi. J. Appl. Phys. 111 (2012) 07A726.

[9] S. Sakurai, S. Kuroki, H. Tokoro, K. Hashimoto, S. Ohkoshi. Adv. Funct. Mater. 17 (2007) 2278.

[10] M. N. Afsar, Z. Li, K. A. Korolev, A. Namai, S. Ohkoshi. J. Appl. Phys. 109 (2011) 07E316.

[11] A.I. Dmitriev, O.V. Koplak, A. Namai, H. Tokoro, S. Ohkoshi, R.B. Morgunov, Physics of the Solid State 55 (2013) 2252.

^{1}H NMR study of hydrogen site occupancy in hydrides of disordered Ti-Nb

V.O. Ievleva[1], M.G. Shelyapina[1], S.A. Lavrov[1], N.E. Skryabina[2], A.G. Aleksanyan[3]

[1]Faculty of Physics, Saint-Petersburg State University, 198504, 1 Ulyanovskaya st.,
Saint Petersburg, Russia

[2]Faculty of Physics, Perm National Research University, 614990, 15 Bukireva st., Perm, Russia

[3]A.B. Nalbandyan Institute of Chemical Physics of Armenian NAS, P. Sevak st. 5/2, 0014,
Yerevan, Republic of Armenian

e-mail: valeriya_ievleva@nmr.phys.spbu.ru

Abstract

In this contribution we report on the results of ^{1}H NMR studies of the fcc $Ti_{1-x}Nb_xH_y$ hydrides ($x = 0.5$, 0.6, 0.3 and $y \approx 2$), perspective materials for reversible hydrogen storage. The samples were synthesized using the method of Self-propagating High-temperature Synthesis. The ^{1}H continuous wave NMR spectra recorded at room temperature evidence that a part of hydrogen is in mobile state, whereas the rest is bounded to the lattice. It was found that in studied hydrides with fcc structure hydrogen atoms are distributed between both tetrahedral and octahedral sites.

Introduction

Efficient and safe storage of hydrogen is one of the most important problems for the extensive use of hydrogen as energy carrier. Transition metal alloys belong to a class of hydrogen storage materials. Properties important for hydrogen storage application, such as a maximum hydrogen uptake, temperature of the hydrogen release, reversibility of reaction etc., depend not only on the composition but on the microstructure as well. The latest is determined by the preparation method of an alloy and its further hydrogenation. Nuclear magnetic resonance (NMR) techniques is quite valuable for studies both the hydrogen location and mobility in hydrides. In this contribution we report on the results of our ^{1}H continuous-wave NMR study of $Ti_{1-x}Nb_xH_y$ hydrides synthesized using the method of Self-propagating High-temperature Synthesis (SHS). [1]

Sample preparation and experimental methods

All the studied samples have been synthesized by the "hydride cycle" in association with SHS (Self-propagating High-temperature Synthesis). The full hydride cycle included: (I) the SHS synthesis of source hydrides (TiH_2 and $NbH_{0.9}$); (II) grinding and mixing the powders of hydrides; (III) compacting this mixture at different pressures; (IV) dehydrogenation of compacted sample; (V) synthesis of the hydride of the formed $Ti_{1-x}Nb_x$ alloy by SHS method implemented under hydrogen pressure. More details can be found in [2].

The structural characterization of the both alloys and hydrides was done using a Siemens D-5000 diffractometer. Fig.1 represents the X-ray patterns for all studied hydrides. It has been obtained that the synthesized $Ti_{1-x}Nb_x$ samples have inhomogeneous structure: the main bcc phase contains an admixture of hcp-Ti (only traces in the $Ti_{0.7}Nb_{0.3}$ sample and several percent in the $Ti_{0.5}Nb_{0.5}$ and $Ti_{0.4}Nb_{0.6}$ samples).

The synthesized hydrides are even more inhomogeneous: besides the main fcc phase they contain several percent of two additional phases, namely, bcc-TiH_x and orthorhombic

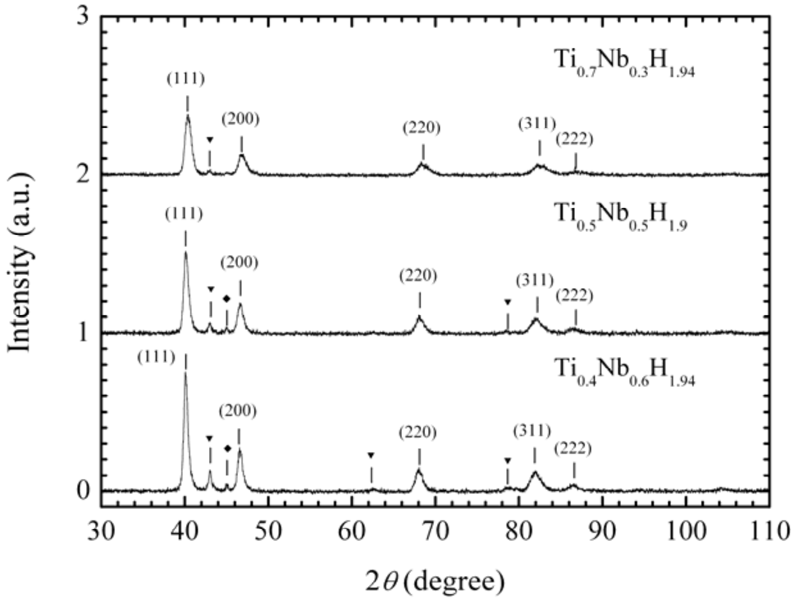

Fig.1. X-ray pattern for studied hydrides hydrides.

NbH_x. It means that in the synthetized hydrides the main phase does not correspond exactly to the initial composition, however, further, when discussing our results we will refer the samples according to the initial composition. The lattice parameters for all studied alloys and hydrides are listed in table 1.

Table 1. Structural parameters of the studied $Ti_{1-x}Nb_x$ alloys and their hydrides

Compound	Structure type	Space group	Lattice parameters (Å)	Volume per metal atom ($Å^3$)
$Ti_{0.7}Nb_{0.3}$	bcc	Im-3m	$a = 3.28543(1)$	17.7315
$Ti_{0.5}Nb_{0.5}$	bcc	Im-3m	$a = 3.29695(1)$	17.9187
	hcp	$P6_3/mmc$	$a = 2.96894(1)$ $c = 4.77581(1)$	18.2285
$Ti_{0.4}Nb_{0.6}$	bcc	Im-3m	$a = 3.28519(1)$	17.7276
	hcp	$P6_3/mmc$	$a = 2.96894(1)$ $c = 4.77581(1)$	18.2285
$Ti_{0.7}Nb_{0.3}H_{1.94}$	fcc	Fm-3m	$a = 4.51225(1)$	23.2058
	orthorhombic	F222	$a = 4.84300(1)$ $b = 4.91700(1)$ $c = 3.46700(1)$	20.6400
	bcc	Im-3m	$a = 3.30650(1)$	18.0749
$Ti_{0.5}Nb_{0.5}H_{1.9}$	fcc	Fm-3m	$a = 4.52364(1)$	23.1422
	orthorhombic	F222	$a = 4.82282(1)$ $b = 4.91700(1)$ $c = 3.46700(1)$	20.5540
	bcc	Im-3m	$a = 3.30650(1)$	18.0749
$Ti_{0.4}Nb_{0.6}H_{1.94}$	fcc	Fm-3m	$a = 4.52778(1)$	23.2058
	orthorhombic	F222	$a = 4.84300(1)$ $b = 4.91700(1)$ $c = 3.46700(1)$	20.6400
	bcc	Im-3m	$a = 3.30650(1)$	18.0749

The ^{1}H NMR line shapes of the samples were recorded with home-built cw NMR spectrometer at 43 MHz at room temperature.

Results and discussion

Fig.2 represents the first derivative of the absorption ^{1}H NMR spectral line recorded at T = 293 K in $Ti_{0.7}Nb_{0.3}H_{1.94}$, $Ti_{0.5}Nb_{0.5}H_{1.9}$ and $Ti_{0.4}Nb_{0.6}H_{1.94}$. As one can see from fig.2 in all studied hydrides ^{1}H NMR spectra consist of two components: narrow and broad, which can be attributed to the mobile hydrogen and hydrogen bounded to the lattice, respectively. This spectral shape is rather typical for metal hydrogen systems [3-6].

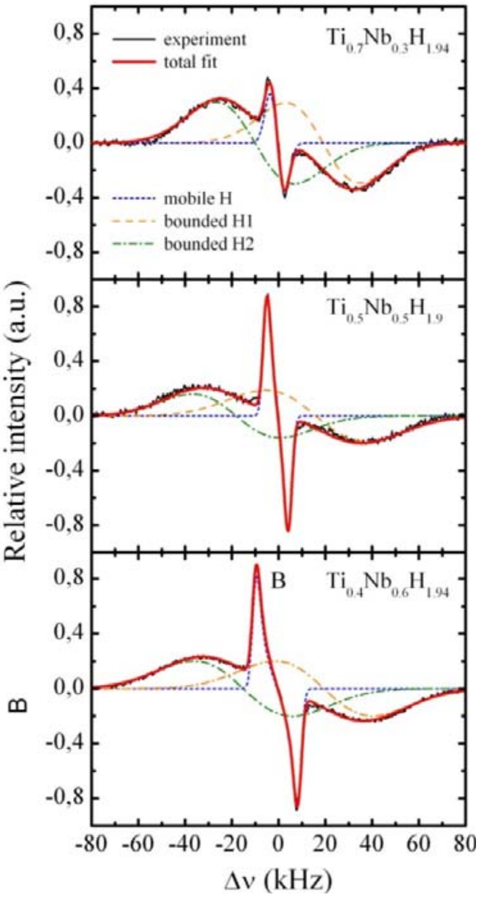

Fig.2. ^{1}H NMR spectra of $Ti_{0.7}Nb_{0.3}H_{1.94}$, $Ti_{0.5}Nb_{0.5}H_{1.9}$ and $Ti_{0.4}Nb_{0.6}H_{1.94}$ hydrides at room temperature at 43 MHz.

A more careful analysis shows that broad line is a superposition of two broad lines, shifted to different sides relatively the narrow line. Both the second moment values of the adsorption lines (S_2) and the relative shift (Δν) are listed in table 2.

Table 2. Experimental parameters of ^{1}H NMR spectra in studied hydrides.

Hydride	Δν (kHz)		S_2 (G^2)	
	broad line 1	broad line 2	broad line 1	broad line 2
$Ti_{0.7}Nb_{0.3}H_{1.94}$	– 9.5(7)	19.6(6)	15.7(2)	14.0(2)
$Ti_{0.5}Nb_{0.5}H_{1.9}$	– 17.7(5)	16.5(9)	19.3(1)	25.4(1)
$Ti_{0.4}Nb_{0.6}H_{1.94}$	– 4.5 (9)	20.1(9)	24.4(1)	24.1(1)

To attribute the broad lines we compared the second moment of the experimental lines with those one calculated using the well-known Van Vleck expression and taking into account an equiprobable distribution of the Nb atoms on the metal sites in the lattice and H atoms on the tetrahedral (T) and (O) interstitial sites. Because of the low natural abundance of ^{47}Ti and ^{49}Ti nuclei (7.75% and 5.51%, respectively) and small magnetic moments (compared to ^{1}H and ^{93}Nb nuclei) their contribution to the dipole-dipole interactions with protons can be neglected. Thus in our calculations only $^1H - {}^1H$ and $^1H - {}^{93}Nb$ dipole-dipole interactions were taken into account. More details can be found in [7].

In fig.3 we plot the second moment S_2 in $Ti_{0.4}Nb_{0.6}H_{1.94}$ as a function of the O-site occupancy. Both contributions from hydrogen located in T-sites (H_T) and O-sites (H_O) are shown. In fig.3, 100% of the O-site occupancy means that all O-sites are occupied and the rest of hydrogen is in T-sites.

The better agreement between the experimental and calculated S_2 values is achieved at the O-site occupancy close to 50% in $Ti_{0.4}Nb_{0.6}H_{1.94}$ (compare fig.3 and table 2) and 70% in $Ti_{0.5}Nb_{0.5}H_{1.9}$. For $Ti_{0.3}Nb_{0.7}H_{1.94}$ the calculation leads to noticeably greater S_2 values as compared to the experimental ones.

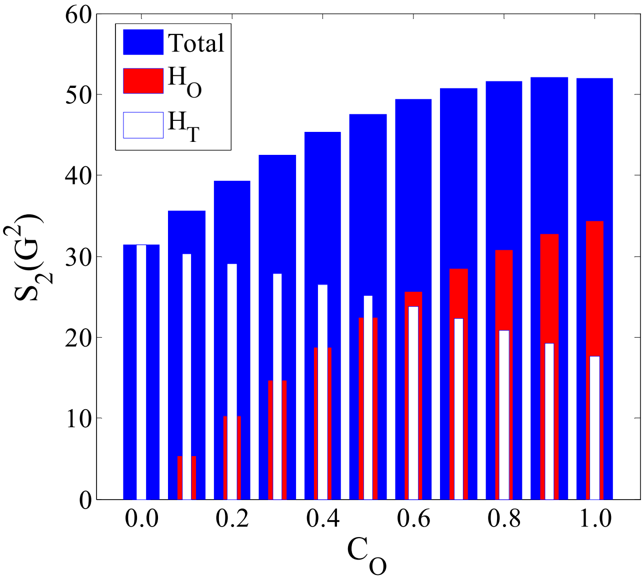

Fig.3. ^{1}H NMR spectra of $Ti_{0.4}Nb_{0.6}H_{1.94}$ hydrides at room temperature at 43 MHz.

References

[1] R.G. Barnes. Hydrogen in Metals III; chap. Nuclear Magnetic Resonance in Metal Hydrogen Systems. Berlin, Heidelberg: Springer-Verlag (1997), p. 93–151.

[2] A.G. Aleksanyan, S.K. Dolukhanyan, V.S. Shekhtman, J. Huot, O.P. Ter-Galstyan, N.L. Mnatsakanyan, “Formation of alloys in Ti–V system in hydride cycle and synthesis of their hydrides in self-propagating high-temperature synthesis regime”, J. Alloys Compds. 509 (2011) S786-9.

[3] E. Kurenkova, A. Vyvodtseva, M.G. Shelyapina, V.I. Chizhik, A.V. Ievlev, N.E. Skryabina, A.G. Aleksanyan, D. Fruchart, “1H NMR Study of Hydrogen Site Occupancy in Hydrides of Disordered Ti-V and Ti-V-Cr Alloys”, Solid State Phenomena194 (2013), p. 254-257

[4] Z. Kudabaev, D. Torgeson, A. Shevakin, “Nuclear magnetic resonance study of the phase transitions in TiH_2 and TiD_2” J. Alloys Compds. 231 (1995) 233-7.

[5] B. Nowak, O. J. Zogal, H. Drulis, “^{51}V and 1h nuclear magnetic resonance in vanadium dihydride” J. Phys. C: Solid State Phys. 15 (1982) 5829-38.

[6] R.L. Corey, T.M. Ivancic, D.T. Shane, E.A. Carl, R.C.B. Jr., J.M.B. von Colbe, M. Dornheim, R. Bormann, J. Huot, R. Zidan, A.C. Stowe, M.S. Conradi, Hydrogen motion in magnesium hydride by NMR. J. Phys. Chem. C 112 (2008) 19784-90.

[7] V.S. Kasperovich, B.B. Khar’kov, I.A. Rykov, S.A. Lavrov, M.G. Shelyapina, Y.S. Chernyshev, V.I. Chizhik, N.E. Skryabina, D. Fruchart, S. Miraglia, “Spinlattice relaxation and mobility of protons in the lattice of the $TiV_{0.8}Cr_{1.2}$ alloy”. Phys. Sol. State 53 (2011), p. 234-41.

NMR in $Li_2M_3Al(MoO_4)_4$ triple molybdates (M = Rb, Cs)

R.D. Nevmyvako[1], N.A. Zhuravlev[1], T.A. Denisova[1], Yu.M. Kadyrova[2], K.N. Mikhalev[3],
E.G. Khaikina[2,4], S.F. Solodovnikov[5]

[1]Institute of SolidState Chemistry, Ural Branch, Russian Academy of Sciences,
Yekaterinburg, 620990 Russia
[2]Baikal Institute of Nature Management, Siberian Branch, Russian Academy of Sciences,
UlanUde, 670047 Russia
[3]Institute of the Physics of Metals, Ural Branch, Russian Academy of Sciences,
Yekaterinburg, 620990 Russia
[4]Buryat State University, UlanUde, 670000 Russia
[5]Institute of Inorganic Chemistry, Siberian Branch, Russian Academy of Sciences,
Novosibirsk, 630090 Russia

e-mail: rndgodlike@gmail.com

The structural variety of triple molybdates and the display of functional properties (i.e., ion-conducting, nonlinear-optical, and luminescent) by many representatives of this class of compounds [1] command the attention of researchers for these compounds. In [2], we reported our discovery of the isostructural family of $Li_2M_3R(MoO_4)_4$ triple molybdates (MR= CsFe, CsGa, CsAl, RbGa, RbAl, TlAl), ordered derivatives of the structure of cubic $Cs_6Zn_5(MoO_4)_8$ and crystallized in tetragonal syngony (space group I 2d, Z= 4). A detailed description of the crystal structures of $Li_2M_3R(MoO_4)_4$ compounds containing open lattices of MoO_4, LiO_4, and RO_4-tetrahedra whose voids hold large, singly-charged cations with coordination number CN = 12 is given in [2, 3]. Most of the elements in these compounds have nuclei with intrinsic magnetic moments (Li, Al, Rb, Cs), so the considered triple molybdates are suitable objects for studies using such local methods as nuclear magnetic resonance (NMR). To date, no such studies have been performed. In this work we present, the first results from an NMR study of triple molybdates with the composition $Li_2M_3Al(MoO_4)_4$ (M = Rb, Cs).

The compounds were prepared by annealing stoichiometric amounts of simple molybdates at 450–500°C for 40–60 h. X-ray diffraction on a D8 Advance automatic diffractometer (Bruker), $\lambda CuK\alpha$, and a secondary monochromator ($2\theta max= 100°$; scan step 0.02076°) was used as a control if the products of synthesis were single-phase.

The NMR spectra were recorded at room temperature on an Agilent VNMR 400 pulse spectrometer at frequencies of 104.2 MHz (^{27}Al), 155.44MHz (^{7}Li), 130.87MHz (^{87}Rb), and 52.43 MHz (^{133}Cs) in the stationary one-pulse mode and with magic angle spinning (MAS). Rotation rate of the sample was 10 kHz. The chemical shift values for ^{7}Li were determined with respect to 9.7M LiCl, for ^{27}Al with respect to 1.1M $Al(NO_3)_3$, for ^{87}Rb with respect to 0.01M RbCl, and for ^{133}Cs with respect to0.1M $CsNO_3$.

The NMR spectra were decomposed into their components from the different crystallographic positions of the nuclei, and the values of the quadrupole frequencies (ν_Q), the asymmetry parameters (η), and the chemical shifts (δ) of the complex NMR lines were determined using the SIMUL powder spectrum simulation program with allowance for the combined effect of magnetic and electric hyperfine interactions.

The stationary NMR spectra of magnetic nuclei in the investigated powder compounds have complex shapes due to the superposition of quadrupole effects according to the nuclear spin (I) and its quadrupole moment (Q): I(^{7}Li) = 3/2 and ^{7}Q= –0,04 b; I(^{27}Al)=5/2 and ^{27}Q= 0.15 b; I(^{87}Rb)= 3/2 and ^{87}Q= 0.13 b; I(^{133}Cs)= 7/2 and ^{133}Q= –0.003 b.

According to the results from our X-ray studies, there is one position for the Li$^+$ ion in the crystal lattice of compounds that corresponds to the singlet line in the ^{7}Li NMR (MAS) spectra. The stationary ^{7}Li NMR spectrum of the $Li_2Rb_3Al(MoO_4)_4$ compounds is also characterized by one signal consisting of the line from the central transition –1/2 ↔ +1/2 and the lines of satellite transitions –3/2 ↔ –1/2 and +1/2↔ +3/2with quadrupole frequency ν_Q=12 kHz. The stationary ^{7}Li NMR spectrum of the $Li_2Cs_3Al(MoO_4)_4$ compound has a somewhat more complicated shape associated with the high asymmetry parameter of the electric field gradient tensor (see table).

The line of the central transition and the first pair of satellites with quadrupole splitting of 240 and 210 kHz for the $Li_2Rb_3Al(MoO_4)_4$ and $Li_2Cs_3Al(MoO_4)_4$ compounds, respectively, are also observed in ^{27}Al NMR spectra recorded without spinning. As it follows from an analysis of the ^{27}Al NMR (MAS) spectra the central transition can be described by one line that corresponds to the single Al position in the lattice with allowance for the second-order effects of perturbation theory, due to the high values of the quadrupole splitting frequencies.

This effect is characteristic for the ^{87}Rb NMR spectrum of the $Li_2Rb_3Al(MoO_4)_4$ but in an even more complicated manner. There are two positions for the rubidium ion in the structure of this compound, and in the stationary (fig.1a) and MAS (fig.1b) ^{87}Rb NMR spectra we observe the superposition of two lines of the central transitions, the complicated shape of which is due to the high values of the quadrupole splitting frequencies (1.9 and 1.3 MHz) and the asymmetry parameter (table).

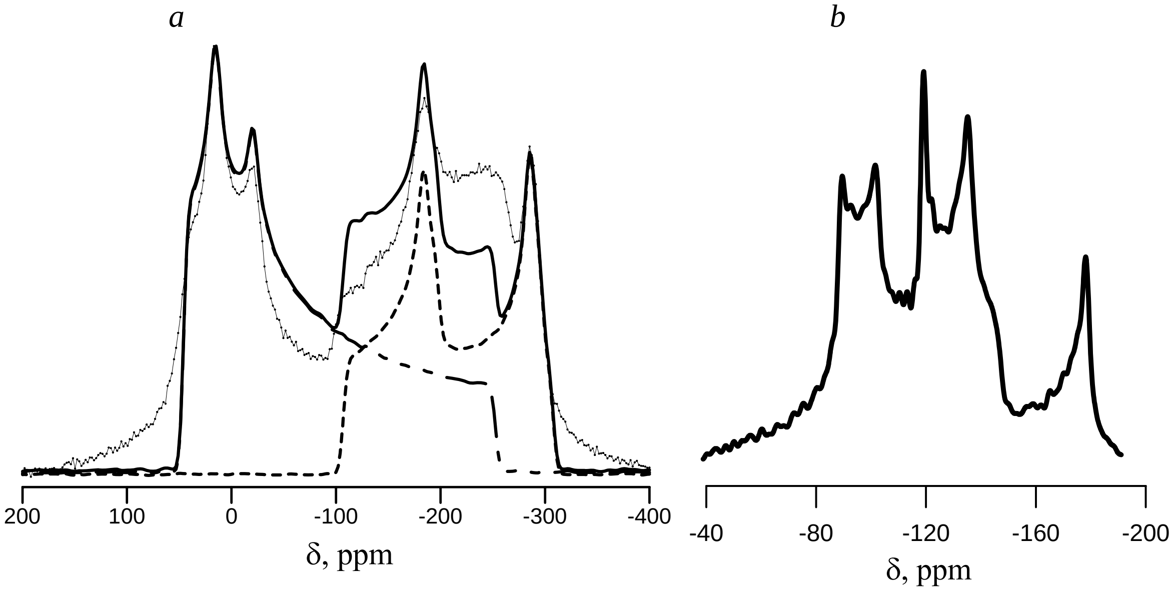

Fig.1. ^{87}Rb NMR $Li_2Rb_3Al(MoO_4)_4$ spectra: (a) experimental (points) and calculated (solid line) spectra. The dotted line marks the components of the spectrum from two crystallographic rubidium positions; (b) ^{87} Rb NMR (MAS) experimental spectrum.

^{133}Cs NMR (MAS) spectrum of the $Li_2Cs_3Al(MoO_4)_4$ compound consists of two singlets with chemical shift values of –118.8 and –170.6 ppm (fig.2b) and integral intensities corresponding to the populations of the two cesium ion positions in the molybdate structure. Analysis of the stationary NMR spectrum (fig.2a) allowed us to establish the high values of asymmetry parameter η= 0.6 and 0.8 at low (relative to 87Rb) values of the quadrupole splitting frequency (in accordance with the values of the quadrupole moments of ^{133}Cs and ^{87}Rb nuclei).

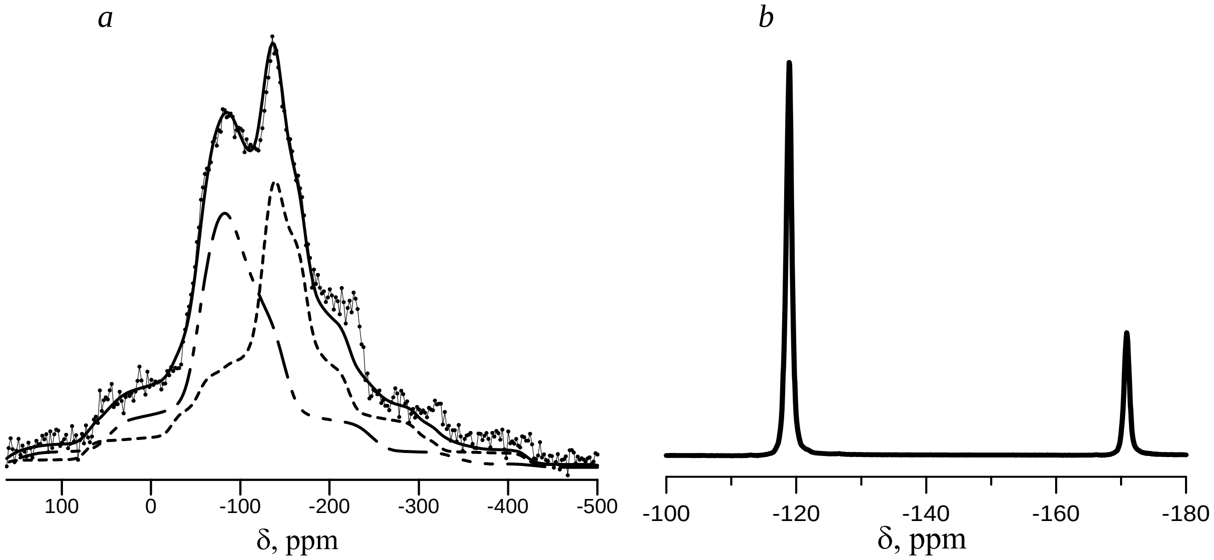

Fig.2. ^{133}CsNMR spectra of the $Li_2Cs_3Al(MoO_4)_4$: (a) experimental (points) and calculated(solid line). The dotted line marks the components from two crystallographic cesium positions; (b) ^{133}Cs NMR (MAS) experimental spectrum.

Table 1. Values of chemical shifts (δ), quadrupole frequencies (νQ) and asymmetry parameters (η) in the NMR spectra of the $Li_2M_3Al(MoO_4)_4$ compound (M= Rb, Cs)

Nucleus	Parameter	$Li_2Rb_3Al(MoO_4)_4$	$Li_2Cs_3Al(MoO_4)_4$
^{7}Li	δ, ppm	-0,5	-0,31
	ν_Q, MHz	0,012	0,013
	η	0	0,45
^{27}Al	δ, ppm	62,6–61,2	61,8–60,9
	ν_Q, MHz	0,24	0,21
	η	0,2	0,25
^{87}Rb	δ, ppm	–	
	ν_Q, MHz	1.9 and 1.3	
	η	0,6 and 0,1	
^{133}Cs	δ, ppm		-118,8 and -170,6
	ν_Q, MHz		0,0065 and 0,0055
	η		0,6 and 0,8

On the whole, the NMR spectra testify to the considerable asymmetry of the distribution of the electric charge throughout the crystal lattice of triple molybdates $Li_2M_3Al(MoO_4)_4$ (M = Rb, Cs), which probably determines their properties as nonlinear optical materials [4].

Acknowledgments

This work was supported by the Ural Branch of the Russian Academy of Sciences, project № 12-M-23-20611 and 12-S-3-1001; by the Russian Foundation for Basic Research, project № 13-03-01020a; and by the RF Ministry of Education and Science, project № 3.6021.2011.

References

[1] Khaikina, E.G., Bazarova, Zh.G., Solodovnikov, S.F., and Klevtsova, R.F., Inzh. Ekol., 2011, № 1, p. 48.

[2] Solodovnikov, S.F., Khaikina, E.G., Solodovnikova, Z.A., et al., Dokl. Akad. Nauk, 2007, vol. 416, № 1, p. 60.

[3] Solodovnikov, S.F., Khaikina, E.G., and Solodovnikova, Z.A., Zh. Strukt. Khim., 2009, vol. 50, p. 85.

[4] Kadyrova, Yu.M., Khaikina, E.G., Solodovnikov, S.F., et al., Materialy Vserossiiskoi molodezhnoi nauchno-prakticheskoi konferentsii “Ekologobezopasnye i resursosberegayushchie tekhnologii i materialy”(Proc. All Russian Youth Sci. Practical Conf. “Ecologically Friendly and Resource Saving Technologies and Materials”), Ulan-Ude: Izd. Buryat State Univ., 2011, p. 26.

Ferromagnetic resonance properties of nanocomposite ferromagnetic thin films

I.N. Razmislov, V.S. Vlasov, V.K. Turkov, L.N. Kotov, A.S. Popova

Syktyvkar State University, 167001 Syktyvkar, Oktybrsky 55, Russia

e-mail: z-project@bk.ru

Description the ferromagnetic resonance (FMR) in composite ferromagnetic films is difficult task. Because nanocomposites metal-dielectric films are plenty randomly oriented magnetic particles with different size and shape in a dielectric medium on substrate usually. Such structures may be used in device for recording and storing information for protective coatings, wireless device and medical equipment [1]. Therefore these structures are studied widely.

We had developed the model for description FMR properties composites ferromagnetic nanogranulated films. The basis of our model is the approaches of Netzelmann[2].

For simplicity, we can imagine the films are ensembles of identical interacting ferromagnetic particles. The shape of such particle is ellipsoid of rotation. According Netzelmann method the demagnetization energy is sum demagnetization energy of particles and demagnetization energy of ensembles as a whole (1) [2].

$$\mathrm{F_D} = \frac{1}{2}x\vec{\mathrm{M}}\overleftrightarrow{\mathrm{N}}_{\mathrm{e}}\vec{\mathrm{M}} + \frac{1}{2}(1-x)\vec{\mathrm{M}}\overleftrightarrow{\mathrm{N}}_{\mathrm{p}}\vec{\mathrm{M}} \tag{1}$$

There x — the volume concentration, $\vec{\mathrm{M}}$ — the magnetization, $\overleftrightarrow{\mathrm{N}}_{\mathrm{e}}$ — demagnetization tensor for the film (ensemble), $\overleftrightarrow{\mathrm{N}}_{\mathrm{p}}$ — demagnetization tensor for the effective particle.

If the coordinates axes coincide witch the ellipsoid axes we can write the demagnetization tensor for the ellipsoid particle [3]:

$$\overleftrightarrow{N} = \begin{pmatrix} N_a & 0 & 0 \\ 0 & N_b & 0 \\ 0 & 0 & N_b \end{pmatrix} \tag{2}$$

Results of comparisons relation resonance magnetic field and volume concentration for experimental data [1] witch modelling the Netzelmann method [2] were insufficient. We had added change of the effective particle shape to the model. We had got better results. The formation of columnar structures was modelled by stretching the shape of particles. Changing of the shape of the metal particles was shown by AFM [1].

Fig.1 show approximate curve view of the demagnetization factor $\mathrm{N_a}$ for different concentration in cause of formation columnar structures. The model works for concentration more 0.3 and less concentration 0.5. For concentration less 0.3 we can't say about ferromagnetic interaction we obtain superparamagnetic state. For metal concentration more 0.5 we have case formation metal matrix witch dielectric particles. We can consider slowly changing effective particles.

We compared angular theoretical dependence magnetic resonance field witch experimental data. The investigation films have composition $(\text{Co-Fe-Zr})_x(\text{CaF}_2)_y$, $(\text{Co-Fe-Zr})_x(\text{Al}_2\text{O}_3)_y$, $(\text{Co-Ta-Nb})_x(\text{SiO}_2)_y$, $0.3<x<0.62$, $3<y<12$. The ion-beam sputtering method are used for preparation the films. The materials of substrate were polycrystalline glass and polyethylene (PET). The films were investigated by X-ray and atomic force microscopy (AFM) [1]. According experimental data the model was corrected.

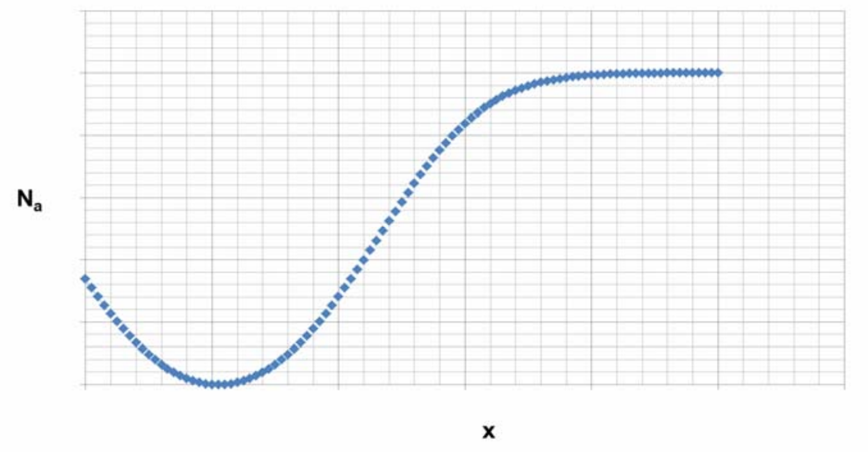

Fig.1. The dependence view of demagnetization factor N_a witch volume concentration.

This work was supported by RFBR (grant 13-02-01401).

References

[1] L.N. Kotov, V.K. Turkov, VS Vlasov, et. al. Nanomaterialy I Nanostructury 21 vek, **4**, 27 (2011).
[2] Netzelmann U., J. Appl. Phys., **68**, 1800 (1990).
[3] Gurevitch A.G., Melkov G.A. Magnitnye kolebaniya I volny. Fizmatlit, Moscow, 1994, 32 p.

^{63,65}Cu NMR/NQR study on the geometric frustrated multiferroic CuCrO$_2$

A. Smolnikov[1], V. Ogloblichev[1,2,3], A. Sadykov[1], A. Yakubovsky[3,4], S. Verkhovskii[1], S. Barilo[5]

[1]Institute of Metal Physics, UD RAS, Ekaterinburg 620990, Russia
[2]Ames Laboratory, USDOE and Department of Physics and Astronomy, Iowa State University, Ames, Iowa 50011, USA
[3]Department of Physics, Faculty of Science, Hokkaido University, Sapporo 060-0810, Japan
[4]Russian Research Centre, "Kurchatov Institute", Moscow, 123182, Russia
[5]Institute of Solid State and Semiconductor Physics, Minsk 220072, Belarus

e-mail: smolnikov@imp.uran.ru

Physical properties of the system with the triangular antiferromagnetic lattice (TLA) CuCrO$_2$, have been intensively studied recently both experimentally and theoretically. The problem of installation of an antiferromagnetic order in TLA leads to the strong geometrical spin frustration revealing some interesting properties.

Magnetic ground state of CuCrO2 was discovered by neutron powder diffraction study and is characterized by incommensurate ”out-of-plane” spin structure with the propagation vector Q = (q, q,0) (q = 0.329). [1-4]

We present the results of the ^{63,65}Cu NMR/NQR observation in paramagnetic and ordered magnetic states of a single crystal CuCrO$_2$ with a triangular lattice consisting of Cr atoms. ^{63,65}Cu NMR/NQR spectra were measured in a wide temperatures range T = (4.2 − 300) K and magnetic fields H = (0 − 94) kOe directed along the *a* and *c*-axis of the crystal. The electric field gradient (EFG) tensor and magnetic shift tensor ($K_{ab,c}$) components were obtained.

The temperature dependences of $K_{ab}(H||ab)$, $K_c(H||c)$ are well described by the Curie-Weiss law for paramagnetic state resembling the magnetic susceptibility ($\chi_{ab,c}$) [5] behavior. The hyperfine field at copper sites $H_{loc,ab,c} = 33$ kOe/μ_B has been determined using the $K_{ab,c}$ vs $\chi_{ab,c}$ diagrams. The principle axis of EFG direction is aligned with the c-axis. The quadrupole frequency $^{63}\nu_Q = 27.0(4)$ MHz and the parameter of asymmetry η are equal to 0.

Below the critical temperature $T_N = 24.2(3)$ K, the NMR line suddenly broadens and splits characterizing the magnetic phase transition with developing the long-range magnetic order (fig.1).

A dashed line is the result of modeling spectra ^{63,65}Cu. In constructing the theoretical line we consided the contribution both the dipole field $h_{loc,dip}$ produced by magnetic moments of the Cr^{3+} ions and hyperfine field $h_{loc,hf}$ generated by the spin polarization transfer from six nearest magnetic neighbors. The configuration of the magnetic moments was taken according to the model described above. Well agreement of the theoretical and the experimental spectrum occurs at ferromagnetic ordering in the neighboring planes of chromium ions with $|h_{loc,hf}| = 1.35(5)$ kOe, $\mu_{eff}(\mathrm{Cr}) = 2.6(3)\ \mu_B$. It should be noted that the description of the experimental spectrum H||c includes two lines that conform to isotopes ^{63,65}Cu. In the case of H||a we used two lines for each isotope. The difference in number of line is explained by appearing multidomain magnetic structure in the sample.

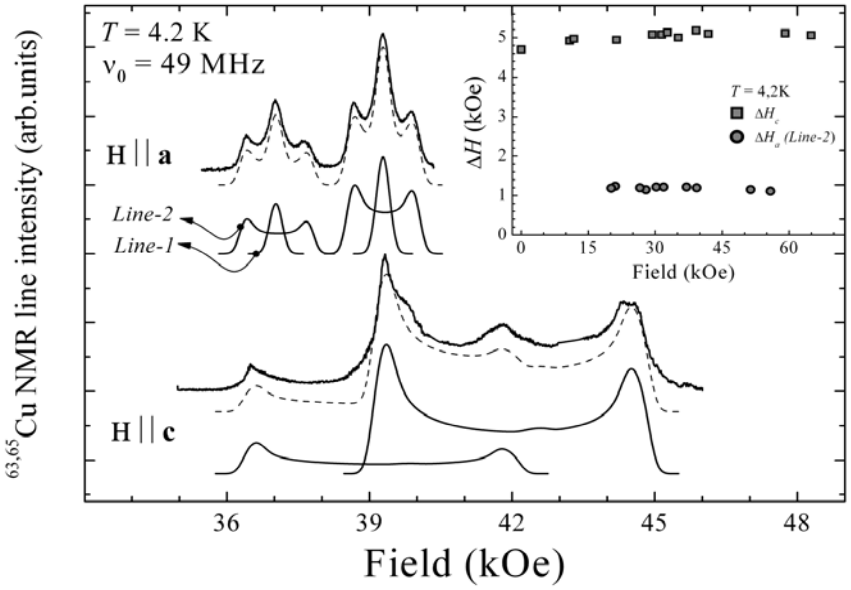

Fig.1. ^{63,65}Cu NMR spectra measured on a single crystal CuCrO$_2$ in a magnetic field H || *c* and H || *a* at the $T = 4.2$ K, $\nu_0 = 49$ MHz into magnetic ordered stats, and result of modeling The inset shows the dependence of splits $\Delta H_{c,a}$ at the magnetic field.

The split ΔH_a and ΔH_c (inset fig.1) remains constant over a wide range of magnetic fields, which indicates that the magnetic structure is not changed.

The parameters of EFG tensor in ordered magnetic states were determined from the ^{63,65}Cu NQR spectra. They were close to the values in the paramagnetic phase.

Acknowledgements

This work was supported in part by the Russian Foundation for Basic Research № 12-02-31814 and № 14-02-00203), by Russian Academy of Sciences Ural Branch (№ 14-2-НП-199 and № 12-У-2-1025)

Reference

[1] M. Poienar, F. Damay, C. Martin et al., Phys. Rev. B 79, 014412 (2009).
[2] M. Poienar, F. Damay, C. Martin et al., Phys. Rev. B 81, 104411 (2010).
[3] M Frontzek, O Zaharko, G Ehlers et al., J. Phys.: Condens. Matter 24, 016004 (2012).
[4] M. Soda, K. Kimura, T. Kimura et al Phys. Rev. B 81, 100406 (2010).
[5] K. Kimura, H. Nakamura, K. Ohgushi et al., Phys. Rev. B 78, 140401 (2008).

The features of the magnetic properties of low-dimensional isostructural cuprates $NaCu_2O_2$ and $LiCu_2O_2$ investigated by NMR

A.F. Sadykov[1], Y.V. Piskunov[1], A.P. Gerashenko[1], V.V. Ogloblichev[1], A.G. Smolnikov[1], A.A. Bush[2]

[1]Institute of Metal Physics, UB RAS, 620041, S. Kovalevskaya Str. 18, Ekaterinburg, Russia

[2]Moscow State Technical University of Radio Engineering, Electronics, and Automation, 119454, pr. Vernadskogo 78, Moscow, Russia

e-mail: Sadykov@imp.uran.ru

Great attention is paid to the study of spin chains with strong intrachain frustration. Magnetic ordering, which can be observed at low temperatures depends on the magnitude of the spin-spin and spin-phonon interactions, both within and between the chains.

The $NaCu_2O_2$ (NCO) and $LiCu_2O_2$ (LCO) are isostructural quasi-one-dimensional magnetic materials with competing ferro- and antiferromagnetic exchange interactions between the nearest-neighbor and next-nearest-neighbor spins in the CuO_2 chain, respectively.

Below the critical temperature T_N = 12 K (T_N= 23 K), the NCO (LCO) compound with pronounced spin chains undergoes a transition to an ordered state characterized by the incommensurate spiral magnetic structure [1-4]. In the case of LCO transition is accompanied by the spontaneous appearance of the macroscopic electric polarization **P** [5], while the co-existence magnetic and electric order in NCO has not yet been found [6]. The length and direction of the vector **P** depend on the external magnetic field. There are several different theories explaining the appearance (or absence) of magnetoelectricity in compounds with the spiral magnetic structure [7–9]. For this reason, for the experimental test of existing theoretical models of magnetoelectricity, it is important to know the real spatial orientation of the planes of spin spirals in the crystal and its evolution depending on the magnitude and direction of the external magnetic field.

The crystal structure of orthorhombic NCO (LCO) can be represented as $–Cu^+–O–Cu^{2+}–O–Na(Li)–$ and $–Na(Li)–O–Cu^{2+}–O–$ layers stacking up along the c axis. The unit cells of NCO and LCO are shown in fig.1. The crystals in equal proportions contain copper ions in a magnetic (Cu^{2+}) and nonmagnetic (Cu^+) states located in the crystallographically nonequivalent positions. Cu^{2+} ions are located in the planes (m=I, II, III, IV).

We present the results NMR/NQR studies of magnetic order in the NCO and LCO. $^{63,65}Cu$ (I = 3/2) and ^{23}Na, ^{7}Li (I = 3/2) NMR and NQR measurements have been performed on the single crystal NCO (LCO) at temperatures T = 290 K, T = 7 K (T = 10 K) and T = 4.2 K, i.e. above and below the critical temperature of the magnetic ordering. NMR spectra of two isotopes of copper $^{63,65}Cu$ located in non-magnetic Cu^+ layers were recorded at the external magnetic field H_0 = 94 kOe for orientation of the single crystal $\mathbf{H}_0 \parallel$ **a**, **b**, **c**. We were not able to observe the signal from the magnetic copper ions Cu^{2+}. The main reason for the impossibility of the detection of the NMR signal is a very high rate of the spin–spin relaxation of the nuclear spin. At $T > T_N$ NMR spectrum for each isotope of copper is a set of three narrow lines ($\Delta f_{1/2}$ <100 kHz), and the NQR spectrum is two narrow lines, and sodium spectrum is three narrow lines, and lithium spectrum is one narrow line. Below the T_N, the spectra of all nuclei have the form characteristic of spiral magnetic structures incommensurate with the lattice. The analysis of the NMR/NQR spectra presented shown that they can be satisfactorily described by the assumption that each of the narrow lines observed above $T = T_N$ is split in two lines in the case of copper and sodium and in four peaks in the case of lithium.

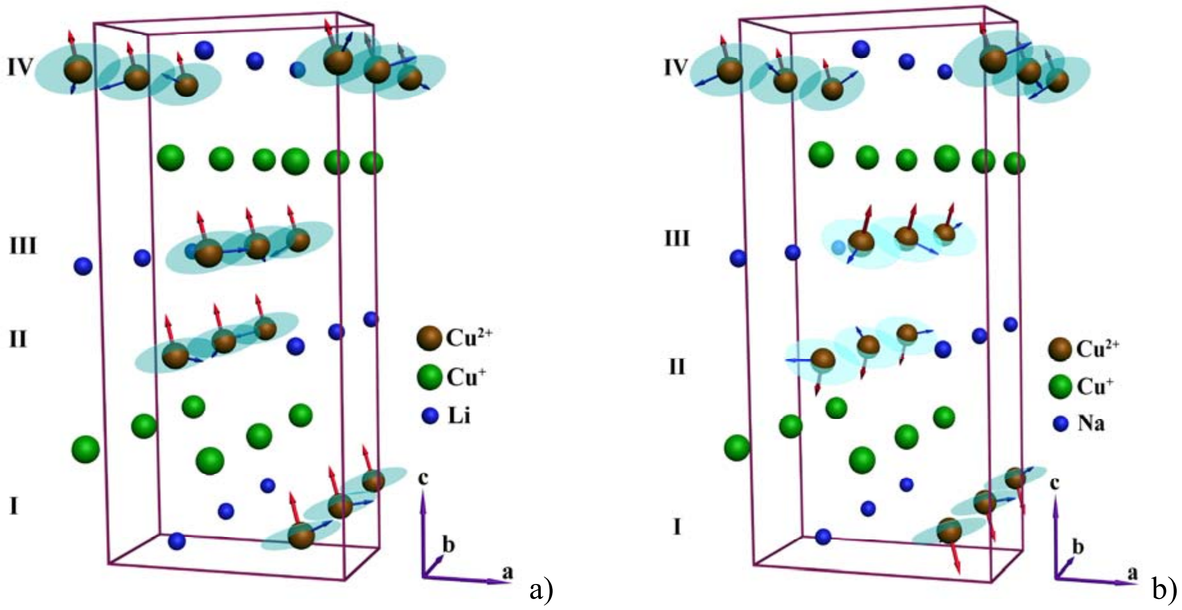

Fig.1. Ions Li^+, Na^+, Cu^+, and Cu^{2+} in the crystal lattices. Shows the spatial orientation of the planar spin spirals in the Cu^{2+}-O chains layers m = I, II, III, IV in zero external magnetic field and H_0 = 94 kOe directed along the crystal axis **c**: a) $LiCu_2O_2$, b) $NaCu_2O_2$.

In the case of the planar spiral, the spatial orientation of the magnetic moment $\boldsymbol{\mu}_{m,i,j,k} = \mu \mathbf{e}_{m,i,j,k}$ of the Cu^{2+} ion with the radius vector $\mathbf{r}_{m,i,j,k}$ is determined by the unit vector $\mathbf{e}_{m,i,j,k} = (e^x_{m,i,j,k}, e^y_{m,i,j,k}, e^z_{m,i,j,k})$ whose components are given by the expressions:

$$e^x_{m,i,j,k} = -\cos\psi_m \cos\theta_m \sin\phi_{m,i,j,k} - \sin\psi_m \cos\phi_{m,i,j,k} \qquad (1)$$

$$e^y_{m,i,j,k} = -\sin\psi_m \cos\theta_m \sin\phi_{m,i,j,k} + \cos\psi_m \cos\phi_{m,i,j,k} \qquad (2)$$

$$e^z_{m,i,j,k} = \sin\theta_m \sin\phi_{m,i,j,k} \qquad (3)$$

The local magnetic moment $\mathbf{h}_{loc}$ (**R**) created at the point **R**(**R** is the position of Cu^+, Na^+ or Li^+) by the magnetic moments of Cu^{2+} ions with the radius vectors $\mathbf{r}_i$ is determined by the long range dipole field H_{dip} and by transferred "contact" hyperfine field H_{hf}:

$$h_{loc}(R) = H_{dip}(R) + H_{hf}(R) = \sum\nolimits_i \left[3\frac{(r_i - R)(\mu_i \cdot (r_i - R))}{|r_i - R|^5} - \frac{\mu_i}{|r_i - R|^3} \right] + \sum\nolimits_i A_{hf}\mu_i \qquad (4)$$

Here, $\boldsymbol{\mu}_i$ is the magnetic moment at the i-th site of the Cu^{2+} ion and A_{hf} is the hyperfine coupling constant. The hyperfine field H_{hf} in Eq. (4) was calculated by summing over four Cu^{2+} magnetic ions nearest to Cu^+. The contribution from neighboring Cu^{2+} ions located inside a sphere with a radius of 40 Å was taken into account when calculating the dipole field H_{dip}. To describe the splitting of the NMR spectra of ^{23}Na (^{7}Li) below $T = T_N$, it is sufficient to take into account only the contribution H_{dip} to the local field $\mathbf{h}_{loc}$ (**R**) with the magnetic moment of the Cu^{2+} ion $\mu_i \approx 0.5 - 0.6\,\mu_B$ ($\mu_i \approx 0.8 - 1.0\,\mu_B$). The amplitude of the local hyperfine field induced at Cu^+ sites by the magnetic moment of one neighboring Cu^{2+} ion, the angles θ_1, θ_2, ψ_1, and ψ_2 specifying the spatial orientations of the spin spirals in the Cu^{2+} chains, and the differences $\Delta\varphi_{21} = \varphi_{II} - \varphi_I$, $\Delta\varphi_{32} = \varphi_{III} - \varphi_{II}$, and $\Delta\varphi_{43} = \varphi_{IV} - \varphi_{III}$ were used as varying parameters when analyzing the spectra of $^{63,\ 65}$Cu. The magnitude of the effective magnetic moment μ on the Cu^{2+} ion in the magnetically ordered phase was varied when simulating the spectra of sodium and lithium.

To calculate the shape of the NMR curves, we used our specially developed simulation program involving the numerical calculation of the energy levels and the transition probabilities with the diagonalization of the matrix elements of the total Hamiltonian (quadrupole H_Q and Zeeman H_M) of the nuclear system taking into account the spatial orientation of the magnetic moments of copper described above.

As an example, the fig.2 shows ^{63,65}Cu NMR experimental and simulation spectra in the magnetically ordered phase of $LiCu_2O_2$. The spatial orientation of the planar spin spirals in the Cu^{2+}-O chains layers m = I, II, III, IV in zero external magnetic field and magnetic field directed along the axis of the crystal **c** is shown in fig.1.

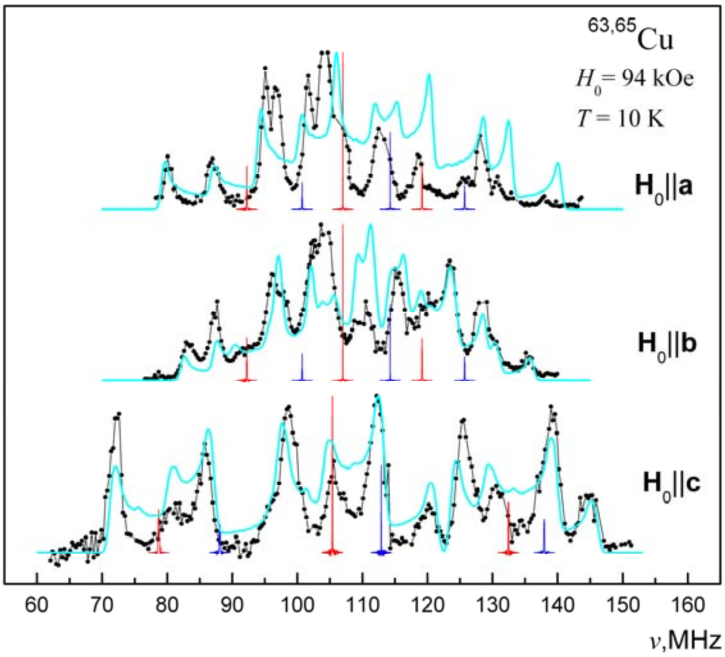

Fig.2. ^{63,65}Cu NMR spectra in the magnetically ordered phase of $LiCu_2O_2$ single crystal at $T = 10$ K for the external magnetic field directions $\mathbf{H}_0$ || **a**, **b**, **c** (•). The narrow spectral peaks conform to ^{63,65}Cu NMR spectra at room temperature. Solid line represents the spectrum simulated in the model of planar helix.

The work was supported by the Ural Division, Russian Academy of Sciences (project no. 14-2-NP-199)

References

[1] T. Masuda, A. Zheludev, A. Bush, et. al., Phys. Rev. Lett. **92**, 177201 (2004).

[2] A. A. Gippius, E. N. Morozova, A. S. Moskvin, et. al., Phys. Rev. B **70,** 020406 (2004).

[3] L. Capogna, M. Mayr, P. Horsch et al., Phys. Rev. B **71**, 140402(R) (2005).

[4] S.-L. Drechsler, J. Richter, A. A. Gippius et al., Europhys. Lett. **73**, 83 (2006).

[5] S. Park, Y. J. Choi, C. L. Zhang, and S-W. Cheong, Phys. Rev. Lett. **98**, 057601 (2007).

[6] Ph. Leininger, M. Rahlenbeck, M. Raichle et al., Phys. Rev. B **81**, 085111 (2010).

[7] H. Katsura, N. Nagaosa, A. V. Balatsky, Phys. Rev. Lett. **95**, 057205 (2005).

[8] I. A. Sergienko and E. Dagotto, Phys. Rev. B **73,** 094434 (2006).

[9] A. S. Moskvin, Y. D. Panov, S.-L. Drechsler, Phys. Rev. B **79**, 104112 (2009); A.S. Moskvin, S.-L. Drechsler, Eur. Phys. J. B **71**, 331 (2009); Yu. D. Panov, A. S. Moskvin, N. S. Fedorova, S.-L. Drechsler, Ferroelectrics **442**, 27 (2013).

Magnetic resonance (NMR, ESR) in the study of the formation mechanism of catalysts based on nickel phosphine complexes and boron trifluoride etherate in the lower alkenes dimerization

Yu.Yu. Titova, L.B. Belykh, F.K. Schmidt

Irkutsk State University, Institute of Oil and Coal-Chemical Synthesis, 664003, Irkutsk,
K. Marks st., 1, Russia.

e-mail: ytitova60@gmail.com

Introduction

Catalysis of lower alkenes (C_2-C_4) dimerization by nickel complexes is the subject of great number of research for over four decades. The processes of low molecular oligomerization of α-alkenes and vinyl aromatic hydrocarbons allow to obtain cheap tonnage petrochemical products (ethylene, propylene, styrene) turning into monomers for synthetic polymers, intermediates for fine chemicals, detergents and floating agents. These reactions are the basis of the industrial production of propylene oligomers. One of such processes is "Dimersol" that is producing of propylene oligomers, which are high octane gasoline, in the presence of catalytic systems based on complexes of nickel and organoaluminum compounds (NiX_2-AlR_nX_{3-n}).

Known nickel-containing catalytic systems for dimerization and oligomerization of lower alkenes can be divided into the following five groups according to the oxidation state of the transition metal in the precursor and the nature of the cocatalyst [1, 2]: (1) nickel(II) complexes with the general formula L_nNiX_2 (X = anionic ligand; L = donor ligand, such as phosphine, phosphite, or diimine; n = 1 or 2) in combination with aluminum alkyl halides; (2) organic or hydrido complexes of Ni(II) activated by Lewis acids, including aluminum alkyl halides; (3) Ni(0) complexes in combination with Brönsted acids; (4) Ni(0) and Ni(I) complexes in combination with Lewis acids; (5) Ni(II) complexes, e.g., $Ni(PPh_3)_2Cl_2$ dissolved in an ionic liquid consisting of aluminum chloride and a weak Lewis base such as triphenylbismuth or N-methylpyrrole.

The conceptions about decisive contribution to the catalytic process of hydride complexes Ni (II), formed by the interaction of nickel (II) with an organoaluminum compound are the most experimentally validated. Hydride mechanism of conversion of lower alkenes is often postulated (without any experimental proving) and when a Lewis acid without hydrogen is used as a co-catalyst.

Here, we report the study of the interaction mechanism between Ni(0) and Ni(I) phosphine complexes with the general formulas $Ni(PPh_3)_2(C_2H_4)$ and $Ni(PPh_3)_nCl$ (n = 2, 3) in combination with Lewis acids by magnetic resonance methods (NMR and ESR). The establishment of the basic steps leading to the formation of active nickel complexes for dimerization of lower alkenes is also presented.

Experimental results and discussion

Although various nickel containing systems have been investigated for half a century, the problem of formation of active complexes and elucidating their nature (composition and structure) in the catalytic systems and in particular reactions is still challenging researchers. A specific feature of the catalytic systems examined is that they consist of many components. There are examples of the formation of catalysts containing five components or more. These systems are distinctive in that a multiplicity of reactions occurs at the active catalyst formation stage and in that they are multiphase ones and are sensitive to various impurities. In addition, the turnover frequency (TOF), turnover number (TON), and selectivity in the processes catalyzed by these systems depend significantly on the substrate, on the proportions of components in the system, on the order of their interactions, on process parameters (primarily on temperature), and on some other factors, for example, the storage time of the toluene solution of BF_3 OEt_2.

For BF_3 OEt_2 that was stored in a Schlenk flask, the following changes were observed in the ^{11}B, ^{19}F, and ^1H NMR spectra. Initially, the ^1H NMR spectrum shows resonance signals from diethyl ether ($\delta = 1.15$ ppm, t, $^2J = 7.3$, CH_3; $\delta = 3.85$ ppm, q, $^2J = 7.3$, CH_2), which forms an adduct with BF_3 (BF_3 OEt_2); in the course of time, a broad signal appears and grows. The ^{11}B and ^{19}F NMR spectra showed, along with the major signals of BF_3 OEt_2 at 0 and – 76.6 ppm, broad singlets at $\delta = -0.9$ ppm (^{11}B NMR) and $\delta = -70.8$ ppm (^{19}F NMR). These data indicate BF_3 OEt_2 hydrolysis under the action of water that is present in the solvent and penetrates into the solution from the environment through the ground glass joints, followed by BF_3 H_2O disproportionation yielding HBF_4 and other boron and fluorine containing acids [3]. Thus, the higher activity of the catalytic system prepared using a stored BF_3 OEt_2 solution is due to the formation of Brönsted acids. To minimize the influence of Brönsted acids the interaction between Ni complexes and BF_3 OEt_2 was performed with freshly distilled BF_3 OEt_2.

The reaction between the $Ni(PPh_3)_2(C_2H_4)$ and BF_3 OEt_2 completed in 1 – 1.5 minutes at room temperature. As a BF_3 OEt_2 solution in toluene-d^8 is added to a $Ni(PPh_3)_2(C_2H_4)$ solution in toluene-d^8 in an ethylene atmosphere, the color of the mixture changes from yellow to dark brown. The ^1H NMR spectra of the $Ni(PPh_3)_2(C_2H_4) - BF_3$ OEt_2 reaction system recorded during the reaction showed, along with signals from the aromatic protons of the coordinated PPh_3 ligands ($\delta = 7.23 - 7.69$ ppm) and from methyl groups ($\delta = 1.14$ ppm) and methylene groups ($\delta = 3.63$ ppm) of diethyl ether, signals from intermediate nickel complexes, namely, complex multiplets at 0.39 – 0.93 and 2.85 – 3.39 ppm and signals in the 6.5 – 7.0 ppm range. The appearance of the complex multiplets centered at 0.66 and 3.12 ppm was accompanied by a weakening of the resonance signal from coordinated ethylene ($\delta = 2.66$ ppm). An upfield shift of the resonance signals from methylene groups ($\delta = 0.6$ ppm) is typical of organometallic derivatives whose methylene groups are bonded to boron or aluminum atoms. In particular, the signals of the CH_2 group in $AlEt_3$ are observed at 0.45 ppm (q, 2H, $^1J = 8.24$ Hz) and those of CH_3 occur at 1.22 ppm (t, 3H, $^1J = 8.24$ Hz). In organoboron derivatives, such as $[PhCH_2CH_2BF_3]^-K^+$, as distinct from organoaluminum derivatives, the methylene group at the boron atom shows itself in the ^1H NMR spectrum as a complex multiplet in the 0.28 – 0.40 ppm range. The second CH_2 group is characterized by a multiplet at $\delta = 2.42 - 2.48$ ppm [3]. This is due to the fact that the ^{11}B nuclei have a spin of 3/2 and a hyperfine structure appears as a result of proton coupling with the nuclei of both boron and fluorine. The spin–spin coupling constants are fairly large; for example, for HBF_2 they are $^1J_{^{11}B\text{-}H} = 211$ Hz and $^2J_{F\text{-}H} = 108$ Hz (q/t) [4].

The multiplets observed in the ^1H NMR spectrum of $Ni(PPh_3)_2(C_2H_4) - 5\ BF_3$ OEt_2 reaction system include quartets with spin–spin coupling constants on the order of 65 Hz ($\delta = 0.66$ ppm) and 60 Hz ($\delta = 3.12$ ppm). The location of the region of multiplet signals, the large spin–spin coupling constants, and the literature data suggest that the resonance signals with multiplet centers at 0.66 and 3.13 ppm are due to the $Ni^+ - CH_2 - CH_2 -$ or $Ni(F) - CH_2 - CH_2 - BF_2$ fragments. This intermediate can result from attack of boron trifluoride on coordinated ethylene in the $Ni(PPh_3)_2(C_2H_4)$ complex. After the completion of the reaction, the multiplets in the ^1H NMR spectrum disappear and, along with new signals from aromatic protons in the 7.20 – 7.25 ppm range (m), a broad weak signal is observed at $\delta = -12.6$ ppm, which is due to hydrides.

The ^{31}P NMR spectrum of the $Ni(PPh_3)_2(C_2H_4)$ – 5 BF_3 OEt_2 reaction system after the end of the reaction shows no signal from the initial complex, $Ni(PPh_3)_2(C_2H_4)$ ($\delta_P = 38$ ppm, s). The major signal from the $Ni(PPh_3)_2(C_2H_4)$ conversion product is a singlet at 26 ppm. Its position corresponds to coordinated PPh_3 ligands ($\Delta\delta = 32$ ppm). The absence of a hyperfine structure indicates the equivalence of the phosphine ligands in the coordination sphere of nickel. In addition, the ^{31}P NMR spectrum exhibits resonance signals at $\delta_P = 21$ ppm (d, J = 24 Hz) and weak signals at $\delta_P = 44$ and 155 ppm. Additional experiments demonstrated that the resonance signal at $\delta_P = 21$ ppm are due to the BF_3 OEt_2 adduct. The appearance of the resonance signals in the low field is rather surprising, since signals from phosphorus nuclei in free or coordinate phosphites ($P(OR)_3$), in phosphines with electron accepting substituents, e.g., $PR_{3-n}X_n$ (X = Hal) [5], and in coordinated PPh_2OH ligands occur in this region.

The formation of the anion as a result of the interaction between the components of the $Ni(PPh_3)_2(C_2H_4)$ – 5 BF_3 OEt_2 catalytic system is confirmed by ^{19}F NMR data. The ^{19}F NMR spectrum of the reaction system after the completion of the process showed, along with a signal from BF_3 OEt_2 ($\delta = 76$ ppm), resonance signals at 59, 64, and – 71 ppm.

The signals at 64 and – 71 ppm are due to BF_3 OEt_2 and the BF_4^- -anion, respectively. The formation of the anion indicates the occurrence of a redox reaction between the components of the catalytic system and the formation of cationic nickel complexes stabilized by phosphine ligands. Thus, BF_3 OEt_2 acts as a Lewis acid in the formation of the nickel catalysts, binding part of the triphenylphosphine, and as an oxidizer.

Additionally in order to verify hypotheses concerning the nature of active complexes in the $Ni(PPh_3)_2(C_2H_4)$ – BF_3 OEt_2 system by EPR spectroscopy, we analyzed samples taken from the system during the conversion of ethylene. In the EPR spectrum of the reaction solution a resonance signal appears only at the reaction beginning (5 s after the beginning of the reaction) and after the addition of triethyl phosphate ($g_{||}(z) = 2.013$, $g_{\perp}(x) = 2.2005$, $g_{\perp}(y) = 2.186$) (fig.1). According to literature data [6], the parameters of this signal are the same as in the EPR spectrum of the $[Ni(PPh_3)_2(P(OEt)_3)_2]BF_4$ complex. The fact that the EPR signal appears after the addition of $P(OEt)_3$ can be explained by the Ni(I) complexes being in the dimeric state [4] or by their formation via a redox reaction between $P(OEt)_3$ and Ni(II), since triethyl phosphite is a strong reductant. Note that, in the EPR spectra of subsequent

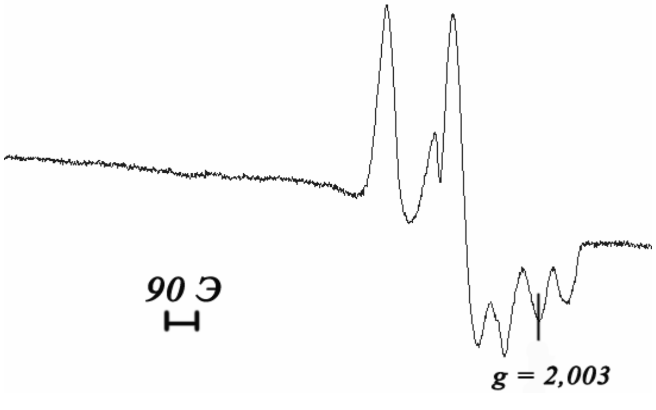

Fig.1. EPR spectrum of the sample obtained with the $Ni(PPh_3)_2(C_2H_4)$ – 5BF_3 OEt_2 system in the course of ethylene conversion after the introduction of triethyl phosphite at 77 K (sample taken at 5 s after the beginning of the reaction).

reaction samples, resonance signals were missing even after the introduction of $P(OEt)_3$, although ethylene oligomerization lasted 90 min and the TON of the reaction in this period was 300 (mol C_2H_4/(mol Ni)).

Conclusion

The experimental data obtained in this study and information available from the literature on the reactions occurring in the system considered suggest the following reaction scheme, which accounts for the role of the substrate in the formation of catalytically active complexes:

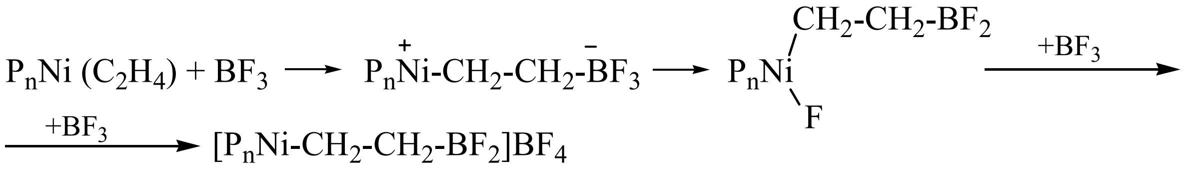

$$P_nNi\,(C_2H_4) + BF_3 \longrightarrow P_n\overset{+}{N}i\text{-}CH_2\text{-}CH_2\text{-}\overset{-}{B}F_3 \longrightarrow P_n\underset{\diagdown F}{\overset{/CH_2\text{-}CH_2\text{-}BF_2}{Ni}} \xrightarrow{+BF_3} \xrightarrow{+BF_3} [P_nNi\text{-}CH_2\text{-}CH_2\text{-}BF_2]BF_4$$

Acknowledgements

This work is supported by Russian Foundation for Basic Research (№ 14-03-32037 mol_a). Authors gratefully acknowledge Irkutsk Supercomputer Center of the Russian Academy of Sciences http://hpc.icc.ru.

References

[1] Shmidt, F.K., Kinet. Catal., 2010, V. 51, № 2, p. 235-243.

[2] Gibson V. Chem. Rev., 2007, Vol. 103, p. 283-315.

[3] Oliveira, R.A., Silva, R.O., Molander, G.A., and Menezes, P.H., Magn. Reson. Chem., 2009, vol. 47, p. 873.

[4] Farrar, T.C. and Covle, T.D., J. Chem. Phys., 1964, vol. 41, no. 9, p. 2612-2613.

[5] Emsleey, J.W., Feeney, J., and Sutcliffe, L.H., High Resolution Nuclear Matgnetic Resonance Spectroscopy, New York: Pergamon, 1969, vol. 2.

[6] Saraev, V.V. and Shmidt, F.K., EPR metallokompleksnykh katalizatorov (EPR of Metal Complex Catalysts), Irkutsk: Irkutsk. Gos. Univ., 1985.

The study of the conformation and dynamics derivative of the new quaternary phosphonium salts by NMR spectroscopy

O.V. Aganova, L.F. Galiullina, A.V. Aganov, V.V. Klochkov

Kazan (Volga Region) Federal University, 420008, 18 Kremlevskaya st., Kazan, RF

email: aganova9@gmail.com

Organophosphorus compounds are widely used in medical chemistry. Among them quaternary phosphonium salts, namely vitamin B_6 (pyridoxine), are of special interest. It participates in over a hundred enzymatic reactions involved in biosynthesis, metabolism, and regulatory functions in living organisms.

Design of new biologically active substances and drugs with desired properties is impossible without the information about three-dimensional structure and dynamics of the compounds in solution. From this point of view, the method of nuclear magnetic resonance (NMR) is one of the most powerful tools for such studies. It allows one to define the spatial structure of the compounds, to investigate the dynamic processes from a qualitative point of view and, finally, to quantify the energy parameters of conformational transitions.

This work represents the study of the conformation and dynamics of some new quaternary phosphonium salts derivatives containing pyridine fragment. ^{1}H (500.13 MHz), ^{31}P (202 MHz), ^{13}C (125.758 MHz) NMR spectra of the investigated compounds 5,6-Bis[triphenylphosphonio(methyl)]-2,2,8-trimethyl-4H-[1,3]dioxino[4,5-c]pyridine dichloride (compound **I,** fig.1) and 5,6-Bis[triphenylphosphonio(methyl)]-2,8-dimethyl-4H-[1,3]dioxino[4,5-c]pyridine dichloride (compound **II**, fig.1) at different temperatures were recorded using Bruker “Avance -500 II TM” spectrometer.

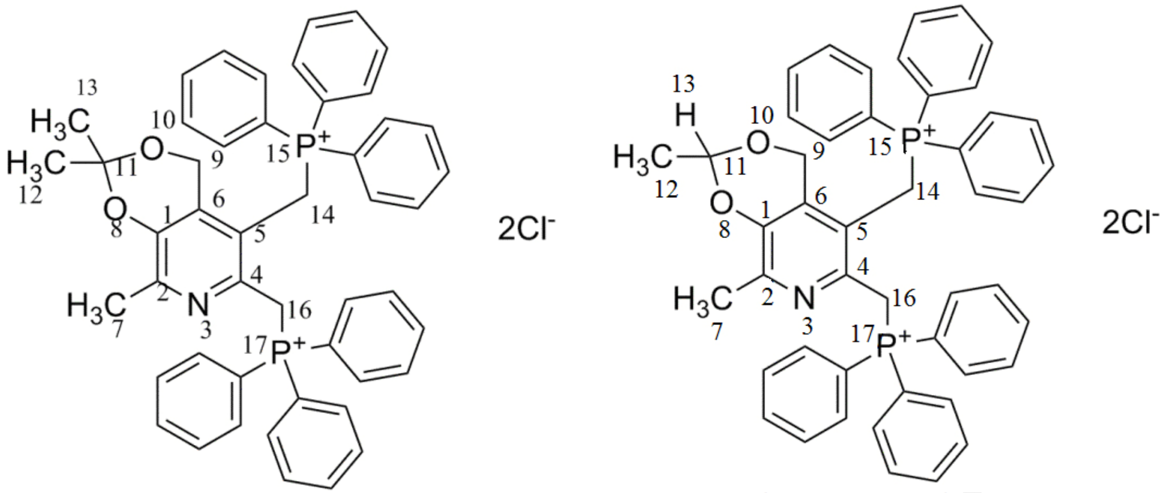

a) Compound I

b) Compound II

Fig.1. The chemical structure of the investigated compounds

Then lineshape analysis of the signals broadened by chemical exchange was carried out by WinDNMR-Pro 7.1.14 program. The activation parameters were calculated using the Eyring equation (values are shown below).

	Functional groups	ΔG_0, kJ/mol	$\Delta H^{\neq}$, kJ/mol	$\Delta G^{\neq}$, kJ/mol (T_c=243 K)
Compound **I**	C$\underline{H}_3$-12,13	-	38.0±0.5	37.9
	C$\underline{H}_2$-14,16	-	38.2±0.5	37.5
Compound **II**	C$\underline{H}_2$-14	1.86	37.4±0.5	37.1
	C$\underline{H}_2$-14’	1.86	37.4±0.5	37.1
	C$\underline{H}_2$-16	1.86	38.0±0.5	36.8
	C$\underline{H}_2$-16’	1.86	37.4±0.5	37.1

Conformational exchange between two forms obtained by simultaneous symmetrical rotation of P+-$(Ph)_3$ groups around the C5-C14 and C4-C16 bonds is observed for the studied compounds **I** and **II**. Two most stable conformations of compounds **I** have almost the same energies and the similar population. The contents of two the most stable conformations of compounds **II** in solution are different. Energetically more favorable dominant form has the concentration about 75% in solution. The content of less energetically favorable minor form is approximately 25 % in solution.

Coexistence of spin crossover and magnetic ordering in the dendrimeric iron(III) complex

V.E. Vorobeva[1], N.E. Domracheva[1], A.V. Pyataev[2]

[1]Kazan E.K. Zavoisky Physical Technical Institute, Russian Academy of Science, 420029, Sibirsky tract, 10/7, Kazan, Russia

[2] Kazan Federal University, 420008, Kremlyovskaya St. 18, Kazan, Russia

e-mail: vvalerika@gmail.com

The motivation of this work is to create a novel multifunctional material, where the cooperative magnetic properties (ferro-, ferri-, or antiferromagnetism) will coexist with spin crossover. Iron ions possessing spin-crossover properties are suitable to prepare multifunctional magnetic materials since they represent one of the best examples of molecular bistability. The strategy proposed by us may open a way to design switching magnets in which the magnetic ordering of the system could be tuned, using the opportunity to induce the SCO phenomenon by applying the external stimuli such as light or pressure. However, this challenging goal requires first the preparation of such a material which is able to display the coexistence of spin crossover and magnetic ordering.

Until now, work in this direction was carried out in the following way. The material structures have been constructed through the self-assembly of two different magnetic sub-lattices of transition metal ions having distinct properties. Namely, spin crossover (SCO) metal complexes have been integrated into 1D, 2D or 3D magnetically ordered sub-lattice of the other metal complexes. Examples of coexistence of the spin crossover behavior with magnetic ordering are very few today [1].

We suggest another way to obtain such bi-functional system: embedded SCO iron(III) complex into the focal point (core) of dendrimer molecule. This bi-functional system will be prepared by only one type of metal complexes. It is known that dendritic molecules can self-assemble into ordered supramolecular structures [2]. So, it can be expected that the self-organization of dendrons will generate a magnetic ordering in a system as it has been in the case of dendrimerfunctionalized gold nanoparticles (NPs) showing ferromagnetism at room temperature [3].

The synthesized iron(III) bis[3,5-di(3,4,5-tris(tetradecyloxy) benzoyloxy)benzoyl-4-oxy-salicylidene-N'-ethyl-N-ethylene diamine]hexafluorophosphate complex was characterized by gel permeation chromatography, elemental analysis, FT-IR, NMR spectroscopy and MALDI-ToF-MS method. Based on these results has been proposed the schematic model of the complex given in fig.1. The compound is a monocationic bis(ligand) Fe(III) complex $[Fe(L)_2]^+PF_6^-$, where iron(III) ion has an octahedral geometry with N_4O_2 donor atoms formed by three atoms (ONN) of tridentate ligand (L). The liquid crystalline properties of the sample were studied by differential scanning calorimetry and optical polarizing microscopy.

EPR is a powerful technique for observing spin transition and studying spin dynamics in Fe^{3+} complexes. This method allows not only a confirmation of the existence of low-spin (LS) and high-spin (HS) fractions in the compound but also an investigation of their evolution with temperature. EPR spectra demonstrate the presence in the system of three types of iron(III) centers: two types of HS ions (I- type – $D = 0.421$ cm^{-1}, $E = 0.109$ cm^{-1}, $g = 2$, with strong low-symmetry crystal field and II- type – 0.02 cm$^{-1} < D < 0.03$ cm^{-1}, $E = 0$, $g = 2$ with weak distorted octahedral crystal field) and one of LS with $g_x = g_y = 2.21$, $g_z = 1.935$.

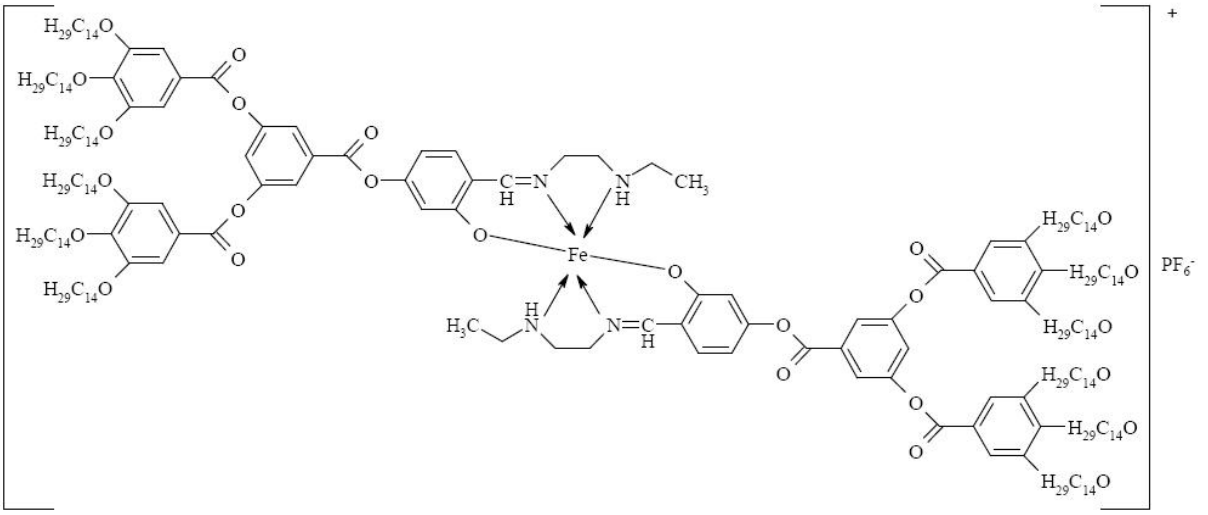

Fig.1. Schematic models of the compound.

It is important to note that the observation of distinct HS and LS EPR signals implies that the spin-state interconversion rates in the region of 4.2 – 300 K are slower relative to the X-band EPR time scale (ca. 10^{10} s^{-1}).

The temperature dependence of the EPR lines integrated intensity (*I*) is one of the sources of information about the spin transition process. The magnetic behavior of the compound reflected by the temperature dependencies of *I* and *I*×*T* product of the whole EPR spectrum is shown in fig.2. One can see that the temperature dependence of *I* has complicated, two-step behavior: it reaches the maximum at 10 K and then drops to a minimal value at about 70 K and further begins to grow (fig.2). Variation of *I*×*T* product from temperature shows that the complex undergoes a gradual spin transition (fig.2b), where the direct (4.2 – 300 K) and the inverse (300 – 4.2 K) thermal cycles practically coincide.

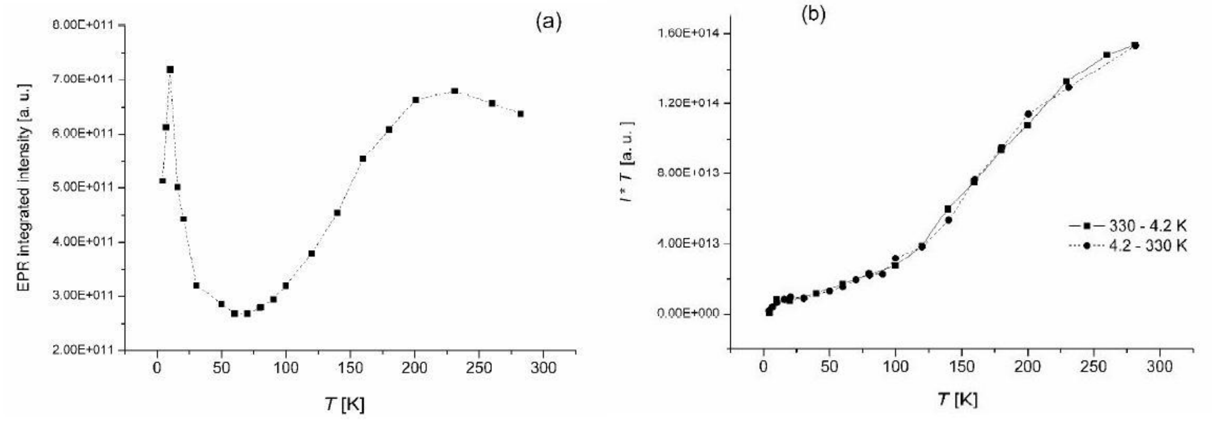

Fig.2. (a) The temperature dependence of the EPR lines integrated intensity of the whole EPR spectrum. (b) The *I* × T vs T plot, showing a stepwise behavior.

For understanding the origin of the observed anomaly in our compound the temperature dependencies of the EPR lines integrated intensity were examined for each type of Fe(III) centers separately. The analysis of the EPR signals for each type of iron centers was based on the procedure of the model spectrum fitting to the observed experimental one. To fit the EPR spectra we used the standard EasySpin-EPR spectrum simulation program. The parameters of the fit were the g- and D-tensor components, D-strain, the line shape and the widths of the individual components ΔH.

The EPR integrated intensities (*I*) for all three types of iron(III) centers demonstrate the maximum at $T_C = 10$ K in the first temperature interval of 4.2 – 70 K. The appearance of maximum on the curves shows that the LS-LS, LS-HS and HS-HS iron centers are coupled by antiferromagnetic exchange interactions. This conclusion is confirmed by Mössbauer spectroscopy data presented below.

The temperature dependence of *I* for HS centers of the I-type shows that the number of these centers monotonously decreases after 10 K. This fact means that HS centers of the I-type do not take part in spin transition.

The magnetic properties of the compound were characterized in details by Mössbauer spectroscopy. Spectrum recorded at 310 K (fig.3) consists of one broad doublet with parameters ($\delta_{Fe} = 0.35$ mm/s, $Q_S = 0.72$ mm/s), which correspond to the high-spin (HS) state of the Fe(III) ion in an octahedral environment.

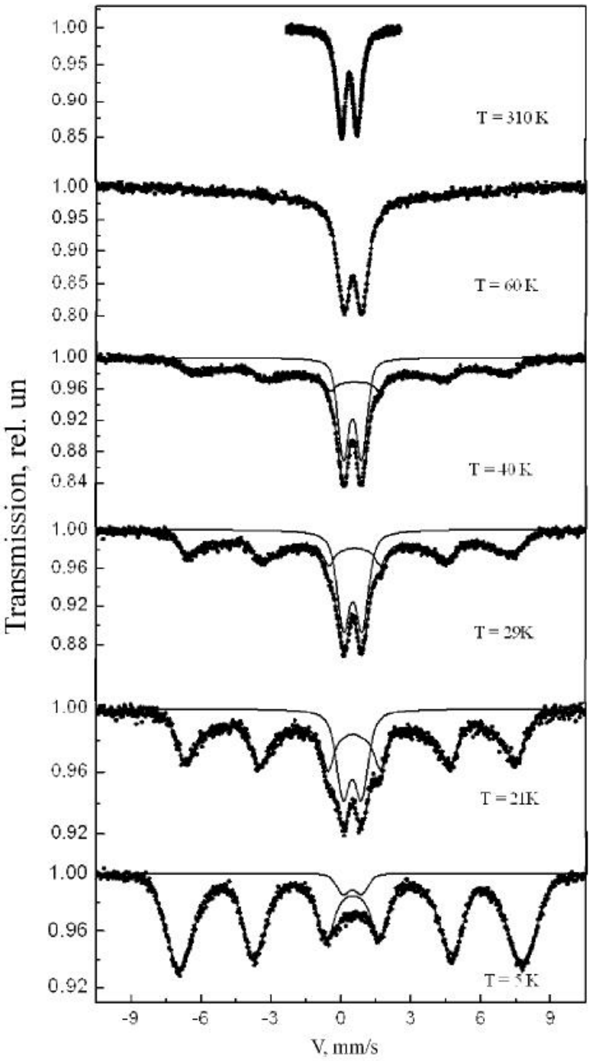

Fig.3. Mössbauer transmission spectra of the compound at various temperatures.

One could expect to find a superposition of the quadrupole doublets of two spin states (HS and LS) at lower temperatures, as observed in the structurally similar complexes in [4] However, only one quadrupole doublet with a broad line width is observed in the whole temperature range. This phenomenon indicates that the electronic relaxation time between the HS and LS state is faster than the lifetime of the nuclear excited state of iron^{57} (1×10^{-7} s) and the iron nucleus “sees” an average of the properties of both states, and that the values of the

Mössbauer parameters are averaged and depend on the population of each form.

At the temperature below 60 K, a magnetic hyperfine structure (H_{obs} = 454.5 kG at 5 K) appears in the spectrum and becomes more pronounced with further decrease of the temperature (fig.3). This indicates a process of magnetic ordering, more precisely, magnetic spin correlations with frequency $\nu < 10^7$ Hz of the spin fluctuations. At the same time, a small part of the quadrupole doublet remains in the spectra at 5 K. In the temperature range between 60 and 10 K, the hyperfine structure of spectra has a superparamagnetic-type of behavior. The relaxation character of the hyperfine components is the result of collective spin flips of small regions (clusters) of the material. So, below 60 K spectra demonstrate a magnetic phase transition from the paramagnetic to antiferromagnetic (AF) type of ordering with a wide temperature range of superparamagnetism existence.

Conclusion

EPR and Mossbauer spectroscopy have been used to study the magnetic properties of spin-crossover dendrimeric iron(III) complex, which possesses mesomorphic properties. So, we may conclude that the antiferromagnetic exchange interactions prevail in the first (4.2 – 70 K) temperature interval, while the spin equilibrium process between LS and HS centers of the II-type dominates in the second (70 – 300 K) one. The magnetic ordering and spin-crosscover coexistence has been detected for the first time in iron(III) dendrimeric compolex.

References

[1] O. Roubeau, M. Evangelisti, E. Natividad, Chem. Commun., 2012, 48, 7604.

[2] J.I. Paez, M. Martinelli, V. Brunetti, M.C. Strumia, Polymers 2012, 4, 355.

[3] B. Donnio, P. Garcia-Vazquez, J.L. Gallani, D. Guillon, E. Terazzi, Adv. Mater., 2007, 19, 3534.

[4] N.E. Domracheva, A.V. Pyataev, V.E. Vorobeva, E.M. Zueva, J. Phys. Chem. B, 2013, 117, 7833.

Complex formation between pravastatin and sodium dodecyl sulfate micelle studied by NMR spectroscopy

I.Z. Rakhmatullin, L.F. Galiullina, E.A. Klochkova, A.V. Aganov, V.V. Klochkov

Kazan Federal University, 420008, Kazan, Russia

e-mail: ilfat89rakhmatullin@gmail.com

Statins, such as pravastatin, play a crucial role in the management of hypercholesterolemia. To understand the biochemical basis of such important properties of statins it is necessary to study their physicochemical characteristics and pharmacology at the molecular level. The efficacy, metabolism, and safety of statins depend on their location in molecular membranes [1]. An understanding of how these drugs interact with cellular membranes may further help to elucidate an origin of their pharmacologic properties.

The chemical structure of the pravastatin (fig.1) dissolved in D_2O was confirmed by the results of 1D ^1H and ^{13}C and 2D NMR experiments. Conformational features of the pravastatin molecule in D_2O solution are studied by 2D NOESY NMR experiments. Observed NOESY correlations proved the proximity of two aliphatic chains of the molecule.

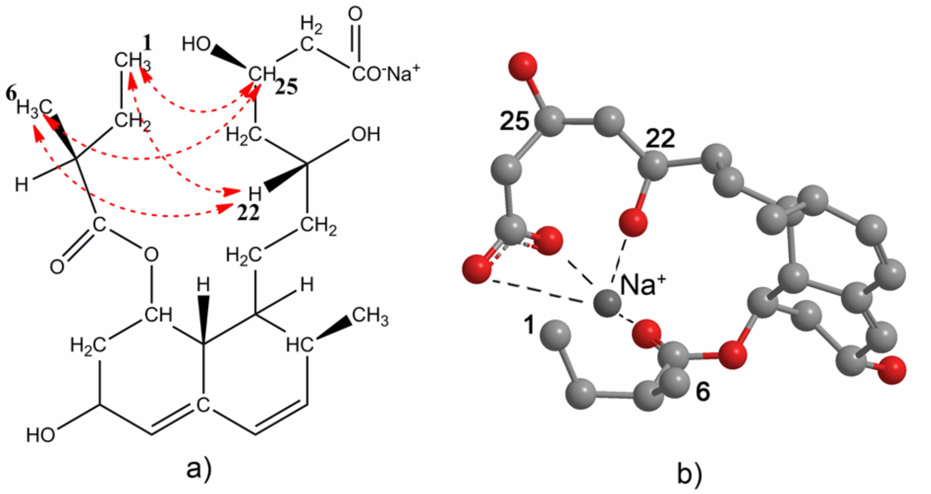

Fig.1. The chemical structure of pravastatin (a, dashed lines – presentation of the observed NOEs) and conformational structure (b, hydrogen atoms are not shown) of pravastatin.

On the basis of the nuclear magnetic resonance experiments it was established that pravastatin can form intermolecular complexes with sodium dodecyl sulfate (SDS) micelles by the interaction of its hydrophilic groups with the polar surface of the micelle. This interaction is similar to the interaction of pravastatin molecules with the surface of cell membranes.

This work was funded by the subsidy of the Russian Government to support the Program of Competitive Growth of Kazan Federal University among World's Leading Academic Centers.

References

[1] Mason RP, Walter MF, Day ChA, Jacob RF 2005. Intermolecular differences of 3 hydroxy-3-methylglutaryl coenzyme a reductase inhibitors contribute to distinct pharmacologic and pleiotropic actions. The American journal of cardiology 96:11F-23F.

Solution NMR structures of the Arctic and the wild types of Alzheimer's Aβ peptides in membrane mimicking environment

K.S. Usachev[1], O.A. Kolosova[1], A.V. Filippov[1,2], O.N. Antzutkin[3], V.V. Klochkov[1]

[1]Kazan Federal University, 420138, Kremlevskaya 18, Kazan, Russian Federation
[2]Chemistry of Interfaces, Luleå University of Technology, SE-97187, Luleå, Sweden.
[3]Department of Physics, Warwick University, CV4 7AL Coventry, UK.

e-mail: k.usachev@kpfu.ru

The "Arctic" (E22G) single-point mutation of the Alzheimer's Aβ peptide is a rare mutation found in a few families in northern Sweden, leading to earlier onset of Alzheimer's disease [1]. It has been shown that the arctic mutation is one of known intra-β-amyloid mutations causing a typical clinical picture of Alzheimer's disease.

We used 2D NMR spectroscopy to investigate the conformation of the "wild type" and the"Arctic" mutation of $A\beta_{1-40}$ Alzheimer's amyloid peptide in a sodium dodecyl sulfate micelle solution mimicking biomembranes [2]. The solution structuresrevealedthat the Arctic mutation of $A\beta_{1-40}$ interacts with the surface of SDS micelles mainly through the Leu17-Asn27 3_{10}-helical region, while the Ile31-Val40 region is buried in the hydrophobic interior of the micelle. In contrast, the wild-type $A\beta_{1-40}$ interacts with SDS micelles through the Lys16-Asp23α-helical region and the Gly29-Met35 fragment. Interactions are hydrophobic in nature for both the mutant and the wild-type peptides.These observations clearly show that both the peptide conformation and the peptide-to-membrane binding are very sensitive to a single amino acid substitution, such as E22G in the case of the Arctic mutation. Single amino acid substitutions may affect the rate of aggregation, structure and interaction of toxic oligomers of Aβpeptides with phospholipid membranesthat may be correlated with pathogenicity differences of Aβ variants causing early onsets of Alzheimer disease.

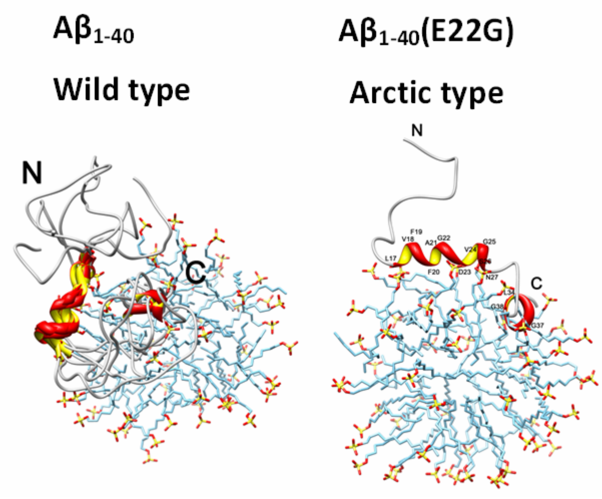

Fig.1. NMRstructures of the arctic and the wild type $A\beta_{1-40}$ bound to a SDS micelle

References

[1] Johansson, A.S., Berglind-Dehlin, F., Karlsson, G., Edwards, K., Gellerfors, P., Lannfelt, L., 2006. Physiochemical characterization of the Alzheimer's disease-related peptides Aβ(1-42)-Arctic and Aβ(1-42)-wt. *FEBS J.* 273, 2618–2630.

[2] Usachev, K.S., Filippov, A.V., Antzutkin, O.N., Klochkov, V.V., 2013. Use of a combination of the RDC method and NOESY NMR spectroscopy to determine the structure of Alzheimer's amyloid $A\beta_{10-35}$ peptide in solution and in SDS micelles. *Eur. Biophys. J.* 42, 803-810.

The study of sugars influence on mobility of lipid bilayer

K.B. Konov[1], N.P. Isaev[2], S.A. Dzuba[2,3]

[1]Kazan Physical -Technical Institute, 420029, Sibirsky tract 10/7, Kazan, Russia
[2]Institute of Chemical Kinetics and Combustion, 630090, Institutskaya 3, Novosibirsk, Russia
[3]Novosibirsk State University, 630090, Pirogova 2, Novosibirsk, Russia

e-mail: kostyakonov@yandex.ru

The sugars are known for their cryoprotective activity [1]. It is well known that sucrose and trehalose can protect cell and its interior from damaging action of freezing and desiccation. It is considered that some sugars might replace the water around polar heads in cell membranes, thus stabilizing its structure in the absence of water. This action of sugars was called the water replacement hypothesis [2]. In addition, it is considered that the cryoprotective action of sugars associates with the affect on mobility of lipid bilayer [3].

To study the effect of sugars presence on the mobility of cell membrane electron spin echo technique was used. This technique allows to obtain information about anisotropic transverse relaxation, which depends on molecular motions. This method provides information about the mobility of different parts of lipid bilayer below a temperature of 250 K. At higher temperatures continuous-wave EPR can give some information about molecular motions.The aim of this work is to study the influence of sugars on the mobility of cell membrane. The stearic acids spin-labeled at 5th and 16th carbon position along aliphatic chain with nitroxide radical were mixed with 1,2-dipalmitoyl-sn-glycero-3-phosphocholine (DPPC) and hydrated in water-sucrose and water-trehalose mixtures. The difference between action of sucrose and trehalose was shown.

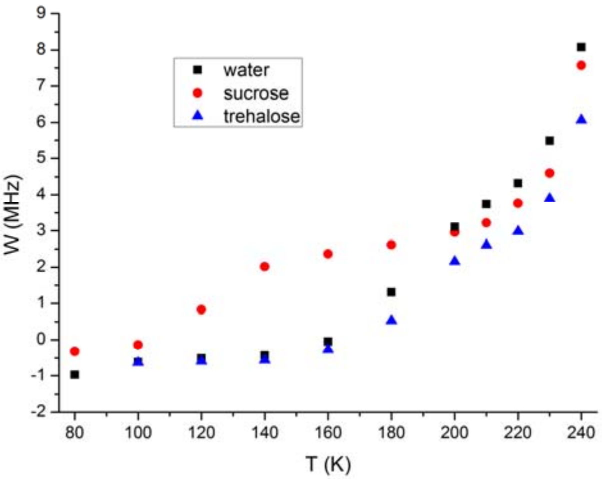

Fig.1. Anisotropic relaxation rate of stearic acid spin-labeled at 5th position hydrated in water, water-trehalose and water-sucrose mixtures.

References

[1] Crowe J.H., Crowe L.M. et al., Carpenter et al., Biochimica et Biophysica Acta, 1988, 947(2), 367-84.

[2] Golovina E. A., Golovin A. V. et al., Biophysical Journal, 2009, 97, 490–499

[3] Geert van den Bogaart, N. Hermans et al., Biophysical Journal, 2007, 92, 1598–1605

NMR and optical study of supramolecular complexes of carotenoids lutein and zeaxanthin

I.E. Apanasenko[1,2], N.E. Polyakov[2], L.P. Suntsova[3], A.V. Dushkin[3]

[1]Institute of Chemical Kinetics and Combustion,630090, Institutskaya 3, Novosibirsk, Russia
[2]Novosibirsk State University, Novosibirsk, 630090, Pirogova 2, Novosibirsk, Russia
[3]Institute of Solid State Chemistry and Mechanochemistry, 630128, Kutateladze 18, Novosibirsk, Russia;

e-mail: airin.nsu@gmail.com

Abstract

Xanthophyll carotenoids play a special role in the prevention and treatment of visual diseases. These carotenoids are not produced by the human body and must be consumed in the diet. On the other hand, extremely low water solubility of these carotenoids and their instability restrict their practical application as components of food or medicinal formulations.The preparation of supramolecular complexesof zeaxanthin and lutein with glycyrrhizic acid, its disodium salt and natural polysaccharide arabinogalactan allows to minimize the aforementioned disadvantages when carotenoids are used in food processing (colors and antioxidant capacity) as well as for production of therapeutic formulations considering the better solubility and stability. In the present study the formation of supramolecular complexes and their stability in model reaction with ozone were investigated by NMR relaxation and optical absorption techniques.

Introduction

Carotenoids belong to the class of tetraterpenes and tetraterpenoids. They are organic pigments that are found in the chloroplasts and chromoplasts of plants and some other photosynthetic organisms, including bacteria and fungi.Carotenoids are effective antioxidants that can neutralize free radicals in photosynthesis. Lutein and zeaxanthin (fig.1)belong to the group of oxygenated carotenoids called xanthophylls.They are accumulated at highest concentration in the macula of the human eye, and perform protective functions from UV radiation and free radicals [1]. These two carotenoids can impede the onset of age-related macular degeneration and have been recently added to the list of potentially beneficial nutrients provided by leafy greens. The main drawback in practical using of these carotenoids is their absolute insolubility in water and poor chemical stability.

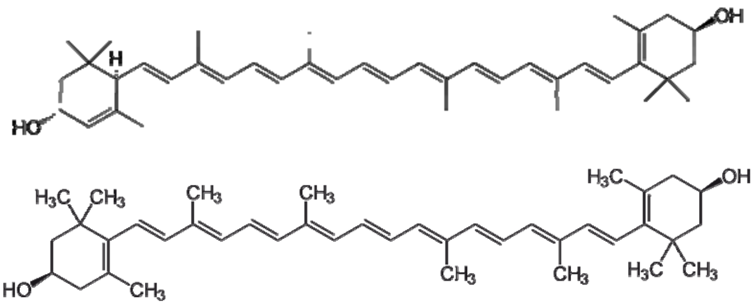

Fig.1. Structural formula of lutein (top) and zeaxanthin

The effective approach to improve the effectiveness and safety of poorly soluble drugs is to increase their solubility and dissolution rate bythe formation of “host-guest” complexes with synthetic or natural water-soluble polymers or oligomers [2-13].This study is devoted to the NMR and optical study of complexation of carotenoids lutein and zeaxanthin with natural complexantsderived from the plant: the triterpene glycoside glycyrrhizic acid (GA) a natural compound extracted from the licorice root [14], its disodium salt (sGA), and arabinogalactan (AG), a natural water soluble polysaccharide extracted from Siberian larch [13]. Some unique properties of GA and AG complexes of β-carotene, canthaxanthin, lutein and zeaxanthin had been already demonstrated earlier by optical and EPR techniques [4-8]. In the present study we used mechanochemical way of complex preparation which allows preparing complexes of insoluble drugs in solid state at one technological step [11-13].

Experimental

Lutein (90%) was purchased from Kemin, and zeaxanthin (90%) fromKalsec;As the "host" molecules we used arabinogalactan from Siberian larch wood [13], glycyrrhizic acid from Ural licorice root [14] and disodium salt of glycyrrhizic acid (CFS, 98%) from Shaanxi Sciphar Biotechnology Co., Ltd.Mechanochemical method of water-soluble complexes preparation is described in details in our previous papers [6, 7, 11-13].

Optical spectra and decay kinetics of carotenoids were recorded usingthe SF-2000 spectrophotometer (Spectrum, Sankt-Petersburg) in the spectral range from 190 to 1100 nm in 1 cm quartz cuvette.

^{1}H NMR spectra in solutions were recorded on a Bruker DPX-200 NMR spectrometer (200MHz) in CD_3OD and D_2O. Measuring of the phase relaxation times T_2 was performed using the standard Carr-Purcell-Meiboom-Gill sequence (CPMG) of the type $P_1(90^o) - (\tau - P_2(180^o) - \tau)_n$ – registration, where $\tau = 0.6$ ms is a fixed time delay, the n value was varied from 0 to 4028.

Results and Discussion

The T_2 relaxation time is very sensitive to intermolecular interactions and diffusion mobility of molecules. Proton relaxation time of molecule inside the complex issignificantly reduced because diffusive and rotary mobility are slow. Change of T_2isusually considered as a proof ofcomplex formation. Relaxation times T_2 was measure for the CH protons at the double bond. Fig.2. shows the echo decaykinetics of zeaxanthin CH protons in pure form in

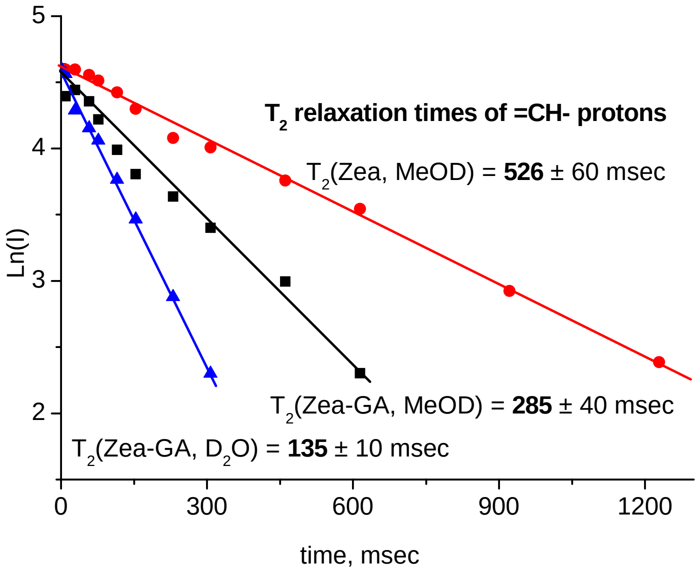

Fig.2. The echo decay kinetics in CPMG experiment of zeaxanthin CH protons in pure form in methanol and in the complex with sGA (5mM) in methanoland D_20.

methanol and in the complex with sGA (5mM) in methanoland D_20.

Complexes with AG and disodium salt of glycyrrhizic acid were prepared bymechanochemical synthesis.

Relaxation time of CH protons of pure carotenoidsin methanolis 560 ± 60 ms. T_2 is slowed down to 285 ± 40 ms after addition to this solution a5 mM of disodium salt of GA, due to complex formation. In the water environment glycyrrhizic acid can forms micelles, therefore the further decrease of relaxation time to 135 ± 10 ms can be explained by incorporation of carotenoid inside the micelle.

The investigationthe oxidation stability of carotenoidsand their complexes was carried out using model reaction with ozone molecule.

Decay kinetics of signals of carotenoids lutein (fig.3) and zeaxanthin were recorded in 75% water-ethanol solution for 5 minutes on the wavelength 380 nm with continuous ozone bubbling.Reaction with ozone results in breaking of double bonds and decrease of carotenoid concentration monitored by optical absorption. For pure lutein fast decay of absorption signal wasobserved. For complexes with AG (5×10^{-5} M) and disodium salt of GA (1 mM) the significant reduce of oxidation rate was detected.

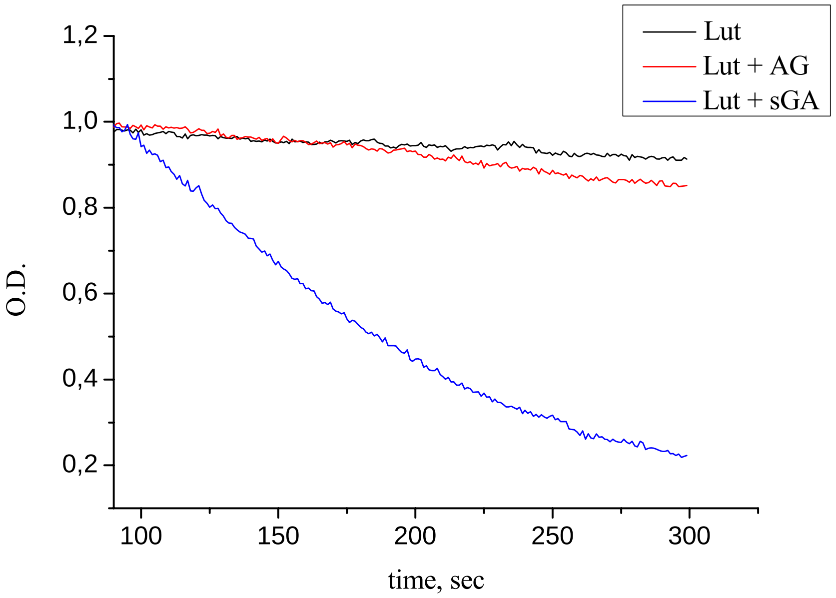

Fig.3.Kinetics of lutein concentration decay in 75% water-ethanol solution during oxidation by ozone in pure form and in the complexes with the AG, 5×10^{-5} M, and sGA, 1 mM.

Mathematical processing of these kinetics by exponentialfitting results infollowing values of decay time: for pure lutein τ =150 ± 20 sec, for lutein with AG τ = 2800 ± 300 sec, and for lutein complex with sGA time τ = 1560 ± 200 sec.

Thus, the interaction of carotenoids lutein and zeaxanthin with arabinogalactan and disodium salt of glycyrrhizic acid leads to the formation of water-soluble supramolecular complexes. These complexes are substantially chemically stable with reaction of ozone, as compared to pure carotenoids.

Acknowledgements

This work was supported by grant RUC-7067-NO-12 from the U.S. Civilian Research & Development Foundation (CRDF Global) with funding from the United States Department of State.

References

[1] J.A. Mares, Carotenoids and eye disease: Epidemiological evidences, in: N.I. Krinsky, S.T. Mayne, H. Sies (Eds.), Carotenoids in Health and Disease, Marcel Dekker, New York, 2004, pp. 427-444.

[2] Polyakov NE,Leshina TV 2011. Glycyrrhizic Acid as a Novel Drug Delivery Vector: Synergy of Drug Transport and Efficacy. The Open Conf. Proc. J. 2: 64-72.

[3] Polyakov, N. E.; Leshina, T. V.; Konovalova, T. A.; Hand, E. O.; Kispert, L. D. Inclusion Complexes of Carotenoids with Cyclodextrins: H-1 Nmr, Epr, and Optical Studies, *Free Radical Bio Med***2004**, *36*, 872-880.

[4] Polyakov, N. E.; Leshina, T. V.; Salakhutdinov, N. F.; Kispert, L. D. Host-Guest Complexes of Carotenoids with Beta-Glycyrrhizic Acid, *J Phys Chem B***2006**, *110*, 6991-6998.

[5] Polyakov, N. E.; Leshina, T. V.; Salakhutdinov, N. F.; Konovalova, T. A.; Kispert, L. D. Antioxidant and Redox Properties of Supramolecular Complexes of Carotenoids with Beta-Glycyrrhizic Acid, *Free Radical Bio Med***2006**, *40*, 1804-1809.

[6] Polyakov, N. E.; Leshina, T. V.; Meteleva, E. S.; Dushkin, A. V.; Konovalova, T. A.; Kispert, L. D. Water Soluble Complexes of Carotenoids with Arabinogalactan, *J Phys Chem B***2009**, *113*, 275-282.

[7] Polyakov, N. E.; Leshina, I. V.; Meteleva, E. S.; Dushkin, A. V.; Konovalova, T. A.; Kispert, L. D. Enhancement of the Photocatalytic Activity of TiO_2 Nanoparticles by Water-Soluble Complexes of Carotenoids, *J Phys Chem B***2010**, *114*, 14200-14204.

[8] N.E. Polyakov, A. Magyar, L.D.Kispert, Photochemical and Optical Properties of Water Soluble Xanthophyll Antioxidants: Aggregation vs. Complexation. *J. Phys. Chem. B*; 117, 10173-10182 (2013).

[9] Polyakov, N. E.; Khan, V. K.; Taraban, M. B.; Leshina, T. V. Complex of Calcium Receptor Blocker Nifedipine with Glycyrrhizic Acid, *J Phys Chem B***2008**, *112*, 4435-4440.

[10] Kornievskaya, V. S.; Kruppa, A. I.; Polyakov, N. E.; Leshina, T. V. Effect of Glycyrrhizic Acid on Lappaconitine Phototransformation, *J Phys Chem B***2007**, *111*, 11447-11452.

[11] Dushkin AV 2010. Mechanochemical synthesis of organic compounds and rapidly soluble materials. In: High-energy ball milling. Mechanochemical processing of nanopowders. Sopicka-Lizer M (ed.). Woodhead Publishing Limited, Oxford. pp. 249-273.

[12] Dushkin AV, ChistyachenkoYuS, Tolstikova TG, Khvostov MV, Polyakov NE, Lyakhov NZ, Tolstikov GA 2013. Pharmacological and physicochemical properties of mechanochemically synthesized supramolecular complexes of acetylsalicylic acid and polysaccharide arabinogalactan from larches *Larix Sibirica*and *LarixGmelinii.*Dokl. biochem. biophys. 451: 180-182.

[13] Dushkin AV, Meteleva ES, Tolstikova TG, Tolstikov GA, Polyakov NE, Medvedeva EN, Neverova NA, Babkin VA 2008. Mechanochemical preparation and pharmacological activities of water-soluble intermolecular complexes of arabinogalactan with medicinal agents. Russ. Chem. Bull. 6: 1299-1307.

[14] Kondratenko, R.; Baltina, L.; Mustafina, S.; Makarova, N.; Nasyrov, K. M.; Tolstikov, G. Crystalline Glycyrrhizic Acid Synthesized from Commercial Glycyrram. Immunomodulant Properties of High-Purity Glycyrrhizic Acid, *Pharmaceutical Chemistry Journal***2001**, *35*, 101-104.

Interaction of the 1,1,3-trimethyl-3-(4-methylphenyl)butyl hydroperoxide with tetraethylammonium bromide

Yu.V. Berestneva[1], E.V. Raksha[1], N.A. Turovskij[1,2], M.Yu. Zubritskij[2]

[1]Donetsk National University, 83 055, Universitetskaya Street 24, Donetsk, Ukraine;
[2]L. M. Litvinenko Institute of Physical Organic and Coal Chemistry National Academy of Sciences of Ukraine, 83 114, R. Luxemburg Str. 70, Donetsk, Ukraine;

e-mail: elenaraksha411@gmail.com

Introduction

Quaternary ammonium salts exhibit a catalytic action for the reaction of radical decomposition of hydroperoxides [1, 2], that promotes the liquid-phase oxidation process of hydrocarbons by molecular oxygen under mild conditions [3, 4]. Variation of hydroperoxides and onium salts structure allows creating purposefully new initiator systems with predetermined reactivity. The results of kinetic studies showed that the catalysis of hydroperoxide decomposition in a presence of onium salts includes a stage of intermediate complex formation [1, 2, 4]. Different structural models of the hydroperoxide - onium salt complexes were proposed on the base of molecular modeling results [2, 4]. The purpose of this work is a complex study of the 1,1,3-trimethyl-3-(4-methylphenyl) butyl hydroperoxide interaction with tetraethylammonium bromide by the kinetic, NMR ^{1}H spectroscopic and molecular modeling methods.

Experimental

1,1,3-Trimethyl-3-(4-methylphenyl)butyl hydroperoxide (ROOH) was purified according to Ref. [5]. Its purity (98.9 %) was controlled by iodometry method. Tetraethylammonium bromide (Et_4NBr) was recrystallized from acetonitrile solution by addition of diethyl ether excess. The salt purity (99.6%) was determined by argentum metric titration with potentiometric fixation of the equivalent point.

NMR ^{1}H spectroscopy investigations of the hydroperoxide and hydroperoxide – Et_4NBr solutions were carried out in acetonitrile-d_3 (D_3CCN). The NMR ^{1}H spectra were recorded on a Bruker Avance 400 (400 MHz) using TMS as an internal standard. D_3CCN was SIGMA-ALDRICH reagent and was used without additional purification, but it has being stored above molecular sieves for three days.

1,1,3-Trimethyl-3-(4-methylphenyl)butyl hydroperoxide ($4\text{-}CH_3\text{-}C_6H_4\text{-}C(CH_3)_2\text{-}CH_2\text{-}(CH_3)_2C\text{-}O\text{-}OH$) NMR ^{1}H (400 MHz, acetonitrile-d_3, 297 K, δ ppm, *J*/Hz): 0.86 (s, 6 H, -$C(\underline{CH_3})_2OOH$), 1.33 (s, 6 H, -$C_6H_4C(\underline{CH_3})_2$-), 2.03 (s, 2 H, -$CH_2$-), 2.28 (s, 3 H, $\underline{CH_3}\text{-}C_6H_4$-), 7.10 (d, *J* = 8.0, 2 H, H-aryl), 7.29 (d, *J* = 8.0, 2 H, H-aryl), 8.49 (s, 1 H, -COOH).

Tetraethylammonium bromide (Et_4NBr) NMR ^{1}H (400 MHz, acetonitrile-d_3, 297 K, δ ppm, *J*/Hz): = 1.21 (t, *J* = 8.0, 12 H, -CH_3), 3.22 (q, *J* = 8.0, 8 H, -CH_2-).

Quantum chemical calculations of the equilibrium structures of hydroperoxide molecule, Et_4NBr and ROOH - Et_4NBr complexes were carried out by AM1 semi-empirical method implemented in MOPAC2012^{TM} package [6]. The nature of the stationary points obtained was verified by calculating the vibrational frequencies at the same level of theory. Solvent effect in calculations was considered in the COSMO [7] approximation.

Results and discussion

Chemically activated hydroperoxide decomposition in the presence of Et_4NBr is suggested to proceed in accordance with following kinetic scheme (Scheme 1). It includes the stage of a complex formation between the hydroperoxide molecule and Et_4NBr ions as well as the stage of complex-bonded hydroperoxide decomposition [1, 2].

$$\mathrm{ROOH} + \mathrm{Et_4NBr} \xrightleftharpoons{K_C} \left[\mathrm{complex}\right] \xrightarrow{k_d} \mathrm{products}\,, \qquad (1)$$

where K_C — equilibrium constant of the complex formation ($dm^3 \cdot mol^{-1}$), and k_d — rate constant of the complex decomposition (s^{-1}).

The interaction between 1,1,3-trimethyl-3-(4-methylphenyl)butyl and hydroperoxide tetraethylammonium bromide can be observed by relative change of the chemical shifts in the NMR spectra. Thus the effect of Alk_4NBr on the signal position of hydroperoxide in the proton magnetic resonance spectrum has been investigated to confirm the complex formation between 1,1,3-trimethyl-3-(4-methylphenyl)butyl hydroperoxide and tetraethylammonium bromide at 297 – 313 K. There is no hydroperoxide decomposition in NMR experimental conditions (rate constant of the hydroperoxide thermolysis reaction in acetonitrile is $k^{313}_{term} = 1.28 \cdot 10^{-10}$ c^{-1} [8]). In the NMR ^1H spectrum of ROOH chemical shift at 8.49 ppm is assigned to proton of the hydroperoxide group (-CO-OH). Changing of hydroperoxide concentration within 0.01 – 0.05 mol dm^{-3} does not lead to a shift of the hydroperoxide group proton signal in spectrum. Addition of an equivalent amount of tetraethylammonium bromide to the system leads to a shift -CO-OH group proton signal to the side of the weak fields without splitting or significant broadening.

Subsequent NMR ^1H spectroscopic studies were carried out in conditions of the quaternary ammonium salt excess at 297 – 313 K. The concentration of ROOH in all experiments was constant (0.02 $mol \cdot dm^{-3}$), while the concentration of Et_4NBr was varied within the range of 0.1 – 0.3 $mol \cdot dm^{-3}$. The monotonous shifting of the NMR signal with increasing of Et_4NBr concentration without splitting and significant broadening shows fast exchange between the free and bonded forms of the hydroperoxide. Such character of signal changing of the hydroperoxide group proton in the presence of Et_4NBr (fig.1) indicates the formation of a complex between hydroperoxide and Et_4NBr in the system. Thus, observed chemical shift of the -CO-OH group proton (δ, ppm) in the spectrum of ROOH – Et_4NBr mixture is averaged signal of the free (δ_{ROOH}, ppm) and complex-bonded (δ_{comp}, ppm) hydroperoxide molecule.

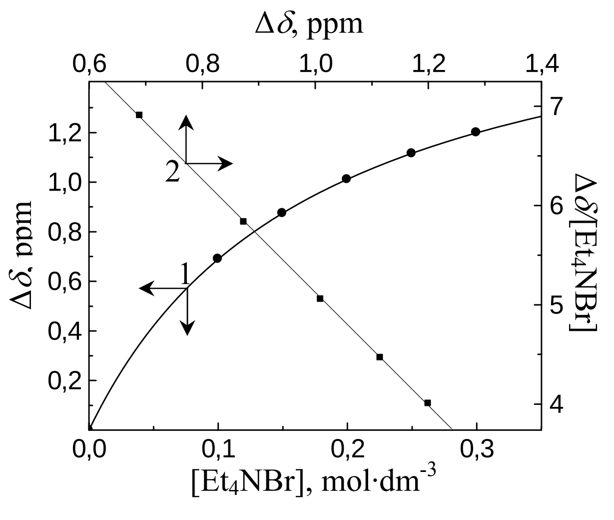

Fig.1 Dependence of change of the proton chemical shift of the ROOH on the Et_4NBr initial concentration in direct (*1*) and Foster - Fyfe equation (*2*) coordinates ($[ROOH]_0 = 0.02$ $mol \cdot dm^{-3}$, $[Et_4NBr] = 0.1 – 0.3$ $mol \cdot dm^{-3}$, 297 K, CD_3CN)

A nonlinear dependence of the changes of the proton chemical shift $\Delta\delta$ ($\Delta\delta = \delta - \delta_{\mathrm{ROOH}}$) of hydroperoxide group on the Et_4NBr initial concentration (fig.1) was obtained. In conditions of Et_4NBr excess and formation of the 1:1 complex for the analysis of the experimentally obtained dependence the Foster - Fyfe equation can be used [9]:

$$\Delta\delta/[\mathrm{Et_4NBr}] = K_C\left(\Delta\delta_{\max} - \Delta\delta\right), \tag{2}$$

where K_C — the equilibrium constant of the complex formation between hydroperoxide and Et_4NBr, $dm^3 \cdot mol^{-1}$; $\Delta\delta_{max}$ — the difference between the chemical shift of the -CO-OH group proton of complex-bonded and free hydroperoxide $\left(\Delta\delta_{\max} = \delta_{comp} - \delta_{ROOH}\right)$, ppm. This dependence of the $\Delta\delta$ on the Et_4NBr initial concentration is linear (fig.1) in the coordinates of equation (2). The equilibrium constants of the complex formation between hydroperoxide and Et_4NBr (K_C) and the chemical shift of the -CO-OH group proton of complex-bonded hydroperoxide were determined and listed in table 1.

Table 1.The thermodynamic parameters of complex formation between the 1,1,3-trimethyl-3-(4-methylphenyl)butyl hydroperoxide and Et_4NBr

T, K	K_C, $dm^3 \cdot mol^{-1}$	δ_{comp}, ppm	$\Delta_{comp}H$, $kJ \cdot mol^{-1}$	$\Delta_{comp}S$, $J \cdot mol^{-1} \cdot K^{-1}$	$\Delta^{297}_{comp}G$, $kJ \cdot mol^{-1}$
297	5.70 ± 0.07	10.35 ± 0.99	-17 ± 3	-43 ± 10	-4.23
303	4.74 ± 0.41	10.52 ± 1.00			
308	4.15 ± 0.18	10.50 ± 0.92			
313	4.06 ± 0.09	10.49 ± 0.92			

The chemical shift of the complex-bonded hydroperoxide δ_{comp} weakly dependent on temperature and is in the range 10.33 – 10.52 ppm (table 1). Enthalpy of the hydroperoxide - Et_4NBr complex formation is $(-17 \pm 3)\, kJ \cdot mol^{-1}$, which is consistent with value of $(-19 \pm 2)\, kJ \cdot mol^{-1}$ determined on the base of kinetic data [1]. The magnitude of the Gibbs free energy of complexation is negative, indicating the complex stability in this system.

Possible structure of the reactive hydroperoxide – catalyst complex has been considered. Model of the substrate separated ion pair (SubSIP) is one of the possible realization of join action of the salt anion and cation in hydroperoxide molecule activation. In this complex hydroperoxide molecule is located between corresponded cation and anion species (fig.2). The solvent effect can be considered by means of direct inclusion of the solvent (acetonitrile) molecule to the complex structure.

Associative interactions of a hydroperoxide molecule with Et_4NBr lead to the peroxide bond dissociation energy ($D_{O\text{-}O}$) decrease. Difference between bonded and non-bonded hydroperoxide $D_{O\text{-}O}$ value is $\Delta D_{O\text{-}O} = 44\ kJ \cdot mol^{-1}$ and is in accordance with experimental activation barrier decreasing in the presence of Et_4NBr: $\Delta E_a = 36\ kJ \cdot mol^{-1}$ [1].

In the framework of proposed structural model the hydroperoxide molecule is directly bonded in complex with ammonium salt anion and cation. This fact is in accordance with experimental observations. Solvated anion approximation allows to directly account the solvent effect on the reactivity of complex bonded hydroperoxide.

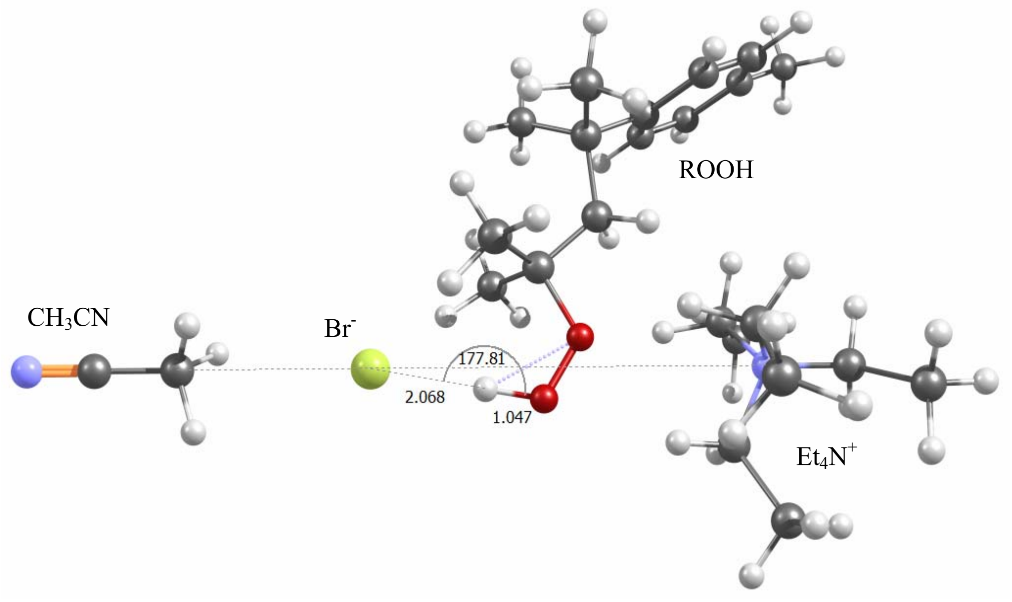

Fig.2. 3D structural model of the 1,1,3-trimethyl-3-(4-methylphenyl)butyl hydroperoxide – Et_4NBr complex with combined action of the cation, anion and the solvent molecule obtained by AM1/COSMO method

Conclusions

Thus, a complex formation between 1,1,3-trimethyl-3-(4-methylphenyl)butyl hydroperoxide and Et_4NBr has been shown by kinetic and NMR ^1H spectroscopy investigations. Complexation enthalpies defined by these methods coincide. Complex formation enhances hydroperoxide reactivity. Lowering of the activation barrier for the complex-bonded hydroperoxide decomposition as compared with its thermolysis in acetonitrile is 36 $kJ \cdot mol^{-1}$. A structural model of the hydroperoxide — Et_4NBr complex has been proposed. Formation of the complex with proposed structural features is accompanied with chemical activation of the aralkyl hydroperoxide molecule.

References

[1] N. A. Turovskij, E. V. Raksha, Yu. V. Berestneva, E. N. Pasternak, M. Yu. Zubritskij, I. A. Opeida, G. E. Zaikov / in: Polymer Products and Chemical Processes. Techniques, Analysis, and Applications, Editors: R. A. Pethrick, E. M. Pearce, G. E. Zaikov. – Toronto, New Jersey: Apple Academic Press, 2013. – 323 p. – P. 269-284.

[2] N. A. Turovskij, E. V. Raksha, O. I. Gevus, I. A. Opeida, and G. E. Zaikov. Oxidation Communications, **32**, 69 (2009).

[3] L. I. Matienko, L. A. Mosolova, G. E. Zaikov. Russ Chem Rev, **78**, 221 (2009).

[4] M. A. Turovskyj, I. O. Opeida, O. M. Turovska, O. V. Raksha, N. O. Kuznetsova, G. E. Zaikov. Oxidation Communications, **29**, 249 (2006).

[5] H. Hock, S. Lang. Chem. Ber., **77**, 257 (1944).

[6] J. J .P. Stewart MOPAC2012, Stewart Computational Chemistry, Colorado Springs, CO, USA, http://OpenMOPAC.net

[7] A. Klamt. J. Chem. Soc. Perkin trans., **2**, 799 (1993).

[8] M. A. Turovsky, O. V. Raksha, I. O. Opeida, O. M. Turovska. Oxidation Communications, **30**, 504 (2007).

[9] L. Fielding. Tetrahedron, **56**, 6151 (2000).

Determination of d(CAGCGGCGTG)·d(CACGCCGCTG) DNA-duplex spatial structure by NMR-spectroscopy

E.A. Sviridov[1,2], A.V. Shernyukov[1]

[1]N.N. Vorozhtsov Novosibirsk Institute of Organic Chemistry of Siberian Branch of Russian Academy of Sciences, 630090, Lavrentjev Ave. 9, Novosibirsk, Russia
[2]Novosibirsk State University, 630090, Pirogova St. 2, Novosibirsk, Russia

e-mail: Svirid93@list.ru

Determination of the spatial structure of DNA fragments is interesting for further investigations of their interactions with various compounds or studying the influence of its modifications. In this paper we have investigated a three-dimensional structure of the DNA-duplex d(CAGCGGCGTG)•d(CACGCCGCTG) by NMR.

Investigations were performed in water solutions: in D_2O (99.99%) and in H_2O:D_2O (9:1). Duplex concentration was about 1 mM. For the presence of the necessary ionic strength, we added a salt buffer comprising 0.1 M NaCl and 0.1 M NaH_2PO_4. In addition, 200 μM Na_2EDTA were added to chelate paramagnetic impurities. ^1H and ^{31}P NMR data were acquired on a Bruker AV-600 spectrometer (^1H: 600.30 MHz; ^{31}P: 243.1 MHz) at temperatures 5°C – 60°C. We used water suppression for the solution in H_2O:D_2O: PE-W5 [1] for one-dimensional and W5 [2] for two-dimensional spectra. ^1H – ^1H NOESY spectra were obtained with standard pulse programs at temperatures 15.3°C and 33.3°C, with 100, 200 and 400 ms mixing times. Chemical shifts in ^1H and ^{31}P NMR spectra are calibrated against an internal standard — DSS (δ Me 0.0 ppm) and by indirect calibration respectively [3]. NMR spectra were processed using Bruker TopSpin 2.1. For the signal assignment we used CcpNmr Analysis 2.3.1 [4].

Assignment of nucleotide signals in ^1H – ^1H NOESY spectra was obtained by the standard strategy "sequential walking" for right-handed forms of the DNA, using the path H1'(i – 1) – H6/8(i) – H1'(i) (fig.1) and the path H2'/H2"(i – 1) – H6/8(i) – H2'/H2"(i) (fig.2) (i — residue number). Assignment of deoxyribose proton signals, H5 – H6 cytosine's and H7# – H6 thymine's cross-peaks was derived with the help of ^1H – ^1H COSY spectra. Signals of adenine's H2 protons were identified by corresponding NOESY cross-peaks H2 – H1'. During the assignment procedure, we determined most proton chemical shifts of the duplex. Chemical shift values are represented in the table 1.

Duplex signals in ^{31}P NMR spectrum (fig.3) are within 1 ppm region. This means that observable fragment of the DNA is in a B form [5]. In ^1H-^1H NOESY spectrum we observe G:H1 – C:H41/H42 and A:H2 – T:H3 cross-peaks for all base pairs, except for terminal pairs. It follows therefrom that corresponding base pairs are coupled by hydrogen bonds according to the Watson-Crick scheme. The first and last base pairs were not detected due to end-fraying. In addition, chemical shifts of guanine's H1 protons and thymine's H3 protons are typical for the B-DNA. Moreover we observe H1'(i) – H5(i+1), H2"(i) – H5(i+1) and H2"(i) – Me(i+1) cross-peaks in ^1H – ^1H NOESY, which are nonobservable or have a negligible intensity for an A-DNA.

Structure calculations were performed in the simulated annealing method with the torsion dynamic using CNS1.21 [6] and ARIA2.3.1 [7].

We thank Dr D. Pyshnyi and G. Shevelev (ICBFM SB RAS) for a given DNA and for their help with the sample preparing.

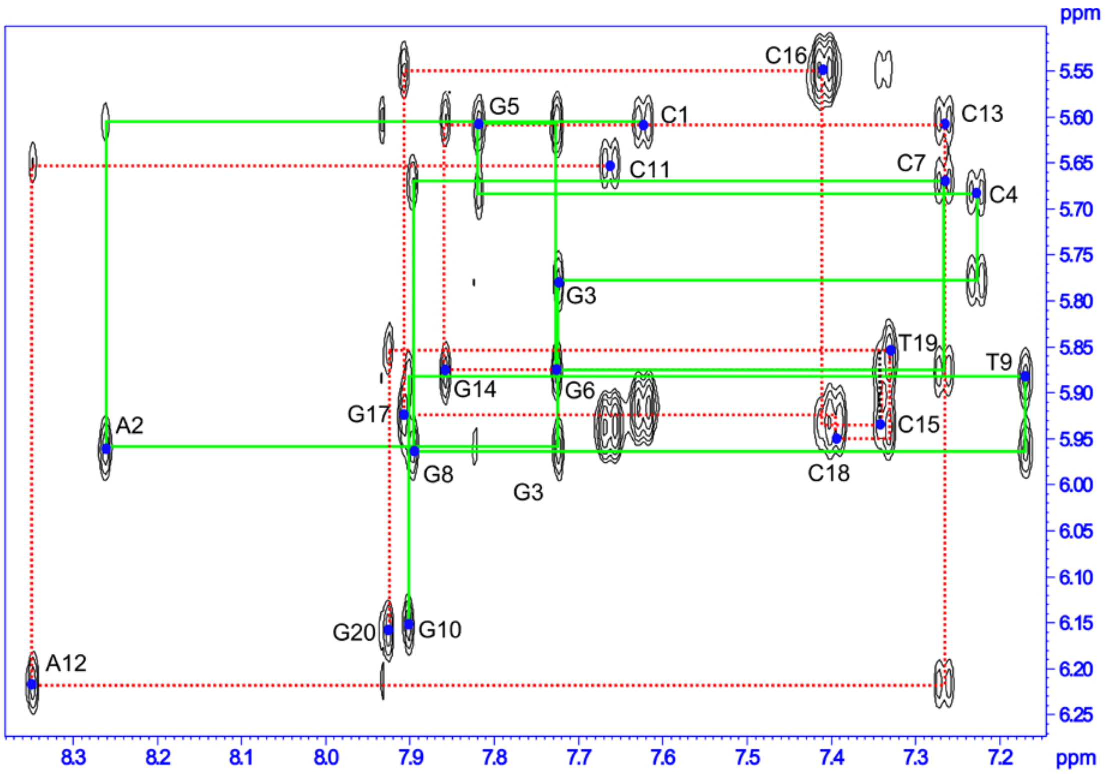

Fig.1. The fragment of $^1H - ^1H$ NOESY spectrum. NOEs between H6/8 and H1' (600 MHz, τ_m = 100 ms, T = 15.3°C). Solid and dashed lines represent sequential assignment for two DNA strands. Numbers specify nucleotides.

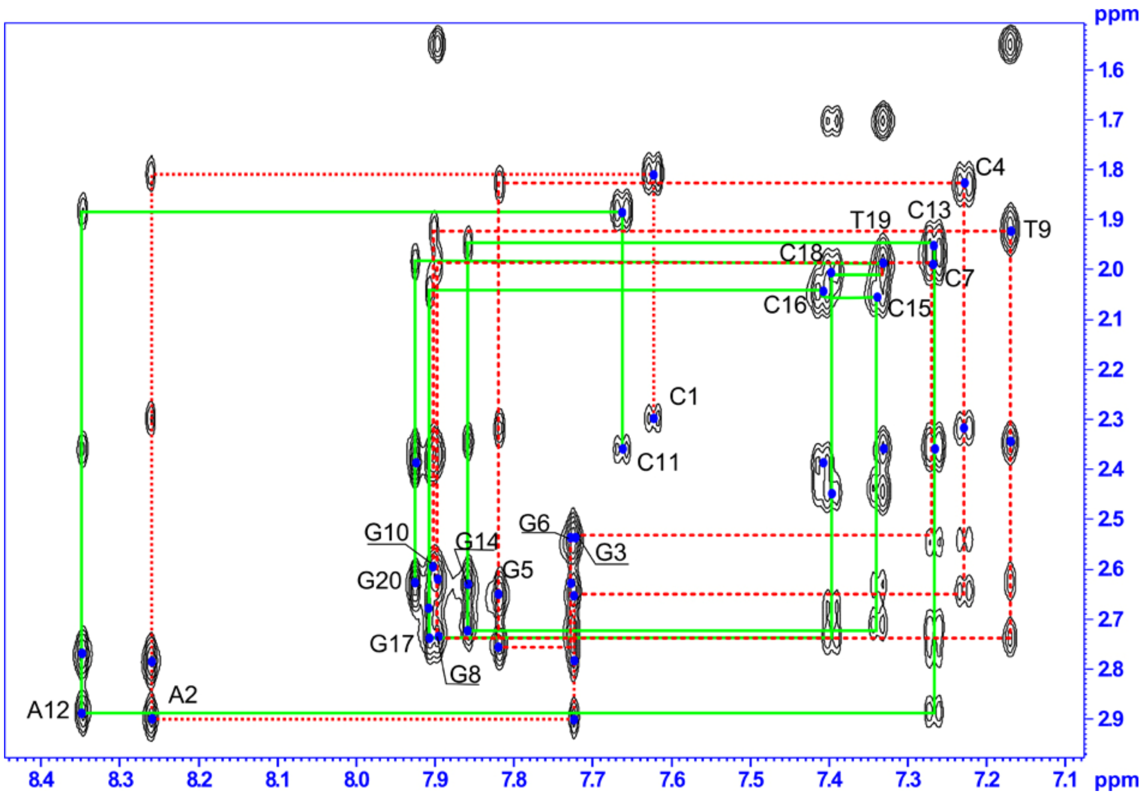

Fig.2. The fragment of $^1H - ^1H$ NOESY spectrum. NOEs between H6/8 and H2'/H2" protons (600 MHz, τ_m = 100 ms, T = 15.3°C). Solid and dashed lines represent sequential assignment for two DNA strands. Numbers specify nucleotides.

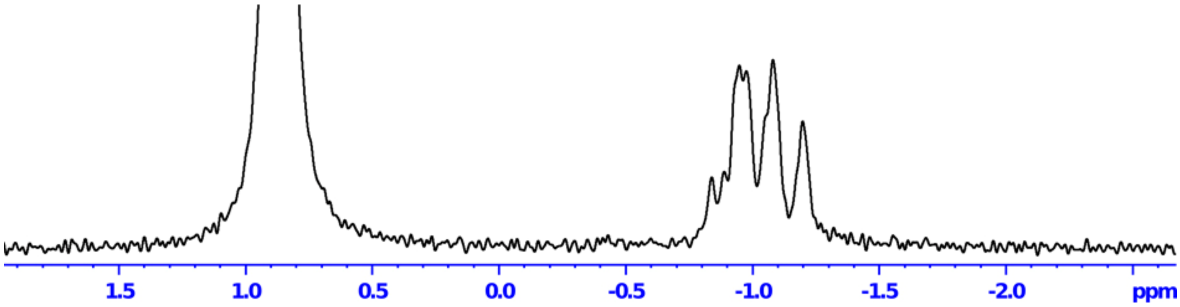

Fig.3. ^{31}P NMR spectrum of the duplex. There is an intensive signal of the phosphate buffer on 0.9 ppm.

Table 1. Proton chemical shifts of the duplex at the temperature 15.3°C. Values are represented in ppm. Chemical shifts of H1, H3, H41 and H42 protons were determined in H_2O:D_2O (90:10), of other protons — in D_2O (99.99%). ND — not determined; "–" — not exist.

Residue	H6/H8	H5/H2/Me	H1'	H2'	H2"	H3'	H4'	H1/H3	H41	H42
C1	7.61	5.87	5.51	1.81	2.29	4.67	4.02	ND	8.17	7.00
A2	8.27	7.79	5.96	2.79	2.90	5.03	4.37	–	–	–
G3	7.74	–	5.77	2.54	2.64	4.98	4.40	12.81	–	–
C4	7.23	5.24	5.66	1.83	2.32	4.81	4.14	–	8.25	6.35
G5	7.84	–	5.59	2.66	2.74	4.98	4.33	13.10	–	–
G6	7.75	–	5.88	2.55	2.72	4.98	4.41	12.94	–	–
C7	7.28	5.29	5.65	2.01	2.37	4.83	4.15	–	8.26	6.37
G8	7.92	–	5.96	2.63	2.75	4.97	4.37	12.82	–	–
T9	7.18	1.54	5.85	1.92	2.34	4.85	4.16	13.92	–	–
G10	7.90	–	6.14	2.62	2.37	4.69	4.18	ND	–	–
C11	7.65	5.89	5.57	1.89	2.35	4.69	4.03	ND	8.13	7.00
A12	8.36	7.91	6.21	2.76	2.88	5.02	4.41	–	–	–
C13	7.27	5.30	5.58	1.96	2.34	4.82	4.17	–	8.20	6.59
G14	7.87	–	5.87	2.63	2.70	4.98	4.37	12.94	–	–
C15	7.35	5.30	5.93	2.05	2.44	4.82	4.05	–	8.15	6.35
C16	7.42	5.54	5.51	2.05	2.39	4.83	4.09	–	8.52	6.78
G17	7.92	–	5.93	2.68	2.73	4.99	4.39	12.96	–	–
C18	7.41	5.38	5.94	2.00	2.45	4.77	4.20	–	8.24	6.62
T19	7.34	1.69	5.80	1.98	2.35	4.84	4.11	14.15	–	–
G20	7.92	–	6.14	2.64	2.37	4.70	4.19	ND	–	–

References

[1] Ralph W. Adams, Chloe M. Holroyd, Juan A. Aguilar, Mathias Nilsson and Gareth A. Morris ;Chem. Commun., 2013,49, 358-360

[2] M. Liu, X. Mao, C. He, H. Huang, J.K. Nicholson & J.C. Lindon, J. Magn. Reson. 132, 125 - 129 (1998)

[3] «Recommendations for the presentation of NMR structures of proteins and nucleic acids», John L. Markley, Ad Bax, Yoji Arata, and others. IUPAC, 1998

[4] «The CCPN data model for NMR spectroscopy: development of a software pipeline» Wim F. Vranken, Wayne Boucher, Tim J. Stivens, Rasmus H. Fogh and others, Proteins 2005, 59, 687-696

[5] «NMR of proteins and nucleic acids» Wuthrich Kurt, 1986

[6] «Crystallography and NMR system (CNS): A new software system for macromolecular structure determination» Brunger A.T., Adams P.D., Clore G.M., Delano W.L. and others, ACTA CRYST. D54 1998, 905-921

[7] «ARIA2: automated NOE assignment and data integration in NMR structure calculation» Rieping W., Habeck M., Bardiaux B., Bernard A., Malliavin T.E., Nilges M., Bioinformatics 2007, 23, 381-382

Collapse of the spinon doublet in the spin-liquid phase of Cs_2CuCl_4

T.A. Soldatov[1,2], K.Yu. Povarov[3], A.I. Smirnov[1,2]

[1]P.L. Kapitza Institute for Physical Problems, RAS, 119334, Kosygina street, Moscow, Russia

[2]Moscow Institute for Physics and Technology, 141700, Institutskii pereulok, Dolgoprudny, Russia

[3]Neutron Scattering and Magnetism, Laboratory for Solid State Physics, ETH Zürich, CH-8093, Zürich, Switzerland

e-mail: tim-sold@yandex.ru

Magnetic crystals with low-dimensional structure of antiferromagnetic exchange bonds remain in a paramagnetic state far below the Curie-Weiss temperature T_{CW}. Low temperature magnetic properties of these magnets are similar to that of spin-liquid phase in zero temperature limit. The suppression or even absence of the ordering is due to strong quantum fluctuations. The spin systems with strong quantum fluctuations and a small order parameter are close to a quantum-critical point separating the ordered and quantum-disordered states. A quasi-two-dimensional (2D) $S = 1/2$ dielectric antiferromagnet Cs_2CuCl_4 is an example of a magnetic system with spin correlations emergent in a wide temperature range below $T_{CW} = 4$ K, but still above the ordering point $T_N = 0.62$ K. In crystals of Cs_2CuCl_4, the Cu^{2+} magnetic ions are placed on stacked 2D layers with a distorted triangular lattice with a strong exchange $J = 4.35$ K along the base of the triangular unit and weaker exchange integral $J' = 0.34\,J$ along lateral sides of the triangle. The interlayer exchange $J'' = 0.045\,J$ is the weakest one; see fig.1.

The continuum of spin excitations observed in Cs_2CuCl_4 corresponds well to the two-spinon continuum of a Heisenberg spin $S = 1/2$ chain [1, 2, 3, 4]. The 1D nature of spinon excitations in this 2D structure is attributed to the geometric frustration of exchange bonds J', as shown in numerical simulations [5] and in the analytical approach [6]. This frustration results in an effective decoupling of spin chains directed along **b**-direction. The spinon continuum corresponds mainly to that of an $S = 1/2$ Heisenberg anti-ferromagnetic chain but is modified by the uni-form Dzyaloshinsky-Moriya (DM) interaction of magnetic ions within a chain [7]. In the previous works [9, 10] the fine structure of the continuum of spin excitations at q → 0 was revealed by electron spin resonance (ESR) method representing a doublet of resonance lines, which was called “spinon doublet”.

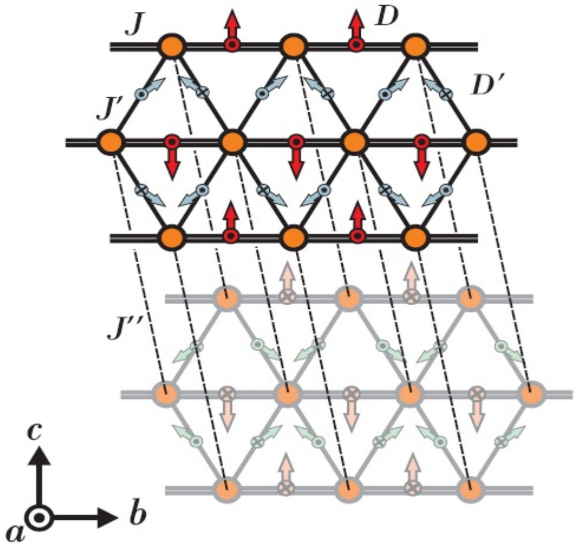

Fig.1. The structure of exchange bonds in Cs_2CuCl_4.

The aim of the present work is to study the evolution of this exotic spinon doublet at the increase of the magnetic field till the saturation value and above. The doublet exists at $\vec{H} \parallel \vec{a}, \vec{c}$. We produced the detailed measurements at $\vec{H} \parallel \vec{a}$.

The spinon doublet in Cs_2CuCl_4 may be explained [8,9] by analyzing the model Hamiltonian

$$\hat{H}=\sum_i J\hat{\vec{S}}_i\cdot\hat{\vec{S}}_{i+1}-\vec{D}\cdot\hat{\vec{S}}_i\times\hat{\vec{S}}_{i+1}+g\mu_B\vec{H}\cdot\hat{\vec{S}}_i \,. \tag{1}$$

Here i enumerates magnetic ions within a chain. It contains three terms: the first describes intrachain exchange J, the second — uniform DM interaction $\vec{D}$ between chain spins, and the third is the usual Zeeman term with anisotropic g-factor. Analysis of the Hamiltonian (1) predicts frequencies of ESR at the arbitrary direction of the field $\vec{H}$ in relation to DM vector $\vec{D}$ [9]:

$$2\pi\hbar\nu=\left|g\mu_B\vec{H}\pm\frac{\pi}{2}\vec{D}\right|. \tag{2}$$

Detailed symmetry analysis of the allowed DM interactions in Cs_2CuCl_4 shows that there are four different orientaitions of the DM vector in four spin chains passing through the elementary cell. The DM vector is expressed via the chain's integer coordinates y, z as follows:

$$\vec{D}_{y,z}=D_a(-1)^z\vec{a}+D_c(-1)^y\vec{c}\,. \tag{3}$$

Here z numerates magnetic **b-c** layers, y numerates chains within a layer. It can be clearly seen that for the Cs_2CuCl_4 four crystallographically inequivalent chains have identical ESR frequencies at $\vec{H}\parallel\vec{a},\vec{b},\vec{c}$:

$$2\pi\hbar\nu_a=\sqrt{(g_a\mu_B H\pm\frac{\pi D_a}{2})^2+\frac{(\pi D_c)^2}{4}}\,, \tag{4}$$

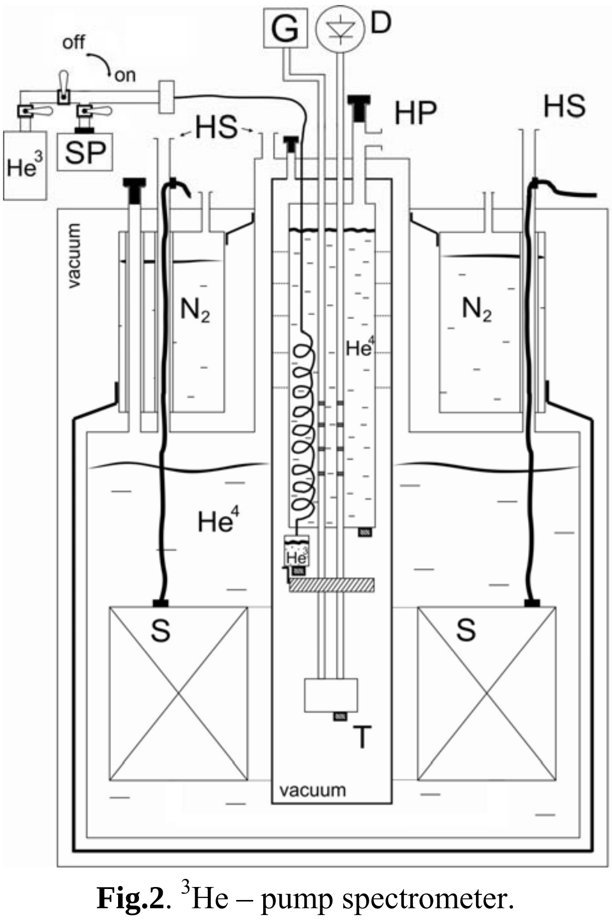

Fig.2. ^{3}He – pump spectrometer.

$$2\pi\hbar\nu_b=\sqrt{(g_b\mu_B H)^2+\frac{\pi^2}{4}(D_a^2+D_c^2)}\,, \tag{5}$$

$$2\pi\hbar\nu_c=\sqrt{(g_c\mu_B H\pm\frac{\pi D_c}{2})^2+\frac{(\pi D_a)^2}{4}}\,. \tag{6}$$

The magnetic resonance signals were recorded as field dependences of the transmitted microwave power in the frequency range $60 < \nu < 210$ GHz at $T = 0.5$ K using microwave resonator and wave-guide insert combined with the microwave spectrometer including ^{3}He pump refrigerator. The sample was fixed by Apeizon N grease inside the copper resonator, which was placed in vacuum and connected via a heat transfer link to the chamber of the ^{3}He pump refrigerator. A RuO_2 thermo-meter placed on the bottom of the reso-nator monitored the temperature of the resonator.

The ESR signal at $T > 10$ K is a typical single resonance corresponding to g-factor values $g_{a,b,c}=2.20, 2.08, 2.30$ for the magnetic field $\vec{H}\parallel\vec{a},\vec{b},\vec{c}$. At cooling below 4 K, a significant change of ESR line shape and position was observed: for $\vec{H} \parallel \vec{b}$ the resonance line is shifted to lower fields whereas for $\vec{H} \parallel \vec{a},\vec{c}$ it is transformed to a spinon doublet [9].

We studied the frequency evolution of ESR signals at $\vec{H} \parallel \vec{a}$ and $T = 0.5$ K. Results are illustrated in fig.3. In spite of the fact that the spin system is in the ordered phase (at $T = 0.5$ K) the spinon doublet found in the spin-liquid phase ($0.62\ \mathrm{K} < T < 4$ K) exists for higher frequencies, $\nu > 60$ GHz. We revealed that the doublet collapses in a field $H \cong 48$ kOe indicating that strong quantum fluctuations are noticeably suppressed by the field about a half of the saturation field $H_{sat} = 84.4$ kOe. This behavior of the doublet is qualitatively confirmed by use of the Müller ansatz [11], see fig.4.

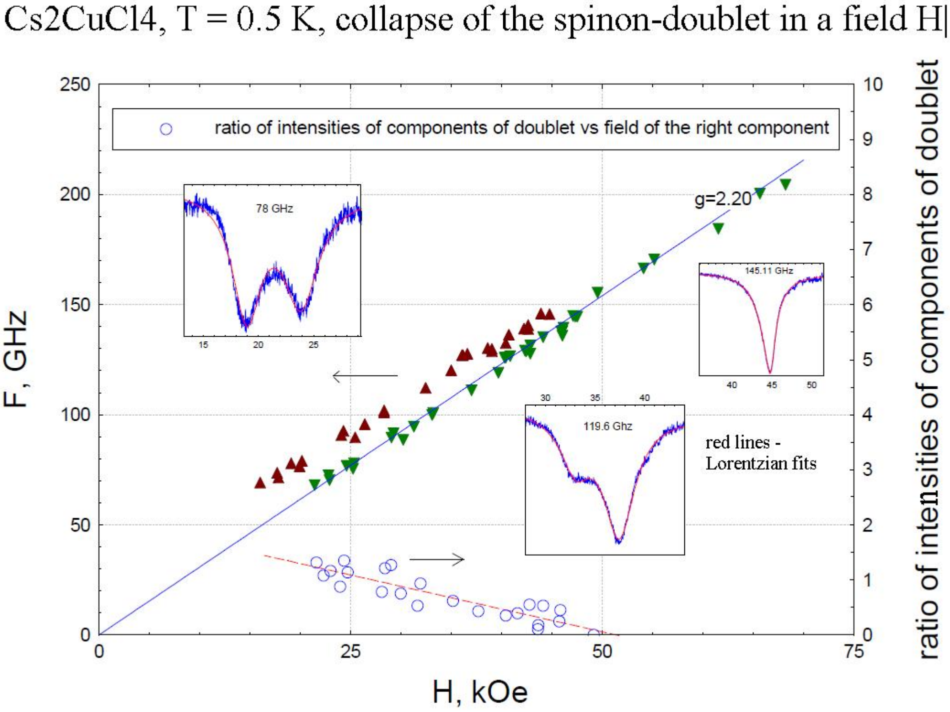

Fig.3. Frequency-field dependence for ESR in Cs_2CuCl_4 at $T = 0.5$ K and $\vec{H} \parallel \vec{a}$.

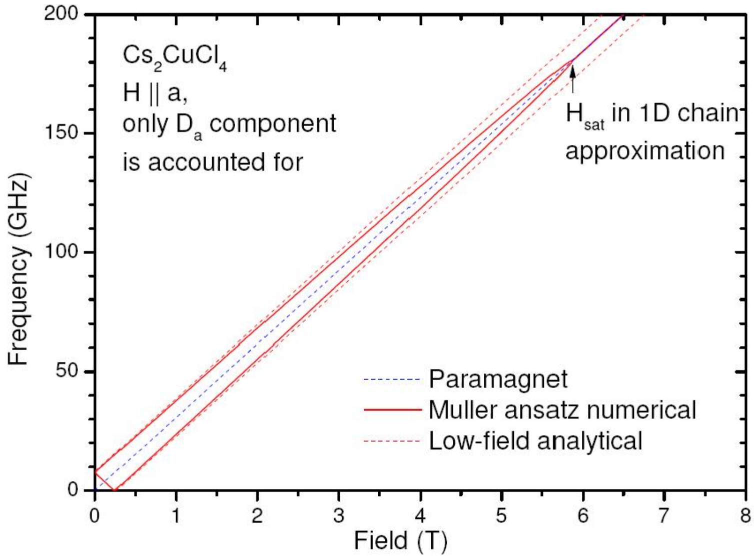

Fig.4. Frequency-field dependence for ESR in Cs_2CuCl_4 at $T = 0$ K and $\vec{H} \parallel \vec{a}$ according to Mueller ansatz model.

References

[1] R. Coldea, D. A. Tennant, R. A. Cowley, D. F. McMorrow, B. Dorner, Z. Tylczynski. *Neutron scattering study of the magnetic structure of Cs_2CuCl_4*. J. Phys.: Condens. Matter **8**, 7473 (1996).

[2] R. Coldea, D. A. Tennant, R. A. Cowley, D. F. McMorrow, B. Dorner, Z. Tylczynski. *The Quasi-1D $S = 1/2$ Antiferromagnet Cs_2CuCl_4 in a Magnetic Field*. Phys. Rev. Lett. **79**, 151 (1997).

[3] R. Coldea, D. A. Tennant, R. A. Cowley, A. M. Tsvelik. Z. Tylczynski. *Experimental Realization of a 2D Fractional Quantum Spin Liquid*. Phys. Rev. Lett. **86**, 7, 1335 (2001).

[4] R. Coldea, D. A. Tennant, Z. Tylczynski. *Extended scattering continua characteristic of spin fractionalization in the two dimensional frustrated quantum magnet Cs_2CuCl_4 observed by neutron scattering*. Phys. Rev. B **68**, 134424 (2003).

[5] D. Heidarian, S. Sorella, F. Becca. *Spin-1/2 Heisenberg model on the anisotropic triangular lattice: From magnetism to a one dimensional spin liquid*. Phys. Rev. B **80**, 012404 (2009).

[6] M. Kohno, O. A. Starykh, L. Balents. *Spinons and triplons in spatially anisotropic frustrated antiferromagnets*. Nature Physics **3**, 790 (2007).

[7] O.A. Starykh, H. Katsura, L. Balents. *Extreme sensitivity of a frustrated quantum magnet: Cs_2CuCl_4*. Phys. Rev. B **82**, 014421 (2010).

[8] S. Gangadharaiah, J. Sun, O. A. Starykh. *Spin-orbital effects in magnetized quantum wires and spin chains*. Phys. Rev. B **78**, 054436 (2008).

[9] K. Yu. Povarov, A. I. Smirnov, O. A. Starykh, S. V. Petrov, A. Ya. Shapiro. *Modes of magnetic resonance in the spin liquid phase of Cs_2CuCl_4*. Phys. Rev. Lett. **107**, 037204 (2011).

[10] A. I. Smirnov, K. Yu. Povarov, S. V. Petrov, A. Ya. Shapiro. *Magnetic resonance in the ordered phases of the 2D frustrated quantum magnet Cs_2CuCl_4*. Phys. Rev. Lett. **107**, 037204 (2011).

[11] G. Müller, H. Thomas, H. Beck, J. C. Bonner. *Quantum spin dynamics of the antiferromagnetic linear chain in zero and nonzero magnetic field*. Phys. Rev. B **24**, 1429 (1981).

Optical and electrical manipulation of a silicon vacancy related defects spin states in Silicon Carbide

V.A. Soltamov[1], P.G. Baranov[1], E.N. Mokhov[1], F. Fuchs[2], G.V. Astakhov[2],
V. Dyakonov[2]

[1]Ioffe Physical-Technical Institute, St. Petersburg, 194021, Russia, victor_soltamov@mail.ru
[2]Experimental Physics VI, Julius-Maximilian University of Wuerzburg, 97074, Wuerzburg, Germany

e-mail: victor_soltamov@mail.ru

In recent decade a special attention has been paid for nitrogen–vacancy (NV) center in diamond because of its' unique quantum properties. Particular, owing to its unique optical excitation cycle that leads to the optical alignment of triplet sublevels of the defect ground state, the NV center can be easily initialized, manipulated, and readout by means of optically detected magnetic resonance (ODMR) at room temperature. Such feature gives rise for application of the NV defects in quantum magnetometry with optical pumping, quantum information processing and bioimaging [1].

The diamond NV defect is in many ways the ideal object but it is currently quite difficult to fabricate devices from diamond. It remains difficult to gate these defects electrically. That is why a search for systems possessing unique quantum properties of the NV defect in diamond that can extend the functionality of such systems seems to be a very promising objective.

A search to find defects with even more potential has now been launched. Silicon Carbide (SiC) was suggested to be able to open up a whole new world of scientific applications [2,3].

The main result is that the optically induced alignment (polarization) of the ground-state spin sublevels of the Si vacancy related defects in two most common hexagonal SiC polytypes (4H- and 6H-SiC) was observed for the first time at room temperature [4]. In distinction from the known NV defect in diamond [1] and recently observed defects in SiC [5], two opposite schemes for the optical spin alignment of the defects in 4H- and 6H-SiC were realized at room temperature upon illumination with unpolarized light. The alignment schemes vary depending on the defect type, temperature, SiC polytype, and crystalline position.

As far as SiC is a well-developed semiconductor material we fabricate the p/n junction based on 6H-SiC polytype and achieve the electrically driven luminescence of the and Si vacancy related defects. Such result potentially means that spin sublevels of the defects can be aligned not only optically but also electrically [6].

So that, SiC with developed device technologies is a very attractive material for practical applications. These altogether make the Si-vacancy related defects in SiC very favorable candidate for spintronics, quantum optics, quantum information processing, magnetometry, biolabelling.

The financial support of the grant of the President 14.122.13.6053-MK, Russia

References

[1] F. Jelezko and J. Wrachtrup, Phys. Status Solidi A 203, 3207 (2006).
[2] P. G. Baranov et al., JETP Letters ...(200?); Phys. Rev. B 83, 125203 (2011)
[3] J. R. Weber, W. F. Koehl, et al., Proc. Natl. Acad. Sci. 107, 8513 (2010).
[4] V. A. Soltamov, A. A. Soltamova et al., Phys. Rev. Lett. 108, 226402 (2012)
[5] Falk, A. L. et al., Nat. Commun. 4:1819 doi: 10.1038/ncomms2854 (2013)
[6] F. Fuchs, V. A. Soltamov et al., Sci. Rep. 3, 1637 (2013).

^{1}H NMR of water colloidal solutions of nanosized crystalline particles $LaF_3:Gd^{3+}$

E.M. Alakshin, B.I. Gizatullin, M.Yu. Zakharov, A.V. Klochkov, T.M. Salikhov, T.R. Safin, V.D. Skirda, M.S. Tagirov

Kazan Federal University, 420008, Kremlevskaya 18, Kazan, Russia

e-mail: mikhailzakharo@yandex.ru

The magnetic resonance imaging (MRI) has a wide range of applications in medical diagnostic. To increase the quality and quantity of obtained information the contrast agents are use. It helps to determine the location of the affected area and its characteristics. The most commonly used intravenous contrast agents are based on chelates of gadolinium. We synthesized the series of nanosized samples LaF_3 and $LaF_3:Gd^{3+}$ and investigated by nuclear magnetic resonance.

Colloidal water solutions of nanosized crystalline particles of LaF_3; LaF_3 with 20 minutes hydrothermal treatment; LaF_3 doped with Gd^{3+}; LaF_3 doped with Gd^{3+} with 20 minutes hydrothermal treatment were prepared. Concentration of Gd^{3+} in respective solutions was 15.9 mM/L. NMR signals of protons were registered by Chromatech 20M NMR spectrometer. Water solutions at different concentrations were prepared and ^{1}H relaxation rates were measured. For comparison, characteristics of the commercial preparations Magnevist®, Gadovist® were used. As a result relaxation rates of LaF_3 doped with Gd^{3+} are higher than rates of commercial preparations (fig.1).

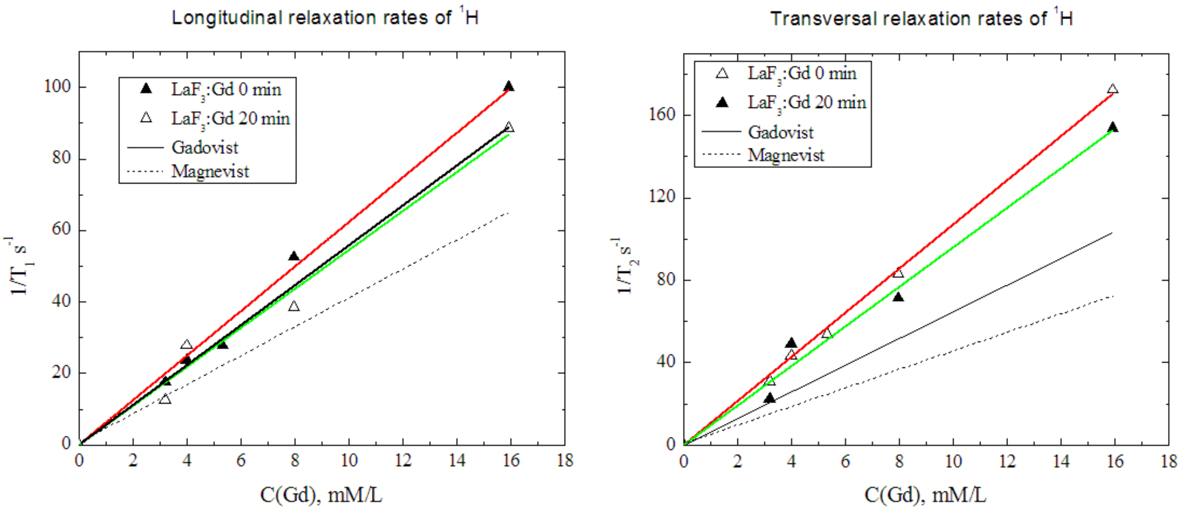

Fig.1. T_1 and T_2 relaxation rates of protons for $LaF_3:Gd^{3+}$ solutions with different concentrations of Gd^{3+} and commercial preparations Magnevist®, Gadovist®. The experiment was carried out at temperature of $37^{0}C$.

Effect of superconducting spin valve and triplet superconductivity in Fe1/Cu/Fe2/Cu/Pb heterostructures

A.A. Kamashev[1], P.V. Leksin[1], N.N. Garif'yanov[1], I.A. Garifullin[1], Ya.V. Fominov[2],
J. Schumann[3], C. Hess[3], V. Kataev[3], B. Buchner[3]

[1]Zavoisky Physical-Technical Institute, Kazan Scientific Center of Russian Academy of Sciences, Kazan, Russia

[2]L.D. Landau Institute for Theoretical Physics RAS, 119334 Moscow, Russia

[3]Leibniz Institute for Solid State and Materials Research IFW Dresden, D-01171 Dresden, Germany

e-mail: kamandi@mail.com

It is well known that ferromagnetism and superconductivity are two antagonistic phenomena because ferromagnetism requires parallel (P) and superconductivity antiparallel (AP) orientation of spins. The exchange field in a ferromagnet which aligns the electron spins parallel is usually much larger than the pairing interaction which couples electrons with opposite spins in a singlet Cooper pair and can easily destroy the superconducting pair. Therefore, when superconducting (S) and ferromagnetic (F) layers are put into contact the Cooper pairs can penetrate into the F layer only over a small distance ξ_F. For example, the value of ξ_F in pure Fe is less than 1 nm (see, e.g., [1]). The exchange field acting on the Copper pair in the F layer gives rise to a finite momentum of the pair whose wave function exhibits therefore a damped oscillating behavior. This results in many new effects: spatial oscillation of the electron density of states, a nonmonotonic dependence of the superconducting transition temperature T_c of F/S/F trilayers on the F-layer thickness and the realization of π Josephson junctions in S/F/S systems.

The physical origin of the spin switch effect based on the S/F proximity effect relies on the idea to control the pair-breaking, and hence the superconducting transition temperature T_c, by manipulating the mutual orientation of the magnetizations of the F layers in a heterostructure comprising, e.g., two F- and one S-layer in a certain combination. This is because the mean exchange field from two F layers acting on Cooper pairs in the S layer is smaller for the antiparallel (AP) orientation of the magnetizations of these F layers compared to the parallel (P) case. The possibility to develop a switch based on the S/F proximity effect has been theoretically substantiated in 1997 by Sanjiun Oh *et al.* [2]. They proposed the F1/N/F2/S layer scheme where an S film is deposited on top of two F-layers, F1 and F2, separated by a thin metallic N-layer. The thickness of F2 should be smaller than the superconducting coherence length to allow the superconducting pair wave function to penetrate into the N layer. For the first time a full switching between the superconducting and the normal states when the mutual orientation of the F layers is changed has been experimentally demonstrated by our group for CoO_x/Fe/Cu/Fe/In multilayer [3]. Further study of the spin valve effect in this system showed its oscillating sign-changing behavior in the dependence on the Fe2-layer thickness $\Delta T_c(d_{Fe2})$ [4].

Bergeret *et al.* [5] have shown for the first time that in the S/F system if the exchange field is homogeneous, not only singlet but also a *spin-triplet* component of the superconducting condensate with the zero projection of the total spin of the Cooper pairs in the direction of the magnetization $\boldsymbol{M}_F$ is generated. This triplet component penetrates into the ferromagnet over a short distance similar to the singlet component. In its turn the triplet component with projection of the total spin of the Cooper pairs in the direction of magnetization $\boldsymbol{M}_F$ $Sz = \pm 1$ can be generated, in particular, by noncolinear magnetizations of F layers. Fominov *et al.* [6] developed the theory for noncollinear orientation of ferromagnetic magnetizations case for F1/F2/S heterostructures. It was obtained that at the perpendicular orientation of ferromagnetic magnetizations the characteristic minimum T_c should be observed in these heterostructures. This effect is a manifestation of triplet superconductivity.

Unfortunately, such experiment on the CoO/Fe1/Cu/Fe2/In system turned out to be unrealizable under well-controlled conditions owing to a low value of T_c for indium and its extreme sensitivity to small out of plane tilting of the external magnetic field. Therefore we replaced In by Pb with higher superconducting critical. We obtained an experimental evidence for the occurrence of the long-range triplet component of the superconducting condensate in the studied spin-valve heterostructure. It is manifested in a nonmonotonic behavior of the superconducting transition temperature T_c of the Pb layer upon gradual rotation of the magnetization of the ferromagnetic Fe1 layer $\boldsymbol{M}_{\mathrm{Fe1}}$ with respect to the magnetization of the Fe2 layer M_{Fe2} from the parallel (P) to the antiparallel (AP) orientation. We observe a clear minimum of T_c near the orthogonal configuration of $\boldsymbol{M}_{\mathrm{Fe1}}$ and $\boldsymbol{M}_{\mathrm{Fe2}}$.

In course of this study very unpleasant fact has been found: that is the sample degradation within one-two weeks (see fig.1). This didn't allow us to study in details the properties of the samples. We suppose that this degradation is caused by the interdiffusion of Fe and Pb atoms through the Fe2/Pb interface. To prevent such interdiffusion may help the introducing of the interlayer between Fe2 and Pb layers.

In the present paper we overcame the degradation of the spin valve samples CoO*x*/Fe1/Cu/Pb by introducing the Cu interlayer between Fe2 and Pb layers. We present new experimental data on the dependencies of the spin valve effect ΔT_c on the thickness of both F layers Fe1 and Fe2. We have demonstrated a full spin valve effect for this system and confirmed the expected appearance of the long range triplet component in the Cooper condensate in the Fe1 layer.

The anti-diffusion Cu interlayer didn't prevent interaction between S and F orders in the heterostructures. It was obtained that Pb layers is sensitive to both Fe1 and Fe2 layers even in the presence of the Cu layers. The consistent replacement both of the Fe layers by the Cu layer leads to T_c increase. The T_c value for Cu(14)/Pb(60) is 1K lower than the bulk value. One can suppose that the T_c-suppression going from the Cu anti-diffusion layer is about 0.1 K. Meanwhile according to fig.3 the T_c difference of the Fe(5)/Cu(1.2)/Pb(60) and Fe(5)/Pb(60) is about of 1 K. At the same time our study of the T_c dependence on the Cu-layer thickness (fig.2) shows that one can neglect the role of the Cu layer in the T_c suppression.

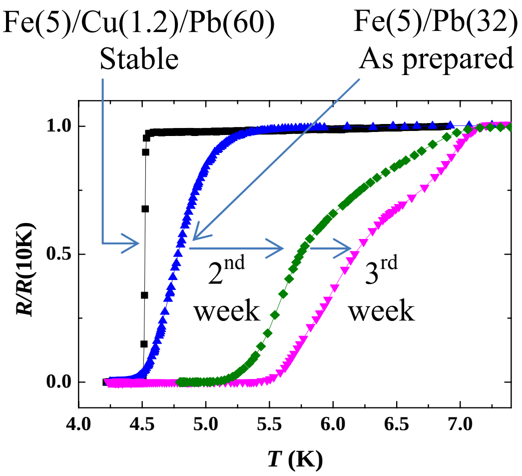

Fig.1. Time evolution of the superconducting properties for the Fe/Pb and Fe/Cu/Pb systems.

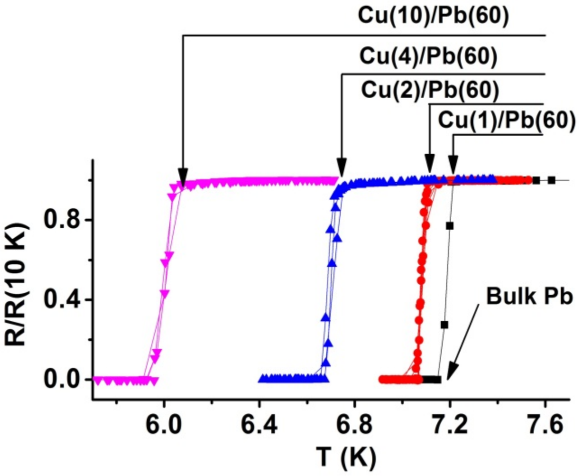

Fig.2. Overview of the superconducting transitions. The T_c increases with decreasing thickness of the copper

Therefore, an additional T_c suppression which is seen from fig.3 is caused by the increasing the transparency of the Cooper pairs when introducing the Cu interlayer between the Fe2 and Pb layers. Low transparency of the Fe/Pb border means that the S order is not strongly influenced by the F order leading to a high T_c value.

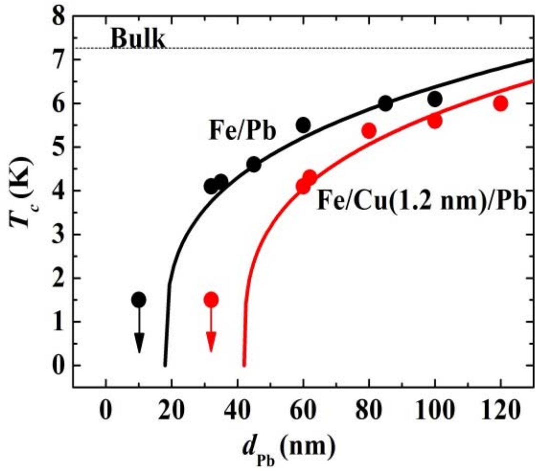

Fig.3.Crtitical temperature vs. Pb layer thickness for the Fe(5)/Pb and Fe(5)/Cu(1.2)/Pb systems

The ordinary spin valve effect results are shown on fig.4. Because of the superconducting properties improvement we were able to obtain full switching effect of the superconducting current.

The triplet spin valve effect results are depicted on fig.5. The minimum of the T_c at orthogonal orientation of the Fe layers is related to the presence of the superconducting triplet components.

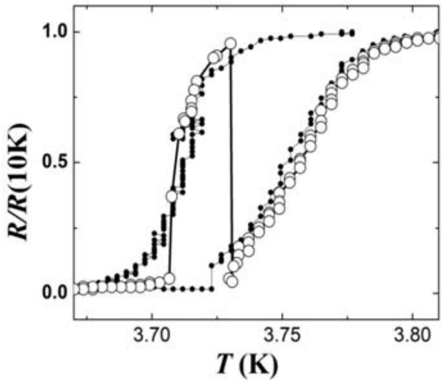

Fig.4. Superconducting transitions for parallel and antiparallel orientation of the Fe1 and Fe2 layers magnetizations for the sample CoOx/Fe1(0.8)/Cu(4)/Fe2(0.5)/Cu(1.2)/Pb(60)/SiN. Full switching effect successfully realized.

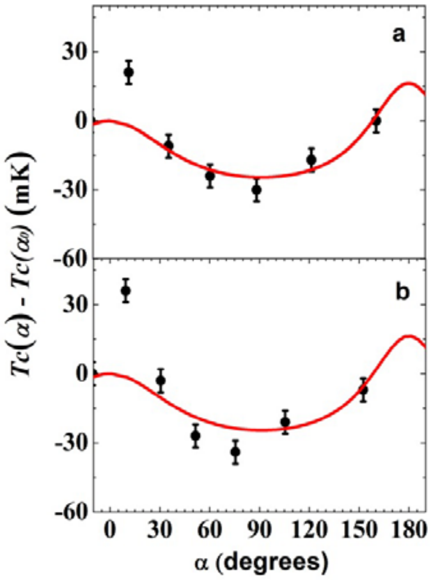

Fig.5. The T_c dependence on the angle between magnetizations (α) of Fe1 and Fe2 layers of the sample CoOx/Fe(5)/Cu(4)/Fe(0.8)/Cu(1.2)/Pb(60)/SiN. The rotating magnetic fields are 500 Oe (a), 1000 Oe (b). Theoretical calculations using triplet spin valve model by Fominov *et al.* [6] on the (a,b) insets are shown by red curves.

Using an additional layer of copper at the interface Fe2/Pb allowed to stabilize the superconducting properties of our samples, in addition managed to improve the transparency of the interface F / S. We have observed the effect of full switching superconducting current in the modified samples, and also managed to observe the effect of triplet superconductivity.

References

[1] L. Lazar, K. Westerholt, H. Zabel, L. R. Tagirov, Yu. V. Goryunov, N. N. Garif'yanov and I.A. Garifullin, Phys. Rev. B **61**, 3711 (2000).

[2] S. Oh, D. Youm, and M. R. Beasley, Appl. Phys. Lett. **71**, 2376 (1997).

[3] P. V. Leksin, N. N. Garif'yanov, I. A. Garifullin, J. Schumann, H. Vinzelberg, V. Kataev, R. Klingeler, O. G. Schmidt, B. Büchner,Appl. Phys. Lett. **97**, 102505 (2010).

[4] P. V. Leksin, N. N. Garif'yanov, I. A. Garifullin, J. Schumann, V. Kataev, R. Klingeler, O. G. Schmidt, B. Büchner, Phys. Rev. Lett. **106**, 067005 (2011).

[5] F. S. Bergeret, A. F. Volkov, and K. B. Efetov, Rev. Mod.Phys. **77**, 1321 (2005).

[6] Ya. V. Fominov, A. A. Golubov, T. Yu. Karminskaya, M. Yu. Kupriyanov, R. G. Deminov, and L. R. Tagirov,Pis'ma Zh. Eksp. Teor. Fiz. **91**, 329 (2010) [JETP Lett.**91**, 308 (2010)].

W-band ENDOR study of V^{2+} and Mn^{2+} in ZnO

Yu.S. Kutin, G.V. Mamin, S.B. Orlinskii

[1]Kazan Federal University, 420008, Kremlyovskaya St.18, Kazan, Russia.

e-mail: yuri_kutin@mail.com

ZnO:Mn has attracted a lot of attention due to a predicted high Curie temperature [1]. Ferromagnetic behavior at room temperature has been confirmed experimentally not only for ZnO:Mn, but also for ZnO doped with Fe, V and other transition metals [2].

Manganese incorporates into ZnO in the Mn^{2+} charge state (electron configuration $3d^5$, $^6S_{5/2}$ electron spin $S = 5/2$). The Mn^{2+} center has been studied by means of electron nuclear double resonance (ENDOR) in various materials [3 – 5]. In the case of ZnO:Mn, however, only the classical cw EPR technique in X-band (frequency around 9.5 GHz) has been employed [6 – 9]. For ZnO:V, the V^{2+} ($3d^3$, $^4F_{3/2}$, $S = 3/2$) [10 – 12] and V^{3+} ($3d^2$, $^3F_2$, $S = 1$) [12] ions have been observed by means of EPR. Another V-related defect in ZnO has also been observed in ODEPR [13]. The ENDOR method has been successfully used in studies of various defects and defect complexes in ZnO [14 – 16]. In this report we present a study of the manganese and vanadium impurities in ZnO by means of high-frequency ENDOR spectroscopy.

Four nominally undoped ZnO single crystals were used in the present investigation: a melt grown, vapor-phase grown and two hydrothermal ZnO samples. All crystals contained Mn as a residual impurity, and the vapor-phase grown sample also contained the V impurity. The EPR/ENDOR experiments were carried out on a Bruker Elexsys 680 EPR spectrometer with the microwave frequency around 94 GHz (W-band) in the temperature range of 6 to 20 K. EPR spectra were detected by monitoring the electron spin echo signal using the standard $\pi/2$ - τ - π pulse sequence. ENDOR spectra were recorded using the standard Mims sequence via the changes in the stimulated echo intensity [17].

Fig.1 shows EPR spectra of manganese and vanadium in ZnO single crystals.

$$\hat{H} = \sum_{k,m} O_k^m B_k^m + \mu_B \mathbf{B}\mathbf{g}\hat{\mathbf{S}} - g_N \mu_N \mathbf{B}\hat{\mathbf{I}} + \hat{\mathbf{S}}\mathbf{A}\hat{\mathbf{I}} + \hat{\mathbf{I}}\mathbf{F}\hat{\mathbf{I}}, \qquad (1)$$

where the first term represents the zero-field splitting; the second and third terms are the electron and nuclear Zeeman interaction; the forth and fifth terms stand, respectively, for the hyperfine (HF) interaction and the quadrupole interaction.

Since the nuclear spin of ^{55}Mn (natural abundance 100%) is $I = 5/2$, the fine structure of the EPR spectrum consists of five groups. The electron spin of the Mn^{2+} ion $S = 5/2$. Therefore, each group is composed of six hyperfine-structure lines. The leftmost lines of the sextets correspond to the EPR transitions $|M_S, m_I = -5/2\rangle \leftrightarrow |M_S + 1, m_I = -5/2\rangle$. With the magnetic field parallel to the c-axis, the spacing between the centers of adjacent sextets is around $2D$, where the zero-field splitting parameter $D = 3B_2^0 = -252.18(4)$ G [6]. ENDOR spectra measured in all six EPR transitions of $M_S = -1/2 \leftrightarrow M_S = +1/2$ are shown in fig.2.

ENDOR line positions of the nuclear transitions within the $M_S = \pm 1/2$ manifolds calculated from the Hamiltonian (1) (without the quadrupole interaction) are $|A|/2 + f_L \approx 148$ MHz and $|A|/2 - f_L \approx 76$ MHz, where f_L is the Larmor frequency of the ^{55}Mn nuclei. The quadrupole interaction leads to the appearance of five nuclear transitions within each M_S manifold, which are numbered 1 to 5 for $M_S = -1/2$ and 1' to 5' for $M_S = +1/2$ in fig.2.

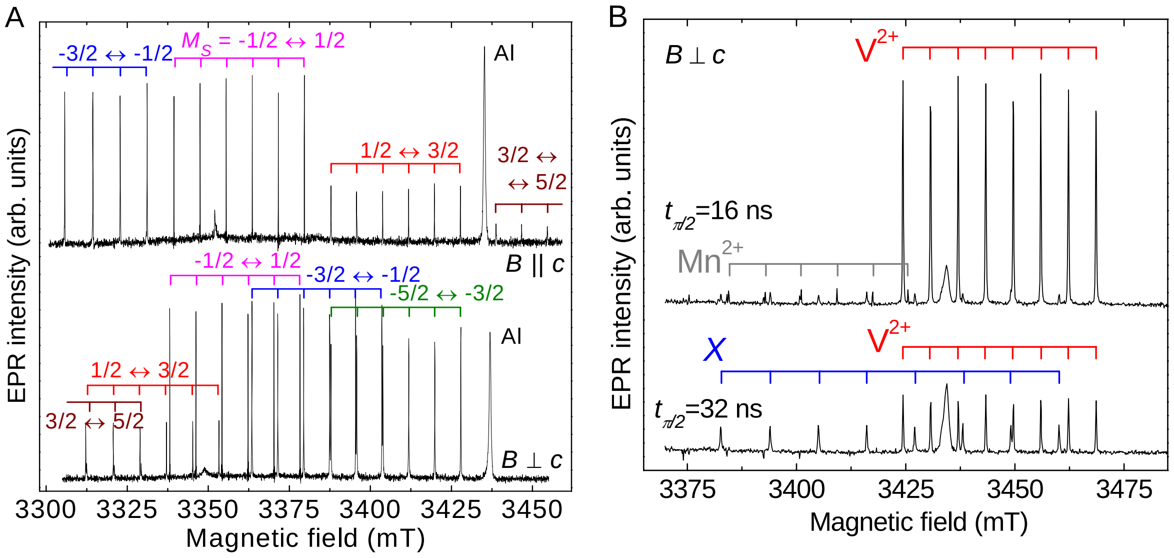

Fig.1. (A) Fragment of EPR spectrum of Mn^{2+} in a melt grown ZnO single crystal recorded for $B \parallel c$ and $B \perp c$. $T = 6$ K, $f \sim 94.1$ GHz. (B) Fragment of EPR spectrum of V^{2+} and unidentified V-related defect X in a vapor-phase grown ZnO single crystal recorded under UV illumination (λ=355 nm) for $B \perp c$ for two different lengths of the microwave π/2-pulse. $T = 10$ K, $f = 93.932$ GHz.

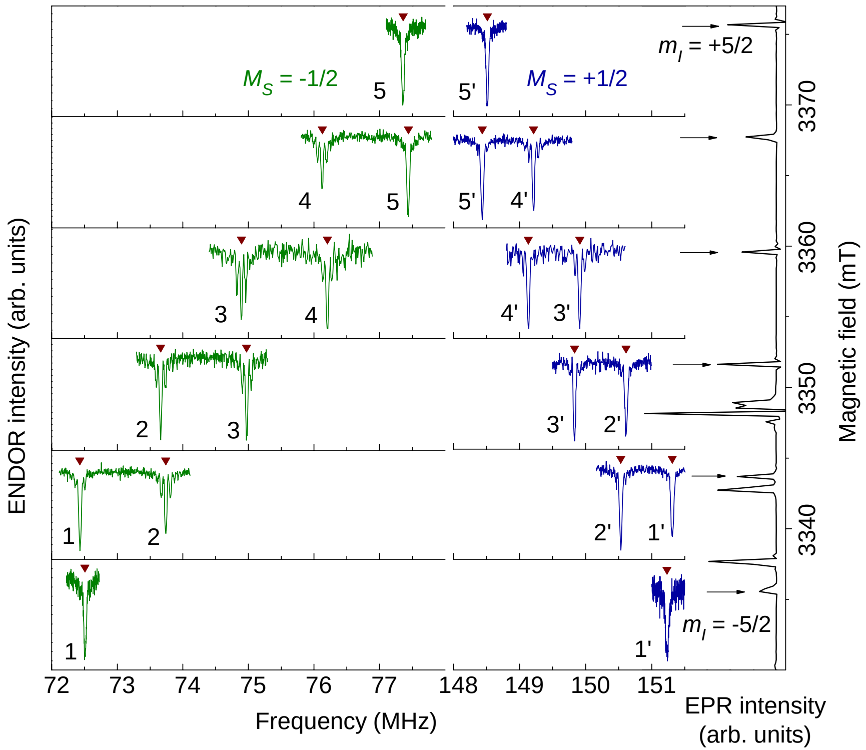

Fig.2. (Right) Fragment of the EPR spectrum of the Mn^{2+} ion a hydrothermally grown ZnO single crystal for $B \parallel c$. $T = 20$ K, $f = 93.892$ GHz. Additional lines in the low-field part of the spectrum do not originate from Mn^{2+}. (Left) ENDOR transitions of the ^{55}Mn nuclei recorded in the six EPR lines of the $M_S = -1/2 \leftrightarrow M_S = +1/2$ transition. $T = 20$ K, $f = 93.931$ GHz. The triangles denote simulated positions of the ENDOR transitions.

Simulation of the ENDOR spectra of the ^{55}Mn nuclei recorded in the EPR transitions of Mn^{2+} were performed in the Matlab environment using the Easyspin package for $B \parallel c$ and $B \perp c$. The triangles in fig.2 show simulated line positions. The following parameters of the Hamiltonian corresponding to the best fit were obtained in a procedure minimizing the difference between the measured and stimulated ENDOR spectra:

$$\begin{gathered}(eQV_{ZZ}/h) = 6{,}889(2) \quad \text{MHz}, \quad g_{\perp} = 2{,}0082, \quad g_{\parallel} = 2{,}0084, \\ A_{\perp} = -224{,}093(8)\ \text{MHz}, \quad A_{\parallel} = -224{,}782(8)\ \text{MHz}.\end{gathered} \tag{2}$$

ENDOR spectra recorded in the eight EPR transitions of the V^{2+} spectrum (see fig.1) under UV illumination are shown in fig.3. Transitions of the ^{51}V nuclei (natural abundance 99.8%, $I = 7/2$) are located at the frequencies around $|A|/2 + f_L \approx 125$ MHz and $|A|/2 - f_L \approx 46$ MHz, where f_L is the Larmor frequency of ^{51}V. In this case the quadrupole interaction leads to the appearance of seven ENDOR lines for each M_S.

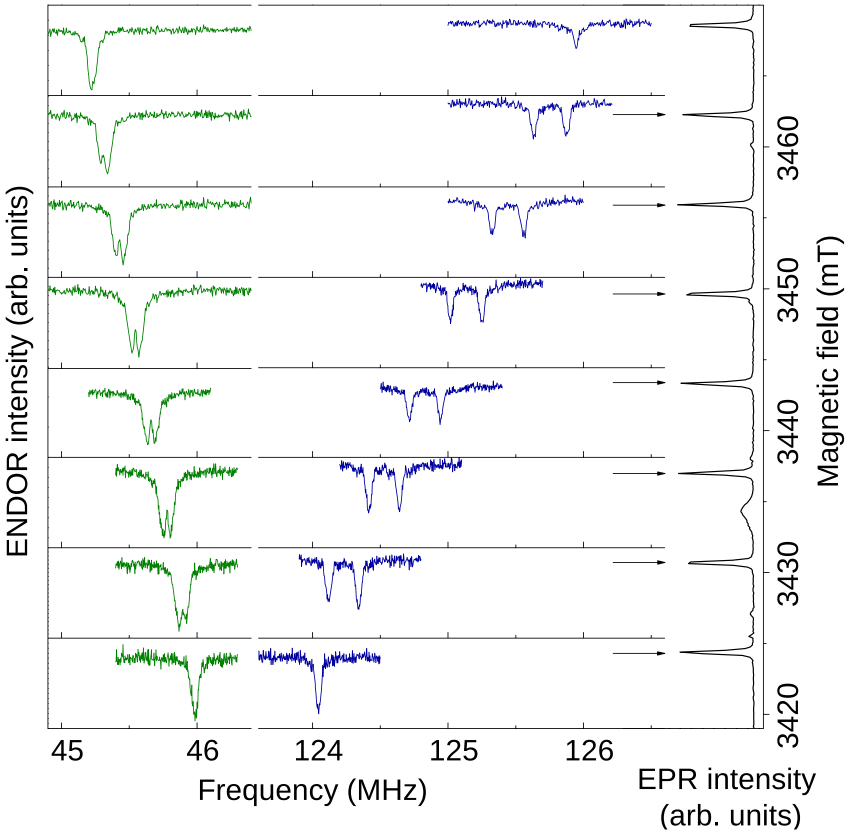

Fig.3. (Right) Fragment of the EPR spectrum of V^{2+} in a vapor-phase grown ZnO single crystal recorded under UV illumination (λ=355 nm) for $B \perp c$. $T = 10$ K, $f \sim 93.932$ GHz. (Left) ENDOR transitions of the ^{51}V nuclei recorded in the eight EPR lines of V^{2+}. $T = 20$ K, $f = 93.932$ GHz.

Due to a structure of the ZnO:V sample no measurements have yet been performed for $B \parallel c$. Thus, the quadrupole interaction constant for V^{2+} has only been estimated using second order correction from the $B \perp c$ ENDOR data:

$$eQV_{ZZ}(^{51}\text{V})/h \approx 3.8\ \text{MHz}. \tag{3}$$

In conclusion, the ENDOR spectroscopy was used to investigate the Mn^{2+} and V^{2+} ions in ZnO single crystals. Nuclear transitions of ^{55}Mn and ^{51}V were observed in the ENDOR spectra recorded in the EPR transitions of Mn^{2+} and V^{2+}, respectively. A well-resolved quadrupole structure of the spectra allowed us to calculate the quadrupole interaction constants for the two paramagnetic centers.

Acknowledgement

Authors thank Dr. F. Herklotz, Dr. Xi Zhang, Prof. E.V. Lavrov and Prof. P.G. Baranov for providing ZnO samples.

References

[1] T. Dietl, H. Ohno, F. Matsukura, J. Cibert, D. Ferrand, Zener Model Description of Ferromagnetism in Zinc-Blende Magnetic Semiconductors, Science, 287 (2000) 1019-1022.

[2] Zinc Oxide Bulk, Thin Films and Nanostructures, Elsevier Science Ltd, Oxford, 2006.

[3] A.H.M. Schrama, P.I.J. Wouters, H.W. de Wijn, Electron-Nuclear Double Resonance of Mn^{2+} in $KMgF_3$ and K_2MgF_4, Phys. Rev. B, 2 (1970) 1235-1239.

[4] W.B. Mims, G.E. Devlin, S. Geschwind, V. Jaccarino, New value for the ^{55}Mn nuclear magnetic moment, Physics Letters A, 24 (1967) 481-482.

[5] J.J. Krebs, J. Lambe, N. Laurance, Electron-Nuclear Double Resonance of Mn^{2+} in Al_2O_3, Phys. Rev., 141 (1966) 425-427.

[6] A. Hausmann, H. Huppertz, Paramagnetic resonance of ZnO:Mn^{++} single crystals, J. Phys. Chem. Solids, 29 (1968) 1369-1375.

[7] A. Hausmann, The cubic field parameter of $^6S_{5/2}$ ions in zinc oxide crystals, Solid State Commun., 6 (1968) 457-459.

[8] J. Schneider, S.B. Sircar, Paramagnetische Resonanz von Mn^{++}-Ionen in synthetischen und natürlichen ZnO-Kristallen (II). Analyse der verbotenen Übergänge $\Delta M=\pm1$, $\Delta m=\pm1$, Z. Naturforschg. , 17a (1962) 651-654.

[9] P.B. Dorain, Electron Paramagnetic Resonance of Manganese (II) in Hexagonal Zinc Oxide and Cadmium Sulfide Single Crystals, Phys. Rev., 112 (1958) 1058-1060.

[10] A. Hausmann, E. Blaschke, ESR of V^{3+} in zinc oxide single crystals, Z. Physik, 230 (1970) 255-264.

[11] G. Filipovich, A.L. Taylor, R.E. Coffman, Electron Paramagnetic Resonance of V^{3+} Ions in Zinc Oxide, Phys. Rev. B, 1 (1970) 1986-1994.

[12] P. Schreiber, A. Hausmann, Vanadium ions in zinc oxide, Z. Physik, 251 (1972) 71-76.

[13] L.S. Vlasenko, G.D. Watkins, R. Helbig, Origin of the 6885-cm^{-1} luminescence lines in ZnO: Vanadium versus copper, Phys. Rev. B, 71 (2005) 115205.

[14] Y.S. Kutin, G.V. Mamin, S.B. Orlinskii, Identification of Fe^{3+}–Li^{+} complexes in ZnO by means of high-frequency EPR/ENDOR spectroscopy, J. Magn. Reson., 237 (2013) 110-114.

[15] F. Herklotz, E.V. Lavrov, J. Weber, G.V. Mamin, Yu.S. Kutin, M.A. Volodin, S.B. Orlinskii, Identification of shallow Al donors in ZnO, Phys. Status Solidi B, 248 (2011) 1532-1537.

[16] D.M. Hofmann, A. Hofstaetter, F. Leiter, H. Zhou, F. Henecker, B.K. Meyer, S.B. Orlinskii, J. Schmidt, P.G. Baranov, Hydrogen: A Relevant Shallow Donor in Zinc Oxide, Phys. Rev. Lett., 88 (2002) 045504.

[17] W.B. Mims, Pulsed Endor Experiments, Proc. R. Soc. London, Ser. A, 283 (1965) 452-457.

Fluoride-modified nanodiamonds studied by HF EPR

B.V. Yavkin[1], S.B. Orlinskii[1], G.V. Mamin[1], D.G. Zverev[1], I. Kratochvilova[2]

[1]Kazan Federal University, 420008, 18 Kremlyovskaya Street, Kazan, Russia
[2]Institute of Physics, Academy of Sciences Czech Republic v.v.i, CZ-182 21, Na Slovance 2, Prague, Czech Republic

e-mail: boris.yavkin@gmail.com

Study of nanodiamond surface is very important task for biomedical application [1]. EPR methods are valuable to approach this task. Recent theoretical [2] and experimental [3] studies show an importance of surface modification and large influence of such modification on the both “bulk” and surface defects of nanodiamond particles.

In this research work EPR method has been applied to characterize surface paramagnetic centers. By means of high-frequency EPR and ENDOR we can distinguish up to four surface centers, by the same time proving that nanodiamond core is unchanged.

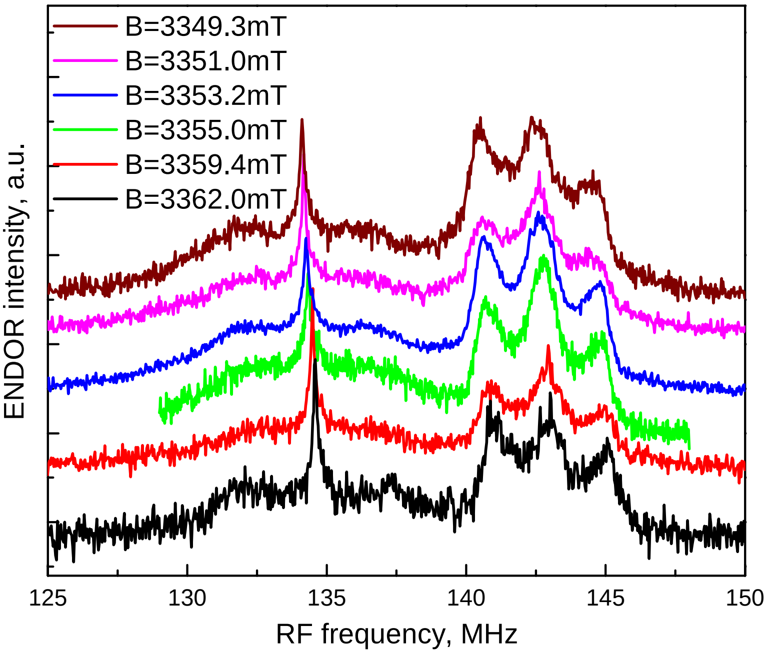

Fig.1. Davies ENDOR spectrum of sample, modified with fluorine.

References

[1] R. Kaur, I. Badea. Nanodiamonds as novel nanomaterials for biomedical applications: drug delivery and imaging systems. International Journal of Nanoscience 2013:B 203-220.

[2] V. Petrakova, A. Taylor, I. Kratochilova, F. Fendrych, J. Vacik, J. Kučka, J. Ŝtursa, P.Cigler, M. Ledvina, A. Fiŝerova, P. Kneppo, and M. Nesladek. Luminescence of nanodiamond driven by atomic functionalization: towards novel detection principles. Adv. Funct. Mater., 22, 812-819, 2012.

[3] T. Dolenko, S. Burikov, J. Rosenholm, O. Shenderova and I. Vlasov. Diamond-water coupling effects in Raman and Photoluminescence spectra of nanodiamond colloidal suspensions. J. Phys. Chem. C 2012, 116, 24314-24319.

EPR, and hydrogenation, and polymerization catalysis by systems based on nickel complexes with 1,4-diaza-1,3-butadiene (α-diimine) ligands

Yu.Yu. Titova, L.B. Belukh, F.K. Schmidt

Irkutsk State University, Institute of Oil and Coal-Chemical Synthesis, 664003, Irkutsk, Karl Marks St.,1, Russia

e-mail: ytitova60@gmail.com

Introduction

In recent years, particular attention is drawn to catalyst systems based on Group 8 metal complexes with a α-diimine ligands for the catalysis of lower alkenes polymerization reactions. It turned out that replacement of phosphine ligands in the coordination sphere of the transition metal on α-diimine leads to the transformation of reactions di- and oligomerization ethylene or propylene to polymerization reactions, moreover the nature of the ligands has a decisive influence on the polyethylene structure [1, 2, 3].

In the literature, published an extensive experimental data regarding of influence the catalytic systems composition on characteristics of catalytic processes, as well as the composition and structure of the catalytically active species. It was obtained sufficiently conclusive results about the nature of active complexes with hydride or alkyl radicals and α-diimine in the first coordination sphere of Ni(II) and with a vacancy for alkene coordination. The anionic part of the complex is a tetra-halides of aluminum, boron, and similar formations. N,N-coordinated ligands acted as electron reservoirs that capable of effectively delocalize the unpaired electron to the antibonding orbitals of 1,4-diazo-1,3-butadiene system, which should be classified as "Non-innocent" ligands.

On the other hand, in the literature practically there is no information about the catalysis of hydrogenation reactions on such systems. Taking into account certain similarities of alkene hydrogenation processes with the processes of di-, oligo- and polymerization seemed appropriate to spend on similar composition and catalytic hydrogenation reaction systems and polymerization and get more information about the mechanisms of formation and nature of the active complexes in catalysis.

Experimental results and discussion

In the study of catalytic systems based on complexes of nickel $NiBr_2$[DAD(-iPr)] (DAD(-iPr) = 1,4-bis(2,6-diisopropylphenyl)-2,3-dimethyl-1,4-diazabuta-1,3-diene) with $AlEt_3$ or $AlEt_2Cl$ the EPR signals were observed. Characteristics of that signals presented in Table. 1. A view of the EPR spectrum of $NiBr_2$[DAD(-iPr)] - $AlEt_3$ with ratio of Al: Ni = 3 showed in fig.1a. Increasing the Al: Ni up to 5 or 10 does not change the shape of the spectrum, but only affects on the signal intensity and its stability. The signal from Ni(I) is reduced during 100 min after mixing the components at Al: Ni = 3 ratio. Parameters of g-factor corresponds to a biaxially anisotropic Ni(I) complex with a diimine ligand and probably two bromine atoms in the first coordination sphere [4]. Moreover, there are new signals in the spectrum, that not previously described in the literature ($g_1 = 2,156$ and $g_2 = 2,388$), which are likely to correspond to a second complex of Ni(I). The identification of this compound requires further investigation.

For the system $NiBr_2$[DAD(-iPr)] - $AlEt_2Cl$ (fig.1b), that active in the polymerization of ethylene in the range of Al / Ni = 5-100, also was observed ESR signals from Ni(I) and an anion-radical (see Table 1). The intensity of the Ni(I) EPR signal virtually unchanged, while the intensity of the anion-radical increases in the time interval 5 - 150 min for ratio $AlEt_2Cl$/ $NiBr_2$[DAD(-iPr)] = 5.

Table 1. Parameters g-factors of paramagnetic nickel complexes and DAD radical forms

Catalytic system	$T_{observation}$, K	Radical	Complex I Ni(I)	Complex (II)
Ni(acac)$_2$+DAD(-iPr) +nAlEt$_3$	77	g = 2,020	g$_1$ = 2,072 g$_2$ = 2,234	
	298	g = 2,004	g = 2,123	g = 2,168
NiBr$_2$[DAD(-iPr)] + nAlEt$_3$	77	g = 2,022	g$_1$ = 2,064 g$_2$ = 2,219	g$_1$ = 2,156 g$_2$ = 2,388
	298	g = 2,005	g = 2,118	
NiBr$_2$[DAD(-iPr)] + nAlEt$_2$Cl	77		g$_1$ = 2,064 g$_2$ = 2,2103	
	298	g = 2,006	g = 2,119	
NiBr$_2$[DAD(-CH$_3$)] + nAlEt$_2$Cl	77		g$_1$ = 2,069 g$_2$ = 2,225	
	298		g = 2,113	
Ni[DAD(-CH$_3$)]$_2$ + nAlEt$_2$Cl	77	g = 2,019	g$_1$ = 2,068 g$_2$ = 2,117 g$_3$ = 2,225	g = 2,279
	298	g = 2,003	g = 2,114	
Ni[DAD(-CH$_3$)]$_2$ + nBF$_3$·OEt$_2$	77	g = 2,015	g$_1$ = 2,064 g$_2$ = 2,107 g$_3$ = 2,226	g = 2,287
	298	g = 2,002		
Ni(COD)$_2$ + nBF$_3$·OEt$_2$	77		g$_1$ = 2,041 g$_2$ = 2,065 g$_3$ = 2,237	g$_1$ = 2,054 g$_2$ = 2,361

Increasing in the AlEt$_2$Cl/NiBr$_2$[DAD(-iPr)] ratio leads to a decrease in signal intensity of Ni(I), although the catalytic activity in the ethylene polymerization is increased.

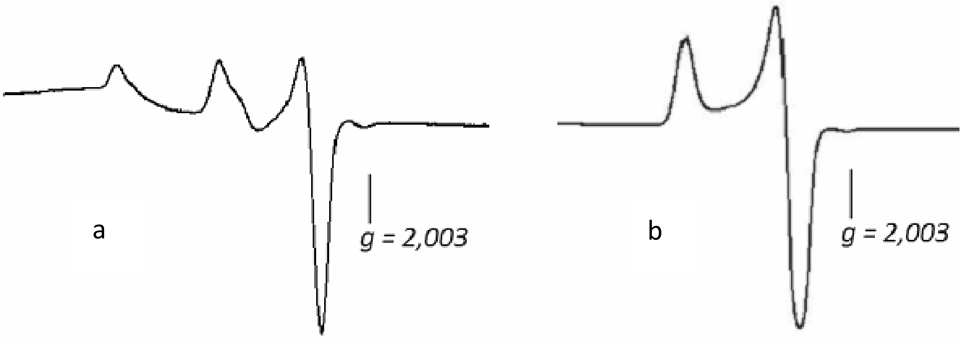

Fig.1. ESR spectrums of NiBr$_2$[DAD(-iPr)] – 3 AlEt$_3$ (a) and NiBr$_2$[DAD(-iPr)] – 5 AlE$_2$Cl (b) systems at T = 77 K.

Similar in shape signals, but with somewhat different parameter g-factor and lower intensity is observed for the Ni(acac)$_2$ – AlEt$_3$ – DAD(-iPr). Differences in the g-factors parameters likely to be due to the replacement of bromine anion at acetylacetonate ligand in the complex Ni(I).

Analysis of the relationship between the intensities of the NI(I) ESR signals and anion - radical depending on the observation spectra temperature and the Al: Ni ratio suggests the existence of an equilibrium between the complexes Ni(I)[DAD(-iPr)] and Ni$^+$[DAD(-iPr)]$^-$ [4].

It was observed a rapid decrease in ESR signal intensity of the Ni(I) in the catalytic hydrogenation of styrene if replacing the argon atmosphere by hydrogen. Consequently, it was suggested that direct relationship between the concentration of paramagnetic complexes and catalytic activity of the system is absent.

For the purpose of modeling the active particles nature complex Ni(0)[DAD(-CH_3)]$_2$ (DAD(-CH_3) = 1,4-bis(2,6-dimethylphenyl)-2,3-dimethyl-1,4-diazabuta-1,3-diene) were synthesized by the Dieck's method [5] and for comparison Ni(COD)$_2$ (COD = 1-cis-5-cis-Cyclooctadiene) [6]. And was studied its behavior under catalytic hydrogenation by EPR spectroscopy.

ESR spectrum during Ni(0)[DAD(-CH_3)]$_2$ synthesis is transformed. In the first sample (30 min after the components mixing) triaxial anisotropic signal with $g_1 = 2{,}051$, $g_2 = 2{,}274$, $g_3 = 2{,}441$ (T = 77 K) is observed, which most likely corresponds to (DAD)Ni(solv)Br (solv = solvent) (fig.2). In the second and third samples only a signal from the [DAD(-CH_3)]$_2^-$ anion-radical with $g_R = 2{,}029592$ (fig.3) was founded.

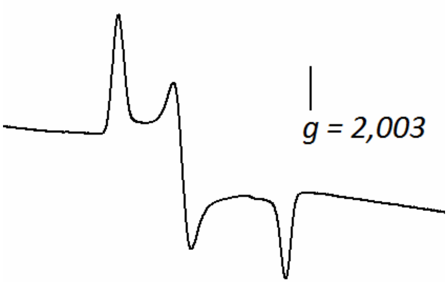

Fig.2. ESR spectrum of the [DAD(-CH_3)]$_2$Ni(solv)Br (solv = solvent), T = 77 K.

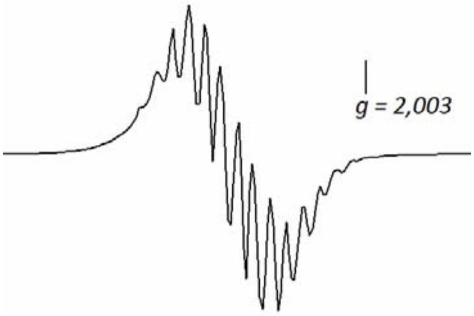

Fig.3. Anion-radical [DAD(-CH_3)]$^-$ ESR spectrum, T = 298 K.

Individual complex Ni(0)[DAD(-CH_3)]$_2$ is active in the styrene hydrogenation (TOF = 2,1 (mol styrene)/(mol Ni·min)), though relatively lower compared to a system based on Ni(acac)$_2$ – $AlEt_3$ – DAD(-iPr). This is due to a catalyst stability decrease. Addition introduction of $AlEt_3$ (Al:Ni = 2) leads to an increase in activity (TOF = 25 (mol styrene)/(mol Ni min)) and stability of catalyst. This result may be due to the binding DAD with $AlEt_3$ and increasing of coordinative unsaturation of nickel active complexes, as that is most likely to perform cluster compounds.

In the EPR spectra of Ni(COD)$_2$-BF_3·OEt_2, obtained in an inert atmosphere, observed triaxial anisotropic signal (1) (fig.4, Table. 1) with $g_1 = 2{,}041$, $g_2 = 2{,}065$, $g_3 = 2{,}237$ (T = 77 K). E. Dinjus observed that same signal previously [7]. Also there are the very weak

Fig.4. ESR spectrum of the Ni(COD)$_2$ – 2 BF_3·OEt_2 system, inert atmosphere, T = 77 K.

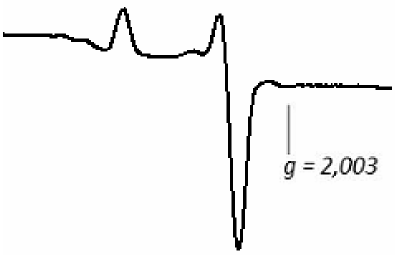

Fig.5. ESR spectrum of the Ni(COD)$_2$ – 2 BF_3·OEt_2 system, ethelene atmosphere, T = 77 K.

biaxially anisotropic signal (2) with $g_1 = 2{,}054$, $g_2 = 2{,}361$ in the spectrum. The identification of that signal requires further investigation. Same signals are observed for $Ni(COD)_2$-$BF_3{\cdot}OEt_2$ system in ethylene atmosphere. In this case there is not direct relationship between the concentration of the paramagnetic complex and the catalytic activity of $Ni(COD)_2$-$BF_3{\cdot}OEt_2$ in ethylene oligomerization too.

A similar form of ESR spectra have been taken for systems based on Ni(0)[DAD(-CH_3)]$_2$ and $BF_3{\cdot}OEt_2$ or $AlEt_2Cl$, under conditions of di- and oligomerization of ethylene (see fig.6, fig.7 and Table 1).

Fig.6. ESR spectrum of the Ni(0)[DAD(-CH_3)]$_2$ – 10$BF_3{\cdot}OEt_2$ system, ethelene atmosphere, T = 77 K.

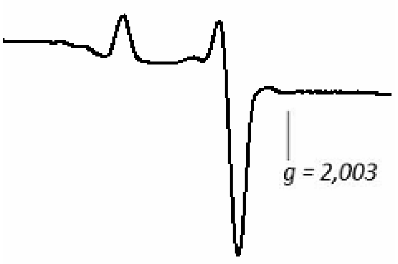

Fig.7. ESR spectrum of the Ni(0)[DAD(-CH_3)]$_2$ – 50$AlEt_2Cl$ system, ethelene atmosphere, T = 77 K.

Conclusion

By EPR spectroscopy it was found that direct relationship between the activity in the polymerization of ethylene (hydrogenation of alkenes) and concentration of paramagnetic particles is absent. Perhaps, paramagnetic particles of Ni(I) play the same function in the regeneration of active alkyl complexes in the oxidation state of nickel is 2, as in modified phosphines systems [8].

Acknowledgements

This work was supported by a base part of Government Assignment for Scientific Research from the Ministry of Education and Science, Russia (№2014/51,project code:627).

Authors gratefully acknowledge Irkutsk Supercomputer Center of the Russian Academy of Sciences http://hpc.icc.ru.

References

[1] B. Bogdanovich, Adv. Organometal. Chem., 17 (1979) 105-140.

[2] F.K. Shmidt, Kataliz kompleksami metallov pervogo perekhodnogo ryada reaktsii gidrirovaniya i dimerizatsii (Hydrogenation and Dimerization Catalyzed by Complexes of First Row Transition Metals), Irkutsk: Irkutsk. Gos. Univ., 1986, p. 230.

[3] V.C. Gibson, Spitzmesser S.K., Chem. Rev., 103 (2003) 283-315.

[4] R.R. Gagne, D.M. Ingle, Inorg.Chem., 20 (1981) 420-425.

[5] H.T. Dieck, M. Svoboda, T. Greiser, Zeitschrift für Naturforschung, Teil B: Anorganische Chemie, Organische Chemie, 36b (1981) 823-832.

[6] D. J. Krysan, P.B. Mackenzie, J. Org. Chem. 55 (1990) 4229-4230.

[7] E.Dinjus, R.Kirmse, Z. Chem., 16 (1976) 286-290.

[8] Yu.Yu. Titova, L.B. Belykh, A.V. Rokhin, O.V. Soroka, F.K. Schmidt, Kinet. Catal., 55 (2014) 37-50.

Analysis of experimental and simulated spectra of thermotropic liquid crystals

E.D. Gerts

Faculty of Physics, St.Petersburg State University, 198504, Ulyanovskaya 3, St.Petersburg, Russia

e-mail: gerts-e-d@yandex.ru

Spectral analysis has become a routine tool for modern materials researchers. NMR spectroscopy is not an exception here. The main task is usually not to get some sort of spectrum, but to interpret the one you've got. It's not a secret that the more complex material you investigate, the more complex spectra you will get. Experimentalists have to use different sophisticated techniques to simplify NMR spectra, but it doesn't reach its goal in some cases. The other way to interpret the spectra is computer simulations of substances. However in this case you usually have to use approximate methods in order to minimize the computational costs. The combination of simulations and experiments is the most efficient way nowadays.

If we want to study the structure of a thermotropic liquid crystal, even the designation of lines in spectrum to the atoms in molecule won't be a trivial task. Fig.1 shows experimental ^{13}C NMR spectra of nematic thermotropic liquid crystal ω-hydroxy-4-hexyloxy-4’-cyanobiphenyl (HO-6OCB) in isotropic and liquid crystalline phases. One can see with the naked eye that some lines in liquid crystalline spectrum absent, others are shifted in different directions. How can we assign the lines in that situation? NMR in liquids has one major advantage: dipole-dipole intramolecular interactions are averaging to zero due to fast

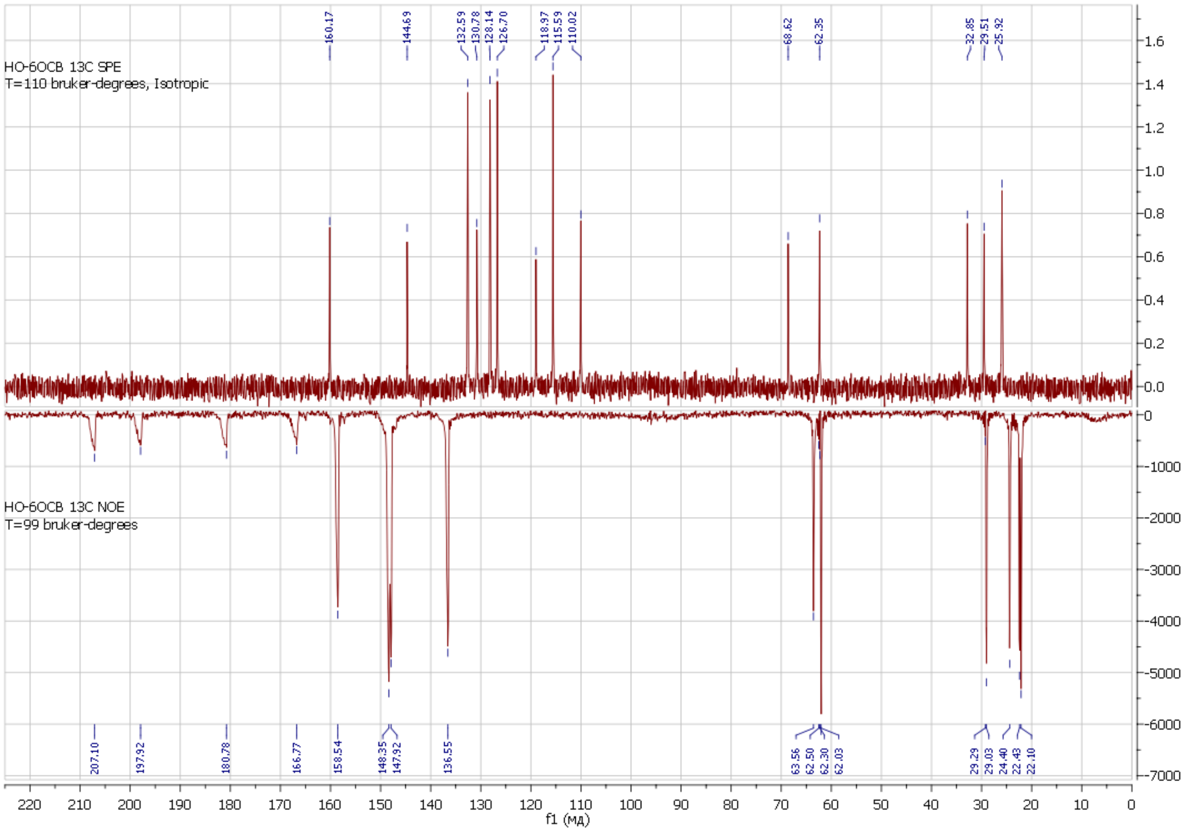

Fig.1. Experimental 13C NMR spectra of HO 6OCB in isotropic (top) and liquid crystalline (bottom) phases.

molecular reorientations and chemical shifts become isotropic. Hamiltonian in that case has only three components: Zeeman, chemical shift and J-coupling. Thus the spectrum of the liquids with low molecular weight can be calculated rather accurately. Many programs for NMR spectra analysis can predict spectra using not only direct calculations but also tables of standard chemical shifts for different molecular groups. Using certain chemical software the isotropic spectrum can be predicted and the correlation between spectral lines and carbon atoms of the molecule can be found (fig.2).

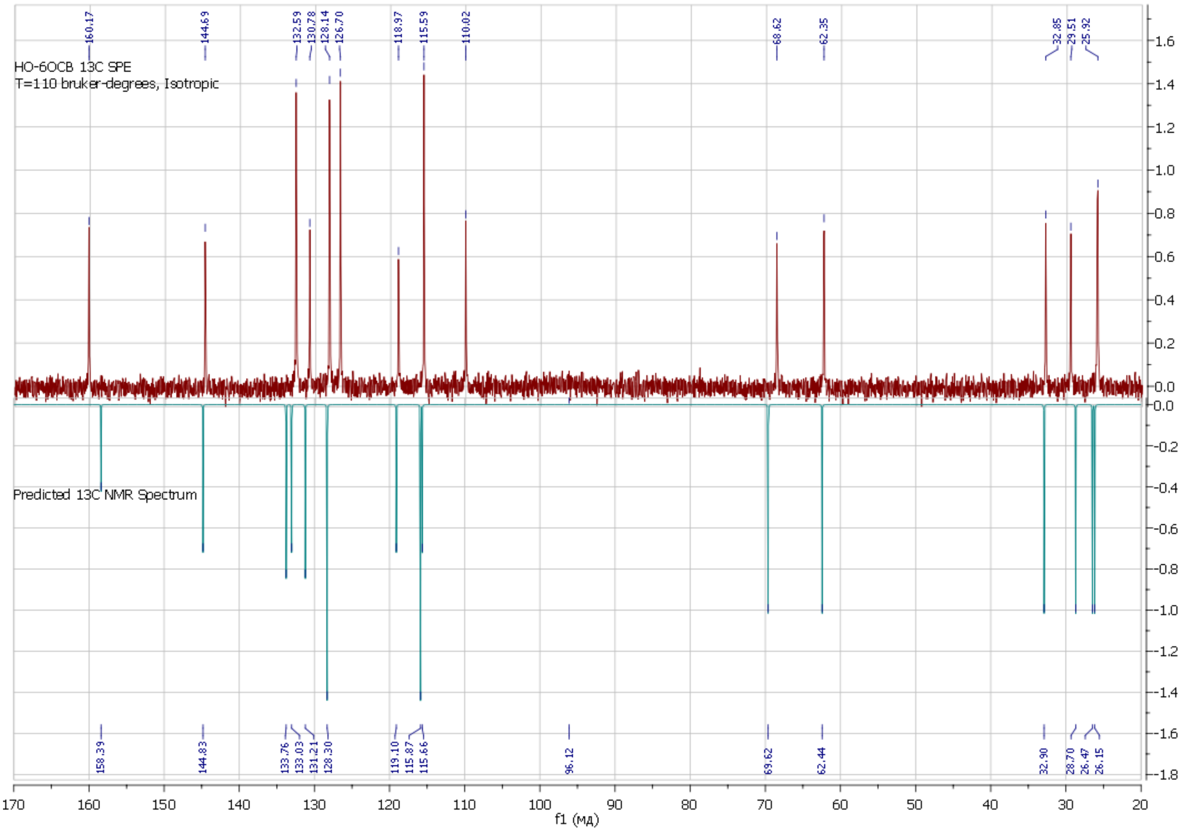

Fig.2. Experimental (top) and predicted (bottom) 13C NMR spectra of HO 6OCB.

In liquid crystalline state due to partial orientation of molecules in the magnetic field one should use heteronuclear ^{1}H-^{13}C decoupling in order to record high resolution ^{13}C spectra. Spectral line shift depends on isotropic and anisotropic parts chemical shift tensor. The temperature dependence of chemical shift can be written as:

$$\sigma(T) = \sigma_{isotropic} + \sigma_{anisotropic} S_{zz}(T), \tag{1}$$

where $\sigma_{isotropic}$ and $\sigma_{anisotropic}$ are the isotropic and anisotropic parts of chemical shift respectively, and $S_{zz}(T)$ is liquid crystalline order parameter. If we plot σ as function of S_{zz}, this will give us a set of points that can be fitted with straight line. All information we need is chemical shifts σ measured from the spectra, temperature of the substance under study for each spectrum T and temperature of nematic to isotropic transition T_{NI}. The latter can be rather rough because we will use it as an adjustable parameter. To get the values of $S_{zz}(T)$ we will use the method described in the paper of Guo and Fung[1], where

$$S_{zz}(T) = S_0 (1 - T / T_{NI})^{\gamma}. \tag{2}$$

S_0 and γ are empirical parameters. Combining formulae (1) and (2) we will get the following equation:

$$\sigma(T) = A + B \, (1 - T / T_{NI})^{C}, \tag{3}$$

where A, B and C are the fitting parameters. Varying T_{NI} in order to minimize average root mean square that is calculated as the sum of $\left(\sigma_{isotropic} - A\right)^2$ for each spectral line divided by the number of lines in the isotropic spectrum, we will get the set of lines on the $\sigma(S_{zz})$ plot (fig.3). Now we can trace how the spectral lines are shifted with the temperature. That means we can assign them with exact atoms in molecule. As we get this information we can go further with the structure analysis, using for example ^{1}H-^{13}C NMR spectra to measure dipolar couplings and compare them to the simulated ones. This will be discussed in detail at the conference.

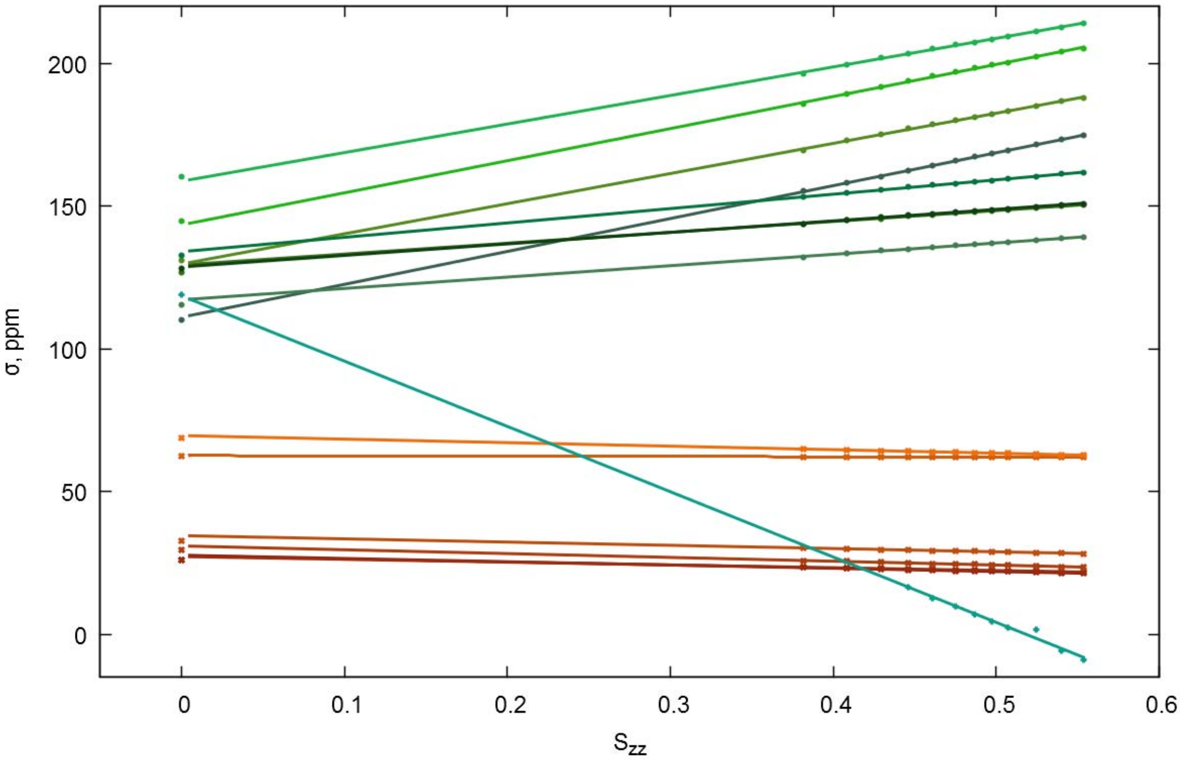

Fig.3. Spectral lines shifts as a function of S_{zz}.

It is a pleasure to thank Saint-Petersburg State University for the research grant 11.37.159.2014. Research was carried out using computational resources provided by Resource Center ”Computer Center of SPbU” (http://cc.spbu.ru).

Refrences

[1] Guo, W., & Fung, B. M. (1991). Determination of the order parameters of liquid crystals from carbon-13 chemical shifts. *The Journal of chemical physics*, *95*(6), 3917-3923.

Supramolecular chemistry of cucurbit[7]uril in solution - inclusion compounds with serine and isoleucine

E.A.Kovalenko, D.A. Mainichev

NIIC SB RAS, 630090, Lavrentiev ave., 3, Novosibirsk, Russia.

e-mail: e.a.kovalenko@niic.nsc.ru

Cucurbit[n]uril host–guest chemistry has widly been studied in strongly acidic aqueous solutions due to its extremely poor solubility in virtually all other solvents. Furthermore, most work has been devoted to the complexation of aliphatic and aromatic ammonium ions which show exceptional affinity towards the receptor. Conclusive evidence for the formation of 1:1 complexes with internal complexation of the alkyl or aryl moiety has been obtained from NMR, UV spectroscopy and calorimetric data. NMR is one of the method which can yield information about the inclusion complex on an atomic level. NMR measurements can be performed in the solution, this method offers the advantage of providing insights into dinamic processes as well as structural information at a molecular level. Complexation of CB[n] with guests molecules causes changes in the chemical shifts of the protons belonging to the CB[n] and/or guest molecule. We measured ^{1}H NMR spectra for system aminoacid (AA = L-isoleucin (Ile), L-serin (Ser), fig.1) and cucurbit[7]uril (CB[7]) in different conditions: concentration, temperatire, pH values.

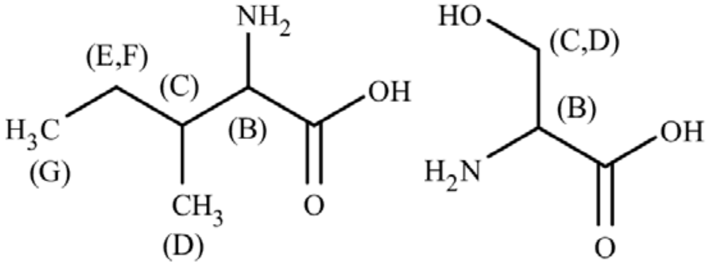

Fig.1. Isoleucine (left) and serine (right).

^{1}H NMR solution spectra (fig.2, 3) of the complex L-isoleucine and serine with CB[7] indicates the presence of an equilibrium between free aminoacid and aminoacid, included in the cucurbit[7]uril.

Investigation of the isoleucine and CB[7] system

The L-isoleucine CH-groups (B, C), CH_2-group (E, F) and CH_3-group (D, G) proton signals proton signals are broadened losing resolved multiplet structure and shifting up field relative to “pure” L-isoleucine for the molar ratios Ile:CB[7] as CB[7] concentration grows. In addition to that CH_2-group (E, F) proton signals coalesce at the lowest Ile:CB[7] ratio (0,8:1). The larger CH_2-group (E) signal up field shift indicates the deeper inclusion of this nucleus in CB[7] cavity in comparison with the CH_2-group (F) proton. In consideration of found proton chemical shifts change at various Ile:CB[7] concentration ratios, it can be assumed that the {Ile@CB[7]} inclusion complex configuration should provide experimentally obtained the largest chemical shift of the CH-group (C) signal. This effect is attained by the inclusion of L-isoleucine molecule from the side of CH-group (C) proton. To confirm proposed inclusion complex configuration, one should note that CH_2-group (E) proton adjacent to CH-group (C) proton also has the chemical shift variation at CB[7] concentration increase characteristic of deeper inclusion in cavity than sterically distant proton (F) of the same CH_2-group.

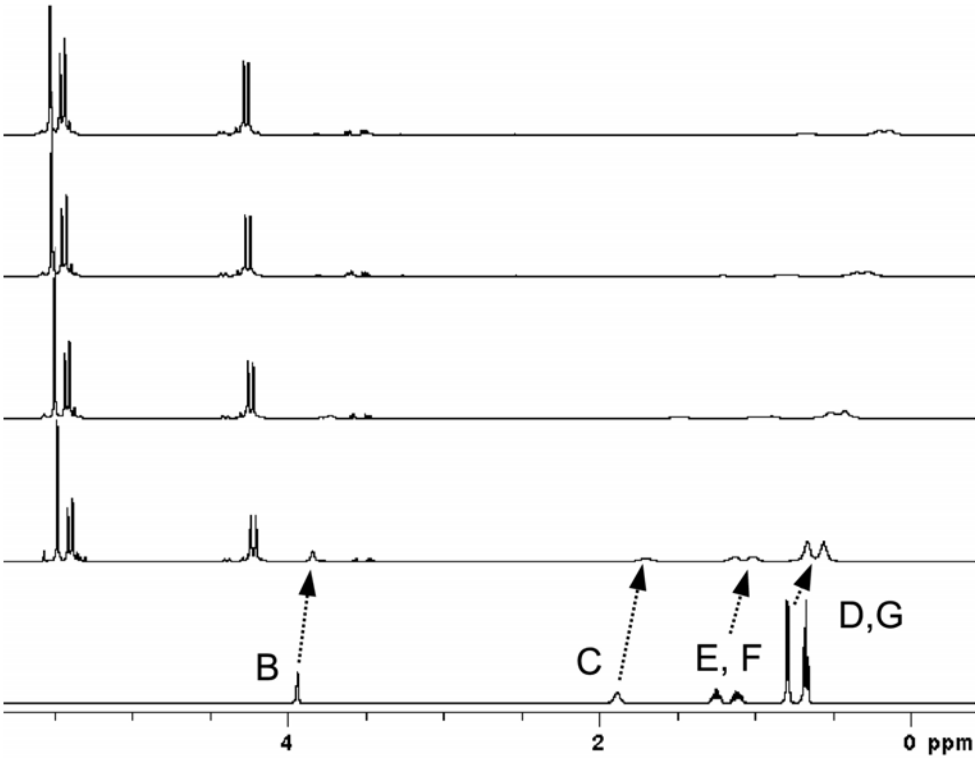

Fig.2. ^{1}H NMR spectra of L-isoleucine, Ile:CB[7] mixture in the molar ratio 3,3:1, 1,6:1, 1,1:1, 0,8:1 (upwards) in DCl/HCl solution

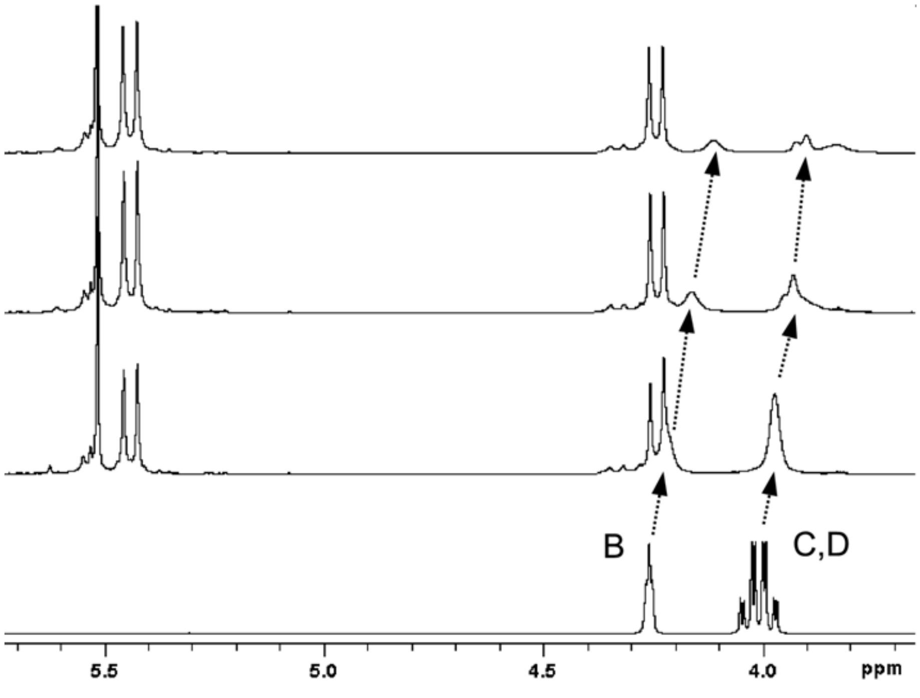

Fig.3. ^{1}H NMR spectra of L-serine, Ser:CB[7] mixture in the molar ratio 3,8:1, 1,9:1, 1,3:1 (upwards) in DCl/HCl solution.

Investigation of the serin and CB[7] system

The serine CH-group (B) proton signal is broadened losing resolved multiplet structure and shifted up field relative to “pure” serine for the molar ratios Ser:CB[7] as CB[7] concentration grows. At the first ratio 3,8:1 AB-system pattern of serine CH_2-group (C, D) protons turns into one broad signal shifted up field by 17 Hz, then at subsequent concentration changes corresponding 47 Hz and 74 Hz a pattern of broad signals appears characteristic to AB-system. This interpretation is testified by temperature increase from 300 K to 320 K producing better resolution of AB-system with the splitting signal pattern to be seen by serine CH-group (B) proton. CH_2-group (C, D) AB-system parameter estimation shows invariance of J_{CD} (as it should be expected) and increase of Δ_{CD} up to 25 Hz at CB[7] maximum concentration. Also Δ_{CD} increase is qualitatively seen from the figure where ABX-system becomes closer to ABC-system. The same character of protons (B, C, D) chemical shift change demonstrates serine inclusion uniformity into CB[7] molecule cavity conforming with the small size of serine. Change of the difference Δ_{CD} of CH_2-group (C, D) proton chemical shifts after CB[7] adding shown by AB-system parameters analysis supports inclusion of serine in CB[7].

The host–guest complexation of AA and CB[7] was confirmed by NMR spectroscopy. ^1H NMR spectra of the AA with CB[7] complexes solutions indicates a balance between free aminoacides and forms, differing in the nature of inclusion in cucurbit[7]uril.

The work is financially supported by Russian Federation President Grant MK-2514.2014.3 and RFBR 14-03-31177.

The influence of metal chelation on photoinduced generation of free radicals by anticancer quinone. NMR and CIDNP study

I.D. Markova[1,2], K.Yu. Fedotov[1], L.G. Fedenok[1], N.E. Polyakov[1], L.M. Weiner[3]

[1]Institute of Chemical Kinetics and Combustion, 630090, Institutskaya 3, Novosibirsk, Russia
[2]Novosibirsk State University, 630090, Pirogova 2, Novosibirsk, Russia
[3]Weizmann Institute of Science, 76100, Herzl St. 234, Rehovot, Israel

e.mail: irina.d.markova@gmail.com

Abstract

We have synthesized the quinone that can form complexes with various metal ions: 2-phenyl-4-(butylamino)naphtho[2,3-h] quinoline-7,12-dione (Q) to study the effect of chelation of metal ions by quinones on the generation of free radicals in photoinduced processes. The anticancer activity of this compound was demonstrated earlier. The chelate complex with Zn^{2+} ion has been investigated by optical, NMR and CIDNP techniques in the present study. The formation of the chelate complex was proved from the changes in optical absorption spectrum of quinone in the presence of Zn ions. The photoinduced oxidation of substituted dihydropyridine by quinone Q was investigated using CIDNP (chemically induced dynamic nuclear polarization) as a model reaction – analog of the biologically relevant oxidation of NADH. It was found that chelate complex of Q with Zn^{2+} ions undergo more fast decomposition under UVB irradiation by excimer laser with $\lambda = 308$ nm. The yields of free radicals and reaction products increase by three timed compared with reaction in the absence of metal ions.

Introduction

Currently, elucidation of the mechanisms of action of drug compounds at the molecular level and finding ways to increase their activity is an important scientific problem. The mechanism of action of anticancer quinones is based on the generation of free radicals inside the cell in dark conditions or under photoexcitation [1, 2].

$$Q + e \rightarrow Q^{-\bullet}$$
$$Q^{-\bullet} + O_2 \Leftrightarrow Q + O_2^{-\bullet}$$
$$O_2^{-\bullet} + O_2^{-\bullet} \xrightarrow{2H^+} H_2O_2 + O_2$$
$$O_2^{-\bullet} + H_2O_2 \rightarrow O_2 + HO^- + HO^\bullet$$
$$Q^{-\bullet} + Fe(\mathrm{III}) \rightarrow Q + Fe(\mathrm{II})$$
$$H_2O_2 + Fe(\mathrm{II}) \rightarrow HO^- + HO^\bullet + Fe(\mathrm{III})$$

Scheme 1. The scheme of the generation of free radicals under dark conditions.

$$Q + h\nu \rightarrow Q^*$$
$$Q^* + D \rightarrow Q^{-\bullet} + D^{+\bullet}$$
$$Q^* + D \rightarrow QH^\bullet + (D-H)^\bullet$$
$$Q^* + O_2 \rightarrow Q + {}^1O_2$$

Scheme 2. The scheme of the generation of free radicals under photoexcitation.

It is known that cancer cells accumulate iron at higher concentration [3]. It was demonstrated that quinone-chelator forms stable complexes with ions Fe^{3+}. Moreover, it was shown that Fe ions provide reversibility of the reduction reaction of quinone. However, it is not known as a quinone binding with metal ions would affect the reactivity of the quinone. In this regard, the purpose of the present work is to figure out how the binding with the metal ion affects the ability of the quinone to generate free radicals. We tried to investigate this question by using the NMR and CIDNP (chemically induced dynamic nuclear polarization) techniques [4]. For NMR and CIDNP studies we used diamagnetic zinc ions instead of ferric ions.

Experimental

Quinone-chelator 2-phenyl-4-(butylamino)naphtho[2,3-h] quinoline-7,12-dione was synthesized according procedure described in [1]. Deuterated solvents for NMR, CD_3OD and D_2O (Aldrich) were used as supplied. Chelating complexes of Q were prepared using $Zn(NO_3)_2$ and $ZnCl_2$ (98%, Aldrich). Optical spectra of Q and its complexes were measured in ethanol using SF-2000 (Spectrum) spectrophotometer with 1 cm quartz cuvette. The mechanism of phototransformation of Q and its complex with Zn^{2+} was elucidated by using CIDNP, UV-Vis and NMR techniques. CIDNP method was applied for detection and identification of free paramagnetic intermediates of the reaction [4]. For CIDNP experiments, samples in standard 5 mm Pyrex NMR tubes were irradiated directly in the probe of an NMR spectrometer at room temperature. An EMG 101 MSC Lambda Physik excimer laser was used as the light source for CIDNP experiments ($\lambda = 308$ nm, pulse duration 15 ns, average pulse energy 100 mJ). CIDNP and NMR spectra were detected using NMR spectrometer DPX-200 (Bruker).

Results and Discussion

At the first stage we have proved the complex formation of the quinone with the zinc ions using optical absorption method. For this purpose the optical absorption spectra of quinone were measured at various $Zn(NO_3)_2$ salt concentrations from 0.01 to 0.1 mM. One can see that optical density at 433 nm growth with increasing salt concentration up to 0.05 mM and than saturated, indicating that the equilibrium is completely shifted to the complex (fig.1).

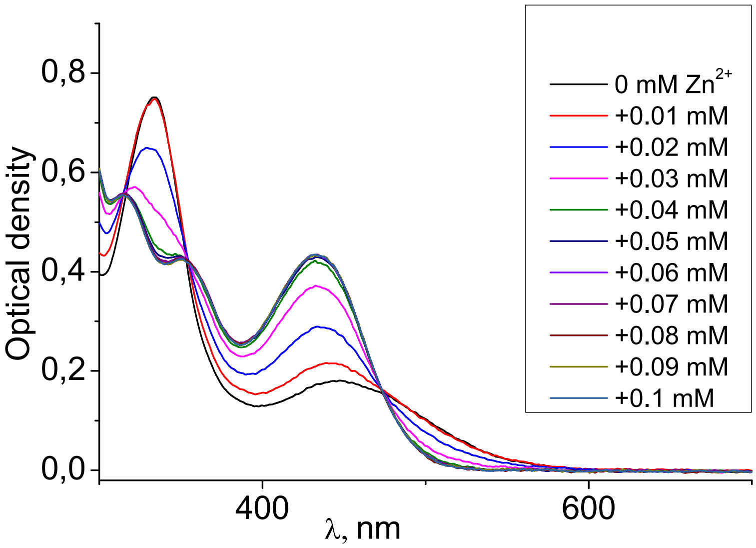

Fig.1. The absorption spectra of 0.05 mM quinone solution at different concentrations of Zn $(NO_3)_2$ (0-0.1 mM) in ethanol.

Taking into account concentration of Q = 0.05 mM and the presence of isobestic points, we can conclude that the chelate complex with Zn ions have 1:1 stoichiometry.

The second stage was the study the influence of metal binding by quinone on the efficiency of the generation of free radicals by NMR and CIDNP techniques. CIDNP method is a powerful tool for the study of photoinduced radical reactions. For this purpose the photoinduced oxidation of dihydropyridine by quinone was investigated in the presence of Zn ions. Reaction of the electron transfer of quinones with the electron donor 2,6-dimethyl-3,5-dicarbomethoxy-1,4-dihydropyridine (DHP) were examined in detail previously [5] fig.2. shows CIDNP spectra detected during quinone irradiation with DHP in the presence and in the absence of $ZnCl_2$. The main polarized lines in CIDNP spectra are 4-H and 2-CH_3 protons of initial DHP and reaction product – corresponding pyridine (Pyr, fig.2) [5]. One can see significant increase of polarization intensity in the presence of metal ions. The same changes were observed in NMR spactra of the reaction products after photolysis (fig.3). Three fold increase of the yield of reaction product was detected in the presence of Zn ions.

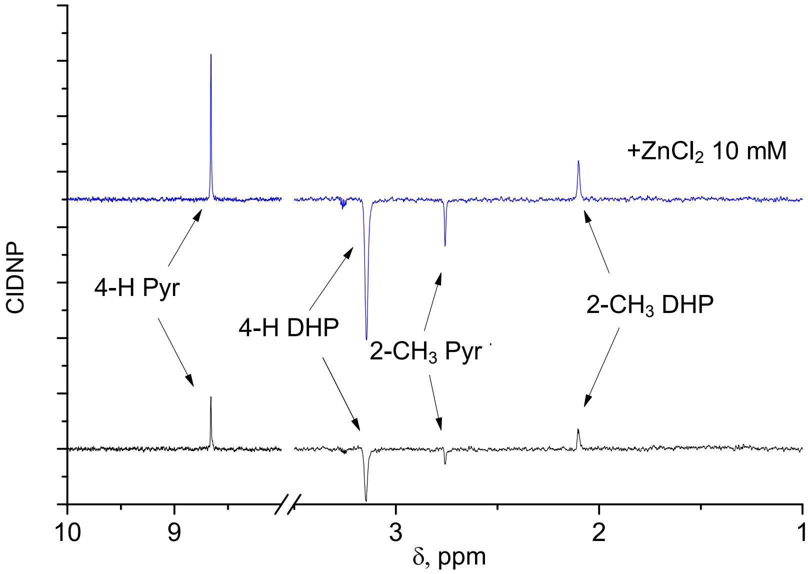

Fig.2. CIDNP spectra registrated during the photolysis of 1 mM Q solution with 4 mM DHP in the absence and in the presence of $ZnCl_2$ (10 mM) in CD_3OD. Irradiation - 256 laser pulses.

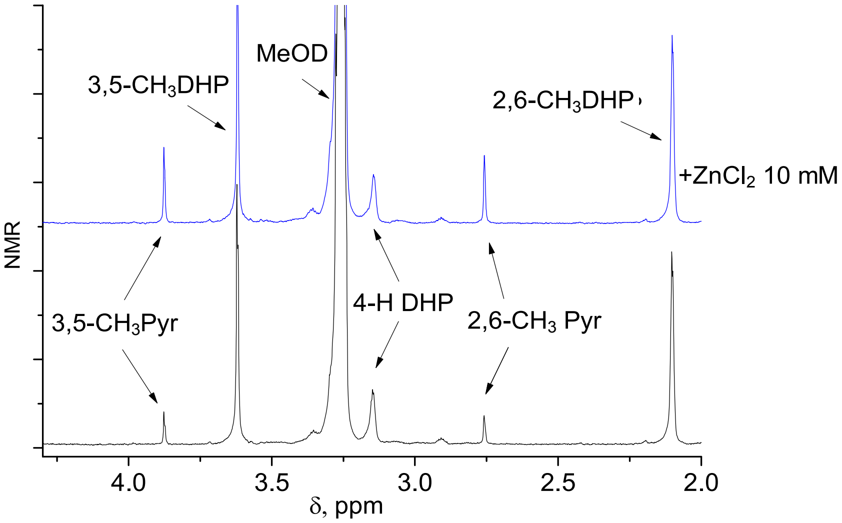

Fig.3. NMR spectra registrated after the photolysis of 1 mM Q solution with 4 mM DHP in the absence and in the presence of $ZnCl_2$ (10 mM) in CD_3OD.

From these results we can conclude that quinone-chelator forms stable 1:1 complex with Zn^{2+} ion. This complex has enhanced absorption below 500 nm and significant reduced absorption at $\lambda > 500$ nm. Increase in the CIDNP intensity and the yield of reaction product allows one to suggest that the reactivity of the quinone increased in the presence of metal ions. Taking into account that the free radicals production is the key step of anticancer activity of this quinone, the present results indicate the perspectives of its practical application.

References

[1]. Shai Rahimipour, Georg Gescheidt, Itzhak Bilkis, Mati Fridkin, Lev Weiner, Towards the Efficiency of Pharmacologically Active Quinoid Compounds: Electron Transfer and Formation of Reactive Oxygen Species. *Appl. Magn. Reson.* (2010), 37, 629–648.

[2]. Sergei I. Dikalov, Galina V. Rumyantseva, Alexander V. Piskunov, and Lev M. Weiner, Role of Quinone-Iron(III) Interaction in NADPH-Dependent Enzymatic Generation of Hydroxyl Radicals. *Biochemistry* (1992), 31, 8947-8953.

[3]. Weinberg E. D., The role of iron in cancer. *European Journal of Cancer Prevention*, (1996), 5, 19-36.

[4]. Yu.N. Molin, K.M. Salikhov, R.Z. Sagdeev, A.L. Buchachenko, eds. Spin Polarization and Magnetic Field Effects in Radical. Akademiai Kiado, Budapest, 1984.

[5]. M.B. Taraban, A.I. Kruppa, N.E. Polyakov, et al. The Mechanisms of the Oxidation of NADH Analogs. 1 .Photochemical Oxidation of N-Unsubstituted 1,4-Dihydropyridines by Various Acceptors *J. Photochem. Photobiol. A Chem.* (1993), 73, 151-156.

UV light induced photodegradation of deferiprone chelate complexes. NMR and CIDNP study

V.A. Timoshnikov[1,2], N.E. Polyakov[1]

[1]Institute of Chemical Kinetics and Combustion, Institutskaya, 3, Novosibirsk,630090 Russia;
[2]Novosibirsk State University, Pirogova 2, Novosibirsk, 630090, Russia;

e-mail: angrymodern@rambler.ru

Abstract

Deferiprone (L1) is an effective iron chelating drug which is widely used for the treatment of iron overload diseases. Although L1 itself absorb light with $\lambda < 310$ nm, the absorption spectra of its metal complexes exhibit intensive absorption band at $\lambda > 310$ nm. In the present study we have investigated the photostability of chelate complexes of this drug with Ca^{2+} and Zn^{2+} ions by using NMR and CIDNP (chemically induced dynamic nuclear polarization) techniques. It was found that L1 chelate complexes undergo fast decomposition under UVB irradiation by excimer laser with $\lambda = 308$ nm. Free radicals of L1 were detected by CIDNP method during UVB irradiation of L1 aqueous solution. We propose that the metabolism of drugs with metal binding properties can be affected by sunlight, as shown by the chelate complexes of L1 and such changes may cause phototoxic and pharmacological effects in patients undergoing treatment.

Introduction

Deferiprone (L1) or 1,2-dimethyl-3-hydroxypyrid-4-one is an active iron chelator. It is used to treat diseases associated with an excess of iron in the blood, such as thalassemia. Moreover, chelators are supposed to be effective antioxidants which prevent oxidative stress and biomolecular, subcellular, cellular and tissue damage caused mostly by iron and copper induced free radicals formation in vivo [1]. Free radical formation is a natural process leading to the production of highly reactive free radical species such as the superoxide, nitric oxide and hydroxyl radicals. Free radicals and other active oxygen species can also cause modification or damage of all known organic biomolecules including DNA, sugars, proteins and lipids [2].

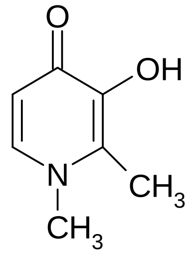

Fig.1. Molecular structure of deferiprone.

There are many studies of pharmacological properties of L1, but so far nothing was known about its photochemical activity and the structure of its radical intermediates. This information can be very important for the thousands of patients taking L1. Although L1 itself does not adsorb visible light, the absorption spectra of its Fe(III) complexes exhibit intensive absorption bands between 300 and 800 nm [3]. Irradiation of the L1-Fe(III) complexes with visible light could result in the decomposition of L1 and formation of free radicals or toxic secondary products which might cause toxicity such as photodermatitis, a toxic side effect observed with other drugs [4]. Recently it was demonstrated by CIDNP method that L1 undergoes fast decomposition via electron transfer mechanism under direct and photosensitized UV irradiation (< 310 nm) [5]. But no data exist on the influence of chelation on the photochemical stability of deferiprone. Within this context the photochemistry of L1 and its chelate complexes are of chemical, biochemical, pharmacological and toxicological importance. So, the goal of present study was to elucidate the effect of metal ions on the photochemical behavior of L1.

Experimental

Deferiprone was received from LIPOMED INC, USA. Deuterated solvents for NMR, CD_3OD and D_2O (Aldrich) were used as supplied. Chelating complexes of L1 were prepared using $CaCl_2$ and $ZnCl_2$ (98%, Aldrich). Optical spectra of L1 and its complexes were measured in ethanol using SF-2000 (Spectrum) spectrophotometer with 1 cm quartz cuvette. The mechanisms of phototransformation of L1 and its complexes with Zn^{2+} and Ca^{2+} were elucidated by using Chemically Induced Dynamic Nuclear Polarization (CIDNP), UV-Vis and NMR techniques. CIDNP method was applied for detection and identification of free paramagnetic intermediates of L1 [6]. For CIDNP experiments, samples in standard 5 mm Pyrex NMR tubes were irradiated directly in the probe of an NMR spectrometer at room temperature. An EMG 101 MSC Lambda Physik excimer laser was used as the light source for CIDNP experiments (λ = 308 nm, pulse duration 15 ns, average pulse energy 100 mJ). CIDNP and NMR spectra were detected using NMR spectrometer DPX-200 (Bruker).

Results and Discussion

To prove the formation of chelate complexes of L1 with various metal ions the optical absorption spectra of L1 ethanol solutions were measured at various concentrations of metal salts. As an example, fig.2 shows the changes of L1 absorption spectrum in the presence of various concentrations of $ZnCl_2$. As seen from fig.2 at certain concentration of salt, the absorption spectrum of L1 solution reaches saturation, which means that all L1 molecules are in the complex.

To investigate the influence of metal ions on the photodegradation of L1, NMR and CIDNP methods have been applied [6]. The combination of these methods allows to detect the formation of short-lived L1 radicals and to explore the intermediate and final products. All experiments were performed in CD_3OD. All photochemical experiments were conducted with a pulsed laser (pulse number = 256) with a wavelength λ = 308 nm. Fig.3 shows ^1H NMR spectra of L1 solution before irradiation, and after laser irradiation at 308 nm in the absence and in the

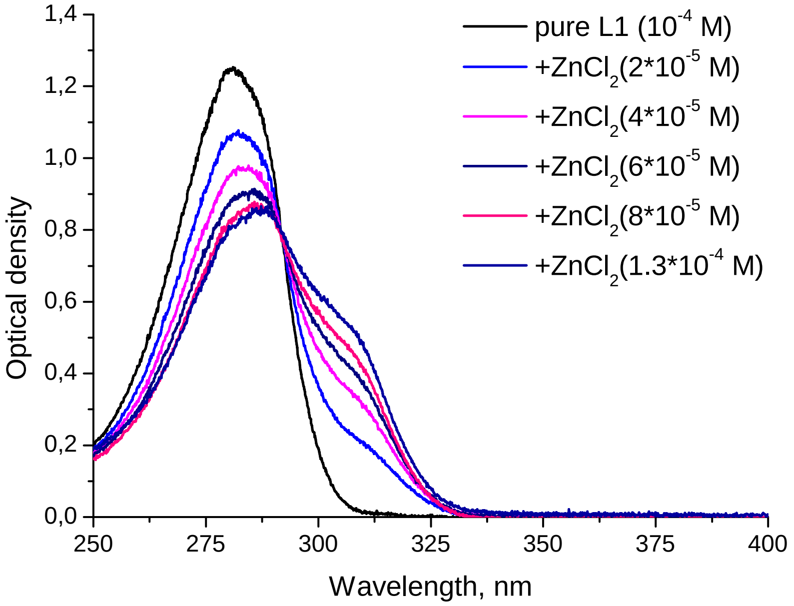

Fig.2. Absorption spectra of 0.1 mM L1 ethanol solution with different concentrations of $ZnCl_2$ (0-0.13 mM).

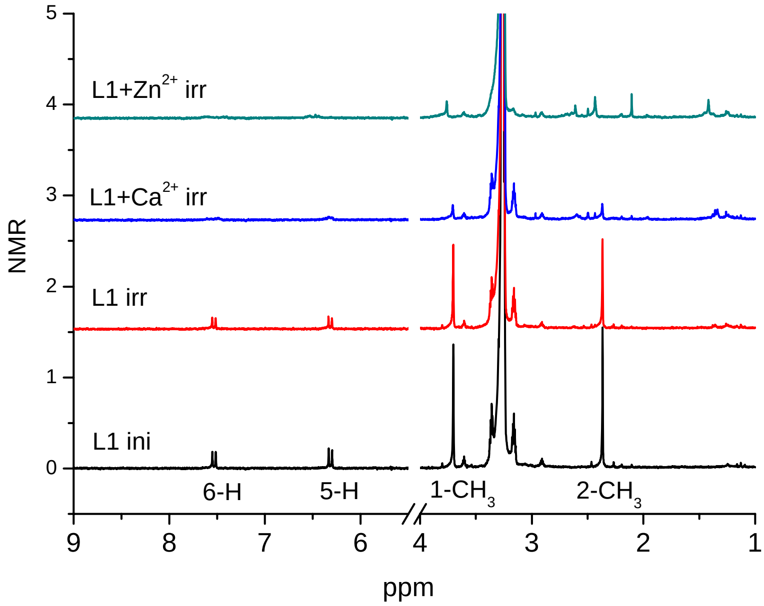

Fig.3. ^{1}H NMR spectra of 5 mM L1 methanol solution before irradiation, and after irradiation in the absence and in the presence of Zn and Ca ions (5 mM).

presence of $CaCl_2$ and $ZnCl_2$. It can be seen that the photodegradation degree and the total yield of products is significantly increased in the presence of metal ions. Previously it was shown that the mechanism of this reaction includes the step of electron transfer between two L1 molecules [5], so we can suggest that two factors contribute to the increase of the reaction efficiency. Namely, the increase in the optical density of the L1 solution in presence of metal ions, and close location of two deferiprone molecules to each other, facilitating the reaction.

Fig.4 shows the CIDNP spectra detected during photolysis of L1 methanol solution

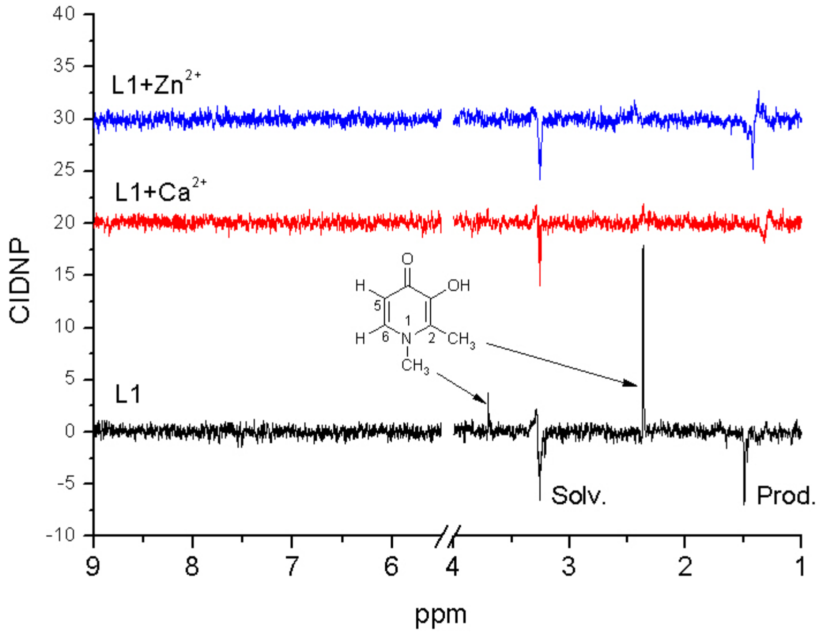

Fig.4. CIDNP spectra recorded during photolysis of L1 methanol solutions and its complexes with Zn and Ca ions.

(5 mM) in the absence and in the presence of Zn and Ca ions (5mM). CIDNP spectrum detected during laser irradiation of pure deferiprone shows polarized lines of methyl protons of initial deferiprone (absorption) as well as methyl protons of reaction product (1.5 ppm). As it was shown in [5], most of the reaction products of L1 photolysis are photochemically unstable and undergo further phototransformations. The only stable product is 1,2-dihydro-2,3,4-trihydroxy-1,2-dimethylpyridine. The most notable effect of metal chelation is the disappearance of polarization of initial deferiprone in the presence of metal ions which indicates that the reaction became irreversible in the complex.

Conclusions

The chelate complexes formation of deferiprone with metal ions Ca^{2+} and Zn^{2+} was proved by optical absorption and NMR spectroscopy. The formation of chelate complexes leads to an additional long-wavelength absorption band, which greatly accelerates the photodegradation of deferiprone when irradiated with ultraviolet light at a wavelength of 308 nm. Photodegradation proceeds via free radical intermediates.

Referenses

[1] Kontoghiorghes, G. J. Prospects for introducing deferiprone as potent pharmaceutical antioxidant. *Front. Biosci. (Elite Ed),* 1:161-178; 2009

[2] Denisov, E. T.; Afanas'ev I. B., eds. Oxidation and antioxidants in organic chemistry and biology. Boca Raton: CRC Press, Taylor and Francis group; 2005.

[3] Kontoghiorghes, G. J. The design of orally active iron chelators for the treatment of thalassaemia. PhD thesis, University of Essex, Colchester UK: British Library Microfilm No D66194/86; 1982: 1-243.

[4] Tonnesen, H. H., Ed. The Photostability of Drugs and Drug Formulations. London: Taylor & Francis; 2002.

[5] V. A. Timoshnikov, V. I. Klimentiev, N. E. Polyakov, G. J. Kontoghiorghes, Photoinduced Transformation of Iron Chelator Deferiprone: Possible Implications in Drug Metabolism and Toxicity. Journal of Photochemistry & Photobiology, A: Chemistry, DOI: 10.1016/j.jphotochem.2014.05.012

[6] Yu.N. Molin, K.M. Salikhov, R.Z. Sagdeev, A.L. Buchachenko, eds. Spin Polarization and Magnetic Field Effects in Radical. Akademiai Kiado, Budapest, 1984.

Investigation of kagome-compound $YBaCo_3AlO_7$ by magnetic methods

M.F. Iakovleva[1,2], E.L. Vavilova[1]

[1]Zavoisky Physical-Technical Institute, Pionerskaya str., Kazan, Russia
[2]Kazan (Volga region) Federal University, Kremlevskaya str., Kazan, Russia

e-mail: ymf.physics@gmail.com

Introduction

The quantum kagome lattice is a fundamental but experimentally elusive frustrated magnet. Neutron spectroscopy now reveals the ground state and elementary excitations of a kagome lattice in which the quantum spins form an exotic pinwheel valence-bond state, spin liquids etc. [1]. $YBaCo_3AlO_7$ is a metal oxide compound with a magnetic kagome substructure. We have investigated the ground state and low energy spin dynamics of this material by nuclear magnetic resonance spectroscopy. These experiments were complemented by measurements of the field dependence of the static susceptibility.

Structure

In this work kagome-compound $YBaCo_3AlO_7$ was investigated. The compound has a layered structure. Cobalt plane represent kagome lattice. But there are possibilities for magnetic coupling between the kagome layers. For the purpose of separating kagome planes were invited to use the aluminium ions. Aluminium could enter the site between the planes, thus destroying the magnetic interactions between Kagome layers [2].

Experiments and results

The ground state of $YBaCo_3AlO_7$ has been studied using local methods, including nuclear magnetic resonance (NMR). NMR measurements were performed on a single crystal at different temperatures. Al NMR spectra were obtained at fixed frequency $f = 85{,}42$ MHz and $f = 33{,}28$ MHz (at $H = 7{,}7$ T and $H = 3$ T respectively) by sweeping the magnetic field. We used a standard Hahn-Echo sequence, and integrated the echo at each field step.

At high temperatures the spectrum has a well-resolved quadrupole structure. At temperatures below 10 K, a sharp line broadening was observed. Also the temperature dependence of the spin-lattice relaxation rates was measured at both frequencies. The most important result of these experiments was that the dependence of relaxation rate $T_1^{-1}(T)$ has a peak which shifts with frequency. Measurements of the field dependence of the static susceptibility also has a peak. Spin glasses are systems whose magnetic moments freeze at low temperature into random orientations without long-range order [3]. It is generally accepted that both frustration and disorder are essential ingredients in all spin glasses.

Conclusion

The absence of a well resolved structure of ^{27}Al NMR line at low temperatures and characteristic features of the temperature dependences of the relaxation rates confirm the scenario [1] that only short-range quasi static correlations occur in the system but not a long-range antiferromagnetic ordering. The realisation of a spin-liquid state is not evident in our data.

Our conclusions are supported by measurements of the dynamic susceptibility [2], which also has a maximum of temperature characteristic that depends on the frequency. The

X-ray diffraction data shows, that we have Al / Co mixed crystal, and most probably it is a structural disorder that leads to a large defect of the magnetic subsystem. For that reason in the compound $YBaCo_3AlO_7$ any conventional or frustrated long-range order does not arise and a spin-glass state is implemented.

References

[1] Christian Rüegg ., *Nature Physics* 6, 837–838 (2010)

[2] M. Valldor et al., *Phys.review B* 78, 024408 (2008)

[3] E. Goremychkin et al., *Nature Physics* 4, (2008)

Crystal field analysis and magnetic properties of the EuF_3 Van-Vleck paramagnet

A.V. Savinkov, A.V. Dooglav, D.P. Pavlov, B.Z. Malkin, M.S. Tagirov

Institute of Physics, Kazan Federal University, Kazan, Russia

e-mail: Andrey.Savinkov@gmail.com

Dielectric Van-Vleck paramagnets are the crystal substances where the crystal field splits the ground $^{2S+1}L_J$ multiplet into electron energy levels so that the ground state is a singlet or nonmagnetic doublet separated from excited energy levels by the interval of 10 – 100 cm^{-1}. Most of studied Van-Vleck paramagnets are the compounds of rare-earth ions with even number of electrons on the not filled electron shell 4f: Pr^{3+}, Eu^{3+}, Tb^{3+}, Ho^{3+} and Tm^{3+} (Re^{3+} ions). The 4f electron shell of rare-earth Van-Vleck paramagnets is polarized at the external magnetic field gathering a nonzero magnetic moment which produces an internal magnetic field at the nucleus. The internal field is much stronger than the external field in most of Van-Vleck paramagnets having Pr^{3+}, Tb^{3+}, Ho^{3+} and Tm^{3+} ions. The Eu3+-based Van-Vleck paramagnets are of interest because the internal field nearly cancels the external field [1]. In this study we report on results of the crystal filed analysis and magnetic properties of the Van-Vleck paramagnet EuF_3 having the orthorhombic crystal structure *Pnma* (62) studied by ^{19}F NMR in powder samples. The crystal field at Eu^{3+} position, spectra of electronic excitations of the Eu^{3+} ions and magnetic interactions between the rare-earth and fluorine ions have been on the focus of the study.

The set of crystal field parameters for the Eu^{3+} ions with the C_S point symmetry in EuF_3 has been estimated using the semi-phenomenological exchange charge model, and then corrected by comparing the results of calculations of crystal field energies with the experimental data.

Transitions of the 4f-electron shell to the excited state and back to ground state occurs at increasing temperature giving rise to fluctuations of Re^{3+} electron magnetic moment. These fluctuations affect the NMR spectrum and nuclear relaxation of ^{19}F through the dipole-dipole and the transferred hyperfine interactions. The ^{19}F NMR spectra were measured in EuF_3 powders in the static magnetic field $B_0 = 5965$ G at the NMR frequency of 23.9 MHz. The NMR spectra taken at temperatures 4.2 K, 77 K and 300 K were recovered by the Fourier transform of the spin-echo patterns. The ^{19}F NMR line was found very narrow (~10 G at 4.2 K and ~7 G at 300 K). This suggests that the dipole and transferred hyperfine magnetic fields induced by the Eu^{3+} ions are negligible because the Eu^{3+} ions are mainly in the ground nonmagnetic state $^7F_0$ at low temperatures, and at $T = 300$ K these fields are averaged to zero due to very fast fluctuations of the Eu^{3+} magnetic moments.

Temperature dependencies of ^{19}F nuclear spin-lattice relaxation (NSLR) rates in the EuF_3 powder samples were measured in the temperature range 55 – 300 K. For Eu^{3+} ion in EuF_3, the energy gap between the ground and the first excided states is ~370 K. Therefore, excited 4f electrons of Eu^{3+} ion can induce the fluctuating magnetic fields at the ^{19}F nuclei only at rather high temperatures. It is seen in fig.1 that the $T_1^{-1}(T)$ increases rapidly at temperatures $T > 110$ K. Values of $1/T_1$ have been found in the range from 5 to 50 s^{-1}, i.e. the ^{19}F nuclear spin-lattice relaxation is rather slow as compared to relaxation rates in other Van Vleck paramagnets. We suggest that the increase of $T_1^{-1}(T)$ in the temperature range 110 – 300 K is determined by weak fluctuations of local magnetic fields induced by Eu^{3+}

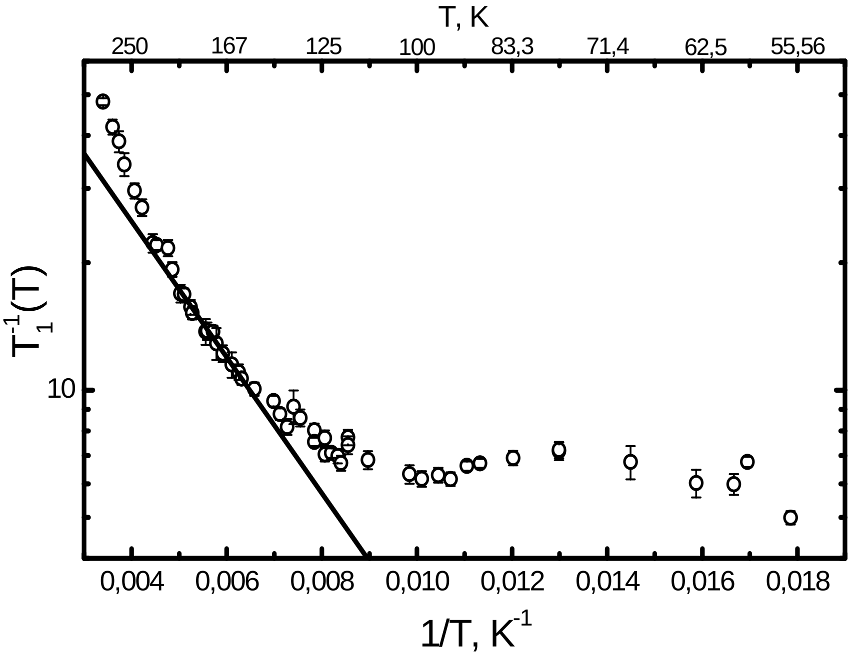

Fig.1. ^{19}F NSLR rate vs. 1/T in EuF_3 powder

magnetic moments. Solid line in fig.1 corresponds to the function $T_1^{-1} \sim \exp(-\Delta_1/T)$ with $\Delta_1 = 370$ K. One can see that the ^{19}F NSLR in EuF_3 is not explained only by the thermal excitations of the Eu^{3+} ions to the lowest excited crystal field level. Most likely the influence of other excited levels should be taken into account. Other mechanisms of ^{19}F NSLR in EuF_3 will be discussed.

The work was partly supported by the RFBR grants 12-02-00372-a and 14-02-00826.

References

[1] R.J. Elliott, Proc. Phys. Soc. B. 70, p.119-123 (1957).

ESR investigation of $YbNi_2$ nanometric alloys

E.M. Gataullin[1], V.A. Ivanshin[1], D.P. Rojas[2], L. Fernández Barquín[3]

[1]Institute of Physics, Kazan Federal (Volga region) University,
Kremlevskaya str. 18, 420008 Kazan, Russia
[2]Departamento de Física e Instalaciones-ETSAM, Universidad Politécnica de Madrid, Av. Juan Herrera, 4, Madrid 28040, Spain
[3]DCITIMAC, Facultad de Ciencias, Universidad de Cantabria, Av. de los Castros s/n, Santander 39005, Spain

e-mail: edikgat@gmail.com

We report changes on the structural and magnetic properties of the heavy-fermion $YbNi_2$ [1] crystalline alloy when submitted to high-energy ball milling. The sample was characterized by means of DC magnetic susceptibility and electron spin resonance (ESR) of the intrinsic Yb^{3+}. The analysis of the x-ray diffraction data shows a reduction of the particle size down to 12 nm for 20 h of milling time. The ferromagnetic (FM) contribution practically dissapears and a new magnetic phase arises at lower temperatures, below T_C, as observed in other rare earth FM alloys under mechanical milling [2]. In the vicinity of T_C = 10.5 K, the ESR parameters (linewidth and g-factor) show distinct anomalies, which can be associated with a presence of strong magnetic fluctuations at an onset of FM ordering. The Orbach-Aminov spin-lattice relaxation processes with the involvement of the first excited crystalline electric field level of Yb^{3+} at $\Delta \approx 75$ K dominate the electron spin dynamics of $YbNi_2$ in the paramagnetic phase [3]. The Yb^{3+} ions in bulk $YbNi_2$ are primarily located in almost perfect cubic crystal field. Data of ESR measurements clearly reflect different types of distortions observed in the core and the surface regions of the nanocrystallites. The sensitivity of ESR is detected both through direct measurement of resonance field and from the linewidth of the resonance itself.

References

[1] D. P. Rojas et al., *Solid State Commun.* 152 (2012) 1834.
[2] D. P. Rojas et al., *J. Phys: Cond. Matter* 19 (2007) 186214.
[3] E.M. Gataullin et al., *JPS Conf. Proc.*, to be published.

List of authors

Table of Contents

TABLE OF CONTENTS

TABLE OF CONTENTS

ACTUAL PROBLEMS OF MAGNETIC RESONANCE AND ITS APPLICATION

XVII International Youth Scientific School

Program
Lecture Notes
Proceedings

Kazan
22 – 27 June 2014

Подписано в печать 16.06.2014.
Бумага офсетная. Печать цифровая.
Формат 60x84 1/8. Гарнитура «Times New Roman». Усл. печ. л. 9,64
Уч.-изд. л. 8,17. Тираж 100 экз. Заказ 66/6

Отпечатано с готового оригинал-макета
в типографии Издательства Казанского университета

420008, г. Казань, ул. Профессора Нужина, 1/37
тел. (843) 233-73-59, 233-73-28